Off-shore Photovoltaics Performance

Design and integration of an off-shore off-grid system and an on-land system for comparison on photovoltaic performance

A. de Gruijter Eguíluz

Sustainable Energy Technology MSc Thesis
in collaboration with PVMD research group (TUDelft)
and Oceans of Energy

TUDelft

Off-shore Photovoltaics Performance

Design and integration of an off-shore off-grid system and an on-land system for comparison on photovoltaic performance

by

A. de Gruijter Eguíluz

to obtain the degree of Master of Science
at the Delft University of Technology,
to be defended publicly in academic year 2022-2023.

Student number:	4675835	
Project duration:	March 18, 2022 – April 16, 2023	
Thesis committee:	Prof. dr. ir. A.H.M. (Arno) Smets,	TU Delft Full Professor.
	Dr. ir. Laura Ramírez Elizondo,	TU Delft Assistant Professor.
	Dr. ir. Hesan Ziar,	TU Delft Assistant Professor, thesis supervisor.
	Ir. Dora de Jong,	Oceans of Energy, daily supervisor.

This thesis is confidential and cannot be made public at least until April 16th, 2025.

Abstract

The purpose of this thesis research was to perform a photovoltaic (PV) performance assessment and comparison between a small-scale land-based PV system and an off-shore off-grid floating PV system. Also from this research design guidelines for off-grid off-shore floating PV systems were developed. The research experiment was carried out in The Netherlands, with one system floating in the North Sea and one system standing on-land. To be able to have a fair comparison two identical 4.32 kW PV arrays were built simultaneously, consisting of two parallel strings, each with six 360 Wp bifacial PV modules connected in series. Each of the two systems was equipped with a monitoring set up consisting of temperature sensors, pyranometers, reference cells, power meters and an inclinometer for the off-shore system. Additional measurements concerning wind, wave and water temperatures off-shore were taken from the Royal Netherlands Meteorological Institute (KNMI) weather station Hollandse Kust Zuid Alpha (HKZA), which was situated in the same region of the North Sea. The two PV experimental set-ups were compared between 15th November 2022 and 1st January 2023. On the DC side being measured, the on-land PV system recorded 96.3 kWh while the off-shore PV system recorded 93.4 kWh, which was subject to lower irradiance levels. The performance ratio (PR) found off-shore during the period of research was 0.92 while on-land this value was 0.934 between the two PV strings, however these values should be re-validated due to a potential malfunction of the Hall effect sensors. The PR off-shore was higher than expected from literature for a similar system being simulated. With respect to module temperatures recorded off-shore, a low thermal variation was found when compared to on-land, with the average module temperature off-shore being 11.3 ^{o}C higher than on-land during this period of research. Ambient temperatures as well as irradiance on the Plane of Array (POA) were found to have a larger influence on the module temperatures for the on-land system than for the off-shore system. Module temperatures throughout the PV array off-shore were found to be the equal. Additionally, four OFPV linear regression models derived from the empirical measurements were presented and compared with existing empirical FPV models found in literature, which were found to be subject to be site and design specific. Additional environmental effects on the module temperature concerning wind, wave and water temperatures were presented, highlighting the dominant effect of the water with respect to module temperatures. The off-shore floating PV system withstood waves of up to 3.4 meters while the system maximum tilts were found to be to be 13.33 ^{o} and 17.36 ^{o} for the X and Y axis of the PV floater respectively. No permanent soiling due to bio-fouling or salt deposition was detected after one month of measurements but dynamic soiling, in the form of bio-fouling, snow and water splashing were identified, with the latter being the most predominant. The work done through this thesis lays the foundation for further research and comparisons of off-shore floating PV systems. It is recommended to perform this comparison for a period of a complete year to yield annual conclusions.

Acknowledgements

The need towards meeting the Paris Agreement goals and keep global temperatures under $2\,^{\circ}C$ greatly motivated me to pursue the completion of this Master in Sustainable Energy Technologies, being involved and learning towards the innovation of renewable energies to achieve a faster energy transition, as time is running out.

A first thank you for my family, especially my parents O. de Gruijter and M. Eguiluz, as well as my sisters E. de Gruijter, I. de Gruijter and S. de Gruijter, who have always been supportive throughout my education, working and helping with the best advice and education possible. Their support was always felt and thanks to them I have been able to develop, learn and take the academic steps that led me to where I stand today.

Moreover, I want to thank M. Ford, with the unconditional support and positiveness shared and who has seen me through the highs and lows. Meeting you has made this time together incredible and unique and I look forward to what is yet to come.

Furthermore, I would like to give a special thanks to my grandparents and especially to L. de Gruijter, who inspired me to pursue the same career path with respect to energy technologies. I look up to him in both a professional and personal level and he is a great guidance for the future that is coming next.

I also want to thank TU Delft with all the support provided, my thesis supervisor Dr. ir. H. Ziar and daily supervisor Ir. D. de Jong, with whom this research was achieved. Thank you to Oceans of Energy for the help provided to be able to carry out this project.

And I would like to thank all those friends and family, when reading this they know who they are, who have been an irreplaceable part of my life to reach this stage. I am incredibly grateful to have them in my life and I look forward to future enjoyable times together.

An last but not least, a thank you to global leaders placing climate change on top of the agenda over short-term, personal and political interests.

Acronyms

PV	Photovoltaics
FPV	Floating Photovoltaics
OFPV	Off-shore Floating Photovoltaics
GHG	Greenhouse gas
OOE	Oceans of Energy
PVMD	Photovoltaic Materials and Devices
KNMI	Koninklijk Nederlands Meteorologisch Instituut
HKZA	Hollandse Kust Zuid Alpha
WEO	World Energy Outlook
NZE	Net Zero Emissions
CN	Carbon Neutral
BAU	Business as Usual
IEA	International Energy Agency
UNFCCC	United Nations Framework Convention on Climate Change
COP	Convention on Climate Change
TRL	Technology Readiness Level
UV	Ultra Violet
PHES	Pumped Hydro Energy Storage
LCOE	Levelized Cost of Electricity
IEC	International Electrotechnical Commission
ISO	International Organization for Standardization
DC	Direct Current
AC	Alternate Current
MPPT	Maximum Power Point Tracker
BB	Battery Bank
RTD	Resistance Temperature Detector
PTC	Positive Temperature Coefficient
NTC	Negative Temperature Coefficient
VRM	Victron Remote Management
SR	Soiling Ratio
TL	Transmission Loss
IP	Ingress Protection
DHCP	Dynamic Host Configuration Protocol
TCP	Transmission Control Protocol
ESS	Energy Storage System
CAD	Computer Aided Design
STC	Standard Test Conditions
NOCT	Nominal Operating Cell Temperature
PR	Performance Ratio
GHI	Global Horizontal Irradiance
DHI	Diffuse Horizontal Irradiance
DNI	Direct Normal Irradiance
POA	Plane of Array

Contents

1 Introduction **1**
1.1 The role of the solar energy industry . . . 1
1.1.1 The Paris Agreement . . . 1
1.1.2 Solar energy towards 2050: Net Zero Emissions . . . 2
1.2 Floating photovoltaics (FPV) . . . 5
1.2.1 Off-shore floating photovoltaics (OFPV) . . . 7
1.3 Oceans of Energy (OOE) . . . 7
1.4 Research project . . . 8
1.4.1 Research motivation . . . 8
1.4.2 Research objectives . . . 8
1.4.3 Research questions . . . 9
1.4.4 Research phases . . . 9

2 Background **11**
2.1 Floating photovoltaics (FPV) . . . 12
2.1.1 FPV potential . . . 12
2.1.2 FPV design classification . . . 13
2.1.3 FPV integration with hydropower reservoirs and investment costs . . . 15
2.2 Off-shore Floating Photovoltaics (OFPV) . . . 16
2.2.1 OFPV technologies . . . 16
2.2.2 Off-grid PV systems . . . 19
2.3 PV performance indicators . . . 20
2.3.1 FPV models for module temperature prediction . . . 23
2.4 Monitoring technologies of interest . . . 24

3 Methodology **29**
3.1 Methods . . . 30
3.1.1 Requirements and limitations . . . 30
3.1.2 Site selection and positioning . . . 30
3.1.3 PV systems design . . . 32
3.1.4 Monitoring devices selection . . . 32
3.1.5 Data analysis procedures . . . 35
3.1.6 Measurements and results validations . . . 37
3.2 On-land experimental set-up . . . 38
3.2.1 Specific requirements and limitations . . . 38
3.2.2 Components . . . 38
3.2.3 Electrical design . . . 39
3.2.4 Design integration and construction . . . 39
3.3 Off-shore experimental set-up . . . 42
3.3.1 Specific requirements and limitations . . . 42
3.3.2 Balance of System (BoS) components . . . 42
3.3.3 Off-shore protection . . . 44
3.3.4 Electrical design . . . 45
3.3.5 Design integration and construction . . . 46
3.4 Dry testing cycles . . . 51
3.5 Experiment . . . 52
3.5.1 Protocol during experiment . . . 52

4 Design guidelines for an off-shore off-grid PV system 53
4.1 Design guidelines overview . . . 53
4.2 Project procedures . . . 54
4.2.1 Policy, regulatory and verification considerations . . . 54
4.2.2 Planning and site assessment . . . 55
4.3 Protection protocols . . . 55
4.3.1 Ingress protection (IP) levels . . . 55
4.3.2 IP against site-specific environmental influences . . . 56
4.4 PV module selection for highly humid sea environments . . . 58
4.5 Orientation, tilt and mismatch considerations . . . 60
4.6 Lightning protection recommendations . . . 62
4.7 Mooring and anchoring types for selection . . . 63
4.8 Off-grid PV system design considerations . . . 65
4.8.1 Solar irradiance availability at location . . . 65
4.8.2 Load assessment . . . 67
4.8.3 System sizing and component selection . . . 67
4.9 OFPV system monitoring, safety and maintenance . . . 71
4.9.1 Application of guidelines . . . 71

5 Results and discussion 73
5.1 Experimental results overview . . . 73
5.2 Power performance . . . 75
5.2.1 DC power output . . . 75
5.2.2 Voltage and current . . . 81
5.2.3 Irradiance at POA . . . 82
5.2.4 Efficiency . . . 84
5.2.5 Performance ratios . . . 87
5.2.6 Capacity factors . . . 87
5.2.7 PV Energy . . . 88
5.2.8 Balance of Systems (BoS) performance . . . 90
5.2.9 Power performance summary . . . 91
5.3 Temperature measurements . . . 92
5.3.1 Ambient temperature measurements and comparison with climate data . . . 92
5.3.2 Module temperatures off-shore against on-land . . . 94
5.3.3 Module temperatures influence by G_{POA} . . . 97
5.3.4 Module temperatures influence by ambient temperatures . . . 100
5.3.5 Module gradient temperatures . . . 102
5.3.6 Floater gradient temperatures . . . 104
5.3.7 OFPV thermal models derived for off-shore conditions . . . 106
5.3.8 Temperature measurements summary . . . 111
5.4 Environmental effects . . . 112
5.4.1 Off-shore water, wind and wave effects on module temperature . . . 114
5.4.2 Tilt effects . . . 120
5.4.3 Soiling and shading effects . . . 123
5.4.4 Environmental effects summary . . . 125

6 Conclusions and recommendations 127

A Background additional information 131
A.1 IEA additional graphs . . . 131
A.2 FPV investment costs and LCOE . . . 132
A.3 Empirical PV models identified in literature for prediction of cell and module temperatures 133
A.4 PV module temperature models expansion . . . 135
A.4.1 Steady state and Duffie-Beckman thermal models . . . 135
A.4.2 Fluid dynamic model adaptations for FPV . . . 136

B Additional monitoring devices considered 139

C Methodology additional information 141
C.1 Loss of Load probability additional calculation 144

D Meteonorm outputs 145

E Additional results 147
E.1 Sensors operational status during experiment period 147
E.2 Additional data from KNMI weather station HKZA 148
E.3 Additional power graphs 149
E.4 Additional voltage and current graphs 151
E.5 Irradiance at the Plane of Array comparison for each PV system 153
E.6 Calculation of module efficiencies 154
E.7 Additional power and irradiance comparison between PV strings 156
E.8 Additional PV energy graphs 157
E.9 PT100 test experiment: PT100 measurements of off-shore system before deployment . . 158
E.10 Ambient temperature and irradiance influence on module temperatures 159
E.11 OFPV linear regression PV thermal models additional information 161
E.12 Module temperatures off-shore against environmental influences on timeline plots 164
E.13 Horicatcher set-up and Meteonorm outputs on-land including custom horizon. 167

F Victron MPPT 450-100 Outputs 169
F.1 PV production and battery storage 169
F.1.1 3 day selection 171
F.2 Additional outputs 172

G KNMI Weather station HKZA additional information 177

H Datasheets 179

List of Figures

1.1 IEA Net Zero Emissions scenario on CO_2 emissions by sector [Mt CO_2] from 2019 to 2050 (IEA, 2021b). 3
1.2 IEA Net Zero Emissions scenario on total energy supply $[EJ]$ from 2019 to 2050 (IEA, 2021b). 3
1.3 IEA Net Zero Emissions scenario on electricity generation by technology $[TWh]$ from 2019 to 2050 (IEA, 2021b). 3
1.4 Global investment in electricity networks in the Net Zero Emissions scenario (IEA, 2021a). 4
1.5 Solar PV and wind installed capacity in the Net Zero Emissions scenario (IEA, 2021a). . 4
1.6 Elemental components of a floating photovoltaic system. Adapted from Vo et al., 2021. 5
1.7 Oceans of energy OFPV system technology (OOE, 2023a). 7
1.8 Research project phases overview, with background (1), methodology (2), design guidelines (3) and results analysis and comparison (4). 10

2.1 Background chapter overview presenting 3 sections divided into floating PV (blue), PV performance (green) and monitoring technologies (orange). 11
2.2 Logarithmic plot of the global yearly produced FPV energy from 2009 (blue, 2019 to be confirmed) and forecast up to 2025 (yellow). Adapted from Cazzaniga and Rosa-Clot, 2021. 12
2.3 Schematic of typical stand-alone large-scale FPV systems and key components (Lee, 2020). 13
2.4 Structural classification of FPV designs. Adapted from Claus and López, 2022. 14
2.5 0.5 MWp FPV system from Ocean Sun and Stakraft on the Banja hydropower reservoir (Albania) in 2021 (Garanovic, 2021a). 15
2.6 Environmental loads on FPV structures in (a) in-land water environment, and (b) marine water environment (Claus and López, 2022). 16
2.7 FPV designs going towards OFPV. 17
2.8 State of the art OFPV designs. 17
2.9 First off-shore solar farm (0.5MWp) integrated with an off-shore wind turbine (Santos, 2022). 18
2.10 Schematic of a typical stand-alone system. 19
2.11 ”Monitored specific yield as a function of total plane-of-array irradiation of photovoltaic systems installed in years 1994, 1997, and 2010 with corresponding performance ratio contour lines. Data shown were acquired during the 1000-Roofs Programme in 1994/1997 and in 2010 by Fraunhofer ISE monitoring services. The shown data notably use on-site irradiation measured by exclusively mono-crystalline silicon reference cells”.(Reich et al., 2012). 20
2.12 Average capacity factors (colorbar) for photovoltaics in Europe (1995–2015) derived from the regional reanalysis COSMO-REA6 and the satellite-based SARAH 2 dataset by Kaspar et al., 2019. 22
2.13 Seasonal cycle of the capacity factors for wind (blue) and PV (red) for Europe by Kaspar et al., 2019. 22
2.14 Efficiency breakdown flow chart for identification of OFPV losses of interest (yellow) and the respective monitoring devices of interest (orange) within this research. 24
2.15 Optical soiling sensors for PV applications. 26

3.1 Methodology chapter overview. 29
3.2 Map with locations selected for each PV system (The Netherlands). 31
3.3 Systems orientation for each PV string for both locations (off-shore and on-land). 31
3.4 PV array single line diagram both on-land and off-shore systems. 32

3.5 PV system design layout with PT100 thermal sensors (red) module locations. 34
3.6 Specific location and labels of PT100 thermal sensors (red) on PV cells within PV module 7 (5 sensors). 34
3.7 Data extraction steps flowchart. 36
3.8 Dry testing cycles for measurement and result outputs validation. 37
3.10 On-land system general visualization: consisting of a PV floater with PV modules (black), monitoring box (dark grey) and the inverter (blue). 39
3.9 Single line diagram for PV system on-land. Components not to size. 40
3.11 Layout of monitoring box on-land components in Fusion360 (CAD). Dimensions in mm. 41
3.12 Description of on-land monitoring box with components integrated. 41
3.13 IP67 gland components used for off-shore protection. 44
3.14 Single line diagram for PV system off-shore. Components not to size. 45
3.15 Off-shore system general visualization consisting of two floaters: PV floater (black) and utility floaters (yellow). 46
3.16 Layout of monitoring box off-shore components in Fusion360 (CAD). Dimensions in mm. 47
3.17 Description of off-shore monitoring box components integrated. 47
3.18 Description of both systems overviews with monitoring boxes zoomed in. 48
3.19 OFPV off-grid system complete installation. 49
3.20 3D printing process of power meter mounts design for off-shore conditions. 50
3.21 Monitoring devices (pyranometer, reference cells and thermal sensor) outside data box. 50
3.22 Resistors test showing a temperature of 449 ^{o}C. 51

4.1 Impact of environmental stresses on module degradation in various operating environments, including FPV (blue stripes) (WorldBankGroup, 2019a). 58
4.2 OFPV movement considerations for the effect of wave response motion on the insolation of OFPV (Bugeja et al., 2021). 61
4.3 Rolling sphere radius and protective angle methods for solar lightning protection methods (WorldBankGroup, 2019a). 62
4.4 Mooring systems (a) catenary, (b) taut mooring, (c) compliant mooring, and (d) rigid mooring (Claus and López, 2022). 63
4.5 Cage mooring types (Turner, 2000). 64
4.6 Anchoring systems for the marine environment layouts for FPV systems (a) dead weight, (b) suction foundation, (c) drag anchor, (d) embedded anchor (Claus and López, 2022). 64
4.7 Example of meteorological climate data from 'Meteonorm 7.2' initial assessment. . . . 66
4.8 Stand alone system component selection and protection considerations for off-shore conditions. 67

5.1 Experimental results analysis overview. Divided in power performance (yellow), temperature measurements (red) and environmental effects (blue). 74
5.2 Power performance of each string for the on-land and offshore systems from 14-11-2022 until 1-1-2023, provided with GHI from pyranometer measurements at each location. . . 76
5.3 Power performance of each string for the on-land and offshore systems, provided with GHI from pyranometer measurements at each location for a week, from 21-11-2022 until 28-12-2022. 77
5.4 Power performance of each string for the on-land and offshore systems, provided with GHI from pyranometer measurements at each location on 24-11-2022, a sunny day with a constant fine cloud coverage. 78
5.5 G_{POA} comparison for each string orientation (North-West strings in blue and South-East strings in red), on 24-11-2022, a sunny day with a constant fine cloud coverage. 78
5.6 Power regression fit for North-West strings, from 15-11-2022 to 1-1-2023. 80
5.7 Power regression fit for South-East strings, from 15-11-2022 to 1-1-2023. 80
5.8 Measured voltage box-plots of each string for the on-land and offshore systems, from 15-11-2022 to 1-1-2023. 81
5.9 Measured current box-plots of each string for the on-land and offshore systems, from 15-11-2022 to 1-1-2023. 82
5.10 Measured irradiance at POA regression fit for North-West PV strings. 83

5.11 Measured irradiance at POA regression fit for South-East PV strings. 83
5.12 Averaged module efficiency on South-East side derived from G_M and T_M and module specifications. 84
5.13 Module efficiency box-plots derived from G_M, T_M and module specifications. 85
5.14 South-East string regression between incoming radiation on the floater surface and DC power production on-land and off-shore including a linear fit. 86
5.15 North-west string regression between incoming radiation on the floater surface and DC power production on-land and off-shore including a linear fit. 86
5.16 Capacity factors identified per string for both off-shore an on-land with strings installed peak power of 2.16 kWp, from 15-11-2022 to 1-1-2023. 88
5.17 Cumulative DC energy outputs off-shore (blue) and on-land (red), from 15-11-20222 to 28-11-2022. 89
5.18 Victron MPPT 450-100 Output: Battery power, current and voltage during the period of research. 90
5.19 Meteonorm 7.2 annual temperatures for the on-land (red) and off-shore (blue) locations. 93
5.20 Meteonorm 7.2 seasonal temperatures for the on-land (red) and off-shore (blue) locations, from 15-11-2022 to 1-1-2023. 93
5.21 Ambient temperature box-plot comparison for the off-shore and on-land locations from annual, seasonal and real data for the period of research between 15-11-2022 and 1-1-2023. 94
5.22 Average module temperatures on-land and off-shore recorded from 15-11-2022 to 1-1-2023, including box-plots. 95
5.23 Specific temperatures concerning average module temperatures, ambient temperatures and water temperatures on-land and off-shore recorded from 15-11-2022 to 1-1-2023. . 96
5.24 Averaged module temperature against G_{POA} for the on-land system South-East oriented modules. 98
5.25 Averaged module temperature against G_{POA} for the on-land system North-West oriented modules. 98
5.26 Averaged module temperature against G_{POA} for the on-land system South-East oriented modules. 99
5.27 Averaged module temperature against G_{POA} for the off-shore system North-West oriented modules. 99
5.28 Averaged module temperature against ambient temperature on the on-land system, from 15-11-2022 to 1-1-2022 100
5.29 Averaged module temperature against ambient temperature on the off-shore system, from 15-11-2022 to 1-1-2022 101
5.30 Averaged module temperature off-shore with respect to ambient and water temperatures recorded, from 15-11-2022 to 1-1-2023. 101
5.31 Module gradient temperatures on-land vs offshore on 24-11-2022, from 08:00 to 18:00 . 103
5.32 Module gradient temperatures on-land vs offshore on 26-12-2022, from 08:00 to 18:00 . 103
5.33 Floater schematic explanation with numbers corresponding to PV module location and red color indicating PT100 thermal sensor is present at the location. 104
5.34 Floater gradient averaged module temperatures off-shore (top) and on-land (bottom) on 24-11-2022, using data from 08:00 to 18:00. 105
5.35 Floater gradient averaged module temperatures off-shore (top) and on-land (bottom) on 26-12-2022, using data from 08:00 to 18:00. 105
5.36 OFPV linear regression model 1 plotted together with module temperatures measured. 108
5.37 OFPV linear regression model plotted together with module temperatures measured off-shore. 109
5.38 Regression fit of module temperatures measured off-shore against empirical module temperature models during the period of research. 110
5.39 Timeline during period of research with module, ambient and water temperatures (top), wind speed and direction (middle) and wave height (bottom), from 15-11-2022 to 1-1-2023.113
5.40 Averaged module temperature off-shore against sea water temperature with linear fitting, from 15-11-2022 to 1-1-2023. 114

5.41 Air cooled FPV module (a) and water cooled FPV module. Adapted from Lindholm et al., 2021. 115
5.42 Air cooled FPV module (blue) and water cooled FPV module (green) cell temperatures with respect to water temperatures and wind speeds at a constant ambient temperature of 20 ^{o}C (Lindholm et al., 2021). 115
5.43 Averaged module temperature off-shore against wind speed with linear fitting, from 15-11-2022 to 1-1-2023. 116
5.44 Averaged module temperature off-shore against wind speed considering ambient temperature, from 15-11-2022 to 1-1-2023. 116
5.45 Wind rose at HKZA weather station from 14-11-2022 to 1-1-2023. 117
5.46 South-West wind direction with respect to off-shore system considering utility and a PV floater locations and orientations (top view). 117
5.47 Wave height as a function of wind speed with linear and quadratic fittings, from 15-11-2022 to 1-1-2023. 118
5.48 Averaged module temperature off-shore against wave height with linear fitting, from 15-11-2022 to 1-1-2023. 119
5.49 Averaged module temperature off-shore against wave height considering sea water temperature, from 15-11-2022 to 1-1-2023. 119
5.50 Tilt axis x (orange) and y (purple) with respect to floater at 150 ^{o} azimuth. 121
5.51 GHI $[W/m^2]$ recorded against raw and pitch angles during the research period. 121
5.52 Tilt angles (top) in x (orange) and y (purple) directions together with a histogram of normalized probability of each tilt and the measured GHI at the respective tilt, for the period from 14-11-2022 to 1-1-2023. 122
5.53 OFPV module with specific soiling effects observed during the period of research. . . . 124
5.54 Sun paths and horizon for the on-land location found using Meteonorm. 124

A.1 Electrical capacity by technology from 2019 to 2050 in the NZE scenario (IEA, 2021b). . 131
A.2 Investment costs of FPV in 2014-2018 (realized and auction results (WorldBankGroup, 2019b). 132
A.3 Pre-tax calculations by WorldBankGroup, 2019b for the Levelized Cost of Energy (LCOE) of Floating Photovoltaics (FPV) against ground-mounted PV, divided per climate. 132
A.4 Duffie-Beckman thermal model comparison with real module temperatures. 135
A.5 Duffie-Beckman thermal model comparison with real module temperatures including irradiance. 135
A.6 FPV schematic for fluid dynamic model. Adapted from Smets et al., 2016. 136

C.1 Layout of power box off-shore components in Fusion360 (CAD). Dimensions in mm. . . 141
C.2 Layout of resistors box off-shore components in Fusion360 (CAD). Dimensions in mm. . 142
C.3 Power meter mount designed in Fusion360 (CAD). Dimensions in mm. 142
C.4 Single line diagram for PV system off-shore enlarged. Components not to size. 143

D.1 Irradiance predicted by Meteonorm for on-land (left) and off-shore (right) with azimuth 150 ^{o} with respect to North and an inclination of 4 ^{o}. 146
D.2 Daily global radiance predicted by Meteonorm for on-land (left) and off-shore (right) with azimuth 150 ^{o} with respect to North and an inclination of 4 ^{o}. 146
D.3 Box-plot of ambient temperatures predicted by Meteonorm for on-land (left) and off-shore (right). 146

E.1 Power performance of each string for the on-land and offshore systems, provided with GHI from pyranometer measurements at each location for a week, from 25-12-2022 until 1-1-2023. 150
E.2 Off-shore voltage and current measurements coupled with POA irradiance and surrounding temperatures for North-West string during a week, from 21-11-2022 until 28-11-2022. 152
E.3 Measured irradiance at POA regression fit for the PV strings of each system. Off-shore system shown in blue and on-land system in red. 153
E.4 Module efficienies comparing influence of irradiance and module temperature off-shore for South-East string, from 15-11-2022 to 1-1-2022 155

E.5 Module efficiencies comparing influence of irradiance and module temperature off-shore for South-East string, from 15-11-2022 to 1-1-2022 155
E.6 Power regression fit for both systems off-shore (blue) and on-land (red) from 15-11-2022 to 1-1-2023. 156
E.7 PV string comparison of power production against incoming irradiation on POA surface of total string (6 panels) for both on-land and off-shore. 156
E.8 Cumulative energy outputs from power meters off-shore (left) and on-land (right) for the initial two weeks, from 15-11-20222 to 28-11-2022. 157
E.9 MPPT controller outputs for individual strings off-shore daily energy yield, from 15-11-2022 to 1-1-2023. 157
E.10 PT100 sensors installed test for off-shore system, before deployment, standing on-land, with data from 11-10-2022 to 27-10-2022. 158
E.11 Averaged module temperature against GHI and ambient temperature on the on-land system, with data from 15-11-2022 to 1-1-2023. 159
E.12 Averaged module temperature against GHI and ambient temperature on the off-shore system, with data from 15-11-2022 to 1-1-2023. 160
E.13 Regression fit of module temperatures measured off-shore against empirical OFPV module temperature model 1 from 14-11-2022 to 1-1-2023. 161
E.14 Module temperatures measured off-shore against empirical module temperature OFPV models from 14-11-2022 to 1-1-2023. 162
E.15 Close up on module temperatures measured off-shore against empirical module temperature OFPV models from 21-11-2022 to 27-11-2022 included. 163
E.16 Module temperature off-shore with respect ambient temperatures (top) to wind direction (middle) and direction (bottom). Timeline from 15-11-2022 to 1-1-2023. 165
E.17 Module temperature off-shore with respect ambient temperatures (top), to water temperature (second from top), to wave height (second from bottom) and swell height (bottom). Timeline from 15-11-2022 to 1-1-2023. 166
E.18 Horicatcher orientation and inclinations taken into account during horizon measurement on-land. 167
E.19 Sun paths and raised horizon (red) for the on-land location found using Meteonorm. . . 167
E.20 Meteonorm 8.1.1 outputs without the custom horizon on-land. 168
E.21 Meteonorm 8.1.1 outputs with the custom horizon included on-land. 168

F.1 Victron MPPT 450-100 Output: PV power and battery power from 14-11-2022 to 1-1-2023169
F.2 Victron MPPT 450-100 Output: Total daily energy and cumulative energy yield from 14-11-2022 to 1-1-2023 170
F.3 Victron MPPT 450-100 Output: PV power and battery from 15-11-2022 to 17-11-2022. . 171
F.4 Victron MPPT 450-100 Output: Battery power, voltage and current from 15-11-2022 to 17-11-2022. 171
F.5 Power recorded from the MPPT controller trackers for off-shore system from 15-11-2022 until 1-1-2023. 172
F.6 VRM Victron MPPT 450-100 Output: PV power from 14-11-2022 to 1-1-2023. 172
F.7 VRM Victron MPPT 450-100 Output: Daily energy yield from 14-11-2022 to 1-1-2023. . 173
F.8 VRM Victron MPPT 450-100 Output: Battery voltage and current from 14-11-2022 to 1-1-2023. 173
F.9 VRM Victron MPPT 450-100 Output: Tracker 1 (South-East) voltage and current from 14-11-2022 to 1-1-2023. 174
F.10 VRM Victron MPPT 450-100 Output: Tracker 2 (North-West) voltage and current from 14-11-2022 to 1-1-2023. 174
F.11 VRM Victron MPPT 450-100 Output: PV power per tracker from 14-11-2022 to 1-1-2023. 175
F.12 VRM Victron MPPT 450-100 Output: Daily maximum charge power from 14-11-2022 to 1-1-2023. 175
F.13 VRM Victron MPPT 450-100 Output: MPPT state from 14-11-2022 to 1-1-2023. 176
F.14 VRM Victron MPPT 450-100 Output: Temperature on power box from 14-11-2022 to 1-1-2023. 176

G.1 Sea map from KNMI weather station with Hollandse Kust Zuid Alpha (HKZA), located in the decimal coordinates 52.319, 4.043. 177
G.2 Wave rose with respect to wind direction at HKZA weather station (2km away from off-shore system) for the period 14-11-2022 to 1-1-2023. 178
G.3 Module temperature rose with respect to wind direction off-shore, from 14-11-2022 to 1-1-2023. 178

List of Tables

1.1 Share of electricity generation for the periods 2020, 2030 and 2050 in the NZE scenario (IEA, 2021a). 4

2.1 Summary of companies largest project implemented by 2022, intended towards off-shore solar applications. Capacities presented from information available in companies webpage or news articles. 18
2.2 Empirical photovoltaic models for module temperature prediction found for FPV. 23

3.1 Monocristalline silicone PV modules pre-selected for experiment, at STC, for both on-land and off-shore systems (relevant PV module characteristics). 32
3.2 Monitoring devices and sensors selected for experimental set-ups. 33
3.3 Monitoring devices and components installed on-land and their respective power consumption. 38
3.4 Monitoring devices installed off-shore and the respective power consumption. 43
3.5 Balance of System components off-shore. 44
3.6 Resistivity tests outcomes for thermal sensors extensions. 52

4.1 Ingress Protection level of first digit (solids) (IEC, n.d.). 55
4.2 Ingress Protection level of second digit (liquids) (IEC, n.d.). 56
4.3 Minimum ingress Protection level recommended depending on system location: FPV in-land, OFPV near-shore and OFPV off-shore. 57
4.4 Recommended autonomous days at several latitudes (Smets et al., 2016). 69

5.1 Maximum power points registered from 15-11-2022 to 1-1-2023 75
5.2 Voltage and current results per string. 81
5.3 Linear fit curves for power and irradiance at POA for off-shore and on-land (with y = off-shore measurement and x = on-land measurement). 82
5.4 Linear fits parameters found for string efficiencies (with y = incoming irradiance on string surface area at POA and x = string power output). 85
5.5 Efficiencies found at module and string level for South-East (SE) and North-West (NW) orientations from 14-11-2022 to 31-12-2022 86
5.6 Performance ratios found for the off-shore and on-land systems. Note the off-shore South-East string had data gaps and thus this value could not be determined. 87
5.7 Ambient temperatures found with Meteonorm and with empirical measurements at the two locations. 92
5.8 Meteonorm 8.1.1 climate data for the months of November and December, presenting average wind speeds for each location. 112
5.9 Meteonorm 8.1.1 outputs for the months of November and December„ with an azimuth of 150 ^{o} with respect to North at an inclination of 4 ^{o}. 123

A.1 Empirical photovoltaic thermal models. Based on Kamuyu et al., 2018 and Micheli, 2022 (only included are models with complete sources). 133

B.1 Pyranometers of interest found for this research. 139
B.2 Reference cells of interest for this research. 139
B.3 Thermal sensors for water and ambient temperatures of interest for this research 139
B.4 Thermal sensors for module and ambient temperatures of interest for this research. . . 140
B.5 Optical soiling sensors of interest found for this research. 140

D.1 Meteonorm results for the months of November and December 145

E.1 Thermal sensor operational status during period of research from 15-11-2022 to 23-11-2023. . . . 147
E.2 Sensors operational status during period of research from 15-11-2022 to 23-11-2023. . 148
E.3 Data retrieved from KNMI weather station HKZA from 15-11-2022 to 1-1-2023. 148

1

Introduction

Chapter 1 gives the introduction on off-shore solar floating photovoltaics (OFPV) and its role and necessity within the energy transition, from which the thesis research is defined. Firstly, Section 1.1 presents the role of the solar energy industry within the energy transition. The scenario towards Net Zero Emissions (NZE) from the International Energy Agency (IEA), is considered, providing the current and future status of the energy sector and in particular the transformation of the electricity generation industry and its shift towards renewable energies, focusing on solar and wind as the predominant sources of energy by 2050. Secondly, Section 1.2 presents the concept of floating photovoltaics (FPV) before introducing the upcoming industry of off-shore floating photovoltaics (OFPV) and its path for integration with other renewable energies, with a focus on wind energy. Finally, Section 1.3 presents the company where the thesis is carried out with and Section 1.4 introduces the thesis research, motivation, research objectives, questions and report overview.

1.1. The role of the solar energy industry

To understand the necessity of solar energy within the energy sector, the Paris Agreement is presented as it contains the goals set to reduce the effects of climate change. From the goals, a pathway towards NZE is discussed. From here, the necessity of further implementation of wind and solar energy is determined. The development and implementation of this technologies requires an expansion to cope with the energy demands projected for 2050. For this reason, innovation and additional technologies such as off-shore floating solar become relevant. The necessity to reach a maturity level within these technologies for large scale deployment is required and thus further research is essential to understand the behaviour of off-shore solar technologies. This research gap is needed to be investigated to help and understand the behaviour, potential and challenges facing off-shore solar systems.

1.1.1. The Paris Agreement

The ultimate goal of the United Nations Framework Convention on Climate Change (UNFCCC) is to “prevent dangerous anthropogenic interference with the climate system” (Protocol, 1997). The Paris Agreement was developed to give the route with regards to climate action. This agreement is the current global settlement for climate action.

The Paris Agreement, a legally binding international treaty on climate change, sets the limit of global warming well below 2 $^\circ C$, with efforts to limit it to 1.5 $^\circ C$ above the pre-industrial levels (Schleussner et al., 2016). The peak of Greenhouse Gas (GHG) emissions should be reached as soon as possible with the goal to reach climate neutrality by 2050 (Agreement, 2015). To reach these goals, the United Nations Climate Change Conferences that followed after the Paris Agreement, including the COP27, are setting the pathways at a global scale. The correct implementation of the goals provided, determines the updated scenarios of climate change globally. It is important to note, the near-term mitigation targets set from 2020 to 2030 appear insufficient to reach the temperature goals set (Schleussner et al., 2016). Business as Usual (BAU), carbon neutrality, net zero and different scenarios depending on actual implementations of the regulations, provides an insight into how the energy sector must be shaped to achieve this goals. Here, the scenario that becomes most relevant is the Net Zero Emissions scenario (NZE), which is further investigated in Section 1.1.2.

1.1.2. Solar energy towards 2050: Net Zero Emissions

The necessity of an energy transition derives from the global warming crisis and the goals set in the Paris Agreement (Agreement, 2015) to avoid detrimental and irreversible effects around the globe. For this, scenarios have been studied to provide recommendations through implementation of policies, technologies and steps required in order to reach this goals. This is the case of the International Energy Agency (IEA), one of the most advanced multilateral energy organization within the energy sector (de Graaf and Lesage, 2009), provides a clear analysis and road-map to meet these goals by providing authoritative analysis, data and policy recommendations, among others. Two of the most relevant scenarios are the Carbon Neutral scenario (CN) and the Net Zero Emissions scenario (NZE). The first focuses on carbon neutrality whereas the second goes further than carbon emissions, as it considers all GHG emitted into the atmosphere, such as methane (CH_4), nitrous oxide (N_2O), hydrofluorocarbons, hydrochlorofluorocarbons and ozone.

To understand the world energy outlook, the International Energy Agency, together with World Energy Outlook (WEO) presents global historical and projected data for the Net Zero Emissions by 2050 scenario annually, with the latest report in 2022 titled ”An updated Roadmap for the Global Energy Sector” (IEA, 2022). To show the path towards a net zero emissions outlook, the trend of CO_2 emissions by sector in million tons of CO_2 is presented in Figure 1.1, as well as the total energy supply and electricity generation by technology projected for 2050, being shown in Figure 1.3. From here, the significant role of renewable energy technologies towards 2050 is identified, with a focus on solar and wind energy technologies to phase out coal, oil and natural gas in order to reach carbon neutrality by 2050 (IEA, 2021a). As of 2020, 13504 million tonnes of CO_2 where produced by the power sector. Electricity generation was the largest individual source of energy related CO_2 emissions, accounting for 36 % of the total energy related emissions (IEA, 2021a). In order to achieve Net Zero Emissions, electricity generation must be shifted towards the use of solar PV, wind energy and hydro-power. It is expected that solar PV will account for 30 278 TWh (109 EJ) of the energy supply of which the majority (23469 TWh) will be directed to electricity generation, meaning emissions from electricity generation will be drastically reduced by 2050 (IEA, 2021b). To meet this goals, at least 600 GW of solar and 340 GW of wind capacity must be added, including replacements (IEA, 2021a). This is a reason why the addition of off-shore wind and solar becomes relevant as well. Furthermore, together with the capacity of renewable energies required to be installed for the Net Zero Scenario is displayed in Table 1.1.

Moreover, CO_2 emissions by the power sector become negative thanks to the introduction of carbon capture, utilization and storage technologies. These technologies allow the capture of carbon for power production.

The emissions by sector, the total energy supply by technology and the electricity generation by technology are displayed in Figures 1.1, 1.2 and 1.3, with solar results highlighted for 2050.

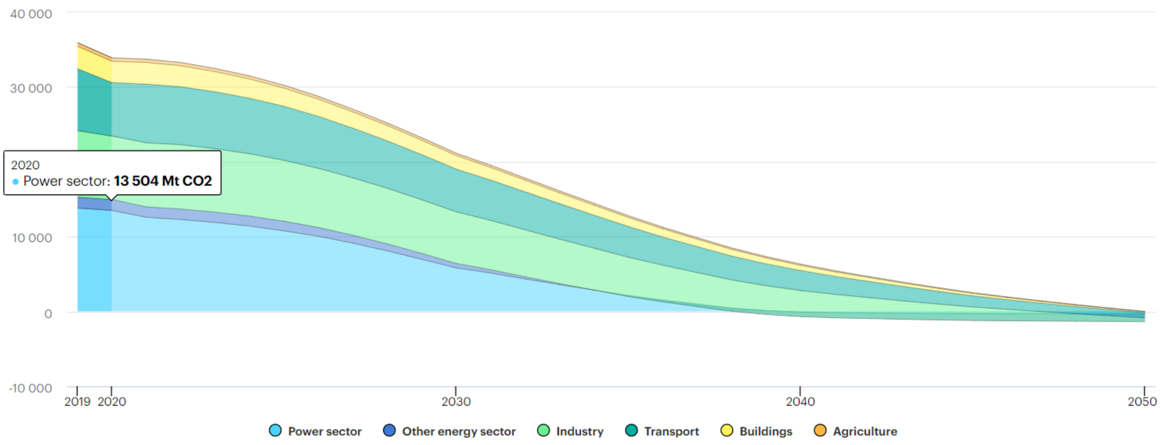

Figure 1.1: IEA Net Zero Emissions scenario on CO_2 emissions by sector [Mt CO_2] from 2019 to 2050 (IEA, 2021b).

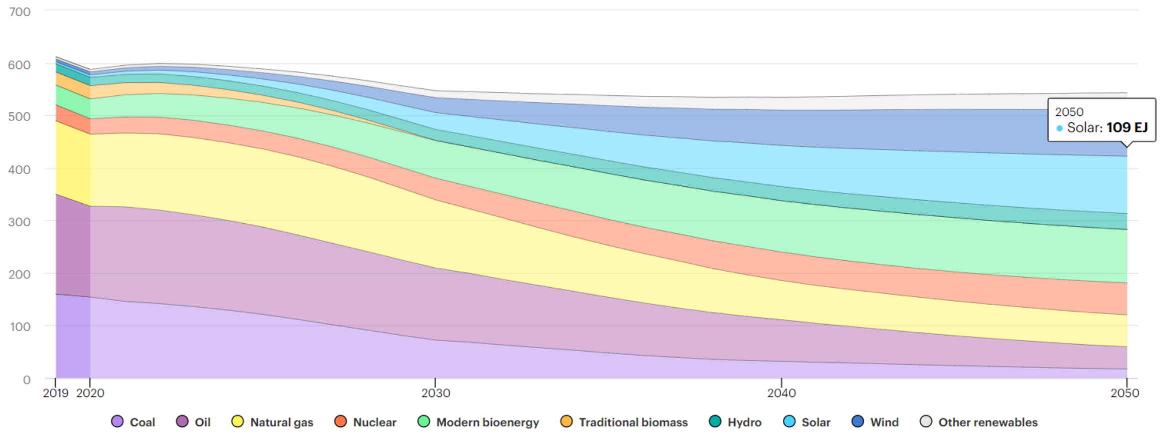

Figure 1.2: IEA Net Zero Emissions scenario on total energy supply [EJ] from 2019 to 2050 (IEA, 2021b).

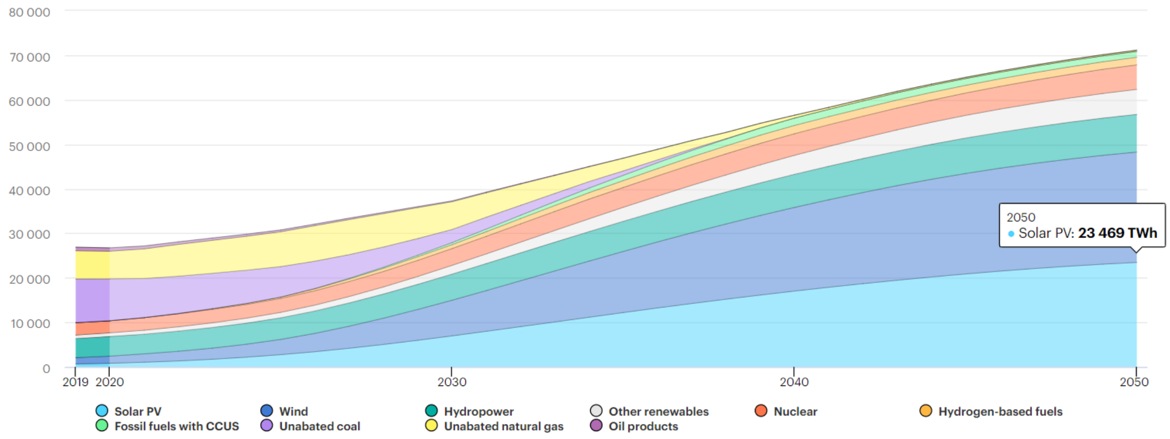

Figure 1.3: IEA Net Zero Emissions scenario on electricity generation by technology [TWh] from 2019 to 2050 (IEA, 2021b).

An important factor to reach the NZE goals is the decarbonization of the electricity sector must be done by 2035 in advanced economies and in developing economies by 2050 (IEA, 2021a). Likewise, the hydrogen-based fuels must be implemented by 2025 with the retrofitting of coal-fired power plants to co-fire ammonia and gas power plants to co-fire with hydrogen. Finally, the phasing out of coal and oil fired power plants between 2030 and 2040 and the reduction of the natural gas predicts a peak expected for 2030 and a reduction of 90 % by 2040. Furthermore, an immense global investment is required in electricity networks for the correct functioning and deployment of these technologies. Investment of 1 trillion USD (at a 2019 valuation) is needed for the grid networks until the share of sustainable energies meets the forecast demand as well as the net zero emission goals (IEA, 2021a). Investment in the upgrade and replacement of the current infrastructure will also be required. The grid investment in electricity networks in the NZE scenario is shown in Figure 1.4. Integration of new renewable technologies to the electric system will also require of a large investment, which is the case of off-shore solar and wind. The solar PV and wind installed capacity projections for emerging and developing economies is also presented in Figure 1.5.

	2020	**2030**	**2050**
Renewables installed capacity (GW)	2990	10300	26600
Annual solar PV capacity additions (GW)	134	630	630
Annual wind capacity additions (GW)	114	390	350
Total electricity generation (TWh)	26800	37300	71200
Share of renewable energies in total electricity generation	29 %	61 %	88 %
Share of solar in electricity generation	3 %	19 %	33 %
Share of wind in electricity generation	6 %	21 %	35 %

Table 1.1: Share of electricity generation for the periods 2020, 2030 and 2050 in the NZE scenario (IEA, 2021a).

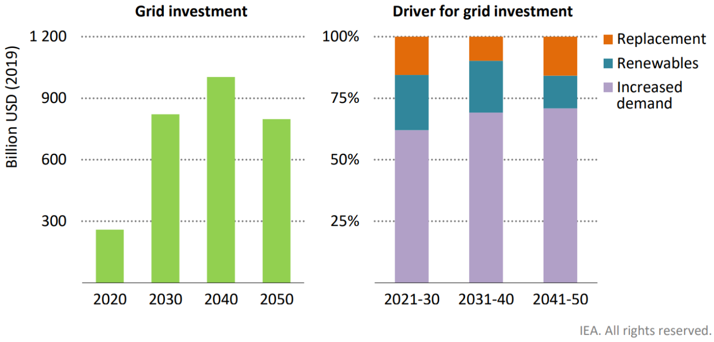

Figure 1.4: Global investment in electricity networks in the Net Zero Emissions scenario (IEA, 2021a).

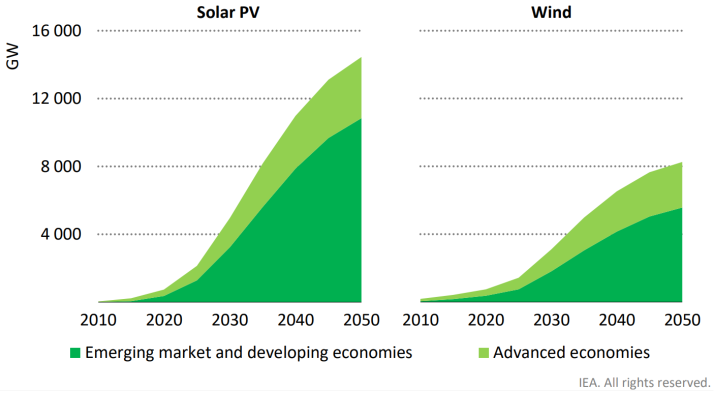

Figure 1.5: Solar PV and wind installed capacity in the Net Zero Emissions scenario (IEA, 2021a).

1.2. Floating photovoltaics (FPV)

Solar power installed capacity has been growing from 0.5 TW in 2008 to an estimated 1.1 TW by the end of 2022 (Gorjian et al., 2021), with Floating Photovoltaics (FPV) as an emerging technology experiencing a significant growth since 2016 (Gorjian et al., 2021).

As seen in Section 1.1, the role of solar is becoming essential in the energy transition. The necessity to reach a generation of 23 469 TWh from solar PV by 2050 (IEA, 2021b) incentives further research and implementation of these technologies in new environments: FPV systems are being researched and implemented with a predicted growth rate until 2030, of around 133 %, depending on the research (Rosa-Clot and Tina, 2020). The necessity to implement upcoming PV technologies by 2050, in particular FPV, shows the relevance to further understand such technologies, to then be able to meet the Paris Agreemnt goals in time.

FPV systems are designed to float on water and thus require several adaptations when compared to an on-land system. The schematic of a typical FPV system is shown in Figure 1.6. The system consists of a support structure where the solar system can be installed on: usually a floating structure which is held in place through mooring lines and anchors. Furthermore the photovoltaic system is thus mounted on top and depending on the application it can hold components of a PV system, such as inverters, MPPT charge controllers or transformers depending on the farm size and location. Additionally, most systems designed for power production will be connected to the grid and thus require a power export cable. If this is not the case, there can be a supplementary energy storage system present on the floating system and thus become an off-grid system.

Designs are being produced, tested and also deployed at mega-watt (MW) scale and different technologies are being investigated that might differ from the standard schematic provided in Figure 1.6. Nevertheless, they all have a common factor which is taking advantage of producing solar energy on water: Lower temperatures leading to higher efficiencies, reduction of algae growth and taking advantage of water reflectivity and reduction of water evaporation, in cases such as dams (Sahu et al., 2016, Ranjbaran et al., 2019). Nevertheless, these advantages come with challenges based on technology development. Furthermore, system integration of floating PV, together with technologies such as hydropower is also in expansion due to the advantages of increase in water conservation for hydro-power production (Farfan and Breyer, 2018).

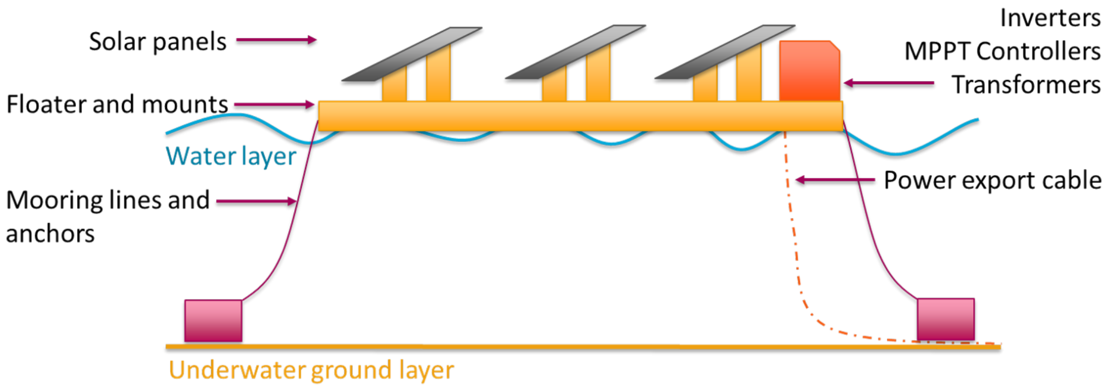

Figure 1.6: Elemental components of a floating photovoltaic system. Adapted from Vo et al., 2021.

From Figure 1.6, the main components of a FPV system consist of:

- Floater: consisting of the float and structure where the FPV system stands on, and can be classified as pontoon or superficial types (Claus and López, 2022). Pontoon types are subdivided into three categories: Class 1 (HDPE floating cylinders with a steel or aluminium support structure), Class 2 (one floater per PV module with built in rails and no support structure being required) and Class 3 (single floating structure with PV modules integrated). Superficial types are divided into rigid (rigid single structure platform that can sink up to two meters) and flexible (single large flexible membrane structure with modules integrated). The floater design classification is further discussed in Chapter 2.

- PV modules may vary between FPV types: for pontoon and superficial rigid structures, a framed glass-glass PV module may be used, due to a higher resilience to humid conditions when compared to glass-back sheet PV modules (Ziar, 2021). Thin film PV can be used in superficial flexible structures types (Claus and López, 2022).
- Balance of System (BoS): consisting of cabling, inverters, MPPT charge controllers and any additional electrical equipment required in the system. Selection of enclosures with Ingress Protection (IP) ratings to protect against the influences detected in the FPV system environment are of great importance for protection. An Ingress Protection 67 rating is required on floating housings (Ziar, 2021).
- Mooring system: it secures the FPV plant by limiting its free movement to prevent damage or hazard to itself or to other floating bodies (Claus and López, 2022). A general classification of mooring systems consists of catenary, compliant, tout and rigid pile mooring (Claus and López, 2022).
- Anchor system: in freshwater plants, the mooring lines are typically anchored through dead weights or helical anchors and for marine FPV systems, traditional marine anchoring systems may be used, such as dead weights, draw anchors, embedded anchors or suction foundations (Claus and López, 2022).

Opportunities within FPV, consider land savings for other land-incentive markets, radiation balance with an albedo of $\sim$ 6 % for water, an increased efficiency when PV modules having a negative temperature coefficient, are subject to lower temperatures cooling the PV modules through convection, and thus a higher voltage leading to a higher efficiency and total energy yield (Ziar, 2021). Reduced water evaporation is also an opportunity that can lead to a reduction of water evaporation losses in hydropower reservoirs (Kakoulaki et al., 2023). Other opportunities found are: improved water quality due to lower light penetration and longer life-time, since modules may experience lower thermal cycles than on-land PV systems, which may lead to delamination (Ziar, 2021). Ease of deployments is also an opportunity found, with deployments being able to be performed between 500 kWp to 1 MWp per day (Ziar, 2021).

Challenges, stated by Ziar, 2021, consider complex mooring and anchoring, dirt and bio-fouling accumulation and hotspots, difficult maintenance, impact on aqueous eco-systems, reduced lifetime of BoS, low technology readiness level (TRL) and lack of FPV standards. Additional challenges, stated by WorldBankGroup, 2019b, highlight the lack of a robust track record: with uncertainty of costs, environmental impact and technical complications of designing building and operating on and in water. Furthermore, challenges with regards to permitting concern a lack of clarity on licensing/permitting water rights and environmental impact assessments, difficulties in designing insurance policies which include liabilities for potential damage and uncertainties about the warranty of the performance or reliability of critical components WorldBankGroup, 2019b.

FPV potential, design classification descriptions, integration with hydropower reservoirs and investment costs are presented in Chapter 2. Additionally, Off-shore Floating Photovoltaics (OFPV) is presented in the introduction and its description is expanded in Chapter 2 as well; technologies and companies within the OFPV sector are presented, as well as the outlook on integration of OFPV with off-shore wind.

1.2.1. Off-shore floating photovoltaics (OFPV)

Within FPV, there is a new upcoming technology defined as off-shore floating photovoltaics (OFPV), which brings floating technology to off-shore conditions. Here the structural integrity under high wave conditions plays a significant role.

An offshore floating solar farm may provide advantages in terms of economies of scale and PV modules cooling. Furthermore, there are also disadvantages as salt water can deteriorate electronics, and reduce irradiance when deposited on the PV modules, and waves can reach over ten metres in height which impose mechanical stress on the modules. OFPV are thus designed to survive extreme environmental effects concerning fatigue on joints and connections, saltwater corrosion and UV radiation and bio-fouling (Liu et al., 2018). Thus, robust PV systems also have to be built to withstand this conditions and IP ratings play an important role for the protection of electrical equipment in marine environments. Additionally other industries such as the aquaculture markets are in need of off-grid sustainable energy systems, which could be enabled by OFPV. Synergies of OFPV plants with other marine activities may also consider including oil and gas platforms, desalinization and port activities (Claus and López, 2022).

Additionally, OFPV technologies enable land intensified areas such as The Netherlands or islands to be able to expand the area available for energy production and allow integration of renewable energies off-shore.

1.3. Oceans of Energy (OOE)

This thesis is performed in collaboration with Oceans of Energy, a Dutch company seeking to deploy and integrate off-shore floating solar farms onto the North Sea and worldwide over the coming years.

Oceans of Energy is focused on investigating the photovoltaic performance in off-shore environments. This thesis research is performed in collaboration with the Photovoltaic Materials and Devices (PVMD) group of Delft University of Technology (TU Delft). The research experiment is carried out within the North Sea 2 demonstrator. Figure 1.7 shows Oceans of Energy OFPV system technology.

Figure 1.7: Oceans of energy OFPV system technology (OOE, 2023a).

1.4. Research project

At this stage, solar energy systems are reaching a technology readiness level where now, the solar industry, is looking to expand further integrating new technologies in different environments. This is the case of off-shore floating photovoltaic (OFPV) technologies. A new solar industry that is set to satisfy the required energy demands and reduce the dependence of land use for energy production.

This research aims to understand the empirical PV performance of a solar PV system off-shore against the same PV system located on-land. As a result, thermal and photovoltaic performance models can be corroborated more precisely and further expand the understanding of performance of solar systems under off-shore conditions.

Two floating photovoltaic (FPV) systems are designed, integrated with the floater technology and equipped with the necessary monitoring devices. The first FPV system is set off-shore, in the North Sea, while the second FPV system is set on-land, within Leiden (The Netherlands), 20 kilometers apart. This allows for an empirical comparison between the performance of a PV system off-shore against the same system placed on-land, while perceiving similar real-time irradiation conditions from the Sun. It is important to note the on-land system is not on water but placed on ground, at an elevation of half a meter from the ground.

The design of the two FPV systems consists of identical photovoltaic modules and array configurations on the DC side and are both integrated with the floaters technology from Oceans of Energy. The structural performance is outside the scope of this thesis. The comparison is made on the DC side as it is desired to determine the floaters individual performance. This can be used to further optimize the sizing of inverters and transformers at farm scale. For this reason the off-shore system is designed as an independent off-grid system. Furthermore, this helps to understand and provide an analysis of what industries can benefit from an off-shore off-grid system.

Consequently, the design procedure, integration and testing for both systems enables the identification of guidelines required to build an off-shore off-grid PV system and data obtained from the systems allows to assess, analyse, and compare performance and thus observations, conclusions and future recommendations can be provided within this research.

1.4.1. Research motivation

The motivation to answer these questions comes due to the early stage of OFPV technology and the necessity to validate predictions with real life data, while being able to have a reference (on-land) to make a valid comparison. The following main motives were identified:

- Understanding photovoltaic behaviour of an OFPV system: No empirical comparisons found in literature for OFPV systems against on-land systems.
- Investigating OFPV performance to comprehend the relevance for OFPV farm up-scaling intended to be operating for years, which may give beneficial input on performance, farm sizes, economical studies and integration with other technologies, among others.

1.4.2. Research objectives

For this thesis, two main research objectives were set:

1. Performance comparison between off-shore floating PV systems and land-based PV systems based on experimental data.
2. Design guidelines for off-shore off-grid floating PV systems.

1.4.3. Research questions

The project is performed in order to answer the following research questions:

1. What is the photovoltaic performance of the off-shore system compared to the on-land system?
    (a) What PV performance indicators can be used to compare OFPV systems?
    (b) Which monitoring technologies are needed to track OFPV performance?
    (c) What off-shore environmental influences cause changes in the OFPV system set up when compared to on-land?
    (d) How does the floater plane of array (POA) change in off-shore conditions?
    (e) Does soiling appear on an OFPV system? And if there is, what type of soiling is it?
    (f) What is the efficiency of the off-shore system compared to on-land?
    (g) What is the energy production of the off-shore system compared to on-land?
    (h) What is the performance ratio of the off-shore system compared to on-land?
2. What is the thermal behaviour of OFPV modules when compared to PV modules on-land?
    (a) How is module temperature of PV and FPV systems being predicted in literature?
    (b) How can the module temperature of an OFPV module be predicted?
    (c) How do FPV thermal models from literature compare to models derived from real measurements off-shore?
    (d) How does the module temperature change between off-shore and on-land? How does the temperature change throughout one OFPV module? And how does the module temperatures change throughout a floater array?
3. What guidelines are required to implement an off-shore off-grid system?
    (a) What are the design steps required for an OFPV off-grid system?
    (b) Which system adaptations are required for an off-shore off-grid photovoltaic system when compared to an on-land system?

1.4.4. Research phases

The research consists of 4 phases; solar energy background, methodology for designing the experimental set ups (design and integration), design guidelines for off-grid OFPV systems and finally results processed with data analysis.

Firstly, the background within the off-shore solar floating photovoltaic industry is investigated and the research process is set. This concerns FPV potential, integration with hydropower, OFPV technologies and integration with off-shore wind and off-grid system designs. Then PV thermal models from literature are investigated to further understand influences affecting thermal behaviour and in turn FPV performance. Also monitoring equipment for the off-shore solar industry is identified.

Secondly, the methodology presents two experimental set ups, a PV system on-land and an OFPV system off-shore. The design procedure is determined, consisting of design requirements, PV system sizing and the electrical and mechanical designs of the monitoring set ups and their respective construction. The two experimental set ups are build simultaneously: the on-land system, which entails a PV floater standing on solid land and the off-shore system, which entails a PV floater which is set within the North Sea 2 demonstrator, an off-shore solar farm 15 km off the coast.

Furthermore, the systems are integrated in Oceans of Energy floating technologies, the floater technology it-self is outside the scope of the thesis. Here components are selected based on the design phase decisions and are tested. This is an interactive step, where changes of the design are made depending on the components actual behaviour during testing. Once components are calibrated, they are integrated into their respective system and are tested further within a complete system. Protection systems are designed and installed for off-shore conditions to protect all components. Furthermore, the cable routing is also adapted and upgraded for protection on off-shore conditions. Components are installed on the floaters and monitoring systems are set for calibration. Data retrieving protocols are set and testing of both complete systems is performed before deployment. This installation of components actively takes into account the surroundings around the PV floater and the incorporation of the off-shore system into the farm, focusing on shading and wind influences caused by the location of components installed, aside from the PV array.

Finally, data analysis from both the on-land and off-shore systems is performed for a comparison on photovoltaic performance between the system on-land and the system off-shore in terms of power performance, temperature influences and environmental influences (wind, wave and water temperatures). Also, a comparison with empirical FPV models from literature is made with OFPV linear regression models derived from measurements to predict module temperature off-shore for the period of research. An overview of the research phases is presented in Figure 1.8.

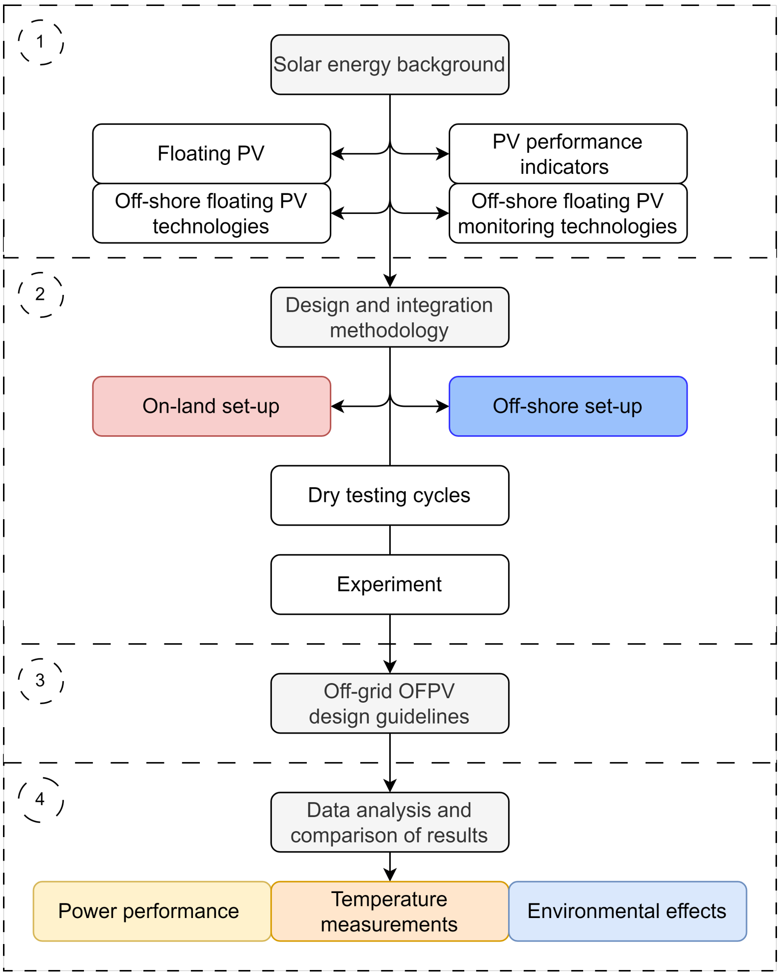

Figure 1.8: Research project phases overview, with background (1), methodology (2), design guidelines (3) and results analysis and comparison (4).

2

Background

Chapter 2 presents the thesis background. A visual overview is provided in Figure 2.1.

Firstly, floating PV is discussed: floating PV (FPV) potential and definitions are presented to understand the direction of the floating industry. Then, off-shore floating PV (OFPV) definition and technologies are presented. Future integration with hydro-power (on-land) and wind energy (off-shore) are also presented. Additionally, off-grid systems and their possible use off-shore is discussed.

Secondly, PV performance indicators are studied: here theory on parameters affecting performance ratios, efficiency, temperature of PV modules, DC energy yield and capacity factors are presented. Then, PV thermal performance is discussed with an emphasis on empirical models found in literature determining module temperatures.

Finally, monitoring technologies are considered. Measuring devices are identified in order to compare an off-shore and on-land PV system. Additionally, weather stations and meteorological software packages are presented as they can be used to provide additional data measurements, concerning wind, waves and water temperatures.

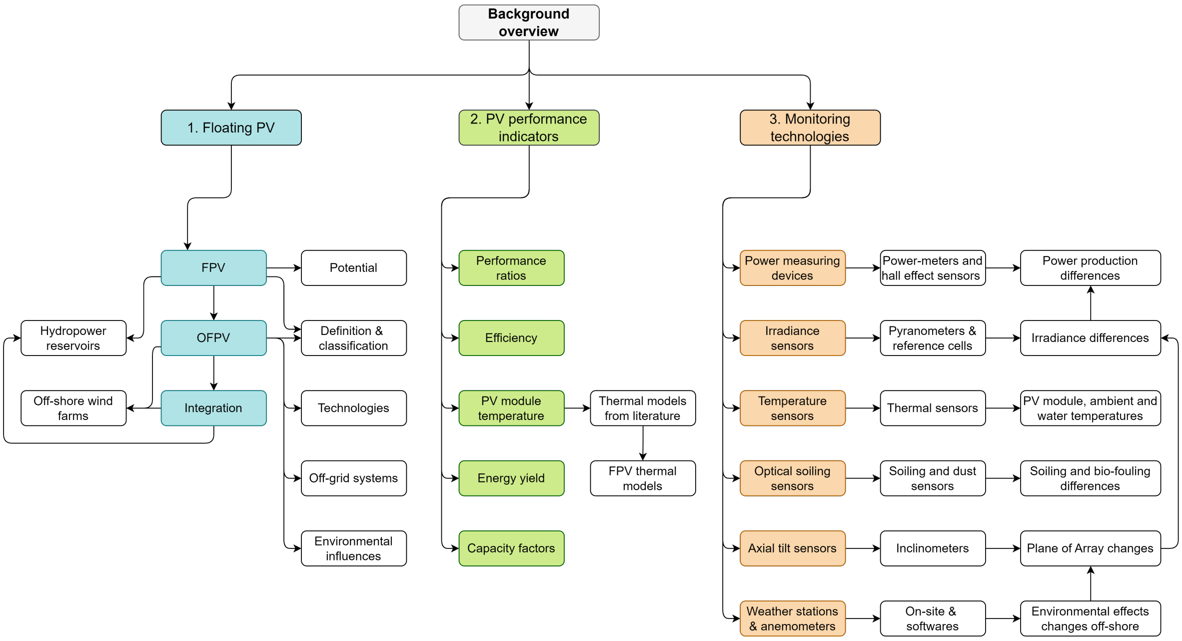

Figure 2.1: Background chapter overview presenting 3 sections divided into floating PV (blue), PV performance (green) and monitoring technologies (orange).

2.1. Floating photovoltaics (FPV)

2.1.1. FPV potential

An introduction to floating photovoltaics (FPV) was presented in Section 1.2. FPV is a section within PV integration that focuses on providing solar energy through the use of photovoltaic systems floating over a layer of water. As of 2018, China led the cumulative installed FPV capacity, with 960 MWp (Vo et al., 2021) of 1314 MWp installed globally. A study by Cazzaniga and Rosa-Clot, 2021 presented the growth trend of FPV from 2009, in terms of annual and cumulative FPV energy production in MWh, up to 2019 and gave an initial prediction within their study until 2025, shown in Figure 2.2. The annual growth is prone to be reduced by 2050; doubling the installed FPV each year implies that by 2050 the world energy production would be produced by FPV, which is unlikely.

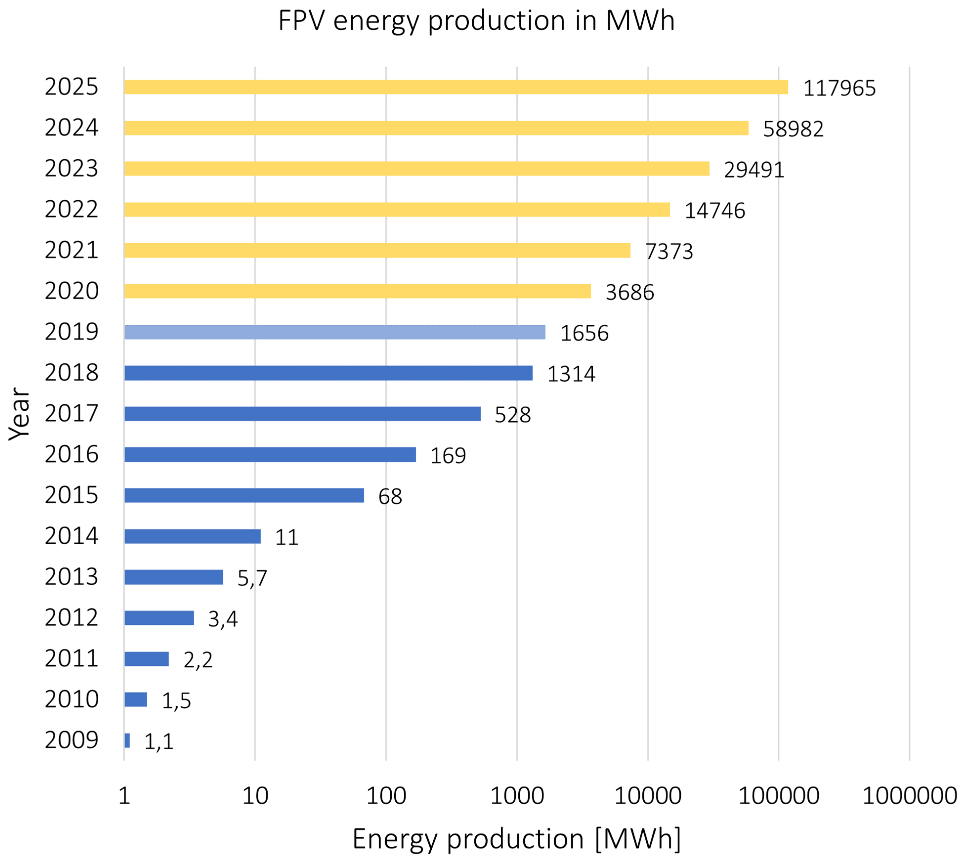

Figure 2.2: Logarithmic plot of the global yearly produced FPV energy from 2009 (blue, 2019 to be confirmed) and forecast up to 2025 (yellow). Adapted from Cazzaniga and Rosa-Clot, 2021.

2.1.2. FPV design classification

FPV designs have been deployed in in-land water, such as canals, lakes, dams and water reservoirs (representative system shown in Figure 2.3a), and as the transition to near-shore and off-shore environments begins, new designs appear (representative system shown in Figure 2.3b).

Classification of FPV is based on structural design and suitability to location either on in-land, near-shore or off-shore waters. An adaptation from the standard classification (Claus and López, 2022) is provided in Figure 2.4, providing descriptions for each design classification. FPV systems are divided into two main subcategories, pontoon and superficial, previously described in Chapter 1. Pontoon types, are divided in classes 1, 2 and 3 depending on the support structure. Superficial types, having a higher contact area with the surface of water, are divided into rigid and flexible structures.

Furthermore, for the design of FPV systems, Det Norske Veritas (DNV) group has published in 2021 the first recommended practices for design, development and operation of FPV systems (DNV, 2021).

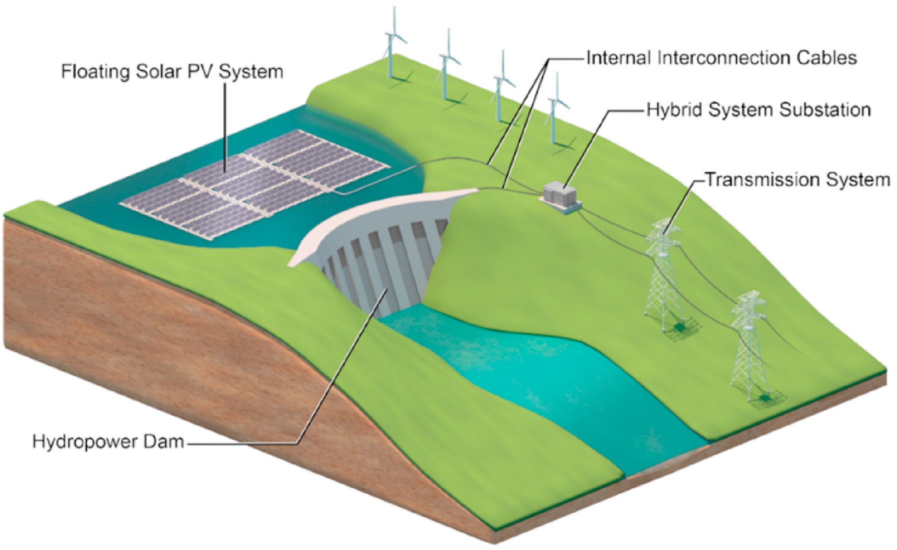

(a) In-land FPV representative schematic.

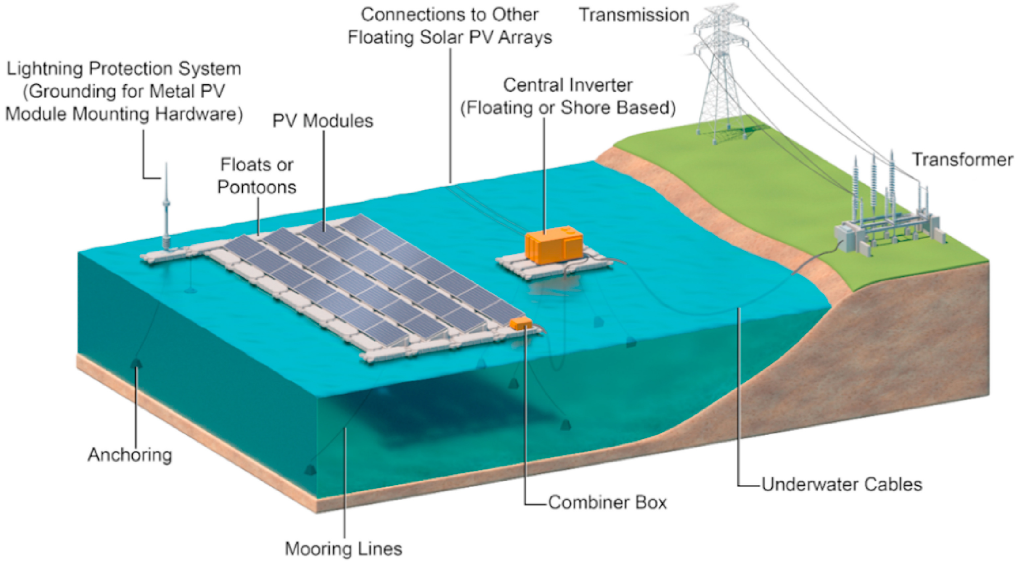

(b) Off-shore FPV representative schematic.

Figure 2.3: Schematic of typical stand-alone large-scale FPV systems and key components (Lee, 2020).

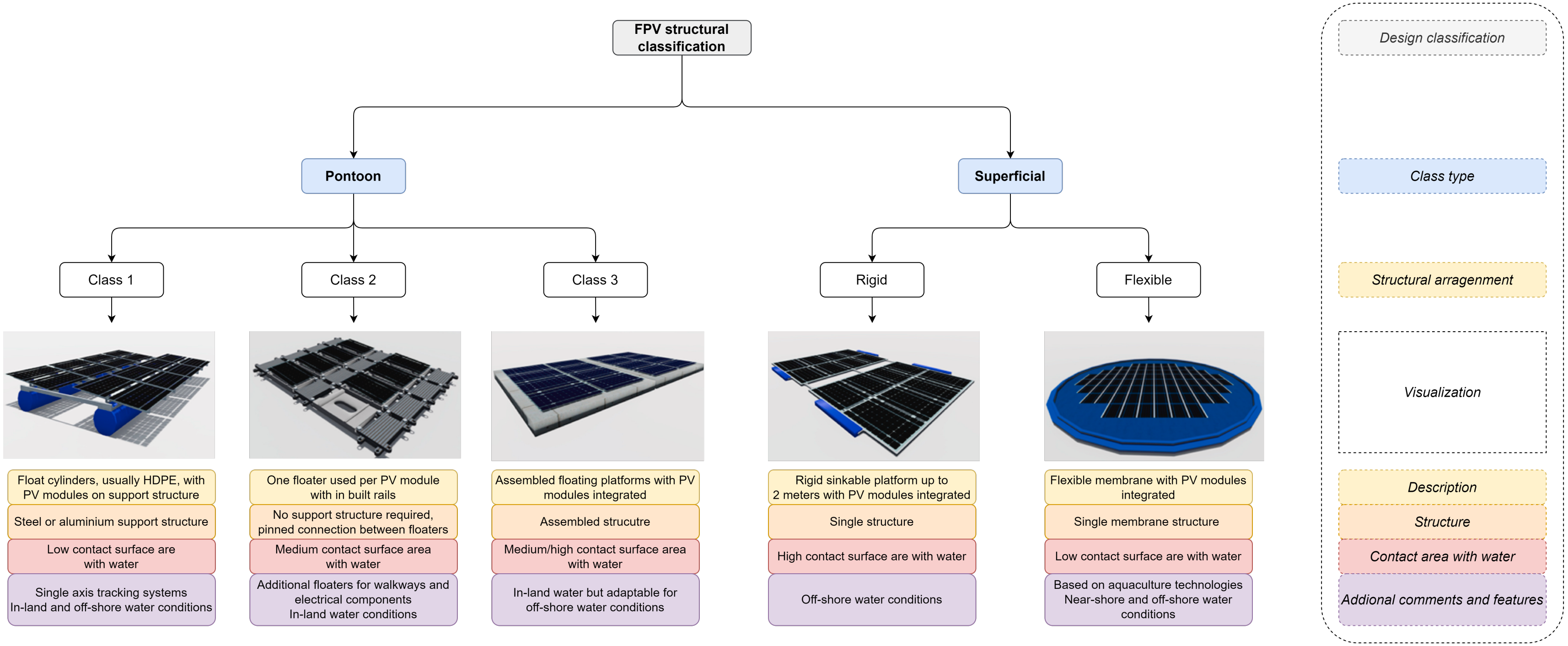

Figure 2.4: Structural classification of FPV designs. Adapted from Claus and López, 2022.

2.1.3. FPV integration with hydropower reservoirs and investment costs

The increase in wind and solar energy installations poses a challenge for grid-stabilization and energy storage due to high variability of electricity production. Furthermore, energy systems require flexibility to match variable demand (Lund et al., 2015). Pumped hydro energy storage (PHES[1]) provides a solution to grid stabilization with respect to energy demand from intermittent renewable energy sources (Rehman et al., 2015). Furthermore, PHES is an established commercially-acceptable technology for utility-scale electricity storage (Rehman et al., 2015). Additional integration of technologies with hydropower reservoirs can pose several benefits: FPV offers a solution for lack of land availability, additional solar energy production and reduction of water evaporation losses (Kakoulaki et al., 2023).

Hydropower was the largest renewable energy source in 2020, with a total energy supply of 16 EJ (without considering modern bioenergy and traditional biomass), producing 4418 TWh (IEA, 2021b). Additionally, Appendix A presents renewable energies trends in the NZE scenario for electrical capacity installed globally, highlighting hydropower capacity Figure A.1.

Farfan and Breyer, 2018 stated that of 1170 GW installed globally, hydropower consisted of 328 GW of hydro run-of-river capacity and 842 GW of hydro reservoirs, with 141 GW of pumped-hydro storage. The reservoirs were found to have an area of 265.7 thousand km^2 to potentially have 4400 GW of FPV at 25 % water surface area, generating 6270 TWh of electricity (Farfan and Breyer, 2018). Additionally, FPV in this case could prevent 74 billion m^3 from being evaporated globally and thus allowing hydropower production to potentially increase to 142.5 TWh (Farfan and Breyer, 2018).

Integration of FPV systems on hydropower reservoirs is increasing in demand. This is the case of Ocean Sun, a Norwegian company, which together with Stakraft, delivered a 0.5 MWp FPV system that was operating on the 72 MW Banja hydropower plant in Albania (Garanovic, 2021a), shown in Figure 2.5. The system covered 4000 m^2, with 1536 PV modules (Garanovic, 2021a). FPV system was stated in the news to have an investment of 2 million euros at the time (Petrushevska, 2022).

For cost reference, the total capital expenditures for turnkey FPV installations in 2018 generally ranged between 0.8 \$ and 1.2 \$ per Watt-peak (W_p) of power installed of FPV , based on realized and auction projects (WorldBankGroup, 2019b). FPV systems costs are considered to be 18 % higher than ground-mounted systems (WorldBankGroup, 2019b). The higher initial capital expenditure costs for FPV are balanced by the higher energy yield expected: the Levelized Cost of Energy (LCOE) of FPV in all conservative scenarios considered by WorldBankGroup, 2019b were higher than for ground mounted systems, with FPV considered to have a 5 % increase in performance ratio (PR). Nevertheless, FPV systems having a 10 % increase in performance ratio (PR), in the optimistic scenario, only showed the LCOE to be 3 % to 4 % higher than ground-mounted systems (WorldBankGroup, 2019b). The investment costs of FPV projects provided by WorldBankGroup, 2019b as well as the LCOE comparison by WorldBankGroup, 2019b are shown in Appendix A.2.

This shows the market necessity to understand the actual PV performance of new FPV designs against on-land systems and the differences in energy yield outputs and costs.

Figure 2.5: 0.5 MWp FPV system from Ocean Sun and Stakraft on the Banja hydropower reservoir (Albania) in 2021 (Garanovic, 2021a).

---

[1] Hydroelectric energy storage solution using two water reservoirs at different elevations which can generate power as water goes down from one to the other (discharge) with the use of a turbine. Power is required during recharge, with water being pumped back into the upper reservoir (U.S.EnergyDepartment, 2023)

2.2. Off-shore Floating Photovoltaics (OFPV)

2.2.1. OFPV technologies

Off-shore floating PV (OFPV), are marine FPV plants which are exposed to higher wind and wave loads (Claus and López, 2022). Additionally, OFPV are designed to survive extreme environmental effects, fatigue on joints and connections, saltwater corrosion and UV radiation and bio-fouling (Liu et al., 2018). In-land systems deal with less severe environmental conditions and have seen a growth in terms of systems, technology, maturity and standardization for mass scale production. On the other hand, off-shore systems are in an earlier stage of deployment, where different research institutes and companies are validating concepts to be mass-produced and additionally be integrated within off-shore wind-farms.

The environmental influences for in-land and off-shore FPV systems are shown in Figure 2.6. FPV systems being researched suffer from lower wind profiles than systems placed off-shore. Furthermore, deep water circular orbits also relate to greater waves, which in turn can influence the system. Finally wave direction and current can cause systems off-shore to suffer from greater roll, pitch and yaw angle changes. Studying the influence of this parameters off-shore on PV performance is under research but little to no real PV data is publicly available. To scale up the technology a better understanding of the real behaviour of OFPV systems is required to be able to scale up this technology. Forces on the structural system (considering wind, current, wave and mooring forces) are of great importance when designing OFPV systems. However, the study of these forces on the structures is outside the scope of this thesis.

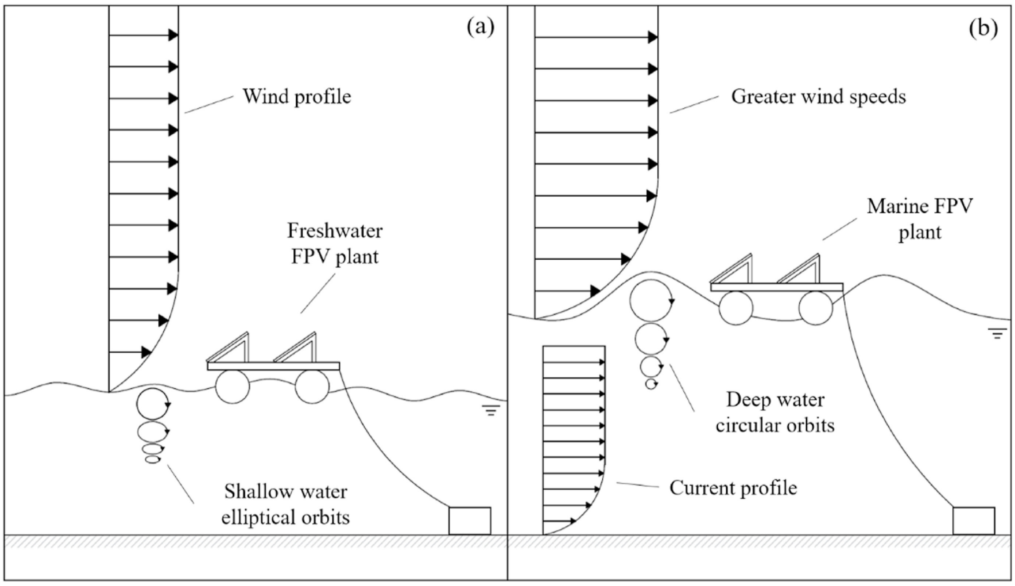

Figure 2.6: Environmental loads on FPV structures in (a) in-land water environment, and (b) marine water environment (Claus and López, 2022).

Furthermore, to provide an overview of the companies scaling up this technology to a commercial level, a study summarizing FPV companies with projects focusing towards OFPV is presented. In-land FPV companies stating interest in OFPV include SeaFlex, Toledo Solar, Hartek Solar, Tata Power Solar, Bay WaRe and Emica Solar. In-land FPV companies accelerating towards OFPV were found to be: Isigenere, Solaris Float and Blue Water, shown in Figure 2.7. Isigenere have products for in-land waters and are now testing them to expand to tougher environments. Isigenere product, the Isofloating is presented in Figure 2.7a. The common point of these systems is standardization and modular design that can be adjusted to different panel sizes and farm layouts. More advanced concepts such as the one from Solaris Float have a technology with tracking axis and rotating a complete farm when necessary. Solaris float tracking technology is shown in Figure 2.7b. Main challenges across the industry remain in the deployment, floater connections, light degradation, fouling prevention and structural integrity with higher environmental loads.

OFPV technologies found being researched, developed and commercialized are listed in Table 2.1, Solar Duck, Ocean Sun and Oceans of Energy systems are additionally displayed in Figure 2.8. FPV companies that have been mentioned in the news or websites, with regards to an announcement about a real research project with intentions to deploy a system off-shore, are also included. Capacities at this stage do not surpass 1 MW but several projects are underway as this technology keeps being developed, including 0.5 MWp OFPV from Ocean Sun integrated with an off-shore wind turbine, shown in Figure 2.9. The integration of this technologies became a reality with State Power Investment Corp. (SPIC) and Oceans sun when in November 2022, they started operating the first OFPV system with an off-shore wind turbine (wind turbine size not found) (Santos, 2022). This is shown in Figure 2.9.

Off-shore floating photovoltaic technologies are being developed with the prospect of integrating these with off-shore wind farms. A hybrid off-shore solar and wind farm would increase power output per unit area of marine space as well as increase power output quality with the reduction of temporal variability (López et al., 2020). Moreover, the study from López et al., 2020, found within the case study in Asturias (Spain) a combined OFPV and off-shore wind farm could reach 57.5 MW/km^2 of capacity density, with an specific energy yield of 61.2 $GWh/(km^2year)$: 10 times what the stand alone wind farm could yield and 7 times what the stand alone solar farm could yield. Power output variability in this study was found to be reduced by 68% with respect to a stand alone wind farm.

Combining OFPV with an off-shore wind farm can be beneficial in technical and economical terms (Golroodbari et al., 2021): adding solar capacity at times with sub-optimal power generation by wind turbines increases electricity cable usage (cable pooling). The profitability of this integration was found to depend on two major factors, the marginal power delivered by FPV, which should aim to be increased, and the solar system costs, which should aim to be decreased (Golroodbari et al., 2021).

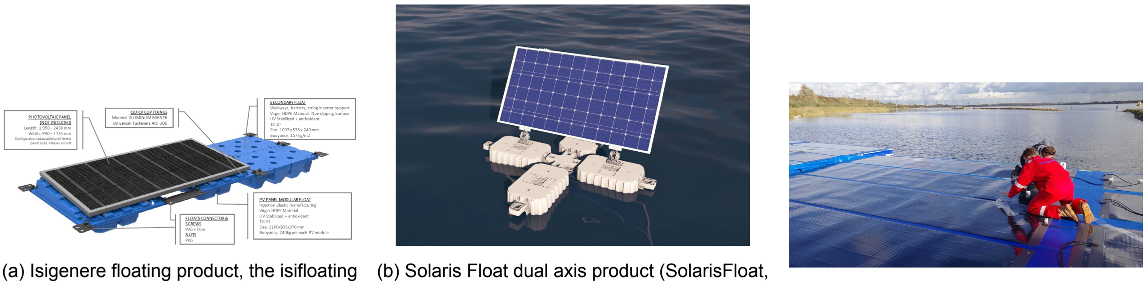

(a) Isigenere floating product, the isifloating (Isigenere, 2021). (b) Solaris Float dual axis product (SolarisFloat, 2018). (c) Blue Water flexible floater (TNO, 2021).

Figure 2.7: FPV designs going towards OFPV.

(a) Solar Duck pontoon floater (SolarDuck, 2023). (b) Ocean Sun membrane floater (OceanSun, 2023). (c) Oceans of Energy superficial floater (OOE, 2023b).

Figure 2.8: State of the art OFPV designs.

Company	Floating technology	2022 Deployment Stage	Capacity
Ocean Sun (Norway)	Circular floating polymer membranes	Off-shore wind with off-shore solar integrated	500 kWp (Garanovic, 2022a)
Oceans of Energy (The Netherlands)	Semi-submersible rectangular floaters	Off-shore	500 kWp (Garanovic, 2023)
Swimsol (Austria)	PV mount structure elevated above water	Near-shore	456 kWp (Swimsol, 2022)
Solar Duck (The Netherlands)	Triangular floaters elevated above water	In-land	65 kWp (SolarDuck, 2021)
SolarisFloat (Portugal)	Rotating tracking floaters	Pilot in-land (TNO)	50 kWp (TNO, 2022)
SolarFloat and Texel4Trading (The Netherlands)	Concrete floaters	Pilot in-land (TNO)	50 kWp (TNO, 2022)
Isiginere (Spain)	Individual PV module Isifloating HDPE floaters	Pilot in-land (TNO)	42 kWp (TNO, 2022) (Isifloating, 2020)
BlueWater Energy (The Netherlands)	Flexible modules and flexible floater units	Pilot in-land (TNO)	20 kWp (Garanovic, 2021b)
HelioRec (France)	Individual PV module floaters connected	Near-shore	10 kWp (Garanovic, 2022b)
Sunlit Sea (Norway)	Semi-submersible PV module	Pilot in-land	2 kWp (SunlitSea, 2022)
Moss Maritime (Norway)	Near-shore and off-shore	Design concept / Pilot	- kWp (MossMaritime, 2022)
Tractebel (Belgium)	In development	Design concept / Pilot	- kWp (Garanovic, 2021c)

Table 2.1: Summary of companies largest project implemented by 2022, intended towards off-shore solar applications. Capacities presented from information available in companies web-page or news articles.

Figure 2.9: First off-shore solar farm (0.5MWp) integrated with an off-shore wind turbine (Santos, 2022).

2.2.2. Off-grid PV systems

Off-grid PV systems, also called stand-alone PV systems, are systems that do not require an additional external power source. These systems are composed of the PV modules and load, and an additional energy storage system if needed. The reason for having such a system off-shore can be due to a lack of connection to the grid. Examples of these systems include: powering of weather stations off-shore, substitution of diesel generators used in aquaculture fish farms or power supply of to remote islands with reduced space. In remote areas, where connection to the grid is limited, such as the ocean, off-grid systems can be implemented.

These systems have a common layout, Figure 2.10 shows the typical components in an off-grid system (Smets et al., 2016). First comes the source of power, in this case the PV modules. Then a control device is selected, this can be in the form of a charge controller, Maximum Power Point Tracker (MPPT) controller, battery protection system, battery management system and/or an inverter, which can have a control system as well. An additional part that stand alone systems may have, is a storage unit, where a battery bank (BB) can used continue to power the loads during times of no power production. The charge controller, together with a battery management system, can be implemented to prevent battery drainage under low voltage. Through this scheme, either DC or AC loads can be powered. In some cases, such as in monitoring devices, AC and DC inputs are permitted. Depending on the voltage, DC-DC converters might be required on the load side.

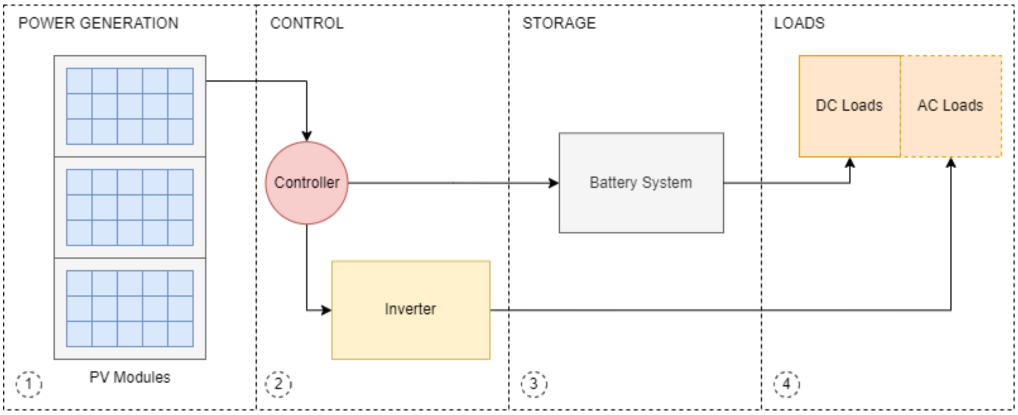

Figure 2.10: Schematic of a typical stand-alone system.

When looking at off-shore off-grid technologies, the protection of the electronic components against the marine environment becomes crucial. Ingress Protection (IP) ratings grade the resistance of an enclosure against the intrusion of dust or liquids (IEC, 2023b). IP ratings may be selected based on IEC 60529 Ingress Protection (IP) code, which rates and grades the resistance of enclosures for electric and electronic devices, as well as the easiness of individuals to access to potential hazardous parts within the enclosure (IEC, 2023b). A selection of IP67 and IP68 is recommended for off-shore environments, being dust tight and allowing temporal or continuous immersion in water.

Off-grid sectors, such as the fish industry, often require diesel generators. The use of PV modules reduces the dependence on these type of generators. However, this industry relies heavily on lighting throughout the night, so a storage system must be included. Power meters can be powered directly from the PV array and therefore don't require an external energy source.

The battery bank capacity required for an off-grid system, depending on the days of autonomy is defined in Equation 2.1, with C_{BB} as the battery bank capacity in Ah, V_{BB} as the battery bank voltage in V, DOD_{Max} as the maximum depth of discharge of the battery and $E_{Daily,Load}$ as the daily load demand in Wh.

The off-shore system design, sizing and protection is based on the principles of the off-grid system provided in this section and is further discussed in Chapter 3.

$$C_{BB} = \frac{Days_{Autonomy} * E_{Daily,Load}}{V_{BB} * DOD_{Max}} \tag{2.1}$$

2.3. PV performance indicators

This section presents performance indicators which allow to compare the PV systems performance. Performance ratios, module and string efficiencies, module temperature influence on efficiency, capacity factors and energy yield are discussed.

Performance ratio

Performance ratio (PR) of a PV system is one of the key parameters used in the industry today to evaluate performance of PV plants (Khalid et al., 2016). The performance ratio of a PV system is defined as the ratio of the final yield to the reference yield of the system (Khalid et al., 2016), as shown in Equation 2.2.

$$PR = \frac{Y_f}{Y_r} \tag{2.2}$$

The reference yield (Y_r) can be defined as:

$$Y_r = \frac{\text{Total in-plane irradiation } [kWh/m^2]}{\text{PV's reference irradiance } [kW/m^2]} \tag{2.3}$$

With the final yield (Y_f) being defined as:

$$Y_f = \frac{\text{Total useful output energy } [kWh]}{\text{Nominal power of the PV system } [kW]} \tag{2.4}$$

Additionally, the array capture losses (L_C) and the system losses (L_S) can be calculated with the Equations 2.5, 2.6 and 2.7 (Khalid et al., 2016).

$$Y_A = \frac{\text{Total energy delivered by the PV array } [kWh]}{\text{Nominal power of the PV array system } [kW]} \tag{2.5}$$

$$L_C = Y_r - Y_A \tag{2.6}$$

$$L_S = Y_A - Y_f \tag{2.7}$$

To have a reference of PR historical trends when calculating the PR within this research, Figure 2.11 presents the specific energy yield against the annual irradiation in the Plane of Array (POA), for PV systems from 1994, 1997 and 2010, with on-site irradiation taken with mono-crystalline silicon reference cells in Germany (Reich et al., 2012).

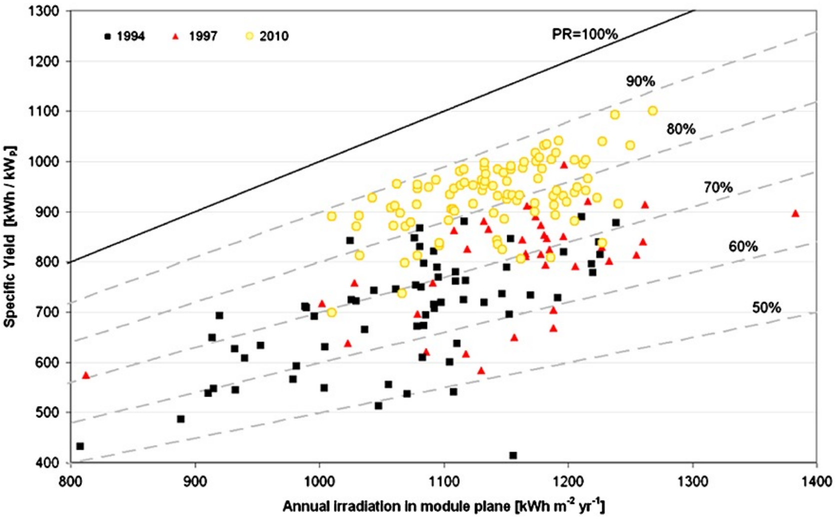

Figure 2.11: "Monitored specific yield as a function of total plane-of-array irradiation of photovoltaic systems installed in years 1994, 1997, and 2010 with corresponding performance ratio contour lines. Data shown were acquired during the 1000-Roofs Programme in 1994/1997 and in 2010 by Fraunhofer ISE monitoring services. The shown data notably use on-site irradiation measured by exclusively mono-crystalline silicon reference cells".(Reich et al., 2012).

Module and string efficiency

If power measurements are only available at string level, being the case within this research, then Equation 2.8 may be used for determining PV (string) efficiency (η_{String}). The power output (P_{String}) is measured in W, irradiance on the POA (G_{POA}) in W/m^2 and the string area (A_{String}) covered by the PV modules in m^2.

$$\eta_{String} = \frac{P_{String}}{G_{POA} * A_{String}} \tag{2.8}$$

If no power measurements are available per PV module, then Equation 2.9 may be used for determining the module efficiency (Smets et al., 2016), which considers module temperature, irradiance and module characteristic as inputs. In the equation, G_m is referred as the irradiance perceived by the module in W/m^2, T_M as the module temperature in ^oC. The complete module efficiency derivation and parameters to be used are presented in Appendix E.6.

$$\eta(T_M, G_M) = \eta(25^o, G_m)[1 + k(T_M - 25^oC)] \tag{2.9}$$

PV module temperature and influence on efficiency

As seen from Equation 2.9, temperature influences PV performance, for the PV modules selected in the research, the efficiency decreases with increasing temperature with a coefficient of -0.365 $\%/^oC$ and thus a comparison of module temperatures off-shore and on-land is to be performed in order to identify differences that may cause a decrease or increase in efficiency of the PV modules.

Energy yield

The energy yield may be used to compare the PV systems total energy production. During a certain period of time, two systems can be compared with the cumulative daily energy yield. This comparison is possible when power measurements are available at module, string or array level.

If no power measurements are available at module level and PV module energy yield wants to be determined, then power output at Standard Testing Conditions (STC) is required (Equation 2.10). Moreover, the actual power output expected for each PV module is required (Equation 2.11 (Smets et al., 2016)). T_M is the temperature of the module, that can be simulated, and G_M the irradiance on the module. Furthermore A_M is the module area.
Finally, the energy yield on the DC side is given by Equation 2.12 (Smets et al., 2016).

$$P_{STC} = \eta(25^o, G_{STC})G_{STC}A_M \tag{2.10}$$

$$P_{DC} = \eta(T_M, G_M)G_M A_M \tag{2.11}$$

$$E_{Y_{DC}} = \frac{P_{DC}}{P_{STC}} * 100\% = \frac{\eta(T_M, G_M)G_M}{\eta(25^oC, G_{STC})G_{STC}} * 100\% \tag{2.12}$$

Capacity factors

PV capacity factor (C_F) can be defined as the current weather-dependent PV performance relative to Standard Test Conditions (1000 W/m^2 and PV module temperature of 25^oC) (Kaspar et al., 2019). It establishes the relationship between the total installed PV power and the power generated on average during a certain time period (Smets et al., 2016).

For determining the capacity factor, Equation 2.13 is presented. Usually PV systems have a C_F of 15% for monocristalline silicon modules (Smets et al., 2016).

$$C_F = \frac{Power\ Produced\ [kW]}{Power\ Installed_{W_p}\ [kW]} \tag{2.13}$$

To have a reference within Europe for this research, Figure 2.12 provides the averaged photovoltaic capacity factors in Europe (1995-2015) derived by Kaspar et al., 2019. Additionally, Figure 2.13 presents the seasonal variability of the capacity factors for wind (blue) and PV (red) in Europe. From the PV seasonal cycle (red), the months between November and March record the lowest capacity factors, below 10 %, while the highest values are reached in the summer months of this region, reaching values just above 20 %.

From this data, the average capacity factor for PV within the region of The Netherlands, where the research is carried out, is in the range between 0.1 and 0.15. Additionally, with the experiment taking place in the winter months (November and December), the capacity factor in this period of the year is expected to be below 0.1.

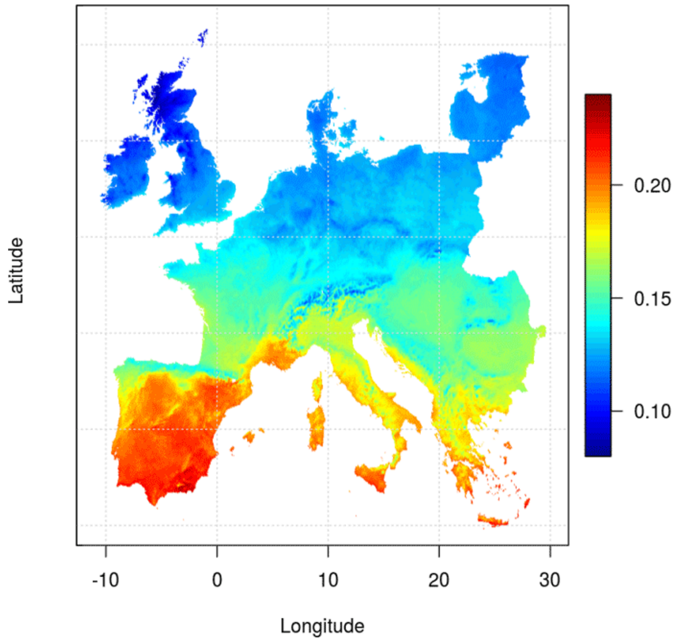

Figure 2.12: Average capacity factors (colorbar) for photovoltaics in Europe (1995–2015) derived from the regional reanalysis COSMO-REA6 and the satellite-based SARAH 2 dataset by Kaspar et al., 2019.

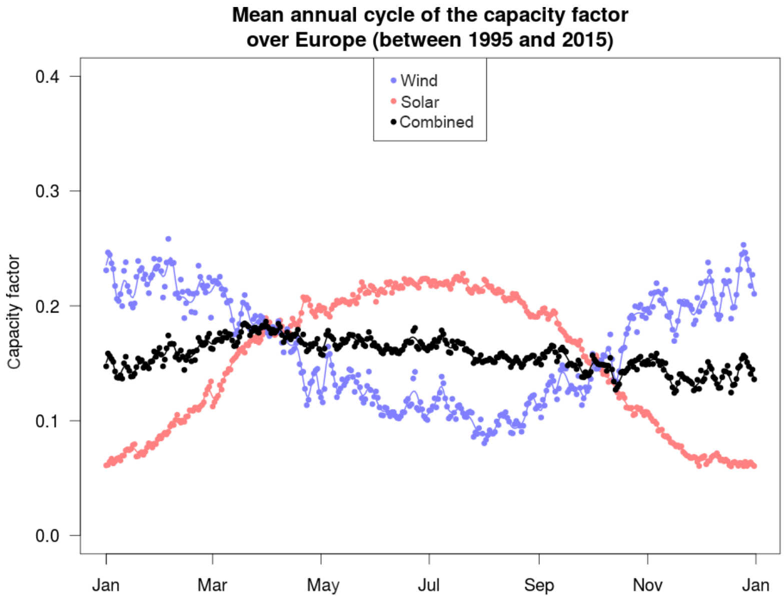

Figure 2.13: Seasonal cycle of the capacity factors for wind (blue) and PV (red) for Europe by Kaspar et al., 2019.

2.3.1. FPV models for module temperature prediction

There are various thermal models currently used for determination of module temperatures. The need to understand the thermal behaviour of PV, FPV and OFPV module temperatures is required as it directly influences power performance of a PV system, as shown in the PV module efficiency equations in Section 2.3.

Models for predicting PV module and cell temperatures were researched in literature to determine which environmental influences are currently considered and to additionally identify if FPV or OFPV environmental parameters, such as water temperatures or wave heights, were considered. The models found, combined together with empirical PV thermal models provided by Kamuyu et al., 2018 and Micheli, 2022, are presented in Appendix A.3, Table A.1, with T_c and T_m as cell and module temperatures calculated. For further details on the model equations, sources and parameters refer to Kamuyu et al., 2018 and Micheli, 2022. From these models it was identified that parameters such as water temperatures and wave heights, were not considered, with the exception of three models specific to FPV, presented later in this section. Therefore, the scarcity of empirical and simulated thermal models, suggests adaptations from current models are required or new models are to be developed. Furthermore, models can be developed simulating fluid dynamic behaviours or models can also be obtained from derivation and correlations with empirical measurements.

Kamuyu et al., 2018 presented two prediction models of PV module temperature for power performance on FPV. Two FPV systems, a test bed and a FPV system of 100 kW and 500 kW respectively, located in the Hapcheon Dam (Korea) were used for the study. Both systems consisted of c-Silicon module types with a fixed module slope of 33 ^{o} connected with aluminum and steel mounts. In that research, annual data considering environmental variables (ambient temperatures, irradiance on the modules, wind speed and water temperatures) was used to determine the linear regression models. The two empirical FPV models were estimated to accurately predict FPV module temperatures of the sites studied, with a 2 % to 4 % error margin depending on the number of equation coefficients incorporated. Additionally, a study by Hayibo, 2021, presented a model based on Kamuyu et al., 2018, and adapted it for a foam-based flexible FPV system, which was directly water cooled. In this case, the wind speed was not considered, due to the dominant cooling effect of water on the back surface.

Morevoer, COMSOL simulations performed by Ziar et al., 2020, with a bifacial module having only the lower frame in contact with water, showed that the cooling effect seen in the EVA and glass materials did not extend to the complete module due to low thermal conductivity. The model discussed predicted a 0.17 % increase in energy compared to a fully air case.

Furthermore, thermal PV models described by Smets et al., 2016 used to predict module temperatures, concerning a fluid dynamic model, which can be adapted to OFPV conditions, a steady-state model and Duffie-Beckman model, are presented in detail in Appendix A.

Also Micheli, 2022, summarized case studies, models and research findings for temperature of FPV. It was concluded that current FPV systems are subject to site or design specific configurations, making it difficult to draw universal conclusions. FPV should be additionally classified in air or water cooled systems, with water cooled ones expected to have lower temperatures, due to the higher heat transfer of water. Additional experimental and comparative studies of thermal performance are recommended to continue being carried out.

Table 2.2 presents the three empirical thermal models found to estimate module temperatures for a FPV system. Although FPV systems are subject to site and design specific configurations, these models were selected to be further investigated to identify how module temperatures measured within this research for OFPV compared with module temperature predictions by these FPV empirical models. $T_{FPV,m}$ is the FPV module temperature in ^oC, T_a is the ambient temperature in ^oC, G_T is the irradiance at the Plane of Array in W/m^2, V_w is the wind speed in m/s and T_w is the water temperature in ^oC.

Model author and year	Empirical thermal model
Kamuyu et al., 2018	$T_{FPV1,m} = 2.0458 + 0.9458T_a + 0.0215G_T - 1.2376V_w$ $T_{FPV2,m} = 1.8081 + 0.9282T_a + 1.021G_T - 1.2210V_w + 0.0246T_w$
Hayibo, 2021	$T_{FPV,m} = -13.2554 + 1.2645T_a + 0.0128G_T - 0.0875T_w$

Table 2.2: Empirical photovoltaic models for module temperature prediction found for FPV.

2.4. Monitoring technologies of interest

Different monitoring technologies are available for comparing OFPV performance with an on-land PV systems. In order to make a fair comparison, both systems should measure power, voltage, and current. Additionally, Global Horizontal Irradiance (GHI) should be measured to ensure both sites receive similar irradiation levels. Irradiance on the modules at the POA is important to determine the efficiency of the systems, as well as the off-shore system change in POA, which is prone to change due to the off-shore environment.

Ambient and module temperatures must also be recorded to understand the behaviour and efficiency of PV modules. Sea and water effects should also be analyzed, these concern wind, wave and water temperatures. In case measurement devices are not able to be implemented, external weather stations and/or meteorological softwares should be considered. Evaluation of techno-economical advantages, availability in the market as well as practicality for OFPV applications is presented.

Monitoring devices include power meters, reference cells, pyranometers, temperature sensors, inclination sensors, weather stations, anemometers, dust sensors and any other device available in the market for this type of research.

Monitoring is required to determine the main PV energy loss mechanisms when comparing an on-land PV system and an OFPV system. The monitoring devices of interest found for the OFPV system being researched are shown in Figure 2.14. For off-shore conditions, wave measurements, as well as wind and water measurements are considered to have stronger environmental influences (Claus and López, 2022), and thus the inclusion in Figure 2.14 of inclinometers, wave buoys and anemometers as devices of interest to monitor OFPV performance. Additionally, soiling due to bio-fouling (Liu et al., 2018) or salt deposition may be identified through the use of a visual camera, optical soiling sensors and/or identification of hot-spots through the use of thermal sensors. A description of the monitoring devices of interest for studying OFPV performance for this research is provided in this section.

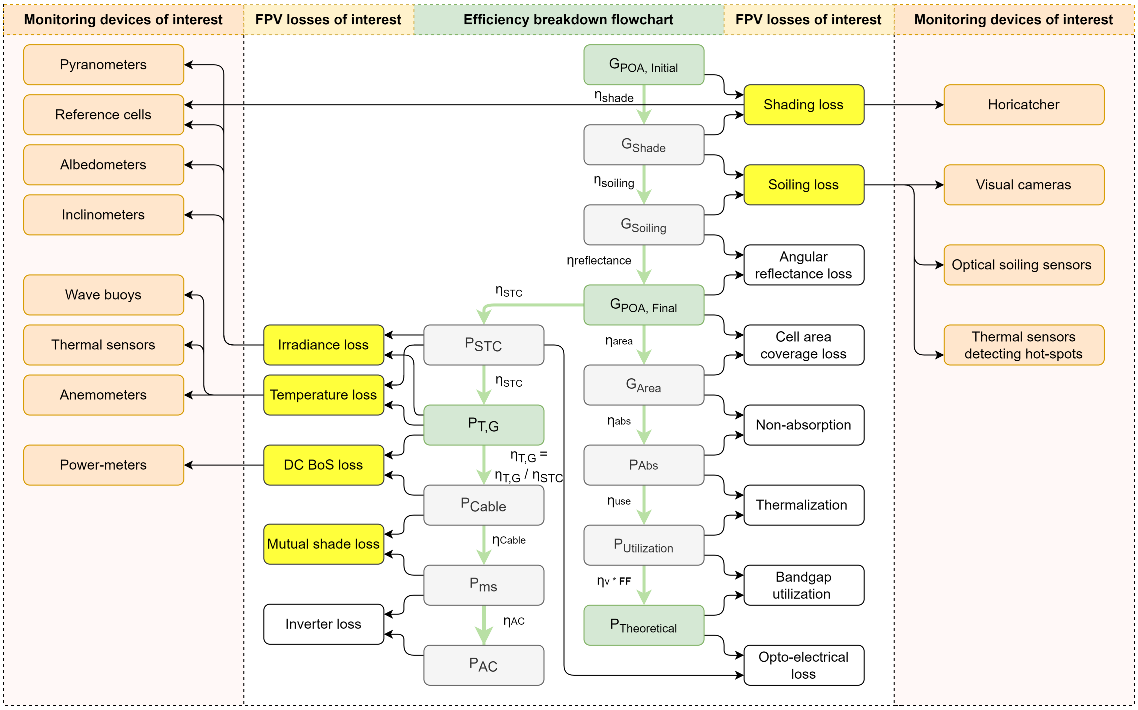

Figure 2.14: Efficiency breakdown flow chart for identification of OFPV losses of interest (yellow) and the respective monitoring devices of interest (orange) within this research.

Pyranometers and albedometers

Pyranometers are of special interest to measure the Global Horizontal Irradiance (GHI). From the irradiation measurements (W/m^2), the efficiency of a module with respect to the GHI can be derived. In this project the pyranoemeter is intended to be used to corroborate measurements at both locations with respect to GHI, having similar levels and irradiance patterns at the same time-step. Additionally, GHI meassurements are used to see the effect of the tilt movements caused off-shore.

Pyranometers are divided into classes A, B or C, depending on overall performance and how they compare to ISO 9060:1990 standards (ESS, 2021). Class A stands as the best performance with B and C decreasing in performance but are commercially more attractive. International standards for calibration are set in ISO 9847, ISO 9845 and ISO 9846 (Meydbray et al., 2012). The list of pyranometers considered, grade, supplier and additional notes is provided in Appendix B, in Table B.1.

Furthermore, albedometers may be considered to measure the albedo off-shore with respect to land. Two pyranometers placed back-to-back may be used. Economical and location feasibility should be performed , since off-shore conditions force albedometers set ups to have a robust mounting system.

Reference cells

Reference cells are of special interest as they can closely match the solar modules spectral response and can also closely match the angle of incidence (Meydbray et al., 2012). Note the temperature response of the reference cell is similar to the PV system, when using the same PV cell technology (Meydbray et al., 2012).

By placing them at the POA orientation of the PV module or system, one can get the PV module or PV array efficiency. Additional measurements sensors included within reference cells, such as cell temperature of the reference cell or ambient temperature can serve to further analyse PV module performance. International standards for calibration are set in IEC 60904 (Meydbray et al., 2012). Reference cells considered for this research are listed in Table B.2, provided in Appendix B.

Temperature sensors

Temperature sensors are required to monitor the ambient temperature and module temperature of the PV system (additionally water temperature may be included in the case of OFPV). Furthermore, safety precautions may be taken: an overheating alarm may be set with a remote management system (an example of a system used to monitor this temperatures is 'Victron Energy Remote Management System (VRM)'). Electrical components temperatures may be recorded for this purpos (MPPT charge controllers or battery temperatures). The list of temperature sensors considered within this research is provided in Appendix B.

The types of thermal sensors available in the market concern thermocouples, resistance temperature detectors (RTD), thermistors, thermometers, semiconductor sensors and infrared sensors.

Thermocouples provide wide range of measuring temperatures, however their accuracy is low. They work on the principle of voltage difference between two wires, which is then converted from voltage to temperature.

RTD sensors are considered stable and accurate, with a large range of temperature but lower than those in thermocouples. Platinum is the main material as it has a clear correlation between temperature and resistance. PT100 and PT1000 are the most common options, the precision is ten time larger with PT1000, but costs are in a range ten times higher as well.

Thermistors, similar to RTDs, use a polymer of ceramics instead of a metal. Their advantage is cost. Two types are available, PTC, corresponding to positive temperature coefficient thermistors (in which resistance directly proportional to temperature) and NTC which correspond to negative temperature coefficient thermistors (resistance inversely proportional to temperature).

Thermometers are directly discarded for this research as they measure the change in volume of a solid or liquid.

Semi-conductor sensors detect changes in temperature through the change in voltage, current or resistance.

Infra-red sensors are electronic sensors that are a non-contacting type. Accuracy in this case goes along side cost. For applications such as measuring the temperature reached by a resistor, this can be applicable.

Optical soiling sensors

Soiling and dust sensors are an upcoming monitoring technology. It is a relevant technology as it can detect soiling and thus can warn against the decrease in PV performance due to the deposition of a layer of dust on the panels if these do not receive enough rain or are not cleaned. Therefore, these devices identify when a solar module that is requiring cleaning of its surface. It is usually accompanied by a cleaning robot which can receive a signal to clean the solar array that suffers from dust. A list of sensors for consideration is provided in Appendix B.

The sensors researched for use were the 'DustIQ soiling monitoring system' from Kipp and Zonnen, seen in Figure 2.15a and the 'Mars optical soiling sensor', from Atonometrics, seen in Figure 2.15b. The DustIQ is described as an optical soiling sensor, with no moving parts and does not need additional powering, as it has its own solar energy being produced (DustIQ, 2022).

The DustIQ correlates the transmission loss (TL) of light with the soiling ratio (SR).The transmission loss accuracy is stated as: $\pm 1\%$ and ± 0.1 of the reading (DustIQ, 2022). The calculation to obtain the soiling ratio is presented in Equation 2.14.

$$SR = 100 - TL \tag{2.14}$$

Additionally, for off-shore conditions, it is of interest to monitor soiling due to environment conditions such as algae and salt since no data is directly available for this. Such a device in large scale farms can be of attractive use to reduce soiling losses. It was investigated to have suppliers providing these expensive systems for this research at a reduced price to in turn be able to test their systems under off-shore conditions. Nevertheless, price was not able to be reduced and thus, it was not possible to include the optical soiling sensors for this research.

(a) DustIQ optical soiling sensor from Kipp and Zonnen (DustIQ, 2022). (b) Mars optical soiling sensor (Atonometrics, 2022).

Figure 2.15: Optical soiling sensors for PV applications.

Power meters and Hall effect sensors

Power meters where required in order to see correlations in small time-steps of minutes, so these can avoid large assumptions over longer time periods. Additionally, current should be measured, thus devices such as Hall effect sensors can be considered for this purpose.

Inclinometers

Inclination sensors are used to measure module angles under wave conditions. This allows to further comprehend the power performance behaviour of the PV strings. A sample frequency increase goes alongside a cost increase. For this research, double tilt axis measurements are required.

Weather stations and anemometers

Concerning weather stations, the 'WS510-UMB Smart weather station' was found robust for off-shore conditions. It measures temperature, air pressure, wind direction, wind speed and radiation.

With regards to anemometers for off-shore wind applications in harsh environments, moving mechanical parts should be avoided. Thus, the found anemometer for marine conditions was the 'VENTUS-UMB Ultrasonic Wind Sensor', which is advised for extreme conditions in cold environments and marine environments. Note these systems tend to be higher in cost when compared to the other sensors presented in this research.

Meteorological softwares and stations

Meteorological softwares are of special interest as they can give a reference with climate data at precise locations where no data is available. For climate data, wind speed on-land and shading analysis tools such as Meteonorm may be used. For the off-shore location, when data is not directly available from experimental data such as from a wave buoy, a Koninklijk Nederlands Meteorologisch Instituut (KNMI) source may be used (KNMI, 2022): The Hollandse Kust Zuid Alpha (HKZA) weather station, located at coordinates 52.3, 4.0, provides information in 10-minute intervals for wave heights, swell, wind speed and direction as well as water temperature. Further information on HKZA is povided in Appendix G. No-other data set was found for this time-period with a higher resolution at this location.

Additional findings

An additional finding was the ’OTT-Parsivel sensor’. A laser weather sensor that could potentially measure wave splashing on the panels and thus correlation of the cooling effect from these could be done. It is designed to measure all precipitation types, measuring the size and speed of the particles hitting the sensor.

3

Methodology

Chapter 3 provides the steps and decision making towards the design and integration of an on-land and off-shore floating solar system for comparison on photovoltaic performance. The methods to achieve the PV performance comparison between the on-land and off-shore systems are presented. From here, the two experimental set-up designs are presented, together with the testing cycles. Finally, the experiment carried out is discussed. A visual overview of the methodology is provided through a flow chart in Figure 3.1, with arrows indicating the order of steps taken.

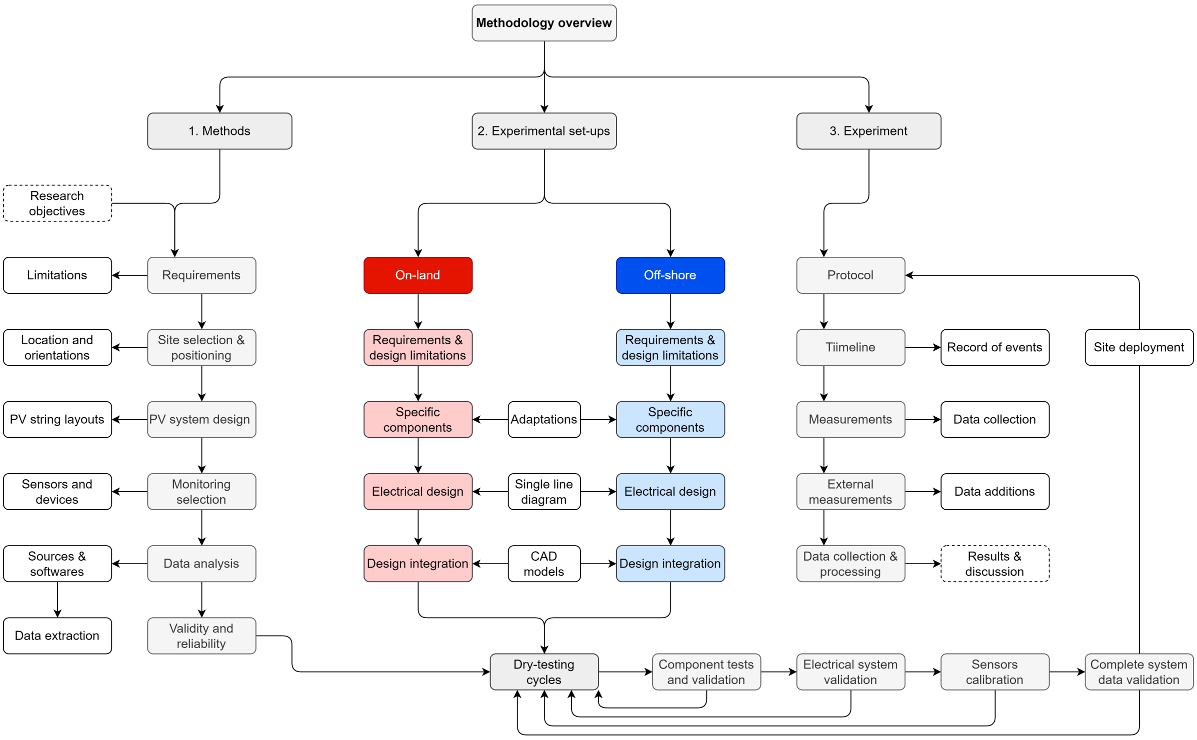

Figure 3.1: Methodology chapter overview.

3.1. Methods

The goal was to perform a PV DC performance comparison between off-shore floating PV systems and land-based PV system based on experimental data. Thus, two experimental set-ups were designed to reach this objective. Additionally, the design process for the system off-shore serves as the base to then provide design guidelines for OFPV off-grid systems in Chapter 4.

3.1.1. Requirements and limitations

Requirements were selected in order to be able to carry a valid comparison between two PV systems. The requirements for both experimental systems were as follows:

1. Must consist of the same type of PV modules, installed at the same time.
2. Must have the same amount of PV modules.
3. Must have the same string layout.
4. Must have PV modules of each string at the same inclination.
5. Must have the same azimuth when deployed.
6. Must be installed on the same floating technology (OOE floater).
7. Must be placed in a location avoiding external environmental shading.
8. Must pass electrical tests, with system running correctly for a month before experiment starts.
9. Must measure DC power production in minute time-steps.
10. Must measure Global Horizontal Irradiance (GHI) in minute time-steps. ‘
11. Must measure irradiance for each POA (G_{POA}) in minute time-steps.
12. Must measure module temperatures and ambient temperatures.
13. Must be deployed for the experiment for the same period of time.

Limitations were:

1. Experiment length within the time-frame of the thesis.
2. Budget conditions set by Oceans of Energy.
3. Deployment date for experimental set ups was subject to Oceans of Energy.
4. PV modules pre-selected for experiment by Oceans of Energy.
5. No power optimizers available per module.
6. Power measurements to be taken at string level.

3.1.2. Site selection and positioning

Two identical PV systems were built within Oceans of Energy floater technology for comparison of performance off-shore against on-land. One system was off-shore, in the North Sea, where as the second system was placed on-land, on solid ground, elevated 0.5 meters from the ground.

The site selection off-shore was predetermined by Oceans of Energy, to be incorporated within the North Sea 2 demonstrator. It was surrounded by other floaters, thus it was important to ensure no shading affected the system as well as obtaining the azimuth at the location. The on-land location was also assessed and the optimal available position was chosen to avoid shading. In the on-land system, the pre-set azimuth orientation of the North-Sea 2 demonstrator, provided by Oceans of Energy, was used to place the on-land system at the same orientation. The site locations for the on-land (red) and off-shore (blue) systems is shown in Figure 3.2.

For the set-ups positioning, both systems (on-land and off-shore) had two PV strings consisting of six PV modules connected in series (per string). One string was set facing a North-West orientation and one string was set facing a South-East orientation. The string layouts are discussed in depth in Section 3.1.3. The orientation of all PV modules on the North-West string had an azimuth of 150 ^{o} with respect to North (Figure 3.3a) and the orientation of all PV modules on the South-East string had an azimuth of -30 ^{o} with respect to North (Figure 3.3b). Each string of PV modules was inclined between 2^o to 4^o (South-East) and also 2^o and 4^o degrees (North-West). This variation in module tilt is due to fabrication tolerances provided by Oceans of Energy during installation. Figure 3.3 presents the PV system orientations for each string.

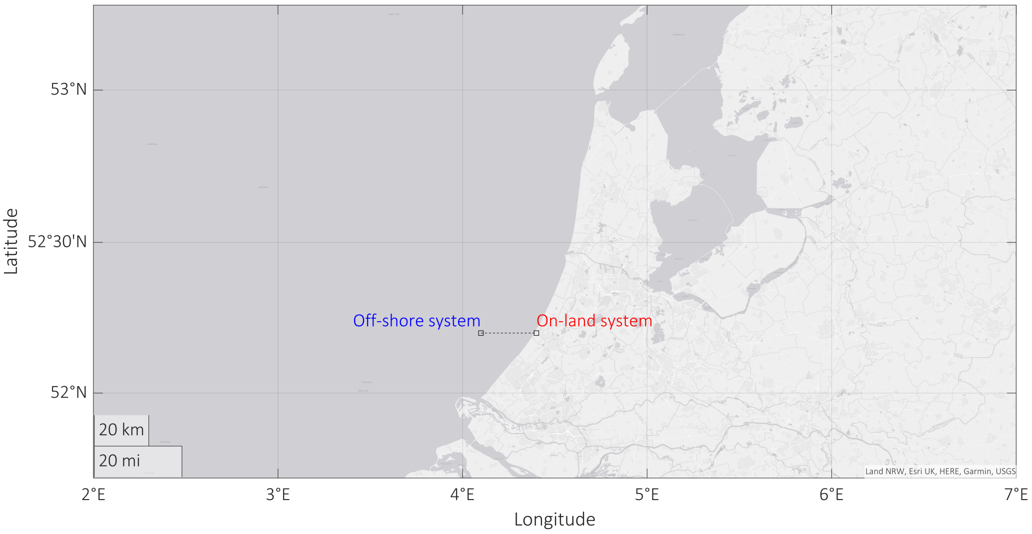

Figure 3.2: Map with locations selected for each PV system (The Netherlands).

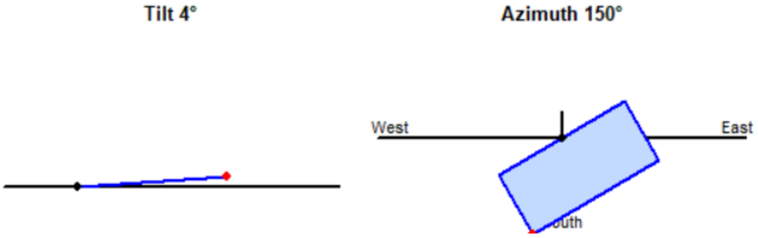

(a) North-West orientation, with an azimuth of 150 ^{o} with respect to North.

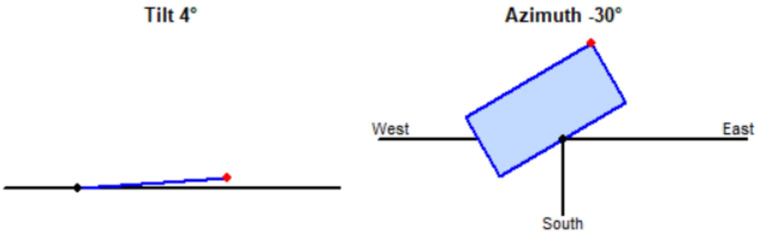

(b) South-East orientation, with an azimuth of -30 ^{o} with respect to North.

Figure 3.3: Systems orientation for each PV string for both locations (off-shore and on-land).

3.1.3. PV systems design

The PV design, focusing on the string layouts on the DC side is presented in this section. It is important to highlight the PV performance comparison was performed on the DC side of the two systems. Both systems (on-land and off-shore) consisted of 2 strings in parallel with 6 PV modules connected in series.

For future reference within the research, each PV module was given an identification number from 1 to 12. Additionally, for identifying each string, the following names were set for future reference: PV string consisting of PV modules 1 to 6 was set to face a North-West orientation, therefore it was referred as 'North-West string'. The PV string consisting of PV modules 7 to 12 was set to face a South-East orientation, therefore it was referred as 'South-East string'.

A single line diagram is provided in Figure 3.4. The pre-selection of PV modules was performed by Oceans of Energy for this experiment. The PV module technology is monocristalline silicon with 120 M6 bifacial half cut cells, with characteristics used in this research presented in Table 3.1. For this experiment, each string consisted of a string peak power ($P_{String_{Max}}$) of 2.16 kWp, a string open circuit voltage (V_{OC}) of 248.46 V and a string short circuit current (I_{SC}) of 11.12 A.

The DC power output measured from the strings off-shore and on-land was based on the same PV array layout. The off-shore system was an independent experimental set up which required to be off-grid. The system design differed from the on-land system after the strings DC output: unlike the off-shore system, the on-land system was connected with an inverter to the grid. The study of the AC side was outside the scope, as the goal was to compare performance on the DC side. The differences in design are presented for each experimental set up in Section 3.2 for the on-land system and Section 3.3 for the off-shore system. Additionally, the design integration of each experimental set up was performed using the computer aid design (CAD) modelling program 'Fusion360', with designs used for installation of devices intended to measure PV performance.

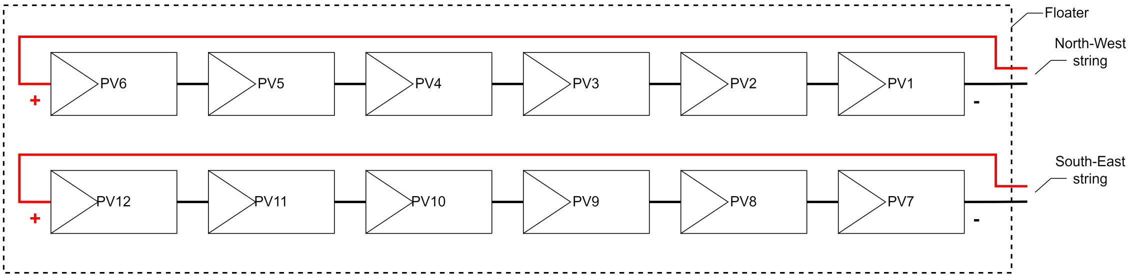

Figure 3.4: PV array single line diagram both on-land and off-shore systems.

Cell type	P_{Max} $[Wp]$	I_{sc} $[A]$	V_{oc} $[V]$	I_{mp} $[A]$	V_{mp} $[V]$	η_{STC} [%]	A_{Module} $[m^2]$
M6 bifacial half-cut	360	11.12	41.41	10.70	33.77 V	19.76	1.82

Table 3.1: Monocristalline silicone PV modules pre-selected for experiment, at STC, for both on-land and off-shore systems (relevant PV module characteristics).

3.1.4. Monitoring devices selection

Monitoring devices and sensors of interest for OFPV performance measurements were presented in Section 2.4. For selection of which devices to implement within this experiment, a feasibility assessment was made with the following parameters:

- Order of significance: depending on the monitoring device and importance, a product was selected. Devices measuring power, irradiance and temperature were prioritized.
- Market availability: monitoring devices had cases of market scarcity, or long waiting times, thus depending on availability and delivery times, a product was selected. Delivery times above 2 months meant a product was discarded or had an alternative proposed. Additionally, products already available at OOE were considered.

- Price and quality: budgeting was performed by OOE, if price (and amount) was considered very large, the order of significance was used, and if the significance was low then a different monitoring device was investigated or else discarded.
- Quantity and redundancy: depending on the quantity of devices, a sensor was selected. The higher amount meant the budget per monitoring device or sensor decreased. Redundancy was also considered, thus products with an expected higher failure probability could be increased in number, such as thermal sensors off-shore.
- Communication protocols: monitoring devices selected we selected to be able to convert analog signals into digital outputs and then transfer the data through Transmission Control Protocol (TCP) or Modbus Remote Terminal Unit (RTU) communications protocols to the data logger device, and finally have the data transferred to the data logger server through the router.

The monitoring devices and sensors selected for this research are displayed in Table 3.2. All devices and sensors considered in the feasibility assessment are provided in Appendix E. Additionally, the output measurements registered for all monitoring devices and sensors during the experiment period are provided in Appendix E.

Device	Product model	Quantity	Location
Reference cell	SI-RS485TC-2T-Tm-MB	2	Off-shore
Reference cell	SI-RS485TC-T-Tm-MB	1	On-land
Reference cell	SI-RS485TC-2T-Tm-MB	1	On-land
Pyranometer	Kipp and Zonen SMP3 Class C	1	Off-shore
Pyranometer	Kipp and Zonen SMP3 Class C	1	On-land
Power meter	AcuDC 243-300V-A2-P1-X5-C-D	2	Off-shore
Power meter	AcuDC 243-300V-A2-P1-X5-C-D	1	On-land
Power meter	AcuDC 243-300V-A2-P1-X1-C-D	1	On-land
Hall effect sensor	HAK21-50-A2	2	Off-shore
Hall effect sensor	HAK21-50-A2	2	On-land
PT100 Module	Adam 4015 6RTD Modbus RS-485 Remote I/O	2	Off-shore
PT100 Module	Moxa ioLogik E1260-T Remote Ethernet I/O with 6RTD	2	On-land
PT100 Sensor	Self Adhesive Patch PT100 Sensor PFA insulated PRT	10	Off-shore
PT100 Sensor	Self Adhesive Patch PT100 Sensor PFA insulated PRT	10	On-land
PT100 Water	Electrotherm RTD, M8 Dia, 40mm , F0.3 +200°C Max	1	Off-shore
Universal controller	Moxa ioLogik E1240 -Universal I/O, 8 AIs	1	Off-shore
Inclinometer	Kelag KAS901-51A	1	Off-shore

Table 3.2: Monitoring devices and sensors selected for experimental set-ups.

Furthermore, 10 PT100 thermal sensors where selected to record module temperatures for each system. The location of the sensors on each PV array is shown in Figure 3.5. These sensors were positioned in the back side of the PV module.

Moreover, PV module number 7 was equipped for both systems with 5 PT100 thermal sensors to identify differences in temperature throughout a single module: The specific location of these sensors on the back-side of the PV module is shown in Figure 3.6. Modules with only 1 PT100 sensor, had the sensor installed in the cell labelled ’middle cell’, with its location also seen in Figure 3.6. The decision of locating 5 thermal sensors on PV module number 7 was based on the hypothesis that the South-East orientation, within a corner of the floater, would have higher chances of exposure to water splashing and bio-fouling, which in turn could cause the appearance of hot-spots.

The positioning of the reference cells and pyranometers differed between the system off-shore and on-land due to different design limitations. Reference cells where positioned at the same orientations of the strings, shown in Figure 3.3 and the pyranometer was positioned with a 0^o inclination. Additionally, the inclinometer sensor position off-shore is also presented in the off-shore system design.

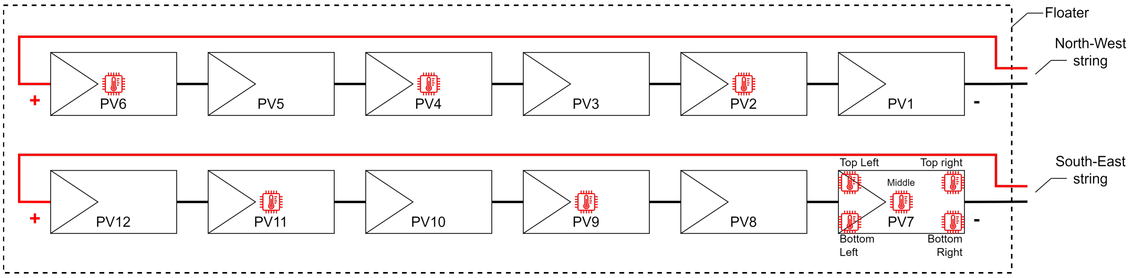

Figure 3.5: PV system design layout with PT100 thermal sensors (red) module locations.

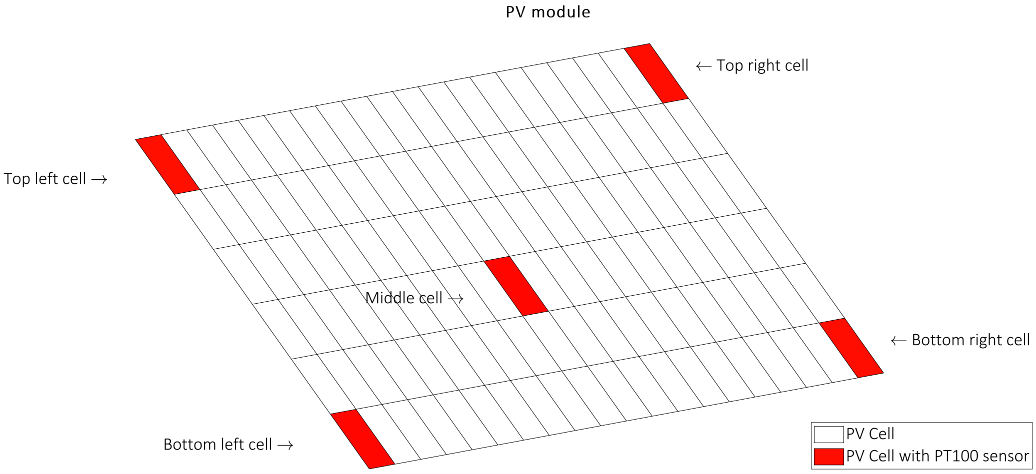

Figure 3.6: Specific location and labels of PT100 thermal sensors (red) on PV cells within PV module 7 (5 sensors).

3.1.5. Data analysis procedures

The procedures to extract and process the data obtained within the experiment are discussed in this section. Data analysis of empirical results obtained from the monitoring devices through the following procedure:

Firstly, monitoring devices converted any analog signal, such as the case of RTD100 thermal sensors, to a digital signal. All monitoring devices communicated through Transimission Control Protocol (TCP) or Remote Terminal Unit (RTU) protocols to a data logger. From here, configuration of all monitoring devices was performed so that the Modbus RTU or Modbus TCP Internet Protocol (IP) addresses were set to have an individual address to avoid data overlaps. The baud rate for all sensors was the same (19200), as well as the data format. The register addresses were kept according to manufacturers configurations.

Secondly, for data extraction it was deemed hourly excel sheets being produced would give the most constant data output type. All measurements for both on-land and off-shore were recorded in hourly sheets and were stored on an SD card (back-up) as well as uploaded into the cloud server.

Thirdly, data analysis was performed from the hourly excel sheets produced. Using the programming tool 'Matlab 2021b', the combination of all excel sheets downloaded resulted in a workspace table with all variables with their respective time-steps. On the off-shore system, since the inclination sensor reported measurements per second, the rest of the off-shore monitoring devices (having their best frequency resolution at 1 minute time-steps) had to state 'Not a Number' (NaN) for 59 out of 60 measurements per minute and thus was post-processed.

Finally, from here variables in a certain range of time were selected for analysis. The complete comparison between both systems ranged from the 15-11-2022 00:00 to 1-1-2023 00:00, when both systems were fully operational.

Additionally, data was also collected and analyzed from the following sources:

- Hollandse Kust Zuid Alpha (HKZA) KNMI station: Wave, wind and water measurements off-shore. Data occurrence: Time steps of 10 minutes (constant).
- MPPT charge controller off-shore. Data occurrence: Time steps of 15 minutes (not constant).
- Meteonorm 7.2 meteorological software was also used. Data occurrence: Hourly time steps (2000 to 2009 climate data).

Tools used within Matlab 2021b included:

- Import, export and data concatenation commands.
- Post-processing operation and analysis commands.
- Basic plotting.
- Mesh-grid plotting.
- Time-dependent plotting.
- Regression plotting.
- Basic fitting commands.
- Histogram commands.
- Box-plot commands.
- Wind-rose models.
- Statistical models.
- Linear regression fitting models.

The data extraction procedure with data imported from the 4 sources (MPPT charge controller, monitoring set ups, KNMI weather station and Meteonorm 7.2) is also shown through a flowchart provided in Figure 3.7, with arrows indicating the flow and order of steps and actions taken.

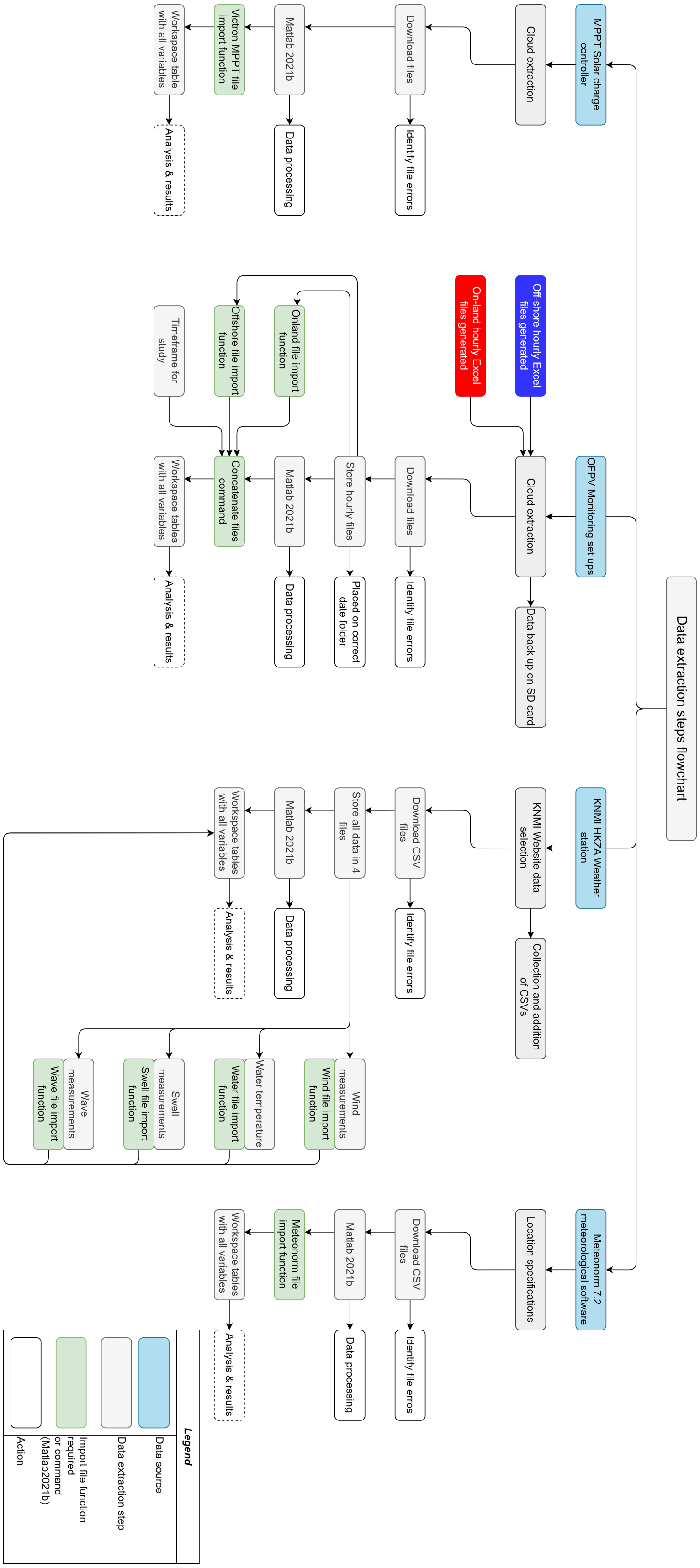

Figure 3.7: Data extraction steps flowchart.

3.1.6. Measurements and results validations

Data validation was performed to ensure measurements and data analysis outputs were proved as reliable. Dry-testing cycles were performed to ensure all devices performed as desired for the experiments. The following procedures were followed to validate measurement readings:

- Dry-testing cycles: testing components before usage during experiment. Testing both on-land and off-shore systems side by side before deployment. Identifying differences on readings for power, irradiance and temperature. Testing components performance after adaptations or extensions of DC and thermal cables. Special focus was made on thermal sensors (PT100) to ensure readings were valid after thermal cable extensions were made. Additionally, tests making sure readings corresponded to the correct reference cell and pyranometer orientations were made.
- Long term monitoring: longer time periods provide information to identify if a measurement is consistent over time and meets expected values. Seven weeks were used for monitoring the experiments. To draw annual conclusions, the experiment should be carried for a year.
- Comparison with literature: using empirical FPV thermal models presented to identify differences and correlations.
- Comparison with meteorological softwares and weather stations: checking ambient temperature measurements compared with climate data and thus identify any disparities. Water temperature is compared with HKZA station readings for validation.
- Comparison between devices: pyranometers provide the GHI which also may show if both locations experience similar levels of irradiance to be compared with respect to PV performance. Additionally, off-shore measurements from MPPT charge controller readings off-shore were used to validate the power meter readings.
- Statistical analysis: to indicate the level of uncertainty and statistic significance of results.

The dry-testing cycles are presented in Figure 3.8. With arrows indicating the flow order of tests and arrows looping in case an error or issue was detected, so that tests could be checked and redone until optimal functioning of components and monitoring sensors was achieved. The dry-testing cycles started with checking that components selected in each system worked correctly upon installation. In this stage, the battery protection system for the off-shore system was tested to ensure correct discharge and voltage levels of the battery storage system. Additionally, resistors were also tested to ensure the power dissipation unit worked correctly and to identify temperatures reached by the resistors (discharge unit). Additionally, the MPPT solar charge controller was tested to ensure it worked under 'Bulk' mode, which meant the controller delivered as much current as possible. Note these off-shore system components mentioned (the battery storage system, dissipation unit and MPPT charge controller) are presented in depth in Section 3.3. Additionally, powering of all monitoring devices at 24 V was tested. Once this stage was completed, the integration of all system components was performed and tested for one month to ensure a correct functioning of all components. From this stage, all monitoring devices were tested, calibrated and set with configurations to ensure a correct data extraction process during the experiment. Once all data outputs were checked, the systems were ready to start the experimental phase. Results of these tests are further discussed in Section 5.

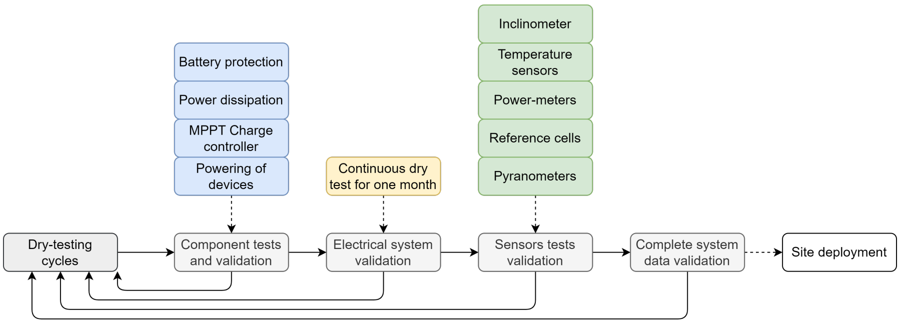

Figure 3.8: Dry testing cycles for measurement and result outputs validation.

3.2. On-land experimental set-up

3.2.1. Specific requirements and limitations

1. Must be standing on solid ground.
2. Must be placed at the same azimuth as the PV system off-shore.
3. Must have the correct ingress protection (IP) number to be able to be deployed in the future off-shore.
4. Must have all monitoring devices be powered from the grid. With the exception of power meters (powered directly from PV strings).

3.2.2. Components

The on-land system BoS within the DC side consisted of the DC cables and monitoring box, where all measuring devices were incorporated. The inverter 'Sunny Tripower 8.0', from SMA, was provided by OOE and was implemented to provide the PV energy, generated by the on-land system, into the grid. Nevertheless, the alternative current (AC) side is outside the scope of this research and thus not included. Power of monitoring devices on-land was done directly from the grid, with a 2 A 12 V AC/DC standard adapter. Power meters, together with Hall effect sensors, powered themselves directly from the PV strings, with a power consumption of 2 W. All monitoring devices within the data box and their respective power consumption are listed in Table 3.3. Data sheets of the monitoring devices are provided in Appendix H.

Device	Power consumption [W]	Quantity	Total power consumption [W]
Data logger	1.5	1	1.5
Router	7	1	7
PT100 Module	2.6	2	5.2
Reference cell	0.6	2	1.2
Pyranometer	0.2	1	0.2
Power meters	2	2	-
Total	-	9	**15.1**

Table 3.3: Monitoring devices and components installed on-land and their respective power consumption.

DC cable losses

The ohmic resistance of the DC wiring induces losses between the power available from the modules and the power at the terminals of each string (PVSyst, 2023). DC cables of 6 mm^2 cross-section were available and selected at OOE, and thus losses were calculated to see the influence affecting PV performance measurements recorded at the power meters. For evaluating the wires ohmic power loss, MPP power was required and the power loss (P_{Loss}) was defined as the wire resistance (R_{Cable}) times the current at maximum power point squared (I^2) (PVSyst, 2023). Power losses were found to be of 0.67 % per string with respect to peak power production. For all strings, for both systems (on-land and off-shore), the DC cables of each string up until the power meters were set to an almost equal length of 50 meters of DC cable with a copper cross-section of 6 mm^2. Therefore DC power losses of 0.67 % per string due to cable losses were assumed negligible in the power performance comparison (same cable losses off-shore).

To obtain the power losses, for a length of 50 meters (25 meters * 2) for each string of DC cables used, the following calculations, based on Smets et al., 2016, were performed:

$$R_{Cable} = \rho \frac{L}{A} = 0.0168\Omega * mm^2/m * \frac{50m}{6mm^2} = 0.14\Omega \tag{3.1}$$

$$P_{Loss} = I^2 * R_{Cable} = 10.2A^2 * 0.14\Omega = 14.57W \tag{3.2}$$

$$P_{Loss,Total} = \frac{P_{loss}}{P_{Wp}} = \frac{14.57W}{360Wp * 6} * 100 = \mathbf{0.67\ \%} \tag{3.3}$$

In these calculations, R_{Cable} is the resistance in the cable $[\Omega]$, ρ is the resistivity of copper (0.0168 $\Omega * mm^2/m$) (Smets et al., 2016), L is the length of the cable $[m]$, A is the cross-sectional area $[mm^2]$, P_{Loss} the power loss related to the cable $[W]$ and I_{mpp} the current at maximum power point $[A]$.

3.2.3. Electrical design

After presenting the PV array configuration and the selection of the monitoring components was complete, the electrical design single line diagram for the on-land PV system was developed and is presented in Figure 3.9.

3.2.4. Design integration and construction

Firstly designs were made to visualize how the system should look like and secondly, CAD designs were made to ensure components within the monitoring box were placed in an optimal layout. The computer aided design (CAD) design was made with the modelling tool 'Fusion360'. This tool was used to for the design of the on-land system monitoring box and thus have a design layout to incorporate all the monitoring devices selected on-land. First,the monitoring box design together with the inverter (blue), the thermal cable extensions for the thermal sensors on the modules (yellow) as well as a PV floater, are shown for an overview in Figure 3.12.

The CAD design was used for determining an optimal layout and spacing of monitoring components upon installation. The monitoring box components layout on-land is shown in Figure 3.11. Once the layout required was known, the installation of the components on the monitoring box on an IP67 box was performed, including cabling and also IP67 glancing, as shown in Figure 3.12.

Additionally, reference cells were placed next to the PV array, at the same PV strings orientation as previously described in Figure 3.3. The pyranometer was also placed adjacent, at an inclination of 0^o.

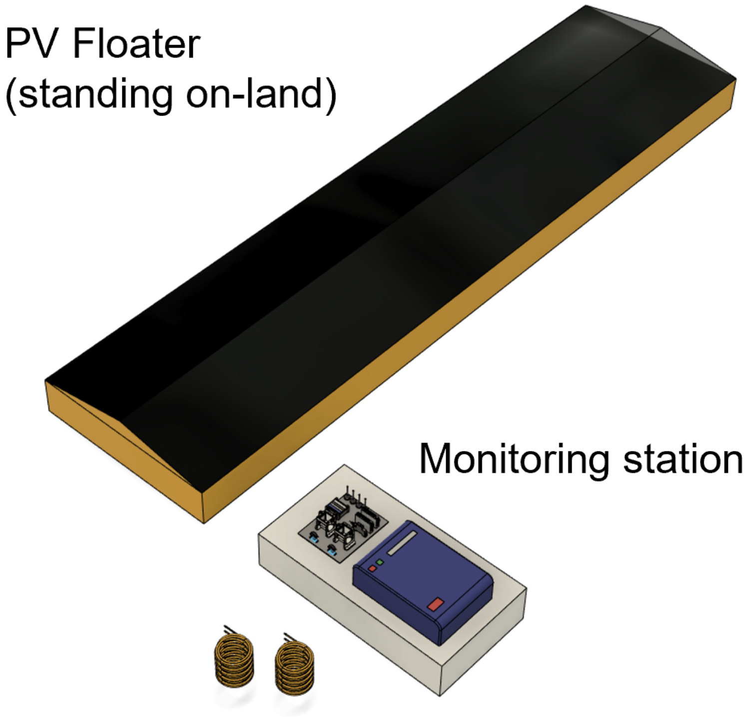

Figure 3.10: On-land system general visualization: consisting of a PV floater with PV modules (black), monitoring box (dark grey) and the inverter (blue).

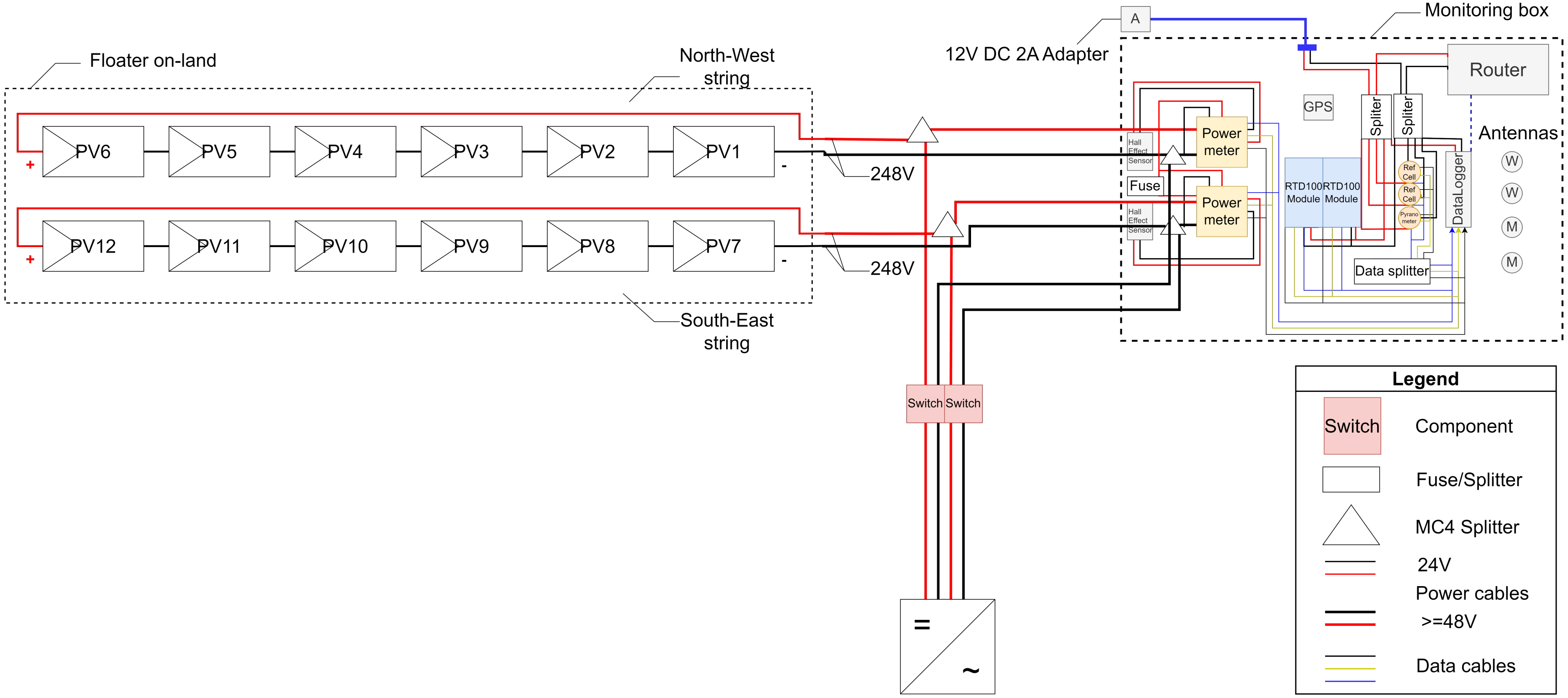

Figure 3.9: Single line diagram for PV system on-land. Components not to size.

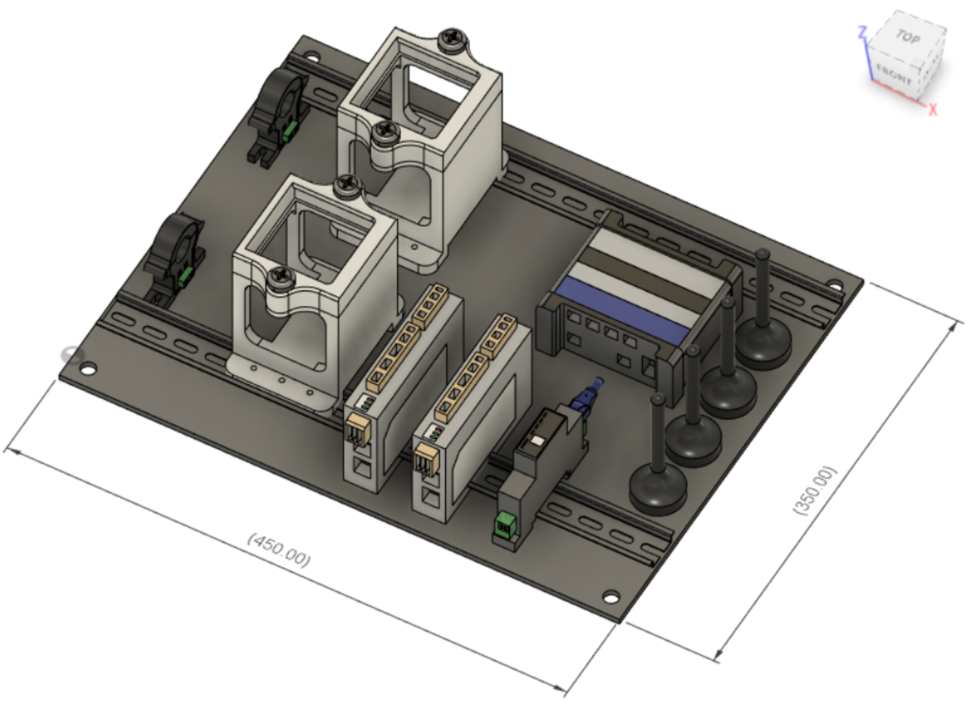

Figure 3.11: Layout of monitoring box on-land components in Fusion360 (CAD). Dimensions in mm.

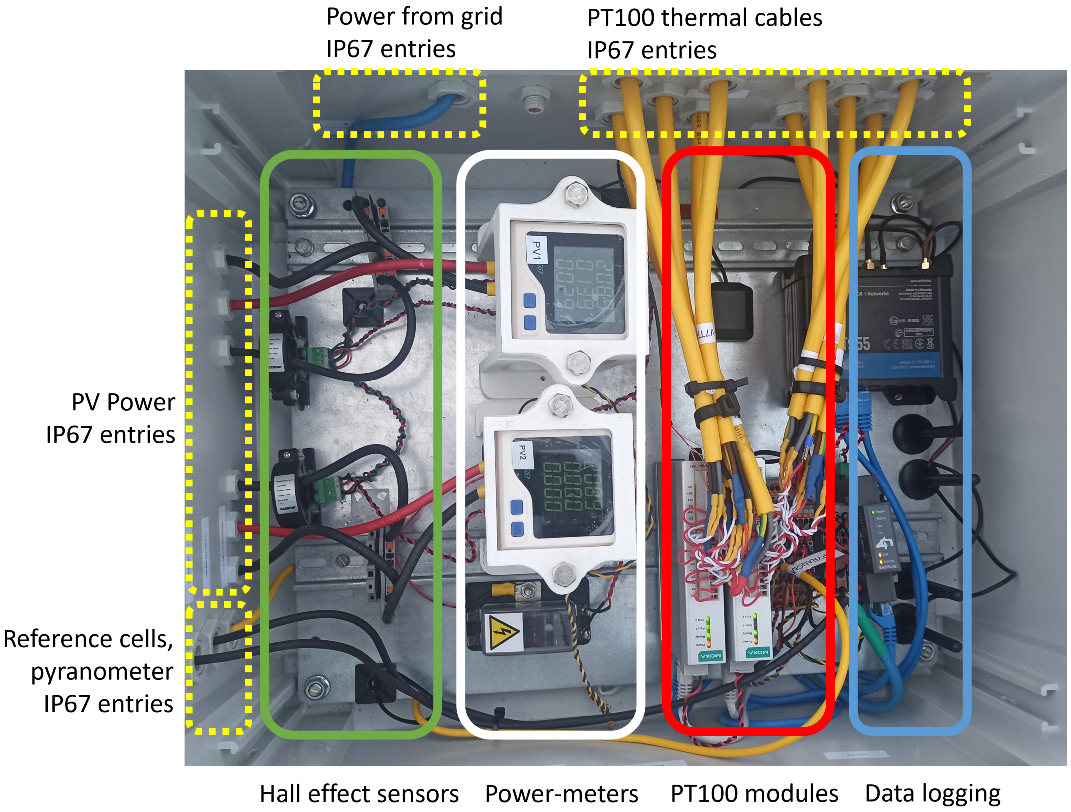

Figure 3.12: Description of on-land monitoring box with components integrated.

3.3. Off-shore experimental set-up

3.3.1. Specific requirements and limitations

1. Must be an off-grid system.
2. Must have all components, including monitoring devices be powered by the PV system and not by an external power source.
3. Must be able to withstand off-shore conditions of the North Sea (The Netherlands).
4. Must have the correct ingress protection (IP) for off-shore conditions.
5. Must be equipped with a battery system and be able to power all monitoring devices at 24V.

3.3.2. Balance of System (BoS) components

Power box components

Firstly, the power system was designed: Maximum open-circuit voltage and current outputs of each string defined the sizing and selection of the solar charger or MPPT charge controller to be used. The following calculations were performed:

$$V_{Max,In} \geq V_{OC} * N_{Modules,Series} = 248.46V \tag{3.4}$$

$$I_{Max,In} \geq I_{SC} = 11.12A \tag{3.5}$$

Secondly, the MPPT charge controller 'SmartSolar MPPT RS 450|100' from the company 'Victron Energy' was then selected, as it could also hold both strings voltage an current (450 V and 18 A as maximum PV operational input current per tracker). The data sheet is provided in Appendix H. The output voltage of the charger was 48 V, thus components after the MPPT charge controller were selected to handle this voltage. Monitoring components mostly run on 24V, thus the use of a 48 V - 24 V DC-DC converter was required. This was also the case for the battery protect relay system, concerning a voltage controller for this voltage range (48 V).

Additionally the communication device 'Cerbo GX' from Victron Energy was added, with the data sheet also provided in Appendix H. This device allowed to monitor, in real time, the battery state of charge, power consumption, power harvest from each PV string, and temperature measurements, among others.

Finally, a battery protection system was implemented to protect the battery voltage levels staying within a safety margin. Victron Energy 'Battery Protect 48 V 100 A' product failed the tests, as the system did not respond correctly when using resistors. A voltage controller together with a relay switch was implemented. When the batteries were full, the use of resistors came in place to burn the PV energy produced (dissipation unit). This is further discussed in the following subsections.

Battery box components

A battery storage system was required since the MPPT charge controller could not be connected directly to resistors as found during testing. The battery storage system was used to power the monitoring devices throughout the experimental period. The design and selection of the battery box components as well as the data box components is explained in this section.

The storage system consisted of 12 V lead acid batteries (provided by OOE), since the MPPT charger output was 48 V, four 12 V batteries (90 Ah) were connected in series. The battery capacity selection is determined in Equation 3.6. Since all monitoring devices being powered from the batteries run in 24 V, a DC-DC converter was implemented (Orion Tr DC-DC 48/24 5A), which was selected based on the power consumption required by the monitoring devices, presented in Table 3.4.

For the battery capacity (Ah) selection, equation 2.1 was used. Since 48V were required, four 12 V batteries connected in series made the battery bank. By assuming a week without power (7 days), the load to be 17.6 W (obtained from Table 3.4) and a maximum depth of discharge of 0.7, the battery capacity was determined to be 88 Ah. Therefore 12 V 90 Ah batteries were selected.

$$C_{BB} = \frac{Days_{Autonomy} * E_{Daily,Load}}{V_{BB} * DOD_{Max}} = \frac{7 * 17.6W * 24h}{48V * 0.7} = 88Ah \tag{3.6}$$

The energy required from the load (monitoring devices) was determined using the maximum power consumption stated in data sheets at 24 V. This is presented in Table 3.4. Additionally, power consumption from power meters is not included, as they are self powered directly from the PV strings. The daily energy consumption was found to be 422.4 Wh (17.6 W * 24 h), which was assumed to be able to be provided by the PV system. An additional calculation considering Loss of Load Probability (LLP) was considered and is provided in Appendix C.

Device	Power consumption [W]	Quantity	Total consumption [W]
Data logger	1.5	1	1.5
PT100 Adam 4015 Module	1.4	2	2.8
Router	7	1	7
Moxa ioLogik 1240 Controller	2.9	1	2.9
Inclinometer	0.5	1	0.5
Reference cell	0.6	2	1.2
Pyranometer	0.2	1	0.2
Power-meters	2	2	-
Data logger	1.5	1	1.5
Total	-	-	17.6

Table 3.4: Monitoring devices installed off-shore and the respective power consumption.

Resistors box components

The goal of the resistors was to be a dump load, thus burn all incoming power from the charge controller when the batteries were full (dissipation unit). This application was required to ensure the MPPT charge controller operated at 'bulk' mode during PV power production. If this was not achieved, the solar charger would change from bulk charging mode to absorption charging mode and could hinder the results of the experiment. Definitions of bulk and absorption mode are provided in Section 3.4.

Three 2 kW resistors were deemed to handle the 4.3 kWp system. A parallel connection between resistors was selected since voltage at each resistor was fixed. The three 2 kW resistors connected in parallel and with an individual resistance of 2 Ω, the equivalent resistance (R_{Eq}) was calculated with Equation 3.7, while taking the safety value of 60 V instead of 48 V to then determine the maximum current the system could be subjected to. This is shown in Equation 3.8 and Equation 3.9.

$$R_{Eq} = \frac{V}{I_{Total}} = \frac{V}{\frac{V}{R_1} + \frac{V}{R_2} + \frac{V}{R_3}} \tag{3.7}$$

$$R_{Eq} = \frac{V}{I_{Total}} = \frac{60V}{\frac{60V}{2\Omega} + \frac{60V}{2\Omega} + \frac{60V}{2\Omega}} = 0.67\Omega \tag{3.8}$$

$$I_{Max} = \frac{V_{Max}}{R_{Equivalent}} = \frac{60V}{0.67\Omega} = 89.55A \tag{3.9}$$

Balance of System components list

All components previously discussed selected for the power box, resistor box, storage and monitoring are listed in Table 3.6. Data sheets of BoS components, as well as for the monitoring devices, are provided in Appendix H.

Device	Location	Quantity
MPPT charge controller	Power Box	1
Cerbo GX	Power box	1
DC-DC converter 48-24	Power box and data box	2
Relay contactor	Power box	1
Voltage controller	Power box	1
12V 95A Lead Acid Battery	Battery box	4
2kW 2 Ω Resistors	Resistors box	3
PV cables	-	50m
Battery cables	-	20m
100 A Fuses	Power box	2
1 A Fuses	Monitoring box	2
Switches	Power and monitoring box	5
Splitters	Power and monitoring box	7

Table 3.5: Balance of System components off-shore.

DC cable losses

DC cable losses calculation was presented in Section 3.2.2. Highlighting that DC cables used off-shore, as well as the lengths used up to the power meters, where approximately the same as on-land. Thus, from Section 3.2.2, DC power losses were found to be of 0.67 % per string with respect to peak power production.

3.3.3. Off-shore protection

IP ratings of IP67 and IP68 were selected for enclosures of components requiring isolation against water in off-shore conditions, as well as for glands used on entry cables.

Off-shore monitoring devices placed outside the data boxes, where further protected as well, as shown in Figure 3.21a. Additionally, the on-land system was also equipped with the same protection, so it could be taken in the future off-shore as well as protecting it against the weather (rain and water) outdoors. IP67 glands used for battery, DC-cables and thermal sensor extensions were IP67 and consisted of 3 parts, the male screw terminal, the cable gland and the female screw terminal, shown in Figure 3.13. Moreover, screw nuts and washers were required when mounting. IP67 glance entries described are provided within the data sheet provided in Appendix H.

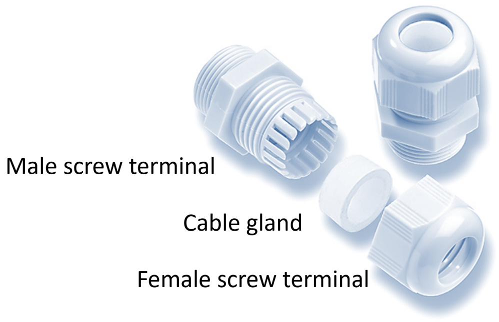

Figure 3.13: IP67 gland components used for off-shore protection.

3.3.4. Electrical design

The PV system off-shore has an electrical design subdivided in two. The components on the PV floater and the Balance of System (BoS) components located on the utility floater. Additionally, the utility floater was divided into 4 sections: The resistor box (dissipation unit), the power box, the battery box and the monitoring box (data acquisition unit). The electrical design is provided in Figure 3.14, which also includes data cables layout. And enlargement of the layout is also provided in Appendix C.

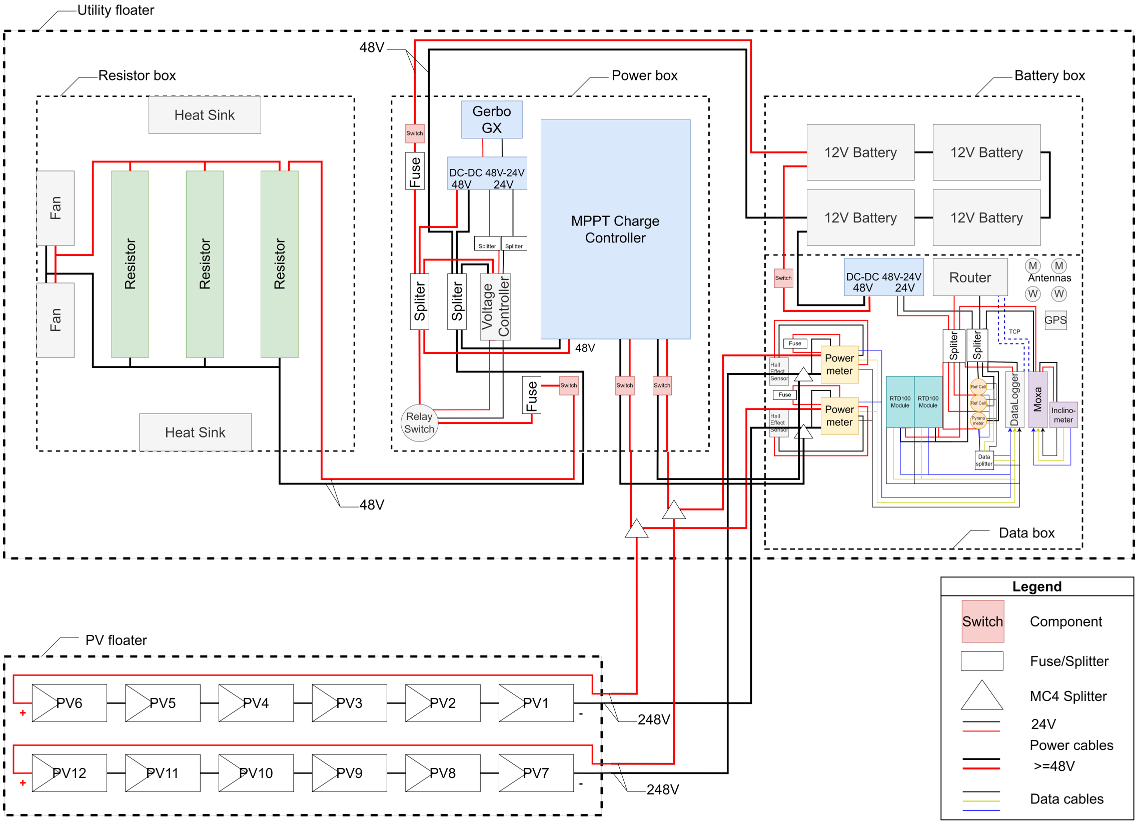

Figure 3.14: Single line diagram for PV system off-shore. Components not to size.

3.3.5. Design integration and construction

Once the electrical design was derived, the design integration phase started. This meant designing a computer aided design (CAD) model using the program 'Fusion360', to determine an optimal of BoS components and monitoring devices upon installation on IP67 boxes.

An overview of the off-shore system is presented in Figure 3.15 for a general visualization of the PV and utility floater. The utility floater was placed closest to the North-West orientation, with respect to the PV floater to avoid shading. Within the utility floater, all components where mounted into a metal plate within the protection boxes. Special emphasis was made on the monitoring box: fitting of the components inside the protective box involved optimizing space so cables would not overlap and no excess space was left, this is shown in Figure 3.16. Resistors box (discharge unit) and power box layouts are provided in Appendix C. Once the layout required was known, the installation of the components on IP67 boxes was performed, including cabling and also IP67 glancing, as shown in Figure 3.19.

Furthermore, additional protection off-shore was required due to wave movements and thus special mounts where designed in Fusion360 for the power meters (data sheet provided in Appendix H), since the suppliers mounts were not designed to hold power meters with tilt and wave movements. A 3D print was made consisting of a base part and a lock with 8M bolts to secure the power meters in place, this is shown in Figure 3.20. Dimensions of mounts designed are provided in Appendix C. Furthermore, Figure 3.21 presents the sensors placed outside the monitoring box: the pyranometer at 0^o, reference cells at their respective angles (shown with their additional protection for off-shore environments with IP67 boxes), the ambient temperature sensor and the module temperature sensors. A complete overview with descriptions of both on-land and off-shore systems, designed for measuring photovoltaic performance, is provided in Figure 3.18.

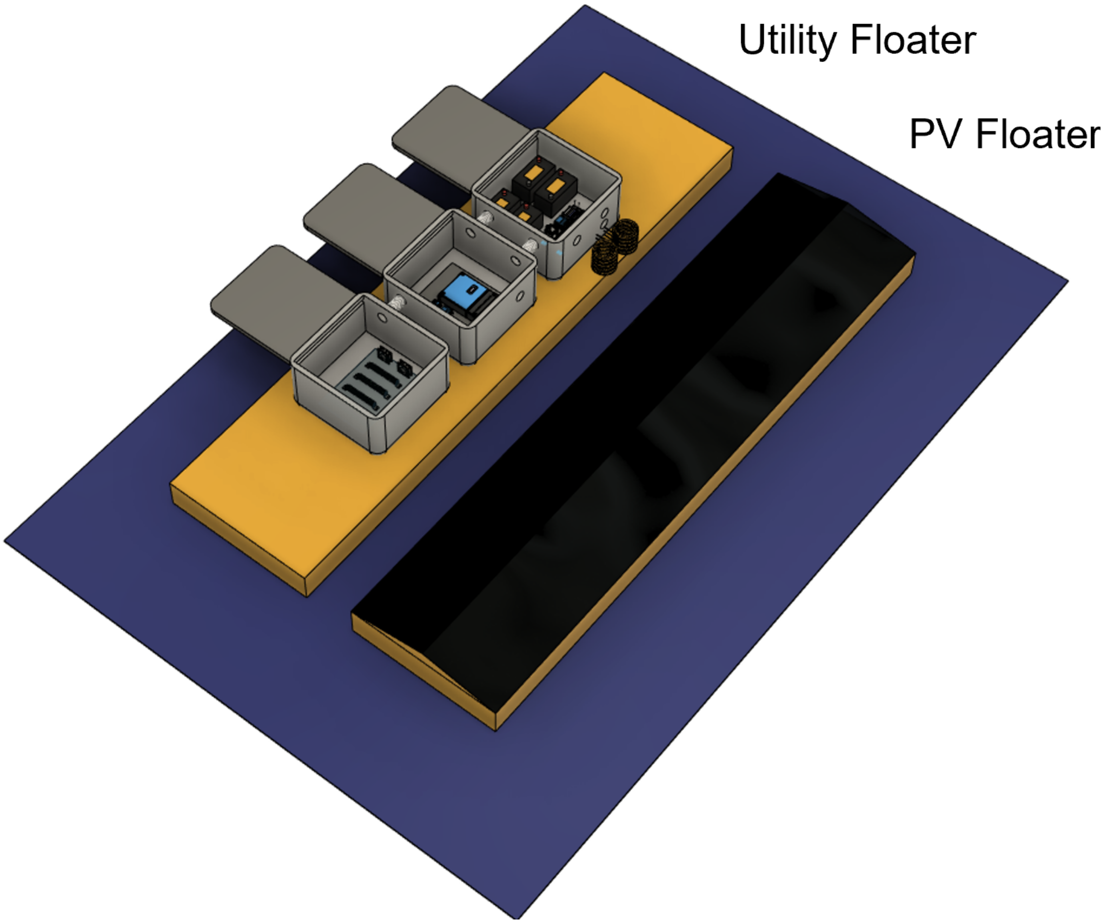

Figure 3.15: Off-shore system general visualization consisting of two floaters: PV floater (black) and utility floaters (yellow).

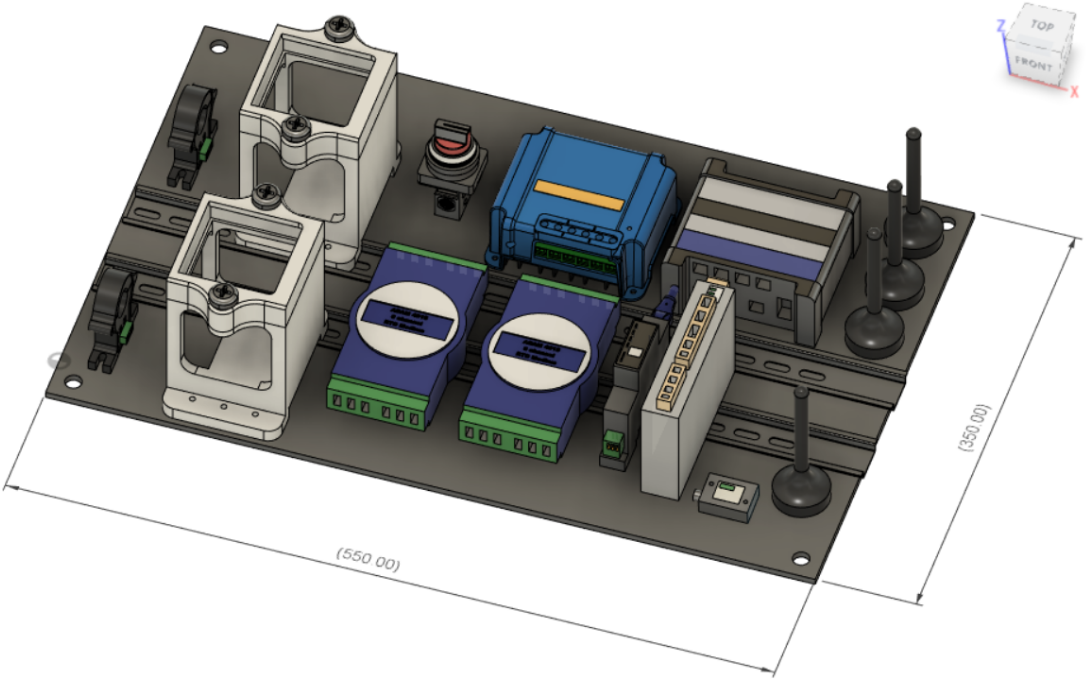

Figure 3.16: Layout of monitoring box off-shore components in Fusion360 (CAD). Dimensions in mm.

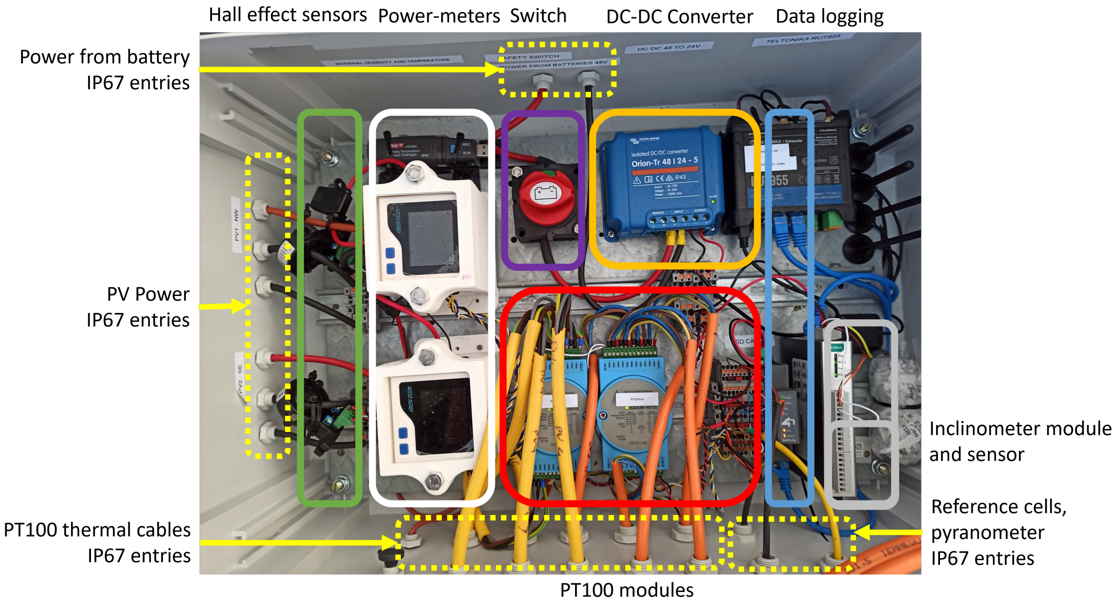

Figure 3.17: Description of off-shore monitoring box components integrated.

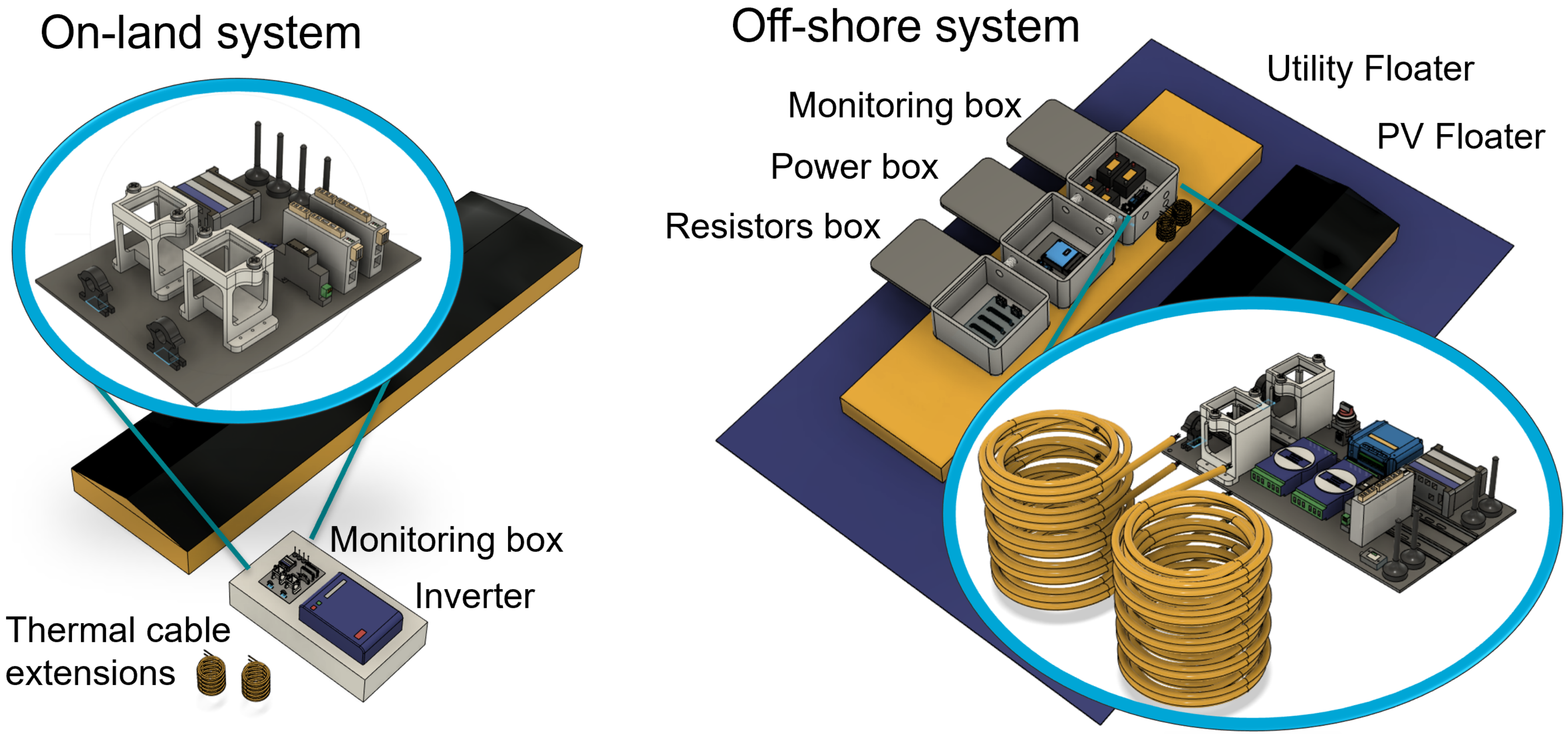

Figure 3.18: Description of both systems overviews with monitoring boxes zoomed in.

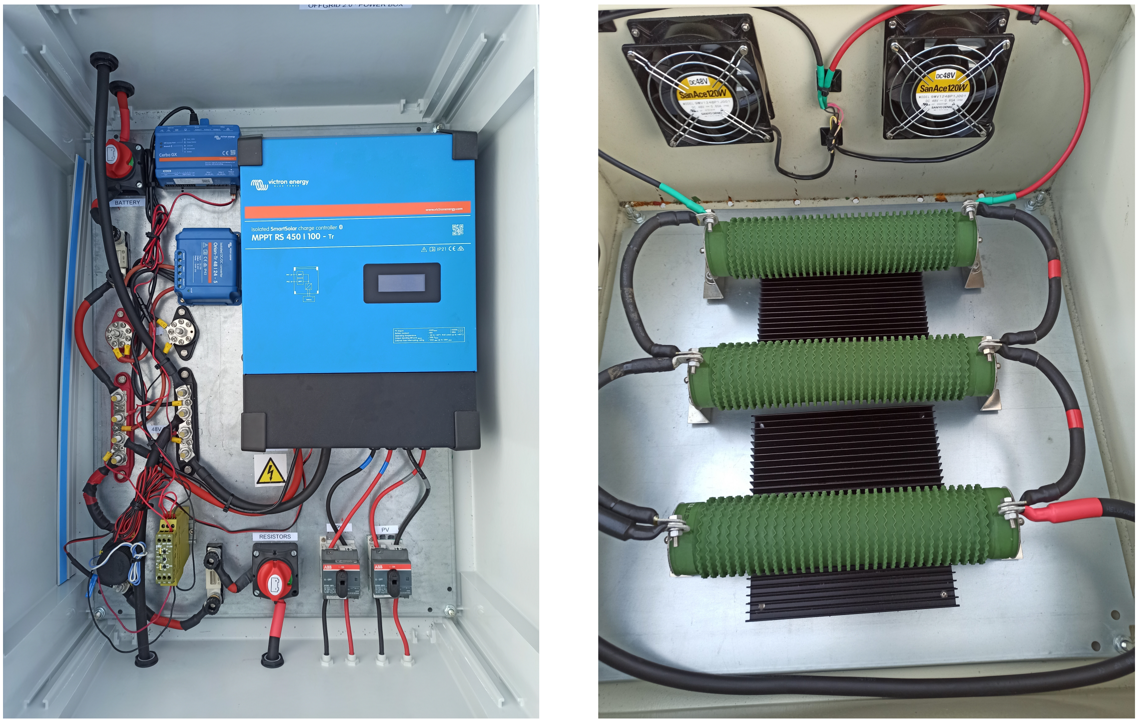

(a) Power box components installed.

(b) Resistors box components installed.

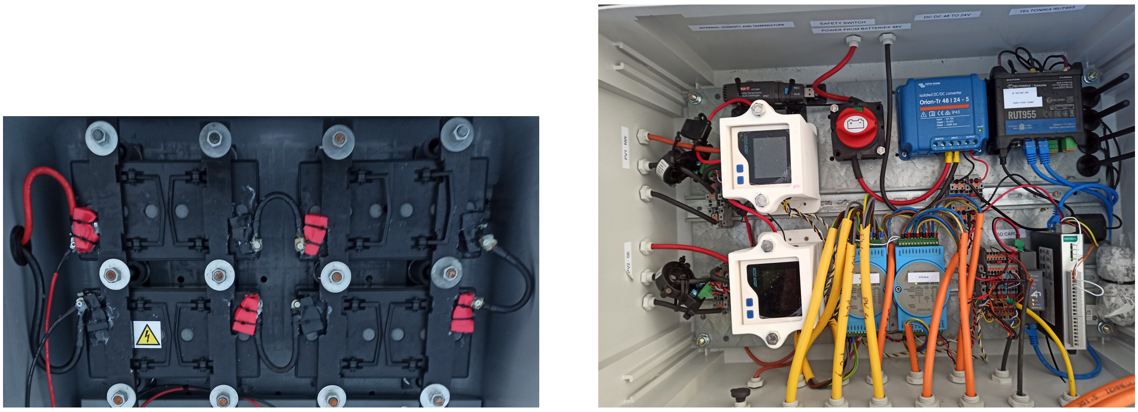

(c) Battery box components installed.

(d) Monitoring box components installed.

Figure 3.19: OFPV off-grid system complete installation.

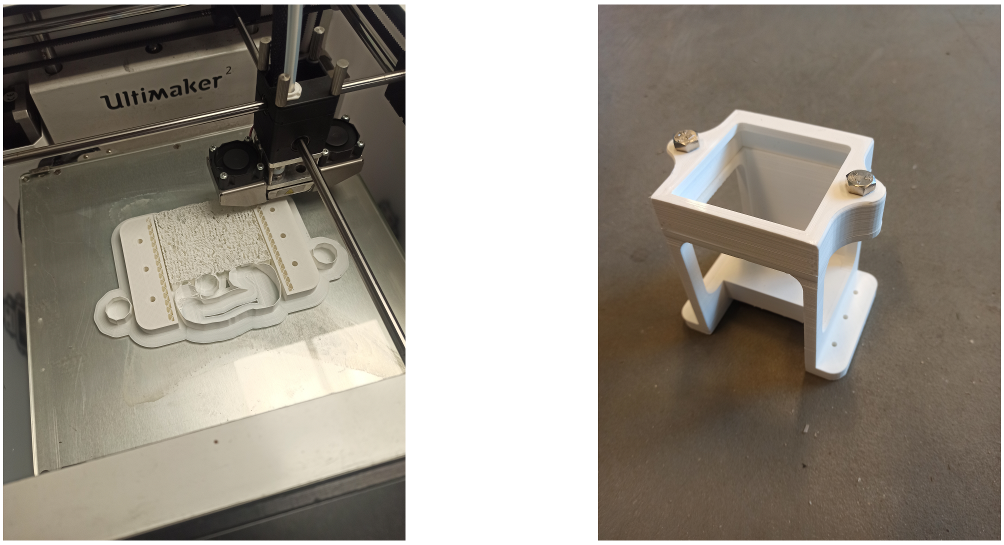

(a) Power meters 3D printing of mounting device.

(b) Power meters 3D printed mounting.

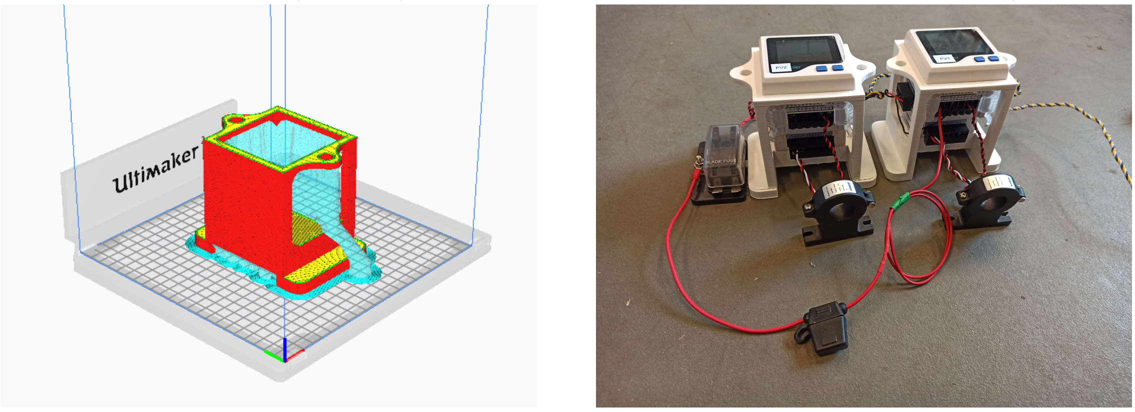

(c) Ultimaker Cura processed design for 3D print.

(d) 3D mounts incorporated with power meters.

Figure 3.20: 3D printing process of power meter mounts design for off-shore conditions.

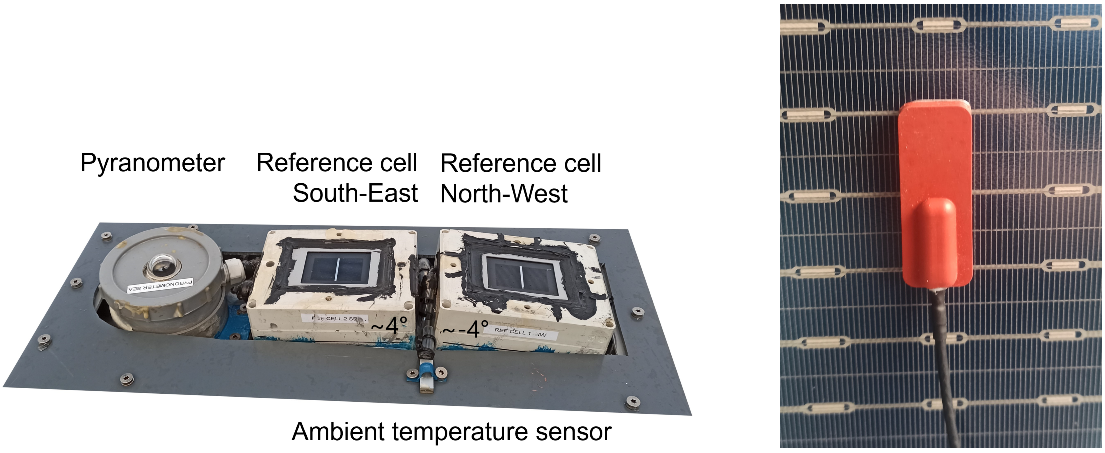

(a) Off-shore irradiance monitoring set up.

(b) PT100 sensor installed on PV modules on-land and off-shore.

Figure 3.21: Monitoring devices (pyranometer, reference cells and thermal sensor) outside data box.

3.4. Dry testing cycles

Dry testing cycles, previously shown in Figure 3.8, were performed to ensure a safe design. Products were first tested individually, to then be tested within the system for a period of 1 month.

An emphasis was made on the battery storage system and battery management systems, which were tested as well as the MPPT charge controller operational mode, to ensure full use of the PV energy, in ”Bulk” mode. Note that Victron Energy MPPT charge controller was configured to have a charging process that could either be in ’bulk’ mode[1], ’absorption’ mode[2] or ’float’ mode[3].

Resistors were also tested, detecting a maximum temperature of 450 ^{o}C during operation, meaning ventilation of resistors off-shore was required. Therefore ventilation, through two 48 V fans with IP68 ratings, was incorporated as well as a heat sink. The fans and heat sink, within the resistors box, installed are shown in Figure 3.19.

Figure 3.22 presents the measurement with an infra-red thermometer reaching 449 ^{o}C.

Figure 3.22: Resistors test showing a temperature of 449 ^{o}C.

Calibration of monitoring devices was also performed. Including thermal sensor extensions increase in temperature: 3 thermal sensors used for module temperature measurements were extended, with cables consisting of poly-urethane 4 wire terminals. These 3 sensors were extended to lengths of 4.3, 8 and 15 meters (A,B,C samples respectively) to see the influence and to determine if thermal sensors could be extended in length from the original length provided by the manufacturers (thermal sensors data sheets are provided in Appendix H).

After 24 hours of measurements, an average offset from the thermal cable extensions of -0.042 $^{o}C/m$ was found and thus it was assumed cables could be extended to utility floater without affecting temperature measurements more than -0.1 $^{o}C/m$.

A month prior to deployment, an additional temperature measurement test was made, on this test, final thermal cable extensions made were tested to check that the sensors still measured the temperatures and these temperature variations were being registered for both the PT100 module temperature sensors and the water temperature sensor off-shore. The measurements of this test are provided in Appendix E.9.

---

[1] When in bulk operation, the controller delivers as much charge current as possible (Victron, 2023).

[2] When in absorption operation, the battery voltage reaches the absorption voltage setting, the controller switches to constant voltage mode. When only shallow discharges occur, the absorption time is kept short in order to prevent overcharging of the battery. After a deep discharge the absorption time is automatically increased to ensure the battery is completely recharged (Victron, 2023).

[3] When in float operation, voltage is applied to the battery to maintain a fully charged state (Victron, 2023).

Module temperature sensor	Length	Off-set [^oC]	Off-set per distance [$^oC/m$]
PT100 reference sensors (x 2)	Product length	-	-
PT100 Sample A extended	4.3 meters	0.3865	-0.048
PT100 Sample B extended	8 meters	0.2885	-0.036
PT100 Sample C extended	15 meters	0.3395	-0.023
PT100 average off-set	-	0.338	**-0.042**

Table 3.6: Resistivity tests outcomes for thermal sensors extensions.

3.5. Experiment

Experimental set ups were deployed in November to their respective locations and the experiment ranged from 15-11-2022 to 1-1-2023.

The time period of research was set once all devices had been tested and calibrated. Additionally, the systems were further tested until the deployment of the off-shore system was possible from OOE logistical perspectives and weather windows availability, which were also subject to OOE competences.

The off-shore system was incorporated on the North Sea, within the North Sea 2 demonstrator of Oceans of Energy. The system on-land consisted of an identical PV system on the DC side up until the inverter. But in this case the floater was placed on solid ground. Both system were placed with the azimuth orientation off-shore provided by OOE at the start of the experiments.

All measurements taken are listed in Appendix E, including external measurements from HKZA station. Also status of measurements and errors found are provided. The detection of errors is further explained in Section 3.5.1.

3.5.1. Protocol during experiment

Once the system was installed by OOE, data collection was performed on a weekly basis, and then was processed through Matlab2021b. Data extraction and post-processing techniques used were presented in Section 3.1.3. Models were updated for post-processing of results and thus were fully defined during experimental period, due to detection of faults. KNMI data was collected once every two weeks until the end of the experimental period.

A detection of records of events was established to detect any faults. If events, such as an excel file not being recorded correctly or a sensor giving signal errors or not working, then these events were recorded to be stated and post-processed when required in the analysis and discussion of results.

Additionally, the off-shore system was constantly monitored through Victron Remote Management (VRM) system, using Victrons's Gerbo GX device. This was done to ensure the correct functioning of components and detect any faults. The focus, looking at live measurements, concerned: PV power at each string, MPPT charge controller charging mode, battery voltage levels and temperature inside the power box. These outputs from Victron's VRM are provided in Appendix F.

4

Design guidelines for an off-shore off-grid PV system

This chapter presents design guidelines required when designing an off-grid PV system (OFPV) for off-shore conditions. This can be considered recommended guidelines and practices for the OFPV design for off-grids and not the structural side of OFPV, as this is outside the scope of this thesis. Protection standards for PV components are provided. These recommendations and guidelines followed should be certified with the respective certification bodies.

4.1. Design guidelines overview

After the research performed with an off-grid system off-shore, a design guideline was developed to provide recommended practices in case of designing such off-grid systems for OFPV in the future. Design guidelines are expanded from Mohanty et al., 2016. OFPV off-grid systems are recommended to include the following design procedures:

- Project procedures:
    - Policy, regulatory and verification considerations.
    - Planning and site assessment.
- Protection protocols:
    - Ingress Protection (IP) ratings.
    - IP for site-specific environmental influences.
- PV module selection for highly humid marine environments.
- Orientation, tilt and mismatch considerations under off-shore conditions.
- Lightning protection.
- Mooring and anchoring selection.
- Off-grid PV design considerations:
    - Solar irradiance availability at location.
    - Load requirements.
    - System sizing and component selection.
- OFPV system under operation:
    - Monitoring, safety and maintenance.

4.2. Project procedures

4.2.1. Policy, regulatory and verification considerations

Based on the technical report ”Floating solar market report” by the World Bank (WorldBankGroup, 2019b), where FPV policies and regulatory considerations are presented, OFPV off-grid systems polices and regulatory necessities are derived and thus it is recommended that these should include:

- Specific cooperation agreements for permits and licenses: Required inter-agency cooperation between energy and water authorities. Environmental impact assessments for the installation should also be provided.
- Water rights and permits: For installation and operation of OFPV plant on the surface of a water body, including anchors and mooring.
- Installation tariff setting: Same as on-land based PV, through feed-in tariffs (FiTs), tenders or auctions depending on project size. This is considered in case off-grid system is within a project which includes connection to the grid.
- Transmission infrastructure: Appointment of responsible bodies, management system in place and specific permits and agreements required. This is considered in case off-grid system is within a project which includes connection to the grid.
- Risk and liabilities.

Furthermore, the low maturity of OFPV technology results in a lack of specific design standards (Claus and López, 2022). However a recommended design practice is available by DNV (Claus and López, 2022). Furthermore design standards may be established and verified by classification societies or government associations (Claus and López, 2022). Therefore a list of organizations is provided in case of needing verfication.

Over 50 organizations focused on marine classification, 12 are part of the International Association of Classification Societies (IACCS), as stated by Claus and López, 2022, these are:

- American Bureau Shipping (ABS)
- Bureau Veritas (BV)
- China Classification Society (CCS)
- Croatian Register of Shipping (CRS)
- Det Norske Veritas (DNV)
- Indian Register of Shipping (IR)
- Korean Register (KR)
- Nippon Kaiji Kyokai (NKK)
- Polski Rejestr Statkow (PRS)
- Registro Italiano Navale (RINA)
- Russian Maritime Register of Shipping (RS)

4.2.2. Planning and site assessment

From the policies and regulatory considerations, a planning to design and deliver an OFPV off-grid system should be derived. Based on the technical report ”Floating solar market report” by the World Bank (WorldBankGroup, 2019b), this planning should include permit and licenses approval times, period for water rights, tender or auctions deadlines and responsible bodies of the project. From here a site assessment can be performed with the policy and regulatory requirement outputs.

Preliminary site assessment to be performed in order to determine the environmental factors present at the location. The site assessment should include solar irradiance, wind speeds, wave heights and any other relevant sea conditions specific to its location. Meteorological data, meteorological softwares and/or weather stations at the location should be used for this purpose.

Furthermore potential environmental impacts should also be considered, influence on eco-systems, wild life and local communities should be considered. This is linked with requirements set in the policy and regulatory considerations previously mentioned.

Additionally, the following site specifications should be checked with respect to site location characteristics (near shore or off-shore) and total surface area available to determine off-grid system maximum size.

4.3. Protection protocols

4.3.1. Ingress protection (IP) levels

Ingress protection (IP) levels are of great importance when designing an off-grid OFPV system, as protection of components within the PV system are required against environmental conditions concerning wave, water and wind influences.

Ingress protection levels may be selected based on IEC 60529 Ingress Protection (IP) Code. This code classifies the level of protection with respect to solid objects (including body parts), accidental contacts, dust and water. The IP code is composed of 2 numerical digits (A and B) from and is written as ”IPAB”. The first digit, A (value from 1 to 6) concerns protection against solids, while the second digit B (values from 1 to 8) concerns protection against liquids. A third and fourth letter may follow this code, but is not always provided by manufacturers.

From IEC 60529 (IEC, n.d.), a complete list of protection levels is provided in Table 4.1, concerning protection against solids and 4.2, concerning protection against liquids.

Level	Solid protection	Effectiveness
0	Not protected	-
1	>50mm	Any large surface of the body, but no protection against deliberate contact with a body part.
2	>12.5mm	Fingers or similar objects.
3	>2.5mm	Tools, thick wires, etc.
4	>1mm	Most wires, screws, etc.
5	Dust protected	Ingress of dust is not entirely prevented, but it must not enter in sufficient quantity to interfere with the satisfactory operation of the equipment; complete protection against contact.
6	Dust tight	No ingress of dust; complete protection against contact.

Table 4.1: Ingress Protection level of first digit (solids) (IEC, n.d.).

Level	Liquid protection	Effectiveness
0	Not protected	-
1	Dripping water	Vertically
2	Dripping water when tilted up to 15^o	No harmful effect when the enclosure is tilted at an angle up to 15° from its normal position.
3	Spraying water	At any angle up to 60° from the vertical shall have no harmful effect.
4	Splashing water	Against the enclosure from any direction shall have no harmful effect.
5	Water jets	Jets (6.5mm nozzle) against the enclosure from any direction shall have no harmful effects.
6	Powerful water jets	powerful jets (12.5mm nozzle) against the enclosure from any direction shall have no harmful effects.
7	Immersion up to 1m	Possible when the enclosure is immersed in water under defined conditions of pressure and time.
8	Immersion above 1m	Suitable for continuous immersion in water under conditions which shall be specified by the manufacturer.

Table 4.2: Ingress Protection level of second digit (liquids) (IEC, n.d.).

4.3.2. IP against site-specific environmental influences

To see what IP level is required, environmental influences at the OFPV off-grid system should be assessed:

- Wind influences should be considered in order to assess the influences of particles entering the system components.
- Water and wave influences should be considered to asses the influences on the internal protection levels required for the system with regards to liquids.

The protection against environmental influences can be divided for off-grid PV systems near-shore and off-shore, the later taking into account larger wave and water influences to a greater extent. Basing protection on the rich experience of the marine industry and off-shore industries is recommended (WorldBankGroup, 2019b)

It is important to note off-shore and near-shore FPV present additional challenges when compared to FPV (WorldBankGroup, 2019b):

- Water splashing conditions increase due to higher wind and waves.
- Mooring and anchoring becomes critical due to tidal movements and currents.
- Seawater salinity is tougher on components
- Bio-fouling is more likely.

The following recommendation of minimal IP level to use for FPV in-land, near-shore and off-shore is provided in Table 4.3. This may serve as a baseline but may vary depending on specific location environmental conditions.

IP	Considered for conditions with	Location
IP54	in-land winds and water splashing	FPV in-land
IP55	in-land winds and water jets	FPV in-land
IP56	in-land winds and water powerful jets	FPV in-land
IP57	in-land winds and water immersion up to $1m$	OFPV Near-shore
IP58	in-land winds and constant water immersion	OFPV Near-shore
IP64	in-land winds and water splashing	OFPV Near-shore
IP65	off-shore winds and water jets	OFPV Near-shore
IP66	off-shore winds and water powerful jets	OFPV Near-shore
IP67	off-shore winds and water inmersion up to 1 m	OFPV Off-shore
IP68	off-shore winds and constant water inmersion	OFPV Off-shore

Table 4.3: Minimum ingress Protection level recommended depending on system location: FPV in-land, OFPV near-shore and OFPV off-shore.

Thus, IP67and IP68 labels are recommended to be selected when having an OFPV off-grid system under off-shore conditions of wave and winds. When considering FPV in-land or OFPV near-shore, one can consider lower IP ratings than off-shore, but must assess the risks involved. If cost is not a limiting issue, the highest IP possible should be applied.

Usually, the higher the IP, the higher the cost, thus a cost-risk assessment should be considered. Additionally components that do not meet these standards must be protected with IP protection boxes with IP67 and/or IP68.

Connection between boxes, with cables must be done through glancing with IP67 and/or IP68.

Additionally, a third letter may be provided (IEC, n.d.) indicating protection against: F (oil resistant), H (high voltage apparatus), M (motion during water test), S (stationary during water test) and W (weather conditions). Letter W can be of interests as systems off-shore will not be stationary due to the environmental influences of wind and waves.

Furthermore, connection between PV cables under off-shore conditions must also meet IP67 and/or IP68 standards: MC4 connectors must have this protection levels as well.

4.4. PV module selection for highly humid sea environments

PV module selection should be assessed within the OFPV off-grid design with a special emphasis on the highly humid and salty marine environment and the expected frequent movements and forces of the system caused by the marine conditions at the location. Figure 4.1 presents the environmental stresses impact on the module degradation, from which the higher impact by WorldBankGroup, 2019a was identified to be due to moisture, mechanical stresses and hot-spot/shading.

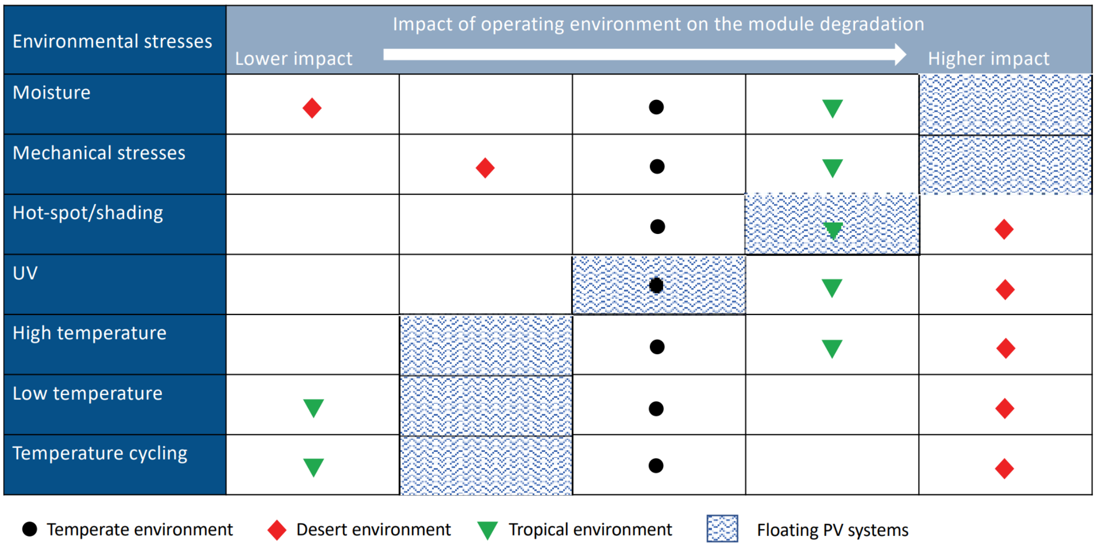

Environmental stresses	Impact of operating environment on the module degradation Lower impact	→			Higher impact
Moisture	◆		●	▼	▨
Mechanical stresses		◆	●	▼	▨
Hot-spot/shading			●	▨ ▼	◆
UV			▨ ●	▼	◆
High temperature		▨	●	▼	◆
Low temperature	▼	▨	●		◆
Temperature cycling	▼	▨	●		◆

● Temperate environment ◆ Desert environment ▼ Tropical environment ▨ Floating PV systems

Figure 4.1: Impact of environmental stresses on module degradation in various operating environments, including FPV (blue stripes) (WorldBankGroup, 2019a).

Firstly, moisture ingress should be considered as it is an important stress factor on the PV module. Considering the off-shore environment, moisture ingress can then deteriorate adhesive bonds at the interfaces between module components, resulting in delamination and ultimately lead to corrosion of metalization elements (Aghaei et al., 2022). Additionally water ingress in large quantities can induce mechanical stresses due to the hydro-dynamic volume expansion and contraction (Aghaei et al., 2022).

The selection of the PV module should withstand off-shore conditions and thus IP should be assessed. Off-shore systems should be aimed to have low maintenance as their location may be hard to reach when compared to on-land system. Therefore, protection of modules against ingress of particles or water should be applied to the highest extent possible. Following IP ratings provided by IEC, 2023b, for the OFPV system, it is recommended that the PV module should have at least an IP67 rating to ensure dust tightness and protection against temporary immersion in water. If the system is expected to be at harsh marine conditions and/or expecting the system to be continuously immersed, then IP68 and IP69 ratings for the protection of the system are recommended.

From here, delamination should be taken into account in the selection process: it can occur at the backsheet/encapsulant interface as well as between the layers of the backsheet with weather induced degradation (Aghaei et al., 2022). For rigid floats (excluding membrane floats) usually framed glass-glass PV modules can be placed as they are more resilient to humidity when compared to glass-back sheet modules (Ziar, 2021). In the case of using a membrane float, flexible PV modules based on thin film technology are recommended and effects of moisture ingress should be further analyzed.

Secondly, soiling effects off-shore caused by the persistence of layers of salt on the modules once the water spray has evaporated (Mannino et al., 2023) should additionally be considered. Furthermore, soiling from bird droppings has been accentuated in PV systems located in coastal and off-shore areas (Mannino et al., 2023) and thus cleaning of the panels should be considered. Cleaning techniques should be considered to mitigate this effect on the PV modules installed off-shore: techniques described by Zahedi et al., 2021 for FPV can be considered for further development for OFPV systems: these techniques concern water and non water based approaches. Water based cleaning approaches to consider can be applied through the use of rainfall, wave splashing, manual cleaning, self cleaning or robotic device cleaning (Zahedi et al., 2021). Non water based approaches may consider airflow and coating techniques (Zahedi et al., 2021). Moreover, PV module surfaces may experience additional bio-fouling if exposed in a water splash zone (Hooper et al., 2021) and can affect light transmittance though the appearance of thin films of organisms that are strong absorbers of light (Harris et al., 2013). The complexity of the bio-fouling issue requires site-specific testing to provide an accurate risk assessment (Hooper et al., 2021)

The application of robot cleaning systems through the use of optical soiling sensors which could detect the soiling levels within the OFPV system, such as using the optical sensor 'Dust IQ' previously presented in Section 2. Mannino et al., 2023 recommended OFPV systems to have a greater cleaning frequency and the possible use of bird deterrents, such as sound systems, however this may increase the environmental impact of the system.

The implications presented, concerning humidity, delamination and soiling implications should be assessed, since the high humidity causing delamination and the high salt content corroding the metal compounds within the PV module components may lead to a potential major fire (Mannino et al., 2023). Therefore resistance certifications when selecting a PV module should be considered. For OFPV systems, the Salt Spray Test (IEC 61701:2020 [1] IEC, 2023a) is recommended.

Finally, the selection of PV modules is recommended to consider the presence of frequent movements caused by the marine environment, subject to site specifics. Selection of the floating structure and PV modules must be considered depending on the installation site (Mannino et al., 2023):

- Protected sea waters sites: conventional FPV systems may be used for protected sea waters, since the site is subject to less wave motion.
- High wave motion sites: OFPV systems may be used in sites with wave motions, and site specific influences should be assessed.

From a mechanical perspective, the waves could affect the degradation of PV modules. Rigid PV modules when exposed to wind and water loads can suffer from cell crack formation, due to limited flexibility and mechanical properties (Aghaei et al., 2022). Therefore the robustness and module safeguard should be tested (Cazzaniga et al., 2018). Tilted PV module arrays will require rigid pontoons (Golroodbari and Sark, 2020). If thin film technology is used, a membrane structure may be installed due to the low weight of the thin film modules (Golroodbari and Sark, 2020).

---

[1] IEC 61701:2020 describes test sequences useful to determine the resistance of different PV modules to corrosion from salt mist containing Cl (NaCl, MgCl2, etc.).

4.5. Orientation, tilt and mismatch considerations

Orientation (azimuth) and tilt of OFPV systems should consider the influences of the marine environment, which is site specific, with a focus on wind and wave influences.

With respect to the system orientation, optimal orientations for OFPV off-grid systems should be aimed at. Ideally PV modules should track the sun, however current tracking systems are not suited for off-shore conditions and is questionable if they can be made cost effective for these conditions (Soppe et al., 2022). Static systems achieve maximum annual production when oriented South (Northern hemisphere) and have a specific tilt angle which is latitude dependent. For an even distribution an East-West distribution may be chosen. Orientation can be optimized by the use of simulation tools similar to the analysis for ground mounted PV plants (WorldBankGroup, 2019a). For an off-grid off-shore system being designed, additional electrical components might be present in the vicinity. The placement of Balance of System (BoS) components should be taken into account to avoid shading on the PV array. Ideally BoS components, such as MPPT charge controller or battery systems, should be placed in the North side of the OFPV system to avoid shading.

With respect to tilt angles, it may be limited by the float design and wind load (WorldBankGroup, 2019a). Higher tilt angles may cause the PV module to be more vulnerable to wind. For standard FPV systems, it is common to use tilt angles no greater than 15 ^{o}, with some commercially available floats allowing angles to be adjusted between 5 ^{o} and 20 ^{o} (WorldBankGroup, 2019a). Tilts at 15^o angles allow for the so-called self-cleaning effect, where rainfall is frequent enough to clean substantial accumulations of dirt and dust on the PV module surfaces (WorldBankGroup, 2019a).

When moving to OFPV systems, many off-shore PV concepts have a 0 ^{o} tilt angle, leading to a much lower production at noon, but a larger production in the early and late hours of the day partly compensates for this. Bi-facial solar modules are an attractive option in the land has a high albedo. However off-shore the albedo of sewater is much lower, on which in ideal conditions it can increase the efficiency between 3 and 12 %: unless special provisions are made to increase the albedo off-shore, bifacial PV modules off-shore may not be cost effective (WorldBankGroup, 2019a).

OFPV systems will have a response to incoming waves and this response is highly dependent on the floating structure design and the response in turn will have an effect on the insolation of the OFPV system installed in the floating structure (Bugeja et al., 2021). It is recommended to assess the wave effect, which is site specific, and optimize the energy yield of the OFPV system. Bugeja et al., 2021 presented a simulation tool, verified with experimental results, that can be used for this purpose. In this tool wind loads are also taken into consideration, highlighting having lower angles, at around 5 degrees, will reduce these wind load effects. Any change in yaw, pitch and roll movements are translated into the fixed azimuth and tilt angles chosen for the OFPV system.

Additionally Golroodbari and Sark, 2020 presented a model to calculate the tilt angle variation based on wave characteristics and how these were influenced by wind speed leading to a wave spectrum analysis. In their study, a comparison between an on-land an off-shore system in the North Sea showed that the energy yield of both systems differed predominantly as a result of lower temperatures.

Research from Bi and Law, 2023 presented simulation results showing the transient change in tilt angle of the PV panel increases near the ends of the platform as the wave height and period increase while the change is much smaller near the middle. It is recommended to study these effects, for the specific site and design, to consider locating the PV array located further from the mooring lines if possible. Bi and Law, 2023 presented a simulation showing power output of floating solar farms remains stable under strong winds and waves. Nevertheless this should be assessed individually for each site and design.

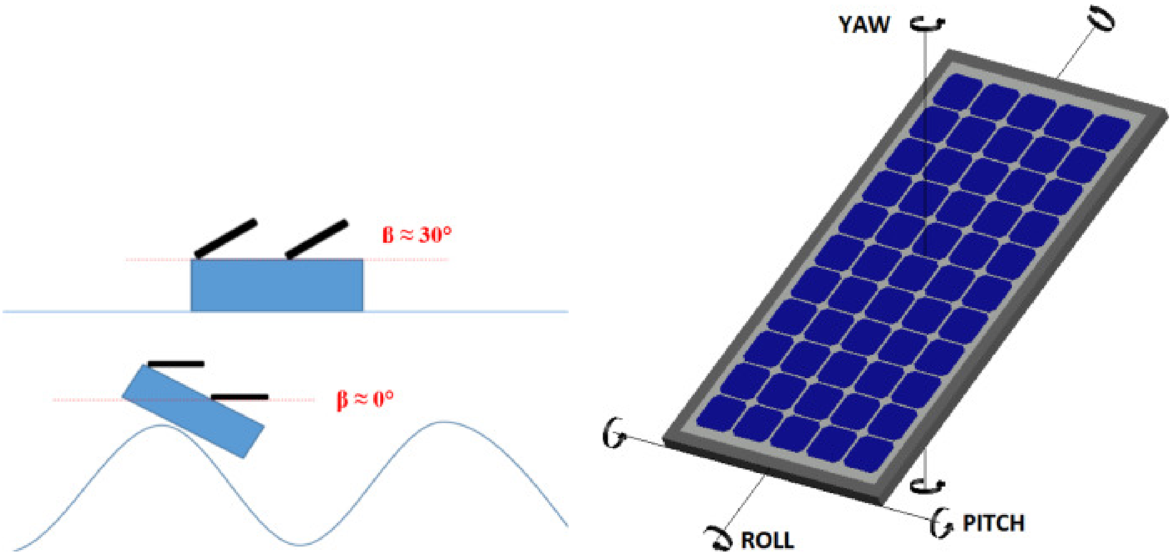

(a) Floating platform at steady state (top) and floating platform responding to incoming wave (bottom).

(b) Yaw, pitch and roll movements with respect to PV system under study.

Figure 4.2: OFPV movement considerations for the effect of wave response motion on the insolation of OFPV (Bugeja et al., 2021).

Additional considerations with respect to tilt and orientation should be adressed within the design. A higher panel slope can increase energy harvesting (depending on the latitude and weather conditions) but reduces the number of panels that can be placed in a floating platform or raft, in this case in the OFPV system, increasing the OFPV cost per kW_p (Cazzaniga et al., 2018). Biofouling should be considered in OFPV installations where low wave smashing (water cleaning) is expected, in this case, depending on the exposure of wave to the system, the design should consider increasing the tilt in case no wave washing is expected in the system. Modules with higher tilt are less likely to get fouled by birds, as it is more difficult for birds to stand for a long time on them (Ziar et al., 2020). If bio-fouling is not avoided it may lead to hot-spots and damage of the PV modules (Ziar et al., 2020).

Following the expected tilt under off-shore conditions, optimization of the PV array layout should be performed to mitigate the mismatch losses caused off-shore due to the uneven distribution of incident irradiation on the PV module connected in the same string (Ravichandran et al., 2022). This additional shading and soiling within a PV module may affect the electrical performance, resulting in a degradation of the efficiency of the system (Ravichandran et al., 2022). Two significant factors that should be considered in selecting the FPV array configuration are having the most optimal operation and having less complexity in electrical connections (Ranjbaran et al., 2019). Ranjbaran et al., 2019 provided a summary of studies about FPV array structures and interconnection topologies that can be considered for off-shore conditions in order to reduce power losses and mismatch effects due to the effect of partial shading conditions. Interconnection methods can be set to static and dynamic configurations. For the off-shore system it is recommended to reduce the complexity of electrical connections to reduce the amount of failures and thus static configurations are advised: these concern interconnections such as series-parallel (SP), total-cross tied (TCT), bridge-link (BL), and honey-comb (HC).

An additional recommendation is to place as many modules of the same string and floater with the same orientation. If modules are set on individual floaters then mismatch effects may be increased.

Additionally the effect of waves and movements should be addressed, if the PV modules are mounted in a flexible system or in a float shorter in length than the waves, the wave movement may cause the modules to have different orientations. This will cause the Maximum Power Point (MPP) of the modules within a string to vary, leading to mismatch losses and a reduced power production of the system.

4.6. Lightning protection recommendations

Lighting protection measures are recommended to avoid damage of the OFPV system caused by a lightining strike. These systems have a lightning threat due to their location at sea, in an open area, where the sharp upper edges of modules mounted at an angle may be places of concentration of the electric field, which may increase the probability of hitting one of them (Sobolewski and Sobieska, 2022).

Lightning protection measures may be required by insurance companies. As an example, the German Insurance Association (GDV) requires that lightning protection measures (Lightining Protection Systems (LPS) of level III [2]) must be taken for PV systems above 10 kW (DEHN, 2014).

According to this class of LPS, the rolling sphere method (Figure 9.19.1) as per IEC 62305-3 (EN 62305-3) can be used to determine the number of air-termination rods (WorldBankGroup, 2019a). The air termination rods will form the protected volume above the PV system. A visualization is provided in Figure 4.3.

Additionally, the risk of a lighting strike must be determined by IEC 62305-2 (EN 62305-2) standard to be considered during the design for which specialized software are available, such as the DEHN support software (DEHN, 2014).

For the OFPV design, based on DEHN, 2014, it is advisable to install electrical components, such as generator junction boxes mounted on module racks and decentralised inverters as far as possible from the air-termination systems.

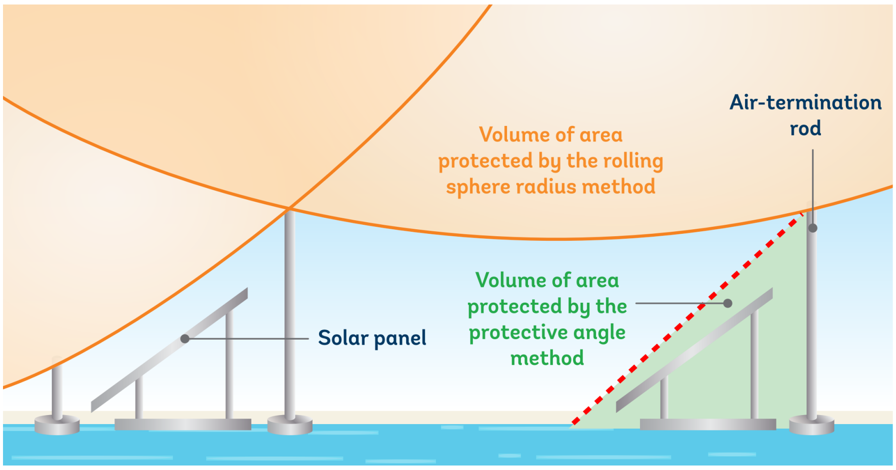

Figure 4.3: Rolling sphere radius and protective angle methods for solar lightning protection methods (WorldBankGroup, 2019a).

---

[2] BS EN/IEC 62305-1 defines four Lightning Protection Levels (LPL) based on probable minimum and maximum lightning currents. The LPS equate directly to Lightning Protection System Classes (LPS)

4.7. Mooring and anchoring types for selection

Mooring systems are required to limit the OFPV free movement and to prevent damages to itself or to other floating bodies (Claus and López, 2022). For off-shore conditions, the structure should be allowed to move vertically with variations in water level, as this requirement can be of several tens of meters vertical variation depending on the location (Whittaker et al., 2020). The choice of the mooring system will depend on the geometry of the OFPV system and on the direction and intensity of external actions and forces: the larger these factors, the higher the number of mooring lines that will be required or else a change in material and diameter of mooring lines will be required (Oliveira-Pinto and Stokkermans, 2020). For off-shore structures, mooring line materials should be composed of steel chains, metal wire ropes and/or synthetic wire ropes and the following should be considered (Vo et al., 2021):

- Steel chains: Chains selected for the marine environment are recommended to be stud-link chains as they are stronger than stud-less chains and can provide stability and better handling of the chain.
- Wire ropes: Wire ropes manufactured with multiple metal wires should be coated to reduce corrosion in the marine environment.
- Synthetic wire ropes: These type may be used in deep waters as the reduce a large amount of vertical loads as well as the complexity of installation.

Mooring system set ups are classified into catenary, compliant and rigid pile moorings (Vo et al., 2021) and are shown in Figure 4.4. When designing the off-grid OFPV system the following should be considered:

- If mooring lines are desired to be kept in tension, then a tout mooring system, which used excess buoyancy for tension may be used.
- If the off-grid OFPV system is on shallow marine waters, a selection a rigid pile system mooring may be viable.
- If a specific spring rate to the moored float is required, catenary moorings may be used, which use the self weight of the chains for the spring rate.
- Compliant moorings are catenary moorings that use floats and weights, and may be used to adjust the layout of the mooring lines.

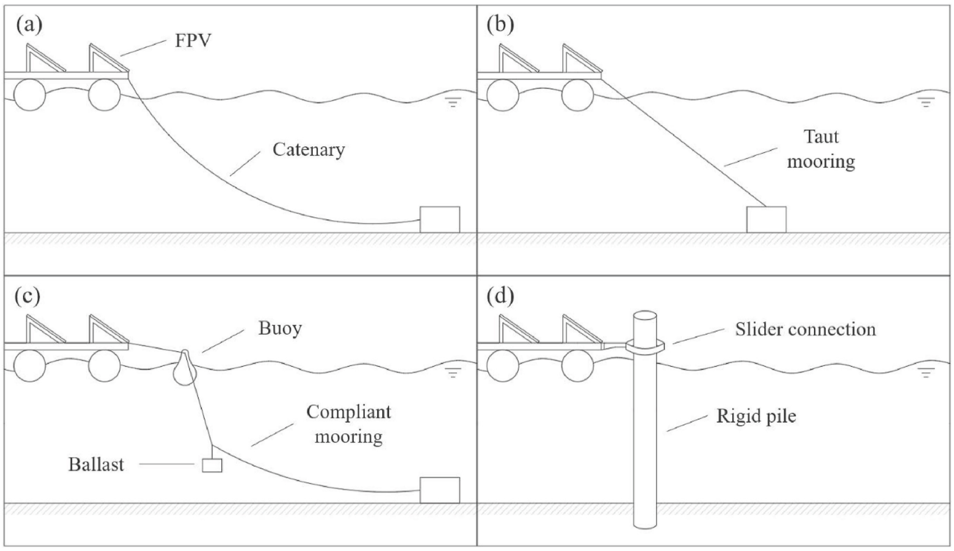

Figure 4.4: Mooring systems (a) catenary, (b) taut mooring, (c) compliant mooring, and (d) rigid mooring (Claus and López, 2022).

Additionally mooring geometry should be considered. For instance, an OFPV off-grid system for a fish farm is set to be a permanent mooring it should withstand all year round weather conditions, while maintaining its station, and orientation (Turner, 2000). For this purpose fixed location and orientation moorings should be considered. Based on the study by Turner, 2000 three common mooring geometries are identified: twin, radial and orthogonal moorings. If a twin mooring is selected, the system will have connections at two ends of the system and will in turn generate huge loads when the environmental forces acting across the principal axis of the system. Therefore radial or orthogonal moorings should be selected, with the advantage that a hinged or flexible floating structure, the extra moorings will provide additional lateral support and reduce internal loads either on the hinges or in the mooring ends. Additionally tension of the mooring lines of opposed moorings can be tensioned one against the other by a relatively small winch. The mooring geometries are presented in Figure 4.5.

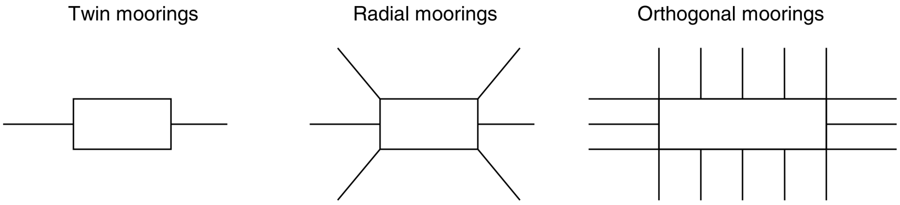

Figure 4.5: Cage mooring types (Turner, 2000).

Anchoring systems for the OFPV system may be set by dead weights, drag anchors, embedded anchors or suction foundations and analysis of the seabed should be performed to determine if scour protection is required (Claus and López, 2022). Anchoring systems mentioned are provided in Figure 4.6. The following considerations, based from Vo et al., 2021, should be considered:

- If a dead weight is selected, the common designs to use are sinker, squat clump, mushroom and wedge.
- If a drag anchor is selected, fluke are and soil penetration into the soil must be considered to determine the holding capacity.
- If an embedded anchor may be selected, the shape will be deeply installed in the soil and is subject to different designs.
- If a pile anchor is selected, it may penetrate the soil using a different procedure.

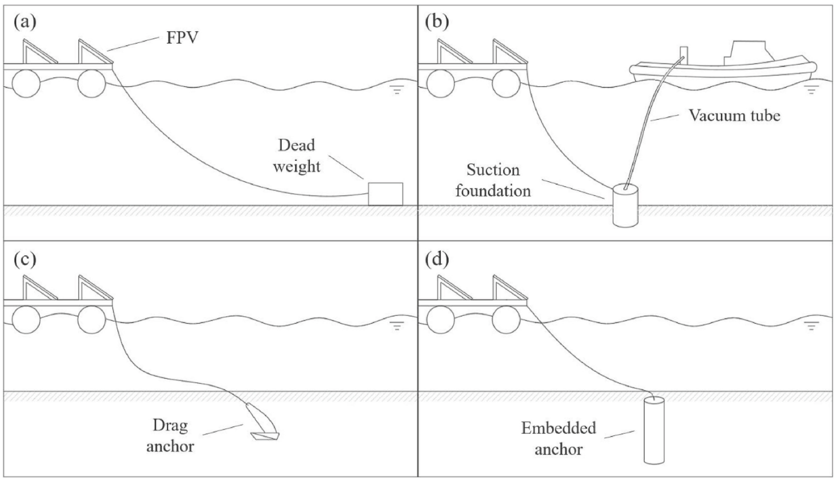

Figure 4.6: Anchoring systems for the marine environment layouts for FPV systems (a) dead weight, (b) suction foundation, (c) drag anchor, (d) embedded anchor (Claus and López, 2022).

International Electrotechnical Commission (IEC) standards for the design requirements of anchoring and mooring systems are yet to take shape (WorldBankGroup, 2019a). The world's first recommended practice on the design, development and operation of FPV systems DNV-RP-0584 can also serve as the base for the anchoring and mooring. However, design standards from other industries, such as off-shore, can serve as an additional reference tool, such as DNVGL-OS-E301 Position mooring (WorldBankGroup, 2019a). Forces exerted by the marine environment on the system, such as wind, cause load calculations to be mandatory: an example guide for the evaluation of wind influences can be the European code EN 1991-1-4 (wind actions on structures) (WorldBankGroup, 2019a).

4.8. Off-grid PV system design considerations

The aforementioned design procedures, focusing on the IP protection required for the off-shore system being designed, as well as the selection of PV modules for highly humid marine environments, orientation, tilt and mismatch effect should be combined with procedures to design the off-grid electrical system. Smets et al., 2016 and Mohanty et al., 2016 design procedures for standard stand alone systems are combined and presented in this section.

Solar irradiance is assessed at the location selected for a project, from which the sizing and components of the PV systems are derived, with a special focus on the battery bank.

Once the complete system is designed, the IP protocol should be applied within the system components and system parts (battery bank, MPPT charge controller and/or inverter, loads and cable connections), with correct IP for components, components protection and glancing. Testing with IP additions on the design are recommended to be performed before deployment of the system at the site location.

4.8.1. Solar irradiance availability at location

Solar irradiance is used in order to determine an optimal PV configuration at the specific location. Solar irradiance expected at location should be assessed from software weather data, however being off-shore means validation with on-site data is recommended:

- Site-specific weather data from direct measurements.
- Meteorological weather data from software (if off-shore site-specific measurements are not available).

Nevertheless, Figure 4.7 presents an example using 'Meteonorm 7.2' on how the irradiance at the POA on an off-shore location may be implemented to obtain daily global irradiance $[kWh/m^2]$ and annual global irradiance $[kWh/m^2]$ values, among other parameters, that can be later used for system sizing and selection of components. Other meteorological softwares or complex simulation softwares destined for OFPV may be used for this purpose as well.

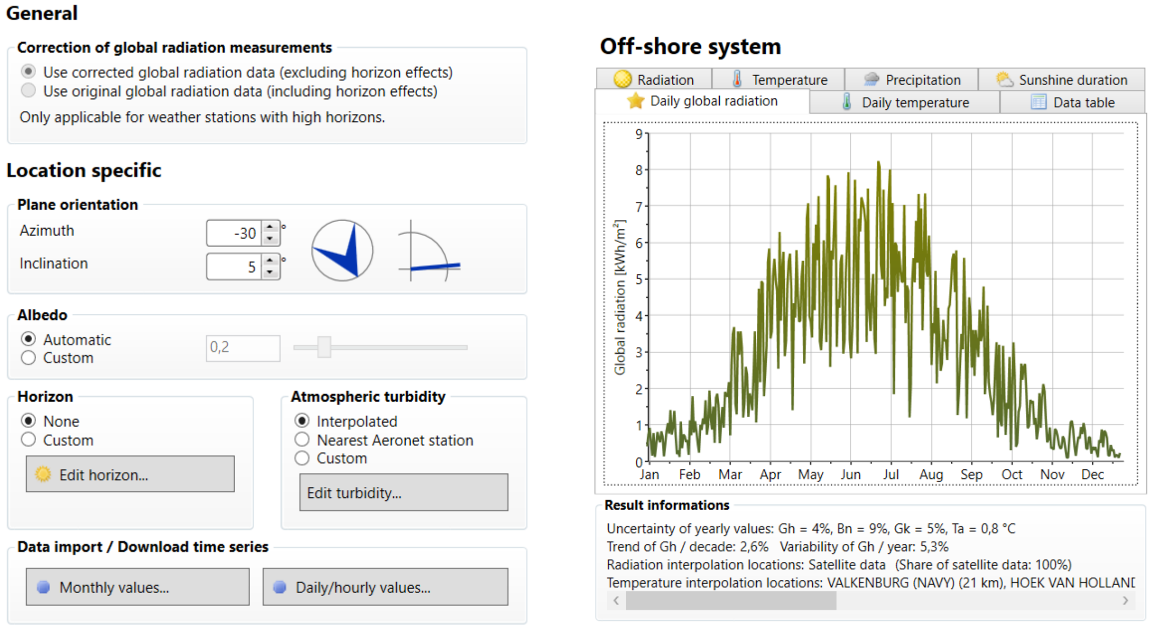

Correction of global radiation measurements
● Use corrected global radiation data (excluding horizon effects)
○ Use original global radiation data (including horizon effects)
Only applicable for weather stations with high horizons.

Plane orientation
Azimuth -30°
Inclination 5°

Albedo
● Automatic
○ Custom
0,2

Horizon
● None
○ Custom

Atmospheric turbidity
● Interpolated
○ Nearest Aeronet station
○ Custom

Data import / Download time series

Result informations
Uncertainty of yearly values: Gh = 4%, Bn = 9%, Gk = 5%, Ta = 0,8 °C
Trend of Gh / decade: 2,6%   Variability of Gh / year: 5,3%
Radiation interpolation locations: Satellite data (Share of satellite data: 100%)
Temperature interpolation locations: VALKENBURG (NAVY) (21 km), HOEK VAN HOLLAN

(a) Example of location specifications, with inclination and azimuth using 'Meteonorm 7.2'.

(b) Example of daily global irradiance [kWh/m^2] with location specifications using 'Meteonorm 7.2'.

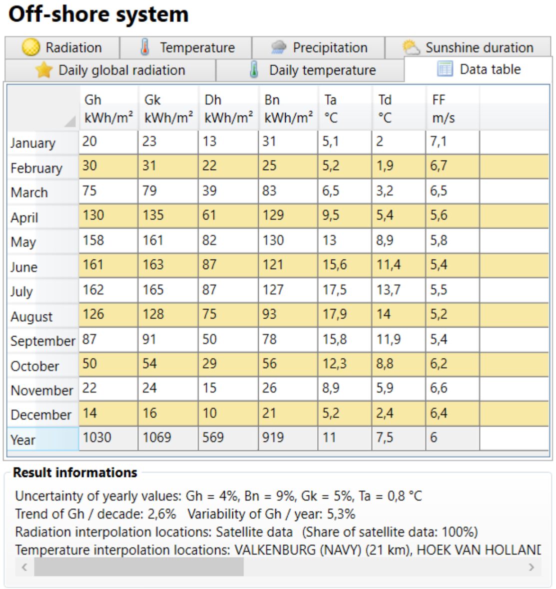

	Gh kWh/m²	Gk kWh/m²	Dh kWh/m²	Bn kWh/m²	Ta °C	Td °C	FF m/s
January	20	23	13	31	5,1	2	7,1
February	30	31	22	25	5,2	1,9	6,7
March	75	79	39	83	6,5	3,2	6,5
April	130	135	61	129	9,5	5,4	5,6
May	158	161	82	130	13	8,9	5,8
June	161	163	87	121	15,6	11,4	5,4
July	162	165	87	127	17,5	13,7	5,5
August	126	128	75	93	17,9	14	5,2
September	87	91	50	78	15,8	11,9	5,4
October	50	54	29	56	12,3	8,8	6,2
November	22	24	15	26	8,9	5,9	6,6
December	14	16	10	21	5,2	2,4	6,4
Year	1030	1069	569	919	11	7,5	6

Result informations
Uncertainty of yearly values: Gh = 4%, Bn = 9%, Gk = 5%, Ta = 0,8 °C
Trend of Gh / decade: 2,6%   Variability of Gh / year: 5,3%
Radiation interpolation locations: Satellite data (Share of satellite data: 100%)
Temperature interpolation locations: VALKENBURG (NAVY) (21 km), HOEK VAN HOLLAN

(c) Example of annual values obtained, including global irradiance [kWh/m^2], provided in a table using 'Meteonorm 7.2'.

Figure 4.7: Example of meteorological climate data from 'Meteonorm 7.2' initial assessment.

4.8.2. Load assessment

Depending on the off-grid project, different energy requirements may be set. Off-shore conditions and remote locations highlight the importance of days of autonomy until an operator can arrive at the off-grid location for inspection. First, load profiling and load categorization is recommended, based on Mohanty et al., 2016, the following is recommended:

For load profiling, the following details should be determined:

- Maximum load: Maximum energy consumption the off-grid system should deliver to the loads at a certain point in time.
- Average daytime energy requirement: Energy consumption of devices required during daytime.
- Average daytime energy requirement: Energy consumption of devices required during night time. These devices can vary from powering up monitoring devices, lights, electric generators, electrical motors to sound alarms among others.

For load categorization, the following details should be determined:

- Load priority: Peak loads, off-peak loads and intermediate loads.
- Load necessity: Essential or non-essential loads.
- Load type: Direct current (DC) loads, alternate current (AC) loads or mixed (AC and DC loads).

The load profiling can be used for system sizing. When encountering the system components requirements and availability, one may be subjected to change, reduce or switch loads in use: In this case a load priority and necessity list will determine the usage of certain loads. Furthermore, the load type will be used when determining if an inverter is required on the OFPV off-grid system.

4.8.3. System sizing and component selection

Sizing and component considerations overview

From the off-grid system load requirements the off-grid system guidelines for off-shore components protection, selection and sizing may be derived. An schematic with considerations for a stand alone system off-shore is presented in Figure 4.8.

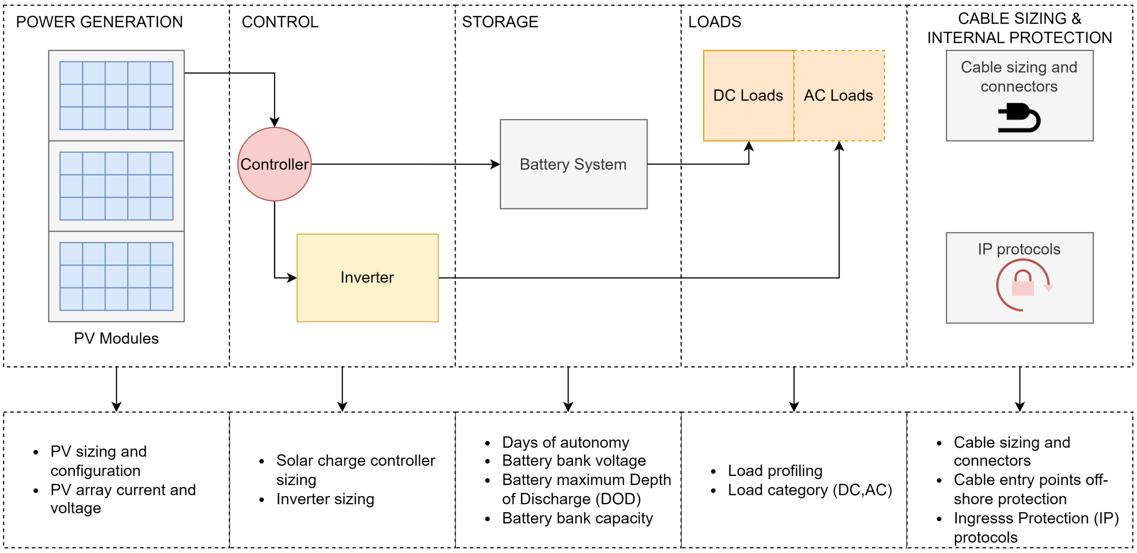

Figure 4.8: Stand alone system component selection and protection considerations for off-shore conditions.

The off-grid system size classification may depend on the loads and application. Thus potential OFPV off-grid applications are listed below with their respective energy requirements. This are defined as:

- OFPV Off-grid monitoring system: Energy requirements of such a system are subject to monitoring technologies in use. Usually the daily energy requirement will be up to 1000 Wh of daily power consumption off-grid.
- OFPV off-grid small scale solution: Powering devices usually less than 2 kWh of daily power consumption off-grid.
- OFPV off-grid large scale solution: Powering devices usually above 2 kWh of daily power consumption off-grid.

All these systems should follow a procedure to select and size the system correctly based on their load.

Load considerations

The system starts with identifying the load type profile and category, as previously described in Section 4.8.2.

The load profile details (energy consumption values) will be used for the battery bank sizing. Additionally, the load category type (DC and/or AC) is used for the inverter and charge controller selection and sizing:

If the load type is DC: No inverter required. If load type is AC: Inverter required. If load type is mixed (AC and DC loads): Inverter required.

From Smets et al., 2016; the annual load is described as:

$$E_L^Y = \int_{Year} P_L(t)\, dt \tag{4.1}$$

From which the average daily energy load may be derived:

$$E_{Daily,Load} = \frac{1}{365} * E_L^Y \tag{4.2}$$

Battery bank considerations

The type of battery should be first selected. Appropriate types for stand alone systems applications can be lead–acid, nickel cadmium, sodium (sulfur), lithium-ion, and sodium (nickel chloride) batteries; lead-acid and lithium batteries have most mature technologies due to low cost, maintenance free and high efficiency (the draw back is the low life cycle) (Hlal et al., 2019). The battery selected provides the open-circuit voltage $[V]$ of the battery as well as the battery capacity $[Ah]$. Depending on accessibility to the system, frequency of maintenance should be considered: One may choose lead-acid batteries if accessibility is possible between 3 to 6 months (topping), if accessibility to the system is limited, lithium batteries should be prioritized (Mohanty et al., 2016).

These properties will be used to correctly size the battery capacity.

The battery bank required energy, as stated by Smets et al., 2016 is set as:

$$E_{BB} = d_A * \frac{E_{Daily,Load} * SF}{DOD_{Max}} \tag{4.3}$$

$$E_{Batery} = V_{OC-Bat} C_{Bat} \tag{4.4}$$

With SF as safety factor (can be taken as 1.1), DOD_{Max} as maximum depth of discharge and d_a as days of autonomy.

The number of batteries, N is then determined as:

$$N_{Batteries} = \frac{E_{BB}}{E_{Battery}} \tag{4.5}$$

In series:

$$N_{Batteries}^{Series} = \frac{V_{OC,BB}}{V_{OC-bat}} \tag{4.6}$$

In parallel:

$$N_{Batteries}^{Parallel} = \frac{N_{Batteries}}{N_{Batteries}^{Series}} \tag{4.7}$$

With $E_B B$ as total energy of the battery bank, $E_{Battery}$ as the rated energy of 1 battery (open-circuit voltage $[V]$ of the battery times battery capacity $[Ah]$), V_{BB} as total voltage of the battery bank, $V_{Battery}$ as voltage of 1 battery,

Then the battery bank capacity may be derived, were depending on the application, the amount of days of autonomy, depending on the location latitude, must be selected. Table 4.4, presents the recommended autonomous days (Smets et al., 2016) depending on the latitude of the system.

Latitude [^{o}]	Recommended days of autonomy
0-30	5-6
20-50	10-12
50-60	15

Table 4.4: Recommended autonomous days at several latitudes (Smets et al., 2016).

The maximum depth of discharge of the complete system can be checked with:

$$C_{BB} = \frac{Days_{Autonomy} * E_{Daily,Load}}{V_{BB} * DOD_{Max}} \tag{4.8}$$

Moreover, the DC loads (usually specified on datasheet) should be studied to see in what voltage they operate. Depending on the voltage required, a buck, boost or buck-boost converter may be used to power the DC loads from the battery bank.

PV array considerations

Once the battery bank is established, the PV sizing may take place:

$$N_T = \frac{E_Y^L * SF}{A_M * \int\limits_{Year} G_M(t)\eta(t)dt} \tag{4.9}$$

$$N_S = \frac{V_{OC-BB}}{V_{MMP,Module}} \tag{4.10}$$

$$N_P = \frac{N_T}{N_S} \tag{4.11}$$

The PV array design, together with the components should be then check with the area available for the project, as well as the area available on floaters. This was set in the 'Project Procedures' Section.

Furthermore, the design should be assessed for redesign with the loss of load probability (LLP) (Smets et al., 2016): If the LLP is within the estimated acceptable range, this value can be used to evaluate the system PV array. If the LLP value is not acceptable, one should increase the PV array size and/or capacity of battery bank.

$$LLP = \frac{E_{fail}}{\int_0^{8760h} P_L(t)dt'} \tag{4.12}$$

Solar charge controller and inverter considerations

Once this is found, the MPPT charge controller must be determined, where the V_{MPP} and A_{MPP} on the array must not be exceeded. Furthermore, data-sheet from solar charge controller manufacturers have requirements for installation, including orientation of component and spacing around for ventilation. Due to the conditions off-shore and in the case of low spacing. Dry tests of components varying from manufacturers set up and use recommendations should be performed. This should also be done in the case of inverters.

The inverter, in case required to power AC loads, must fulfill 3 requirements as stated in Smets et al., 2016:

The inverters maximal power output must exceed the maximal power required by the loads within the off-grid system:

$$P_{DC,Max}^{inv} > P_L^{Max} \tag{4.13}$$

The nominal power of the inverter should be close to the maximal load power:

$$P_{DC,0} \simeq P_L^{Max} \tag{4.14}$$

The nominal inverter input voltage should be close to the nominal battery bank voltage:

$$V_{DC,inv} \simeq V_{OC,BB} \tag{4.15}$$

Cabling

A special focus should be made on cabling length. Cable lengths from PV array to BoS should be reduced to reduce power losses

To determine the DC cable losses between the PV array and the BoS, the following equations may be used (Smets et al., 2016):

$$R_{Cable} = \rho \frac{L}{A} \tag{4.16}$$

$$P_{Loss} = I^2 * R_{Cable} \tag{4.17}$$

$$P_{Loss,Total} = \frac{P_{loss}}{P_{Wp}} \tag{4.18}$$

Additionally, in case of requiring additional data cabling extensions, a special focus to protection against off-shore conditions should be made. Polyurethane (PUR) cables with 3 wire terminals may be used, as the resistance against the off-shore environment is greater than standard data cable protection materials. This can also be applied for 3 wire cables for AC outputs from the inverter.

4.9. OFPV system monitoring, safety and maintenance

Monitoring and maintenance should be done regularly. Router connection off-shore may allow to retrieve live data from the systems charge controller or inverter. This information may serve for studying performance and alert of any possible failures off-shore.

Additional safety switches should be included between the PV array and the load, and between the load and the battery. Relay control systems may be included to control the State-of-Charge (SoC) of the battery bank. Depending on accessibility to the system; if lead acid batteries are used, supervision of these should be done between 3 to 6 months. If accessibility is not possible, lithium batteries are recommended, as maintenance checks are not required as frequently as 3 to 6 months.

Maintenance should be done in order to check the correct functioning of the systems under high wave conditions. If corrosion, condensation, or high temperatures above manufacturers recommendations are detected, the system should be assessed and the necessary components should be replaced.

Additional monitoring devices, such as pyranometers and reference cells may be reinforced to withstand high environmental conditions off-shore. Calibration should be performed afterwards to ensure the correct functioning. Monitoring of the system through remote systems such as Victron'S Remote Management (VRM) system may be used to monitor the off-grid system in real time and be able to detect any faults, including an increase in temperature within a protection box containing electrical components.

4.9.1. Application of guidelines

The application of this off-grid OFPV recommended guidelines may serve for industries within the aquaculture sector, monitoring stations off-shore, small construction or islands off-shore or additional power stations for any application off-shore without the need of a connection of the grid in a remote area, such as off-shore seas and oceans.

These recommended guidelines derive from the research project performed for an off-grid PV system off-shore, in the North Sea. The author of this document does not accept any liabilities derived from these guidelines recommendations. These are recommendations provided to help towards standardization of the industry, since there is still a need to further develop specific standards for OFPV technology (Claus and López, 2022).

5

Results and discussion

This chapter presents the results obtained for the comparison between the PV systems on-land and off-shore and discusses the findings. These results come after the process of designing, integrating and testing, before the experimental set-ups were launched at their respective locations. Results are obtained for the period 15-11-2022 up until 1-1-2023. Results are covered in 3 sections: power performance, temperature measurements and environment influences.

5.1. Experimental results overview

This section aims to provide an overview of the structure on which results are derived. This overview is also provided visually in Figure 5.1, where the topics of study concerning power, temperature and environment effects are displayed, with arrows indicating the order of topics discussed.

Results within this research are experimental. These results aim to answer what are the differences in PV performance and the possible causes of these differences between off-shore floating PV systems and on-land based PV systems. All measurements presented have a minute time-step between measurements, with the exception of the inclinometer, which measured in one second time-steps, and additional data retrieved from KNMI weather station, which provided data in 10 minute time intervals. All measured parameters are presented in Appendix E. Additionally, simulation results for meteorological climate data from Meteonorm are presented in Appendix D.

Experimental results are divided into:

1. Power performance.
2. Temperature measurements.
3. Environment influences.

Firstly, power performance is addressed. Here the DC power outputs for each system are presented. These are divided into the individual strings of the system. The 2 PV strings on each system, consisting of 6 bifacial PV modules connected in series, are measured individually. The PV module specifications were previously presented in Table 3.1. Since in each system one string was facing North-West and the other string was facing a South-East orientation, this terminology was used when referring to each PV string. The PV system designs was previously presented and can be found in Chapter 3. Voltage and current results are presented through the use of box-plots. Relationships of voltage and current concern temperature and irradiance, thus incoming irradiance at the Plane of Array (POA) is then presented to explain the differences found. Temperature influences are covered in the next section. It is important to note that the measurements from reference cells at the same azimuth and inclination (POA) for each string are used to determine the efficiencies. These string efficiencies, using the DC power measured and the incoming irradiance at the POA are derived through the use of linear regression fits. Additionally, derivation of module efficiencies for each string, are derived from theory relating measured ambient temperature, module temperatures and irradiance on the modules

(Smets et al., 2016) in Appendix E. Capacity factors for the period of the experiment are also provided. Energy yield results during the period of research is also provided.

Secondly, temperature influences are examined. Ambient temperature measurements at each location are compared with climate data for validation of the temperature trends during the period of research. Specific temperatures (referring to ambient temperatures, module temperatures and water temperatures (off-shore) at each location) are also shown together in the same timeline plot and are then discussed. Combining the ambient and specific temperatures with the module temperatures, the resultant module temperatures and their variations are examined. From here, module temperatures are individually studied to see the gradient within a module for expected water splashing, salt, algae or other environmental conditions that could cause soiling effects and thus change the temperatures throughout a module. Also, the module temperatures throughout a floater are shown and compared with the on-land system. Additionally, a comparison is performed between OFPV thermal models derived from the empirical measurements and the FPV empirical models found in literature.

Thirdly, from the results seen in power and temperature measurements, environmental influences are analyzed to provide observations during the experimental period. These concern the influence of wind and wind direction, waves that the off-shore system had to endure and the effect of sea water temperatures and their cooling effect. Finally tilt and azimuth changes are analyzed. Furthermore, soiling is identified through the use of a visual camera pointing at PV module 7 (previously described in Chapter 3) and shading on-land is also analyzed using a Horicatcher (horizon measurement device) and the software 'Meteonorm'.

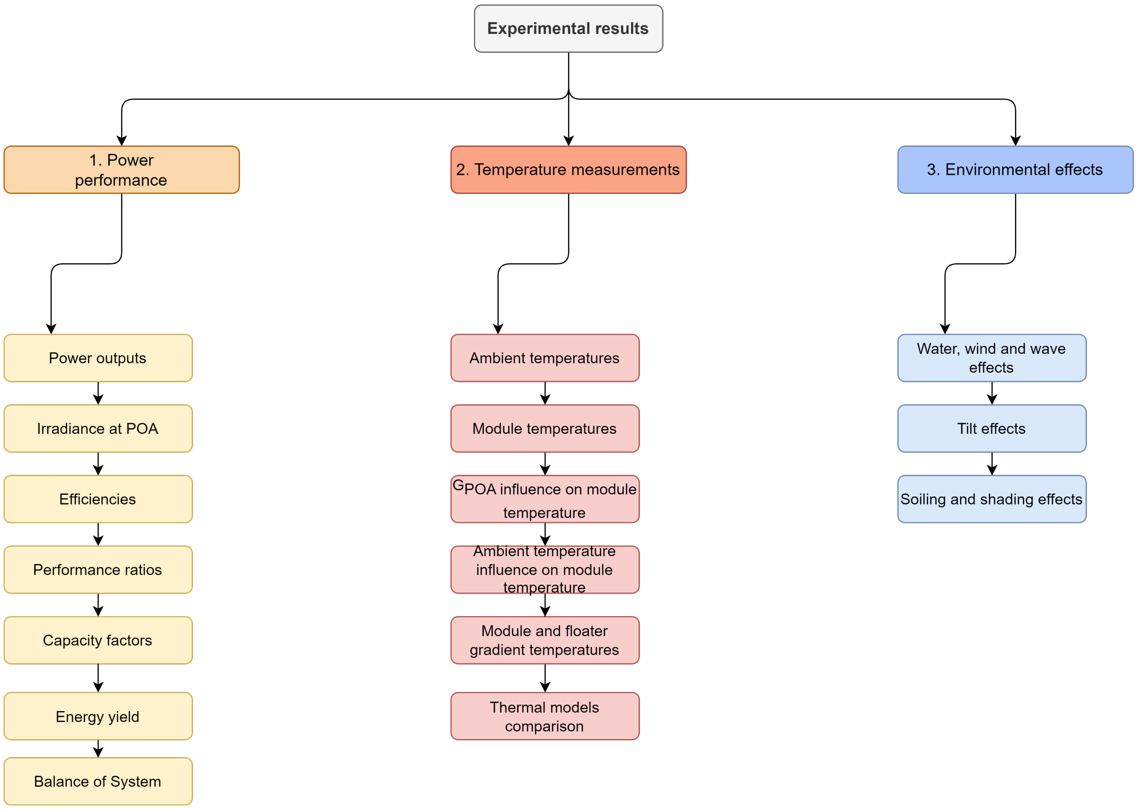

Figure 5.1: Experimental results analysis overview. Divided in power performance (yellow), temperature measurements (red) and environmental effects (blue).

5.2. Power performance

This section aims to provide a comparison for the DC power production measured at each of the 2 PV strings with 6 modules each for both the systems on-land and off-shore. The power production is first presented for the complete period. Then, the performance behaviour is examined in smaller time frames: weekly and daily plots are provided. From here characteristics of voltage and current are also presented and examined through the use of box-plots. Irradiance and temperature of the surroundings is presented to see the influence on voltage and current on a time frame of a selected week. Furthermore, a regression fit of power comparing both set-ups at each orientation is provided. Incoming irradiance at each POA is also presented. Finally, the performance indicators are presented.

5.2.1. DC power output

The results of the power produced on the DC side for on-land and off-shore, divided per string are presented in Figure 5.2. Power measurements were obtained in 1 minute resolution (1 measurement per minute). Figure 5.2 provides the power production per string off-shore and on-land. Additionally, the GHI, from pyranometer measurements at each system is presented to show the similarity in irradiance at each location on the same time-step. The irradiance at the POA of each string is then compared to determine the differences in irradiance perceived by the PV systems on-land and off-shore. Power meter data for the South-East string off-shore was not available for the period 28-11-2022 until 20-12-2022 due to a malfunction of the power meter measurements recorded on the data logger.

Power results from 21-11-2022 to 28-11-2022 are provided in Figure 5.3 to give a weekly overview on power performance. The highest power peaks were obtained for the South-East orientation off-shore. The last week of measurements from 25-12-2022 to 31-12-2022 are also provided in Appendix E. Figure 5.4 was then presented to analyze the power performance on a relatively sunny day, indentified from the weekly plot, the day corresponds to the 24th November 2022. Additionally Figure 5.5 is provided to show the irradiance at the POA for this day, showing the similar irradiance levels perceived by the PV strings at each location. From Figure 5.4, the on-land power production at the sun-rise and sun-set showed a higher production for the North-West string than off-shore. Note the orientation of the strings, previously presented in Figure 3.3, indicated the orientation of the South-East string was set at -30 ^{o} from North, with the North-West string with an orientation of 150 ^{o} from North. Off-shore power production does not experience the effect that the North-West string power production surpasses the South-East string power production at the first and last sunlight hours of the day, suggesting that orientations of the off-shore system may have changed from the one provided in the methodology. The orientation is likely to be set to a higher azimuth, with the South-East string coming close to 180 ^{o} from North. So facing a more favourable South orientation. This change in orientation theory was unable to be corroborated due to unavailability of orientation trackers within this research set-up. Furthermore, a more favourable tilt of the floater is suspected to cause this difference and is further investigated in Section 5.4.

For the period of research, the maximum power points obtained and their respective pyranometer measurements are also provided in Table 5.1. Maximum power measurements were obtained within the off-shore location (when comparing with the on-land system power measurements). Note that measurements on-land and off-shore also matched with the time (minute) when the pyranometer was recording its maximum GHI values. Table 5.3 provides the linear fits found within this results.

Location	Off-shore	Off-shore	On-land	On-land
String	South-East	North-West	South-East	North-West
Maximum power [W]	925.31	911.53	852.13	721.23
GHI [W/m2]	395	374	386	386
Date	Nov 16 2022	Nov 16 2022	Nov 19 2022	Nov 19 2022
Time (GMT +01:00)	12:31	13:17	11:49	11:49

Table 5.1: Maximum power points registered from 15-11-2022 to 1-1-2023

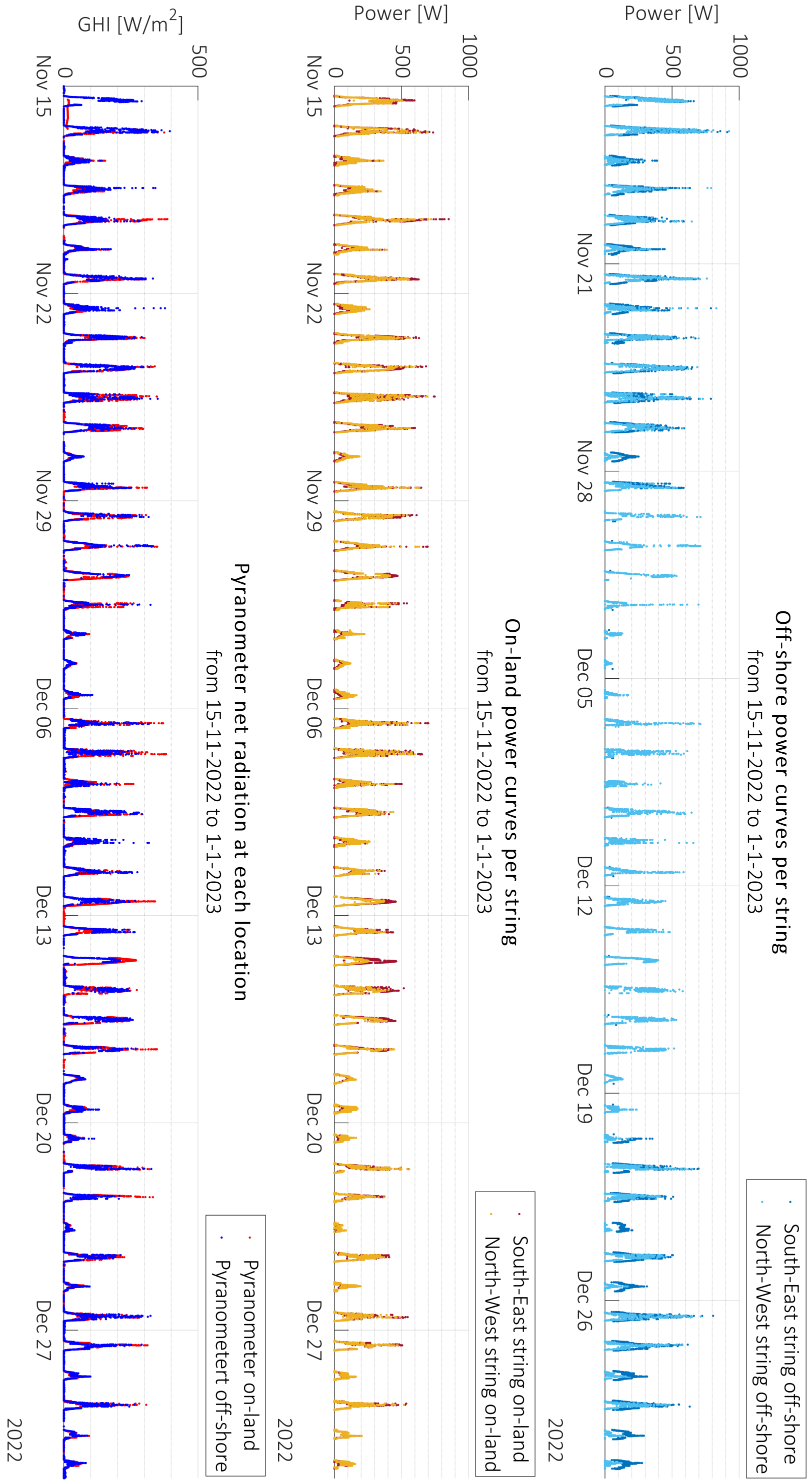

Figure 5.2: Power performance of each string for the on-land and offshore systems from 14-11-2022 until 1-1-2023, provided with GHI from pyranometer measurements at each location.

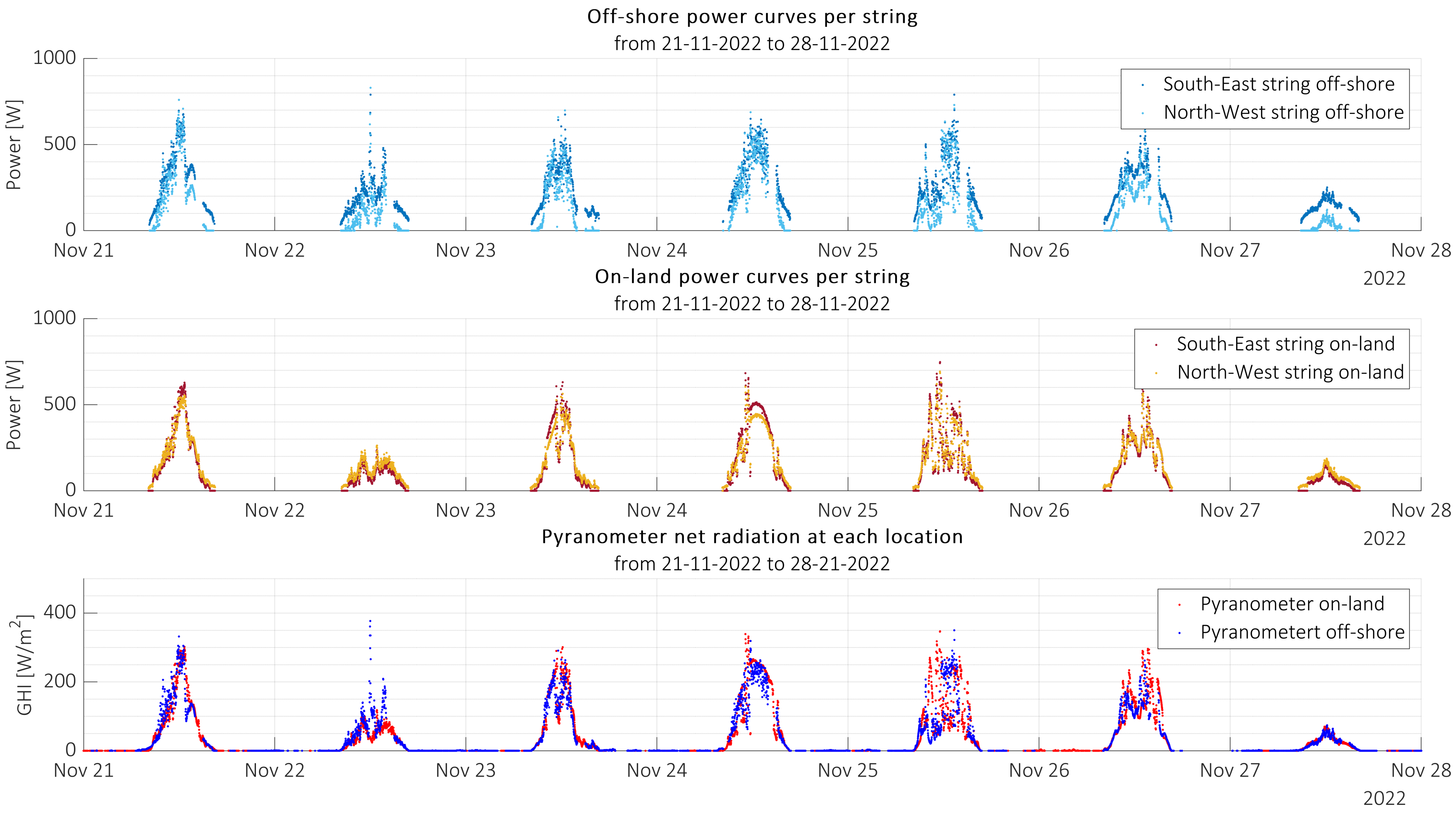

Figure 5.3: Power performance of each string for the on-land and offshore systems, provided with GHI from pyranometer measurements at each location for a week, from 21-11-2022 until 28-12-2022.

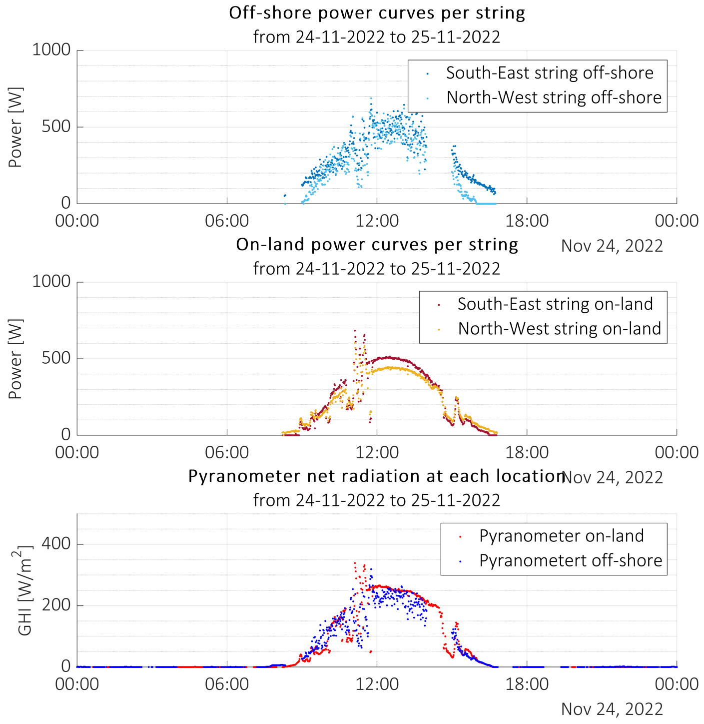

Figure 5.4: Power performance of each string for the on-land and offshore systems, provided with GHI from pyranometer measurements at each location on 24-11-2022, a sunny day with a constant fine cloud coverage.

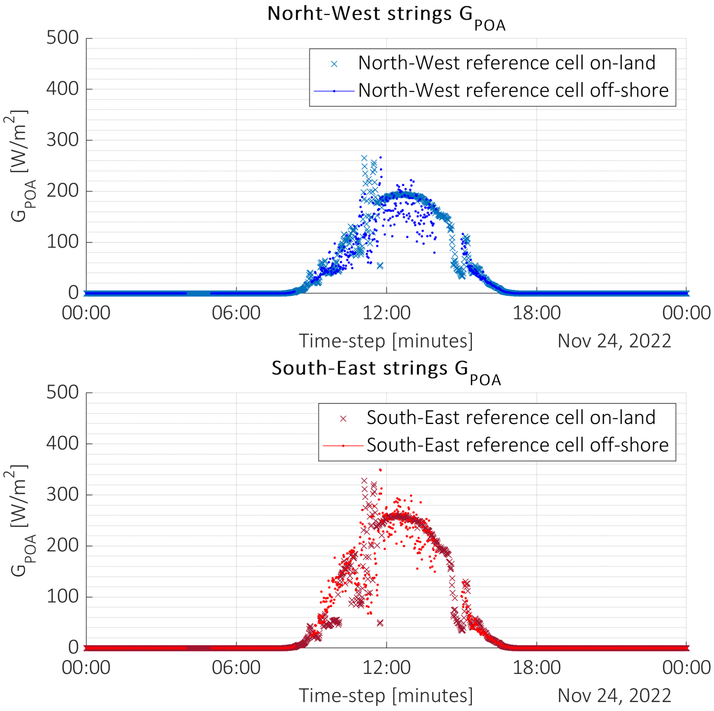

Figure 5.5: G_{POA} comparison for each string orientation (North-West strings in blue and South-East strings in red), on 24-11-2022, a sunny day with a constant fine cloud coverage.

From the power measurements timeline presented, power regression plots were performed to compare the off-shore and on-land systems. For the North-West strings, presented in Figure 5.6 with a linear regression fit, it is found the the North-West string power production off-shore, was found to be lower than on-land. For the South-East orientation this was not the case, as the South-East string was recording much higher power outputs, shown with the linear regression fit in Figure 5.7: from the linear regression fit the output off-shore was 150 W higher when on-land this vlue was near zero. This is suspected due to a more favourable orientation off-shore for the South-String or else due to misreadings of the Hall effect sensor of the south-east string. From this power measurements recording higher outputs on-land than off-shore suggests a difference of irradiance levels at the plane of array of each string. Therefore the irradiance was investigated in Section 5.2.3 to further understand the power outputs recorded. An additional graph (Figure E.6) showing the power outputs of all PV strings of both on-land and off-shore PV systems is provided in Appendix E.

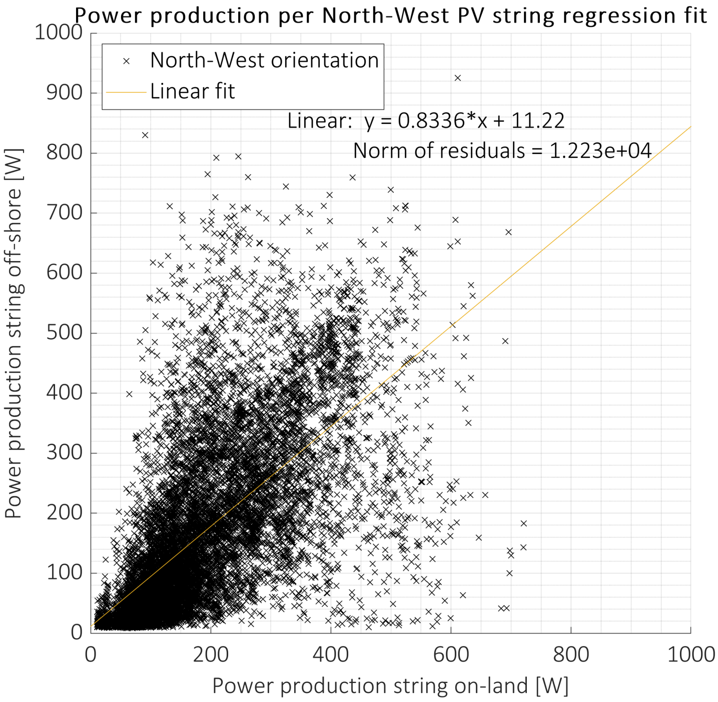

Figure 5.6: Power regression fit for North-West strings, from 15-11-2022 to 1-1-2023.

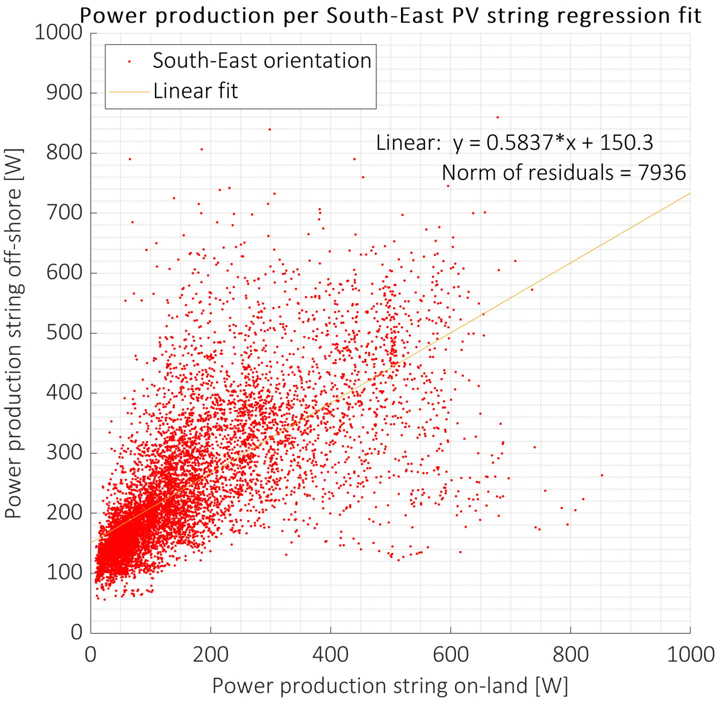

Figure 5.7: Power regression fit for South-East strings, from 15-11-2022 to 1-1-2023.

5.2.2. Voltage and current

Following the results from power; voltage and current measured results are presented as they directly correlate to power through Ohm's Law. The analysis is performed with the use of box-plots. Measurements for voltage and current from 15-11-2022 to 1-1-2023 are studied per PV string, both off-shore and on-land during power production. From the measurements in this period, the mean, median and maximum values recorded for each string both off-shore and on-land are presented for voltage and current in Table 5.2.

Location	Off-shore	Off-shore	On-land	On-land
String	South-East	North-West	South-East	North-West
Voltage mean [V]	194.864	195.131	201.100	199.532
Voltage median [V]	198.127	197.939	201.343	202.72
Voltage maximum [V]	234.95	244.667	228.579	208.918
Current mean [A]	1.105	0.584	0.643	0.664
Current median [A]	0.917	0.287	0.524	0.455
Current maximum [A]	3.524	4.328	3.375	3.698

Table 5.2: Voltage and current results per string.

The voltage box-plot is presented in Figure 5.8. The mean voltages off-shore were found to be lower than on-land by 6.2 V and 4.2 V for the South-East and North-West strings respectively. This difference in voltages was subject to higher module temperatures recorded off-shore when compared to on-land. The module temperatures recorded are presented and its influences are further discussed in Section 5.3.

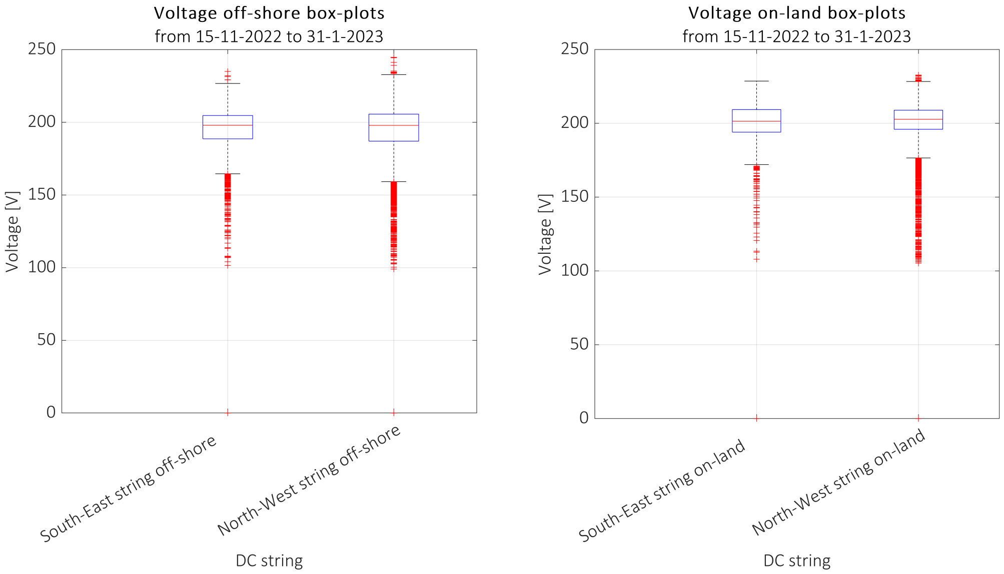

Figure 5.8: Measured voltage box-plots of each string for the on-land and offshore systems, from 15-11-2022 to 1-1-2023.

The current box-plot is presented in Figure 5.9. The mean current values off-shore were found to be 0.462 A higher than on-land for the South-East string and 0.08 A lower than on-land for the North-West string. The large difference found for the South-East strings with respect to current is suspected to be predominantly influence by irradiance levels and thus the measurements of irradiance at the plane of array (G_{POA}) were analyzed next, in Section 5.2.3, to check if the South-String off-shore G_{POA} was significantly higher than on-land and thus explain the large difference in current. Another reason could be due to soiling: at string level, the PV module delivering the lowest current determined the current level of the string, since they were connected in series. If shading and/or soiling occurred, then current levels might have been subject to lower current levels. The environmental effects with respect soiling are analyzed and discussed in Section 5.4.

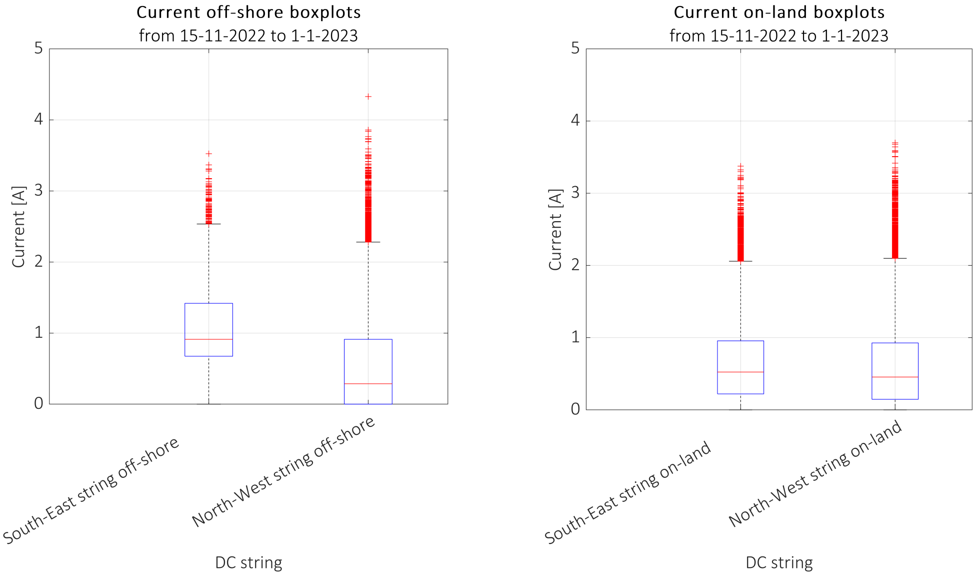

Figure 5.9: Measured current box-plots of each string for the on-land and offshore systems, from 15-11-2022 to 1-1-2023.

It is important to mention North-Sea water temperatures are higher than ambient temperatures off-shore and on-land during this period of research. To show the the behaviour and influence of irradiance and temperature on power, additional timeline plots are presented in Appendix E, for the week from 21-11-2022 to 28-11-2022 for voltage and current with respect to irradiance, ambient temperature and water temperatures off-shore. The large difference identified off-shore with respect to current between the South-East and North-West string can be analyzed from the figures presented in Appendix E: The average module temperature recorded at each string is presented together with the ambient temperature. Module temperatures between strings give similar outputs, which is discussed in Section 5.3.

5.2.3. Irradiance at POA

From the boxplots in Figure 5.9, a large difference in current between the South-East strings off-shore and on-land was identified. Therefore, a regression fit comparing on-land and off-shore with respect to irradiance at the POA for the strings at South-East and North-West orientation was provided in Figure 5.10 and Figure 5.11 respectively. An additional comparison between the irradiance on the PV strings of the same system (off-shore and on-land) is provided in Appendix E, in Figure E.3.

The linear regression fit are provided in Table 5.3. The irradiance at each POA linear regression fits showed a positive trend for both South-East and North west strings. It is seen that that the off-shore G_{POA} for both strings was higher than on-land when comparing the measurements taken at the same time. This was also the case for the South-East strings. Therefore the performance ratio should serve as the reference as it takes into consideration the difference in irradiance experienced by the two systems.

Additionally, when comparing the irradiance perceived strings with the power production, it is suspected that the power measured by the South-String off-shore may have been subject to the Hall Effect sensor reading incorrect values. It is suspected that the sensor became de-attached and thus the readings might be subject to additional noise. This is further analyzed with the efficiency and performance calculations, were results are checked to see if power measurements of this string were reliable.

Regression parameters	North-West	South-East
Power fit $[W]$	$y = 0.8336x + 11.22$	$y = 0.587x + 150.3$
Irradiance fit $[W/m^2]$	$y = 0.72991x + 10.75$	$y = 0.767x + 15.37$

Table 5.3: Linear fit curves for power and irradiance at POA for off-shore and on-land (with y = off-shore measurement and x = on-land measurement).

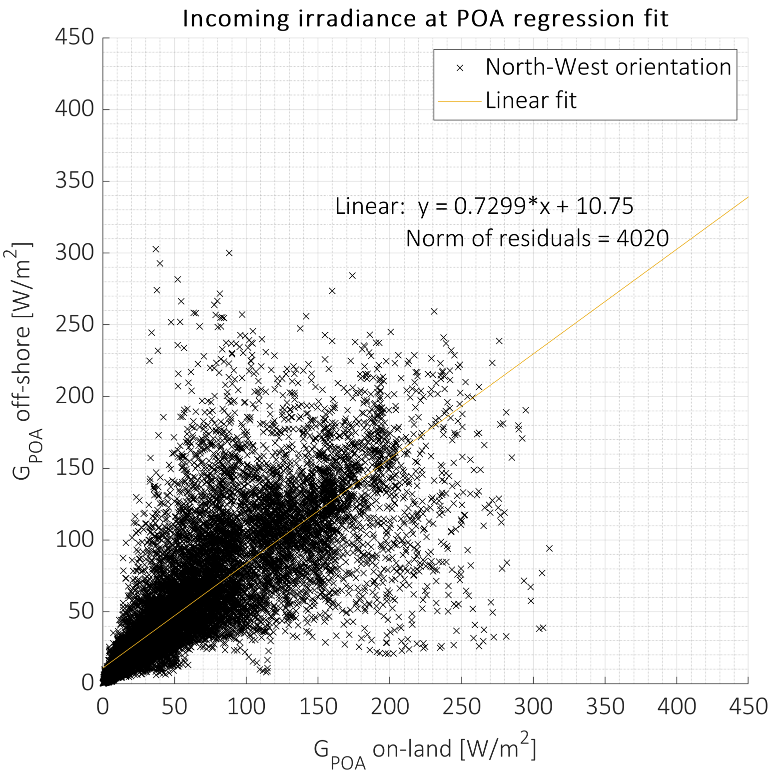

Figure 5.10: Measured irradiance at POA regression fit for North-West PV strings.

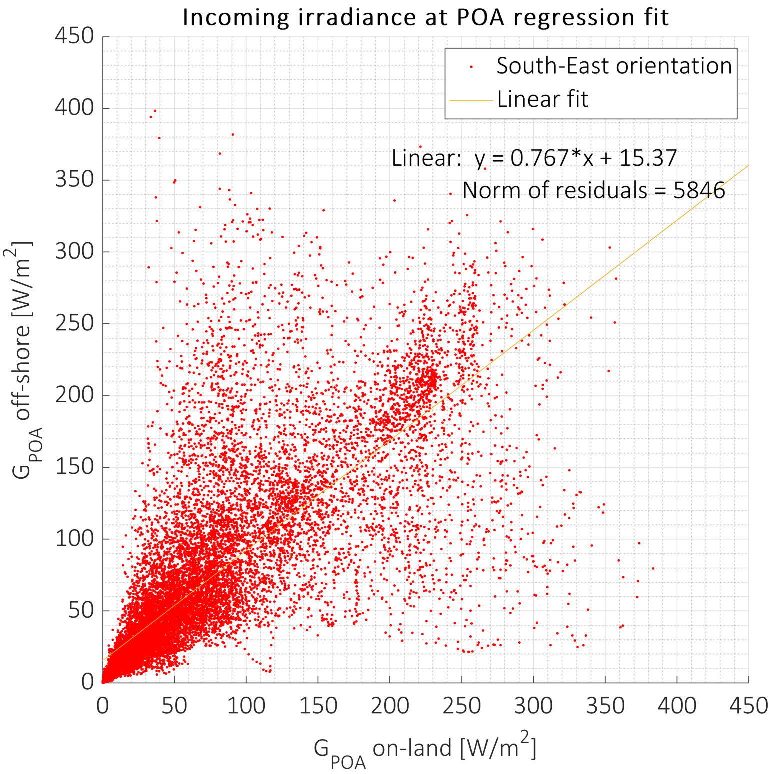

Figure 5.11: Measured irradiance at POA regression fit for South-East PV strings.

5.2.4. Efficiency

Efficiency was evaluated both at module and string level. The efficiency at module level was calculated since there was no power meter at each PV module and to compare the predicted efficiency with the efficiency measured. On one hand, efficiency at module level was determined using the PV module characteristics provided by the manufacturer at STC, previously presented in Chapter 3, Table 3.1, and with the use of incoming irradiance at the plane of array (POA), ambient and module temperatures recorded, the calculation is presented in Appendix E. On the other hand, efficiency at string level was evaluated using the DC power recorded from the power meters and the incoming irradiance at the respective POA, from the reference cells.

Derived module efficiencies

The module efficiency at STC provided by the manufacturer is stated at 19.76%. However, as shown in Appendix E, this efficiency is subject to change due to the influence with temperature and irradiance. With the module specifications and considering the irradiance at the POA for each inclination as well as the ambient and module temperatures, the averaged efficiency of a module from PV theory and real data is obtained for both orientations and locations.

Figure 5.12 presents the module efficiency during the presence of irradiance (day-light) for STC, and for on-land and off-shore conditions for the South-East strings. The efficiency for all string orientations at module level, is presented at the end of this section. For the determination of this efficiency, the average module temperatures per minute of the south-east string are used, as well as the ambient temperature at location and the irradiance at the POA obtained from the reference cell at the same orientation and inclination.

A box-plot is provided to show the differences in module efficiencies expected from theory for both on-land and off-shore. These box-plots are shown in Figure 5.13. On-land the mean efficiency on the North-West and South-East orientations were found to be 20.92 % and 20.78 % respectively. Off-shore the mean efficiency on the North-West and South-East orientations were found to be 20.15 % and 20.17 % respectively. From here we see the high efficiencies achieved for on-land with also high variations, which are due to the effect of higher module temperature changes on-land. Off-shore efficiency is subject to less variations, since module temperatures do not vary as much as on-land and as seen during the experimental period. the individual efficiency based on the POA irradiance is provided together with the efficiency which also takes into account module temperature for a complete vision of the module temperature influence on efficiency. The effects on module temperatures are further discussed in Section 5.3. The complete derivation of module efficiencies from module temperatures and irradiance, based on theory from (Smets et al., 2016), is provided in Appendix E.6.

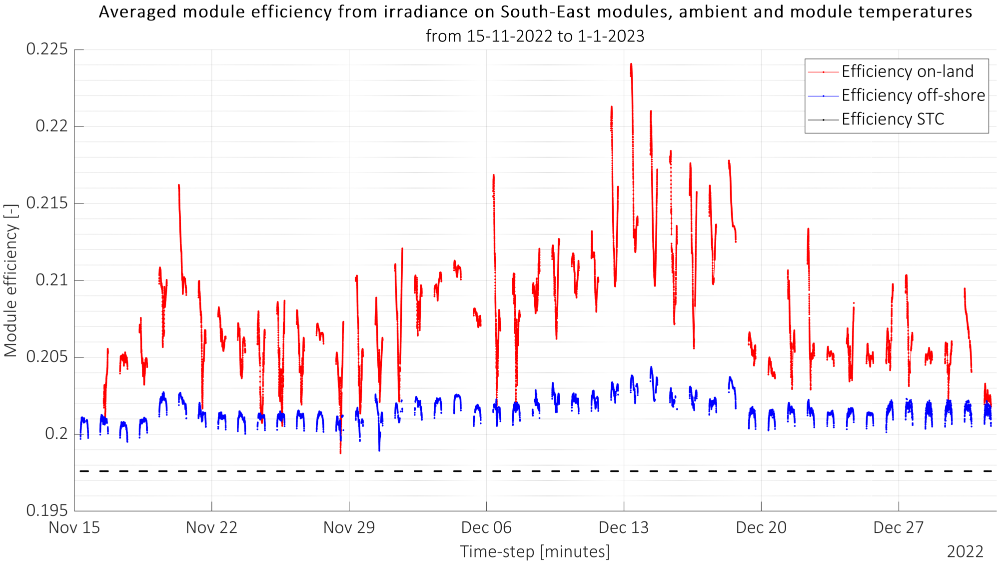

Figure 5.12: Averaged module efficiency on South-East side derived from G_M and T_M and module specifications.

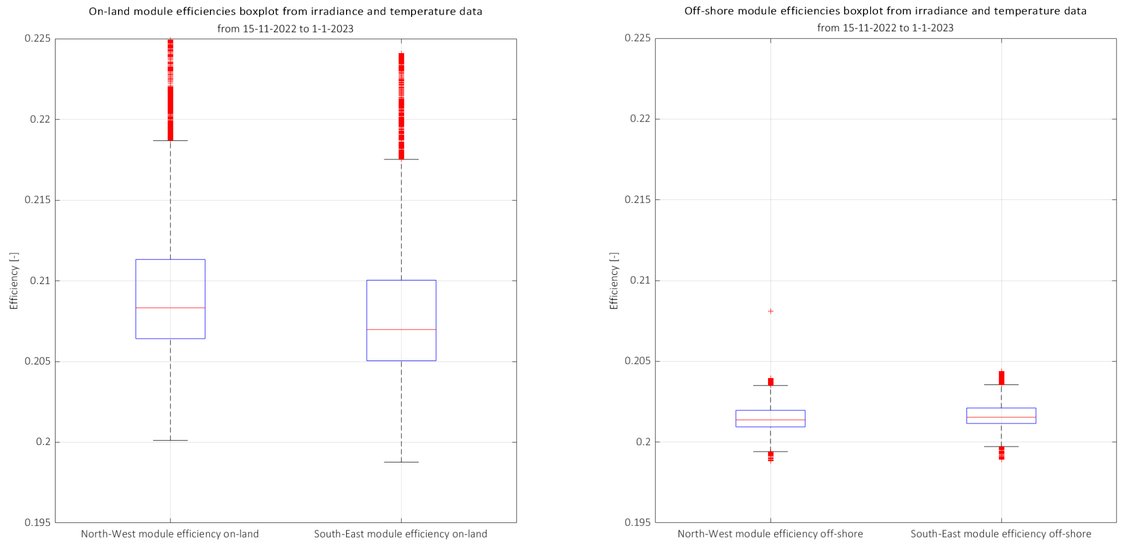

(a) Derived module efficiency on-land.

(b) Derived module efficiency off-shore.

Figure 5.13: Module efficiency box-plots derived from G_M, T_M and module specifications.

DC string efficiency

String efficiencies are also evaluated based on Equation 5.1, where incoming irradiance on the surface of the string consisting of 6 PV panels in series is compared with the DC power measured at the end of each string. Knowing the total surface covered by the PV modules within a string and the incoming irradiance at the POA (G_{POA}) for each string, both on-land and off-shore, the efficiency from minute time-steps measurements can be approximated. Efficiency in this case is not plotted as a function of time since the reference off-shore can be subjected to different POA in certain occasions since their location was set in the utility floater, which could suffer from different tilt variations. Therefore a regression line plot style is used instead to be able to discard the outliers. The plot containing both-string on-land and both strings offshore is provided in Appendix E, Figure . All linear regression fits presented in Table 5.4 were used to calculate the efficiencies for the period of research.

$$\eta_{String} = \frac{P_{DC_{String}}}{G_{POA} * A_{String}} \tag{5.1}$$

Location	Off-shore	Off-shore	On-land	On-land
String	South-East	North-West	South-East	North-West
Linear fit	$y = 5.87x$ -492.8	$y = 3.472x$ $+227$	$y = 5.495x$ $+45.21$	$y = 4.957x$ -3.575
R^2	0.9247	0.8671	0.9696	0.9683

Table 5.4: Linear fits parameters found for string efficiencies
(with y = incoming irradiance on string surface area at POA and x = string power output).

From the efficiencies obtained from the linear regression fits, it is found that off-shore efficiencies were higher, however when looking at the values, a 25.43 % efficiency implies an increase of 29 % in relative efficiency when compared to the efficiency at STC (19.7 %), which for normal silicon technology, the temperature should be 96 % lower, implying the temperature was of -71 ^{o}C, which was not the case. Thus, this result was discarded, confirming the power measurement disparity previously shown for the South-East string off-shore. It is suspected that the Hall effect sensor readings, which could influence the power measurements were having misreadings as it may have become partially de-attached as this sensor was not attached to the monitoring box. In this case the South-East power measurements should be discarded and thus this efficiency should not be considered as a reliable result.

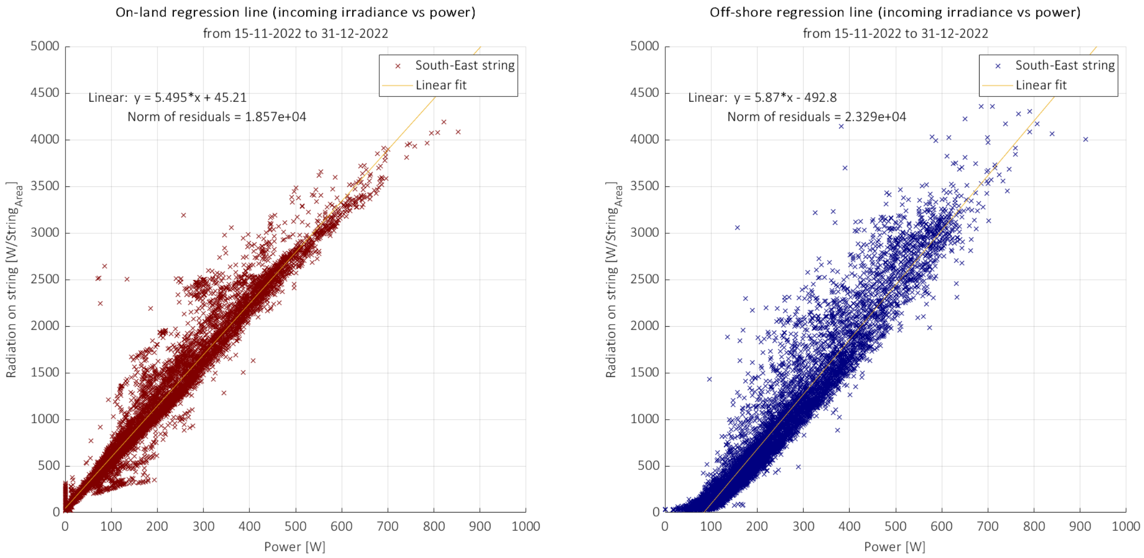

(a) South-East string regression line on-land.

(b) South-East string regression line off-shore.

Figure 5.14: South-East string regression between incoming radiation on the floater surface and DC power production on-land and off-shore including a linear fit.

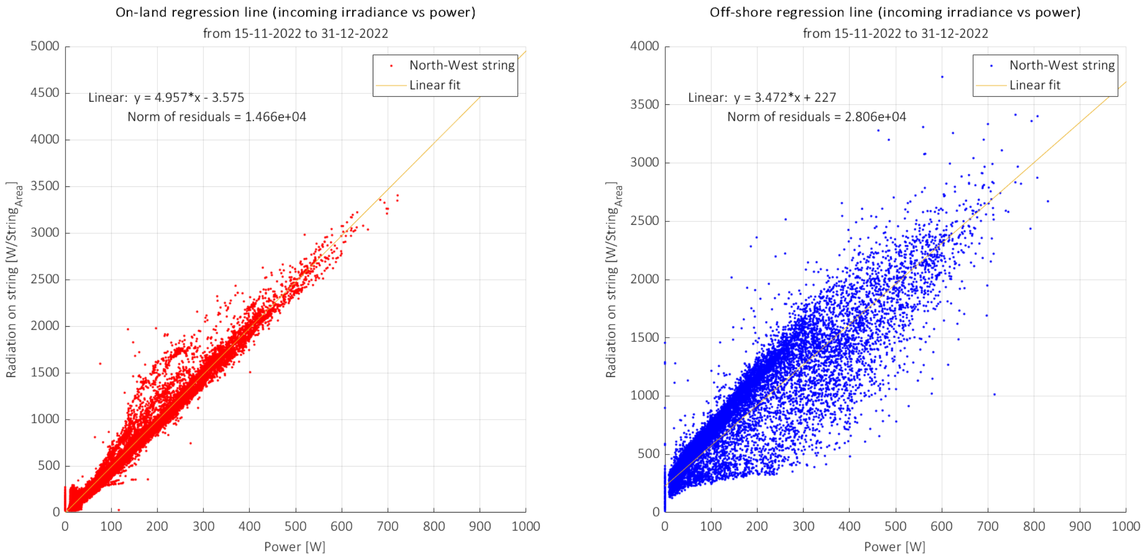

(a) North-west string regression line on-land.

(b) North-west string regression line off-shore.

Figure 5.15: North-west string regression between incoming radiation on the floater surface and DC power production on-land and off-shore including a linear fit.

Efficiency per orientation	On-land SE	On-land NW	Off-shore SE	Off-shore NW
Derived per module	20.78 %	20.92 %	20.17 %	20.15 %
Measured per string	17.376 %	20.246 %	(25.43 %)	22.26 %

Table 5.5: Efficiencies found at module and string level for South-East (SE) and North-West (NW) orientations from 14-11-2022 to 31-12-2022

5.2.5. Performance ratios

The performance ratios (PR), with definitions previously discussed in Chapter 3, were calculated with the cumulative energy recorded by each power meter together with the total irradiance perceived by each reference cell at each POA. The PR are presented per PV string in Table 5.6.

For the PR calculations it was assumed the power meter power readings (W), which had one measurement per minute, remained constant throughout the minute until the next measurement was taken. The cumulative energy and total irradiance at the POA of each PV string (G_{POA}) were used to determine the performance ratio during the experimental period. Additionally, the maximum power at STC (P_{Wp}) of the PV modules was used, equal to 360 W_p.

The off-shore PR is found to be 92 % for the North-West string, while on-land the PR is found to be 87 % for the South-East string and 100 % for the North-West string, meaning the average PR ratio found on-land was of 93.5 %. The South-East string off-shore had a data gap and afterwards it was suspected from the measurements that this sensor was no longer operating correctly, which meant PR for this string could not be determined. One cause could be the Hall effect sensor coming loose. In literature, for the month of December, Golroodbari and Sark, 2020 simulated a similar off-shore PV system which predicted an 85 % PR for a system with 12 PV modules located in the Dutch North Sea.

The difference found between the strings on-land was considered large and thus was suspected to have had an additional influence within the electrical system or from the environment. The difference between the on-land strings PR is suspected to be an anomaly. Note the PR was calculated using characteristics of the PV module under standard test conditions (1000 W/m^2 and 25 ^oC), meaning that under the influence of certain environmental or electrical factors, this value could reach and exceed 100 % (SMA, n.d.) Shading of the North-West reference cell on-land, located closest to the surrounding building, may have caused the PR to be higher. Shading effects are thus further studied in 5.4. Another factor suspected to influence the PR difference is the distance between Hall effect sensors; these are recommended by the manufacturer to be located such that they avoid high electrical noise sources; in the monitoring box this space was limited and noise by the DC cables in the splitter prior to the Hall effect sensor may have had an influence. The hall effect sensors' influence could not be verified but it is recommended for future research to install these sensors in a fixed position further apart. Additionally other influencing factors mentioned by SMA, n.d. could be the recording period (winter months of November and December) and the differences in solar cell technologies (bifacial modules) with respect to the reference cell. It is thus recommended to perform such a PR comparison over an annual period to yield conclusions rather than observations.

Location	Off-shore	Off-shore	On-land	On-land
String	South-East	North-West	South-East	North-West
Performance ratio	-	0.92	0.87	1.00

Table 5.6: Performance ratios found for the off-shore and on-land systems. Note the off-shore South-East string had data gaps and thus this value could not be determined.

5.2.6. Capacity factors

The capacity factor results are provided through the use of a box-plot analysis in Figure 5.16. Off-shore, the mean capacity factors found for the South-East and North-West strings were 10.40 % and 5.63 % respectively. On-land, the average capacity factors found for the South-East and North-West strings were 6.16 % and 6.31 % respectively. The high capacity factor obtained for the South-East string was previously discussed and is likely to have an error in the measurement reading of the Hall Effect sensor. Note the North-West string off-shore was slightly lower on average than on-land, however, high capacity factor measurements (red crosses) where recorded for the North-West string off-shore, this can be due to the tilt effect off-shore that may have caused a more favourable orientation than on-land at a certain point during the experimental period.

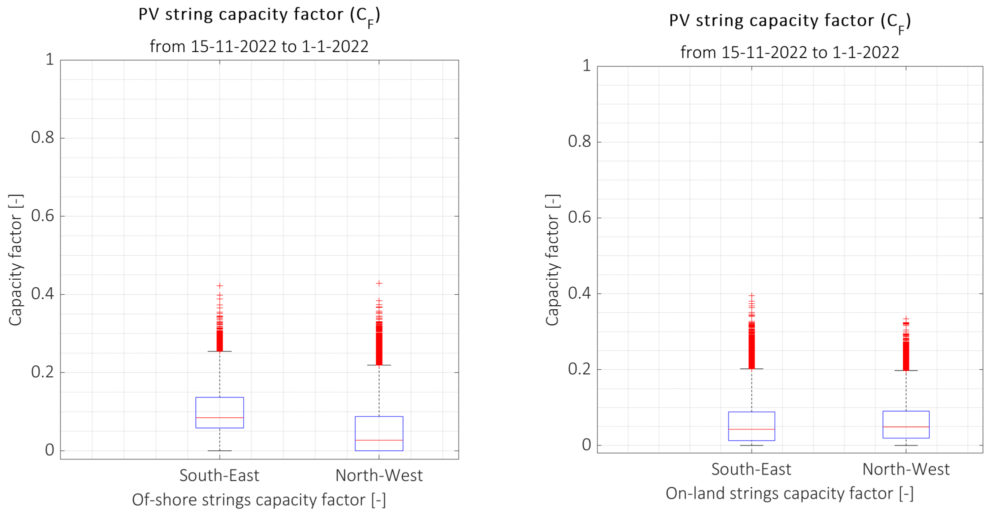

Figure 5.16: Capacity factors identified per string for both off-shore an on-land with strings installed peak power of 2.16 kWp, from 15-11-2022 to 1-1-2023.

5.2.7. PV Energy

The cumulative energy yield is presented to compare the energy production of the two systems. Figure E.8 presents the comparison for cumulative energy yield. For the period from 15-11-2022 to 1-1-2023 the on-land system recorded 96.3 kWh while the off-shore system recorded 93.4 kWh, on the DC side of the systems. Note the off-shore system measurements were taken from the MPPT charge controller instead of from the power meters, since there was a data outage error for the power meters of the South-East string off-shore.

From the results presented, the cumulative energy yield was higher for the on-land system: this output was checked with previously presented Figure 5.10 and Figure 5.10, comparing irradiance on-land and off-shore for each string where it was determined that both on-land strings were also perceiving higher levels of G_{POA}. Moreover, to show the behaviour of each string, when measurements were available for all strings, the first two weeks are presented, from the 15-11-2022 to 28-11-2022 in Appendix E. Also Appendix E presents the daily energy yield outputs recorded by the MPPT charge controller off-shore and the cumulative energy yield together with the daily energy yield.

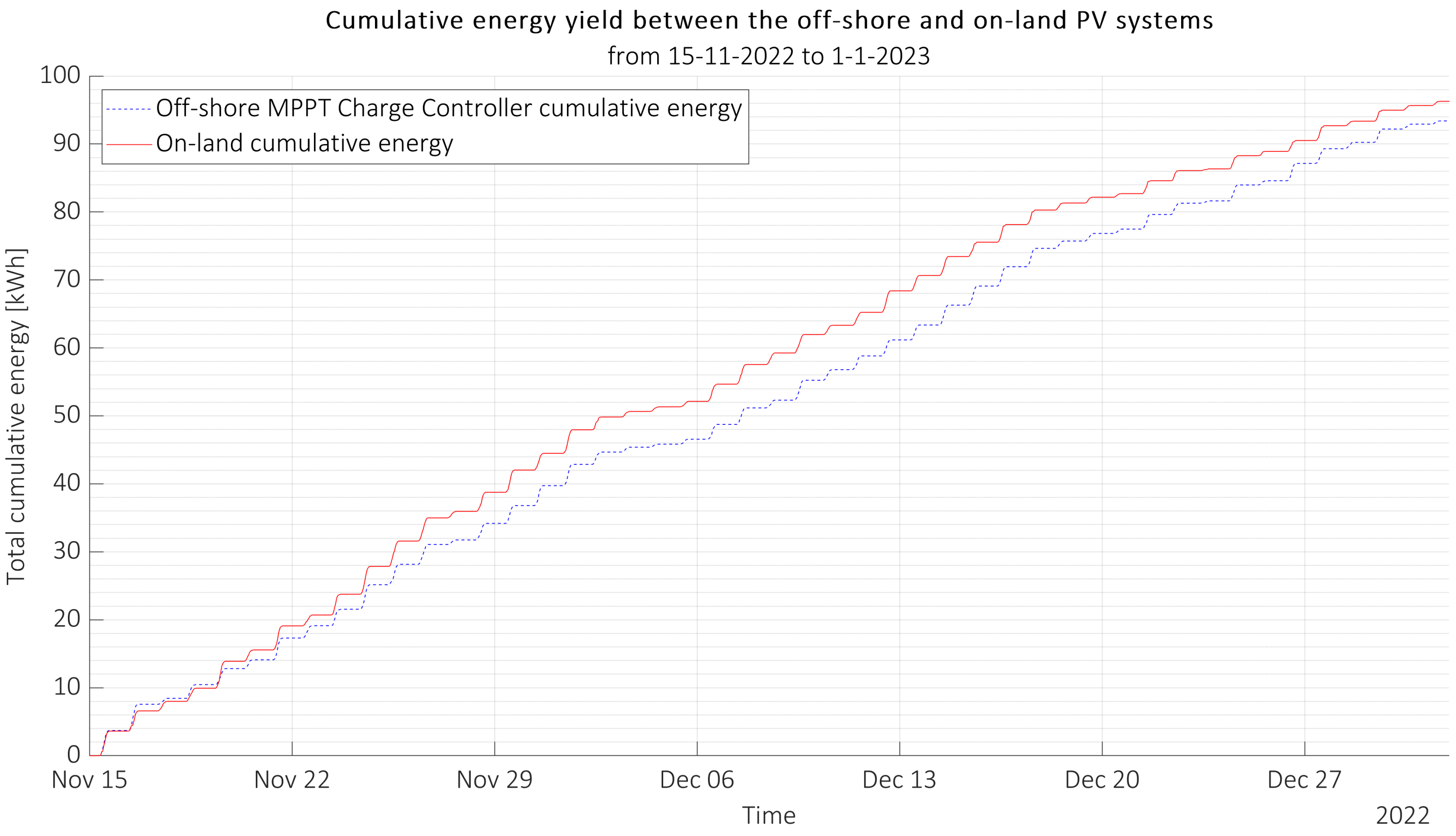

Figure 5.17: Cumulative DC energy outputs off-shore (blue) and on-land (red), from 15-11-20222 to 28-11-2022.

5.2.8. Balance of Systems (BoS) performance

The BoS performance of this section focuses on performance in off-shore conditions, as the systems where upgraded and designed to withstand the North Sea environment during winter. The BoS on-land performed correctly with no issues recorded.

Firstly, the result highlighting the off-shore system survivable rate, which withstood up to 3.4 meter waves in the North-Sea is acknowledged. Moreover, the MPPT charge controller, sized for up to 450V from the two strings and 100A, performed correctly and survived the period of research from 15-11-2022 to 1-1-2023. The data box and batteries also performed correctly and survived the winter off-shore conditions it was designed for. It is important to note the placement of the MPPT charge controller horizontally and the absence of air flow did not cause any issues to the systems. Temperatures recorded within the power box are presented in Appendix F, with temperatures ranging from 0^oC to 40^oC at maximum. Additionally, all power cable connections survived off-shore and glancing systems functioned as designed on the protection boxes for IP67 and IP68 conditions, 3D printed mounts for power meters also performed correctly, as well as all additional components, such as data loggers, RTD100 converters, DC-DC converters, resistors and inclinometer, among others. It is important to note four thermal sensors did provide data errors, most failures occurred during installation or re-connection procedures. Two of these thermal sensors provided issues due to external influences from irradiance or floater material. The complete sensors operational status is presented in Appendix E.

Furthermore, during the research period, the MPPT charge controller operated at bulk charging mode during day-time, from sun-rise to sun-set, meaning that, according to the manufacturer, the controller delivers as much charge current as possible to rapidly recharge the batteries. This allowed to receive the maximum power from the PV side at all times. Additionally, it means that the resistors managed to burn the excess energy when the batteries reached the maximum voltage level indicated by the battery relay, which operated correctly and dissipated all excess power. All results concerning battery voltage and current levels, as well as power input and power output from the MPPT charge controller are also in Appendix F. The behaviour of the four 12 V batteries connected in series during the period of research is presented in Figure 5.18. Additionally a 3 day amplification is also presented in Appendix F, on Figure F.4.

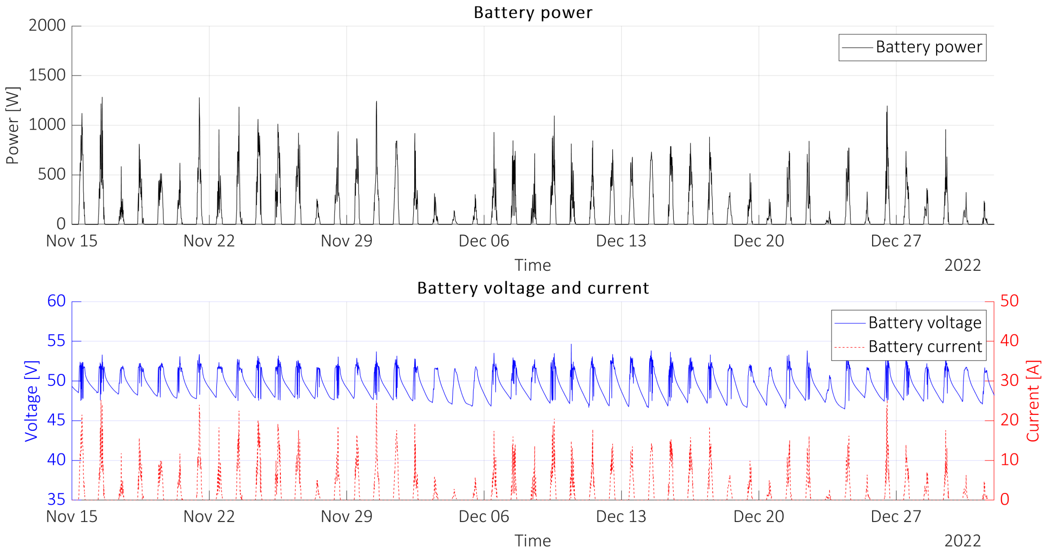

Figure 5.18: Victron MPPT 450-100 Output: Battery power, current and voltage during the period of research.

5.2.9. Power performance summary

The power measurements were presented and discussed in this section. From the DC power outputs presented in Figure 5.2 the maximum power outputs were identified. Through the use of linear regression fits, the power outputs for the North-West string were observed to be higher off-shore than on-land for the North-West string, however this values on the South-East string were found to be higher off-shore and this was further investigated together with the irradiance at the Plane of Array. Additionally from the power outputs during the start and end times of the day, it was observed that the off-shore system had a more favourable orientation towards South than what was predetermined by the set azimuth of 150 ^{o} from North. The average voltage off-shore was found to be lower than on-land by 6.2 V and 4.2 V for the South-East and North-West strings respectively and was suspected to be due to a higher temperature experienced by the modules off-shore. This was then verified in Section 5.3. Current values for the South-East string were found to be, from the average, 0.462 A higher off-shore than on-land, while the averaged North-West string output only measured a difference of 0.08 A. This large difference in current was then checked by using the irradiance at the POA for each string. From the linear regression plots it was observed that the on-land system suffered higher and similar irradiance levels for both strings. Therefore, when looking at the power and irradiance together, and when comparing the predicted efficiencies with the efficiencies measured from the power meters, it was observed that the power meter for the off-shore South-East string had power measurements which were 150 W higher than the measurements on-land. From here it was then suspected that in addition to the data outage suffered by the South-East power meter off-shore, the Hall effect sensor had become de-attached and thus possibly gave misreadings.

After taking into account these findings the performance ratios were calculated and presented in Table 5.6. Capacity factors were also calculated per string and the energy produced by each system on the DC side was presented.

Finally, the behaviour of the MPPT charge controller connected to the battery were presented and discussed, showing the stability of the voltage levels when using the batteries together with the dissipation unit consisting of resistors. Also the MPPT charge controller charging mode and battery behaviour shows the PV system designed for off-shore conditions survived and performed as expected under the North Sea winter conditions thanks to the systems protected with IP67 and IP68 ratings.

5.3. Temperature measurements

Temperature measurements are discussed as temperature influences power performance, as presented in Chapter 2. As described in Section 3; up to 10 PT100 temperature sensors were installed on PV modules of each system. Additionally, the off-shore system also had a water temperature sensor and two ambient temperature sensors. All temperature sensors used are presented in Appendix E, on Table E.1. The off-shore protection power box additionally had a thermal sensor. On-land one ambient temperature sensor was present and the data box temperature was also monitored. These sensors allowed to present ambient temperatures recorded at each location during the period of research. Ambient temperatures were compared with climate data at the location obtained through the PV computer program 'Meteonorm'. Specific temperatures concerning water, module and ambient temperatures were also studied. This was followed by the results obtained for the gradient temperatures recorded in a module at each location, with the use of 5 thermal sensors. String and floater temperatures were also determined to showcase the thermal behaviour throughout a floater. Finally, OFPV empirical models were derived from measurements in order to determine module temperatures. Module temperatures obtained were then also compared with FPV module temperature models found in literature, which allowed to observe and determine the accuracy of these FPV models compared to the OFPV thermal models derived.

5.3.1. Ambient temperature measurements and comparison with climate data

Ambient temperatures measured both off-shore and on-land are discussed in this section and compared with climate data for the period of research from 15-11-2022 to 1-1-2023.

Firstly, annual ambient temperatures from climate data for each location are presented in Figure 5.19. A box-plot is also provided.

Secondly, a zoom into the climate data for the period of research from is provided to determine if the ambient temperatures recorded were in the same range and identify differences and similarities with real ambient temperature measurements. This is shown in Figure 5.20, which also provides a box-plot. From here it was found that the average climate temperature off-shore when compared to on-land, during the period of research, was 1.8 ^oC higher.

Thirdly, ambient temperatures recorded during the period of research from 15-11-2022 to 1-1-2023 are presented for comparison with the climate data. These temperatures were compared with climate data at each location obtained from Meteonorm 7.2. The reason was to see the differences in average temperature, maximum and minimums, and to verify if such climate data could be used for future OFPV thermal models, initially for the same period of research. This is shown in Figure 5.21.

When comparing measured ambient temperatures during the period of research, it was found that off-shore temperatures were 2.8 ^oC higher than on-land, following the same pattern for both predicted data and measured data. Additionally, it was found that the average climate temperatures difference between off-shore and on-land was of 1.8 ^oC. Furthermore, for the on-land location, larger extremes were found. From these findings, prediction of temperatures off-shore performed by Meteonorm could be considered in the future for OFPV simulations: a difference of 0.9 ^oC was found between what was predicted by Meteonorm and what was measured off-shore. This finding should be further studied to obtain annual conclusions. The box-plot results obtained for ambient temperatures are summarized in Table 5.7.

Measurement	Median	25 %	75 %	Max	Min	Average
Annual climate temperature off-shore	10.9	6.7	15.3	30.5	-5.4	11.0
Annual climate temperature on-land	10.5	5.6	15.5	30.6	-7.6	10.6
Seasonal climate temperature off-shore	6.4	3.3	8.7	14.9	-4.4	6.0
Seasonal climate temperature on-land	4.3	1.8	6.8	14.5	-5.9	4.2
Measured ambient temperature off-shore	7.7	4.5	9.1	13.6	-2.6	6.9
Measured ambient temperature on-land	5.2	1.0	8.3	15.8	-15.3	4.1

Table 5.7: Ambient temperatures found with Meteonorm and with empirical measurements at the two locations.

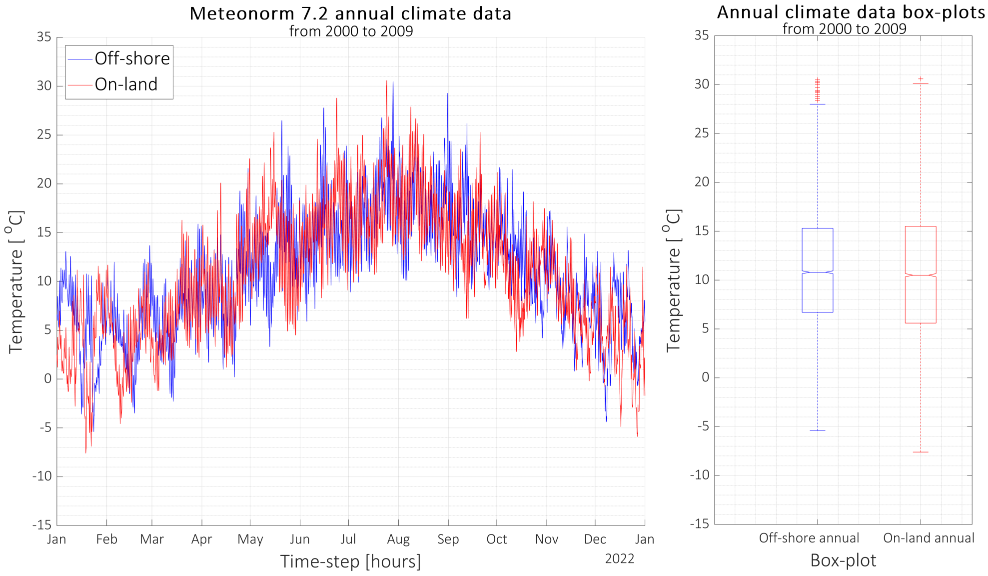

Figure 5.19: Meteonorm 7.2 annual temperatures for the on-land (red) and off-shore (blue) locations.

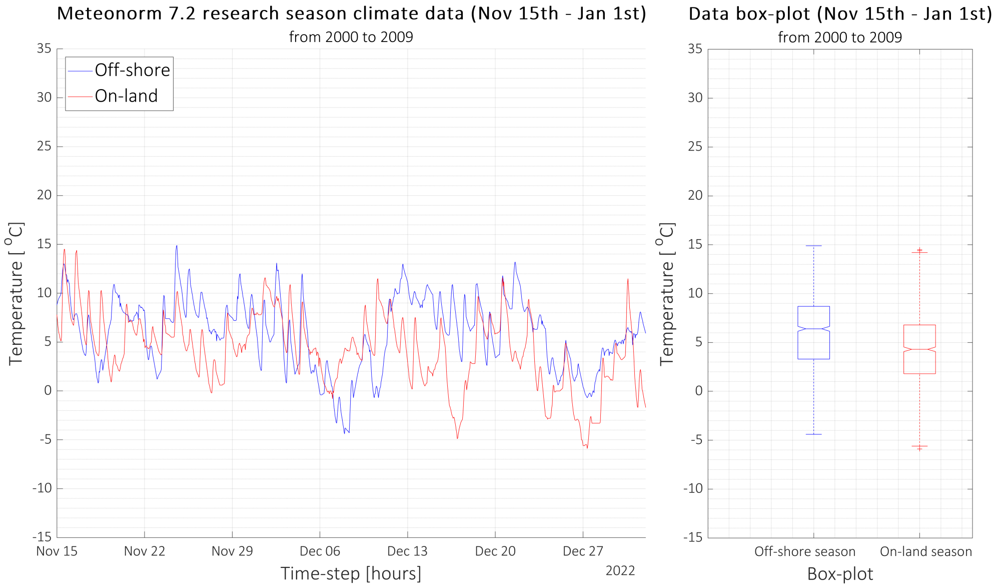

Figure 5.20: Meteonorm 7.2 seasonal temperatures for the on-land (red) and off-shore (blue) locations, from 15-11-2022 to 1-1-2023.

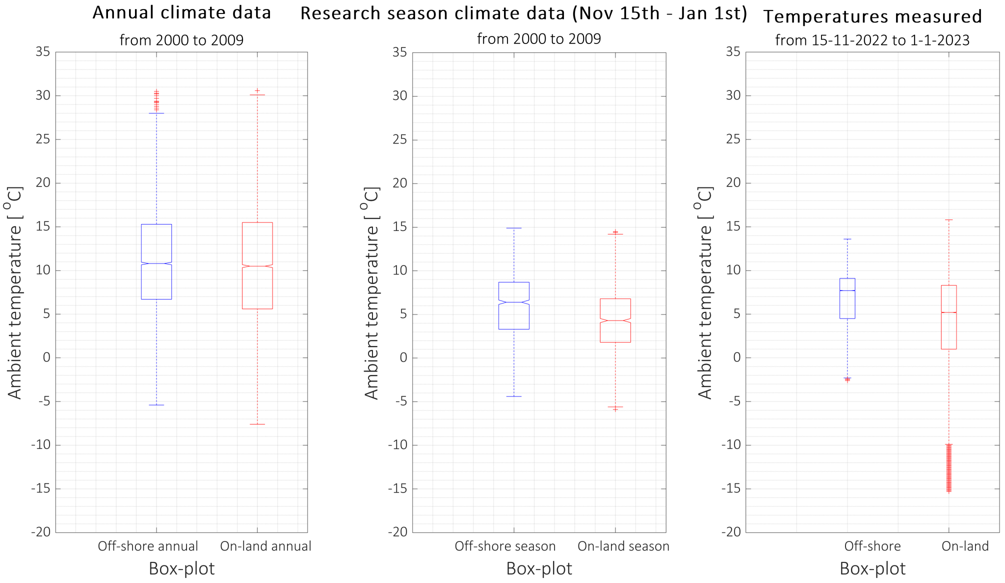

Figure 5.21: Ambient temperature box-plot comparison for the off-shore and on-land locations from annual, seasonal and real data for the period of research between 15-11-2022 and 1-1-2023.

5.3.2. Module temperatures off-shore against on-land

Module temperatures recorded on-land and off-shore are presented in Figure 5.22, additionally box-plots are provided on the same figure. The averaged module temperature found off-shore and on-land during the period of research was 18.2 ^oC and 6.9 ^oC respectively. Off-shore module temperatures did not experience high temperature changes when compared to the on-land PV modules, where a higher temperature cycling was detected. When looking at this data alone, this lower change in module temperatures off-shore could lead to lower thermomechanical stresses and to failures of the PV module (Kawai et al., 2017).

To additionally see the influence of temperatures in the surroundings, focusing on ambient and water temperatures, Figure 5.23 was also provided as it included ambient temperatures on-land and off-shore. Furthermore water temperatures were included within this figure: water temperature measurements off-shore on-site gave data errors and thus the KNMI weather station HKZA, located 2 km away off-shore, was used for providing the sea water temperature measurements. HKZA weather station location information is provided in Appendix E.2.

Additionally Appendix E.9 provides 2 weeks of module temperature measurements, from 11-10-2022 to 27-10-2022, for the off-shore system before deployment to show module thermal variability prior to the experiment off-shore; the off-shore system was standing on-land and showed that variations of more than 10 ^oC were recorded by the PT100 sensors. This 'test experiment' was provided to show large thermal variations were recorded before deployment in contrast to the low thermal variations recorded off-shore.

From these measurements presented, it was concluded module temperatures off-shore were found higher for this period than on-land: the average module temperature off-shore was 11.3 ^{o} higher than for the PV modules on-land. With respect to water temperature, the effect that the water had on the module temperatures was observed to act as a 'heat sink; in winter, the ambient temperature off-shore was lower (in most cases) than the water temperature, thus the water did not cool the system through heat transfer, but rather heat it up. However, from this large 'heat sink', the ocean in this case, it was observed that off-shore module temperatures had less variations than on-land, where minimums reached up to -15 ^oC. The water and wind effects on module temperature are further investigated in Section 5.4.

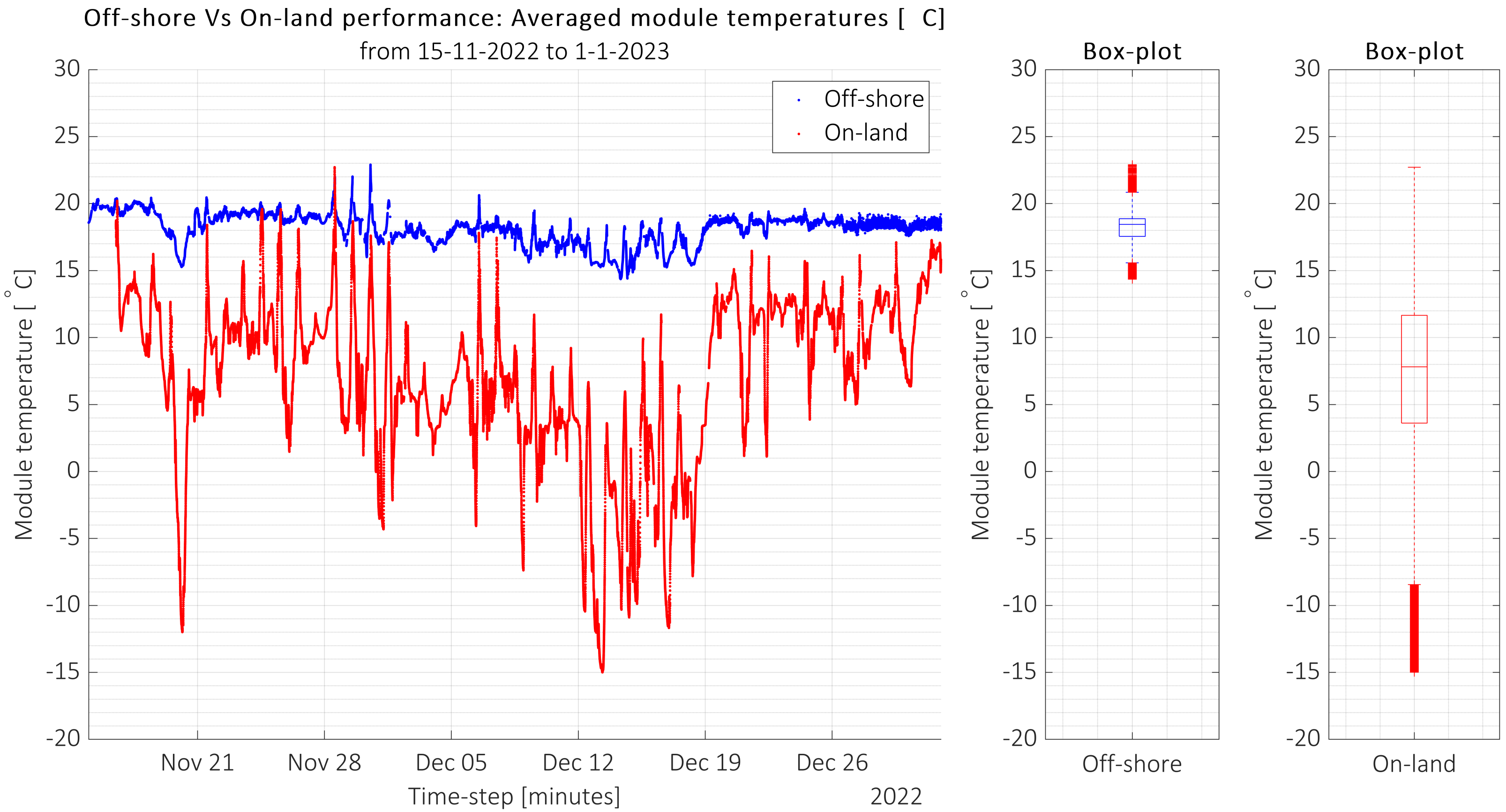

Figure 5.22: Average module temperatures on-land and off-shore recorded from 15-11-2022 to 1-1-2023, including box-plots.

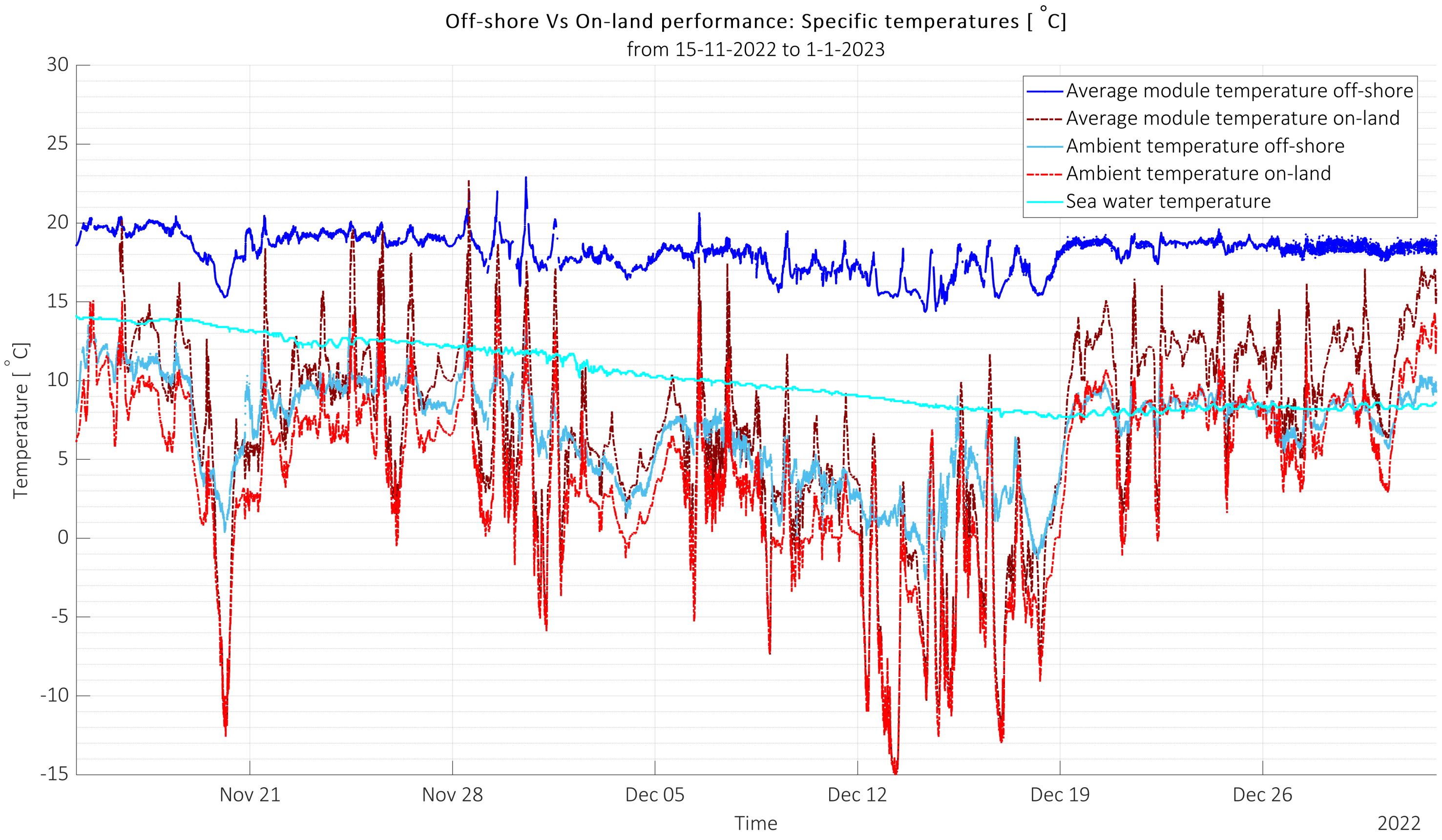

Figure 5.23: Specific temperatures concerning average module temperatures, ambient temperatures and water temperatures on-land and off-shore recorded from 15-11-2022 to 1-1-2023.

5.3.3. Module temperatures influence by G_{POA}

A comparison between module temperatures and irradiance was performed for the period 15-11-2023 until 1-1-2023 to further understand the influence of irradiance on the OFPV module temperatures recorded. For this comparison, the module temperatures measured off-shore were averaged per string orientation and were plotted against irradiance on the plane of array (G_{POA}) measurements at each location. G_{POA} measurements were available off-shore for both South-East and North-West module orientations through the use of reference cells. The same was done for the on-land system, with the averaged module temperatures recorded on-land for each PV string orientation against the G_{POA} from the reference cells on-land.

Figure 5.24 presents the on-land correlation between the South-East string module temperatures and the G_{POA} recorded by the South-East reference cell, showing a positive trend. Figure 5.25 presents the North-West string outputs for the on-land system. Linear regression fits are provided for these trends for comparison with the off-shore measurements.

When comparing these trends with the off-shore system, it was found that for both South-East and North-West strings off-shore, shown in Figure 5.26 and Figure 5.27 respectively, the positive trend recorded off-shore had a lower slope than on land, suggesting irradiance on the plane of array had a lower effect on the increase of module temperatures off-shore. It is observed that due to additional environmental effects off-shore the system off-shore experienced a lower influence from the G_{POA} to increase module temperatures: this is suspected to be due to the stronger influence the water had on the PV system off-shore. It is important to highlight the observation is made with data from the period of research and should be extended to obtain annual conclusions. Nevertheless, in Section 5.4, the off-shore environmental effects are further studied, concerning water, wind and wave influences on the PV system behaviour.

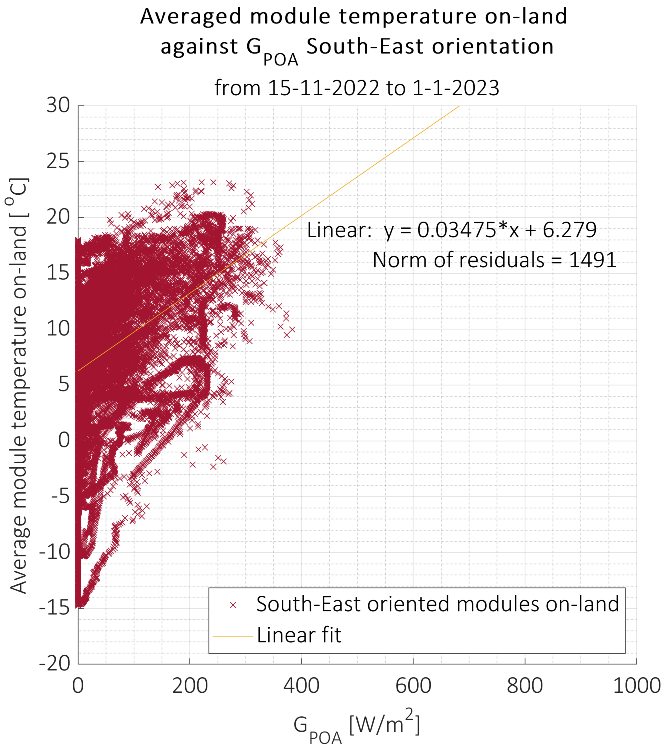

Figure 5.24: Averaged module temperature against G_{POA} for the on-land system South-East oriented modules.

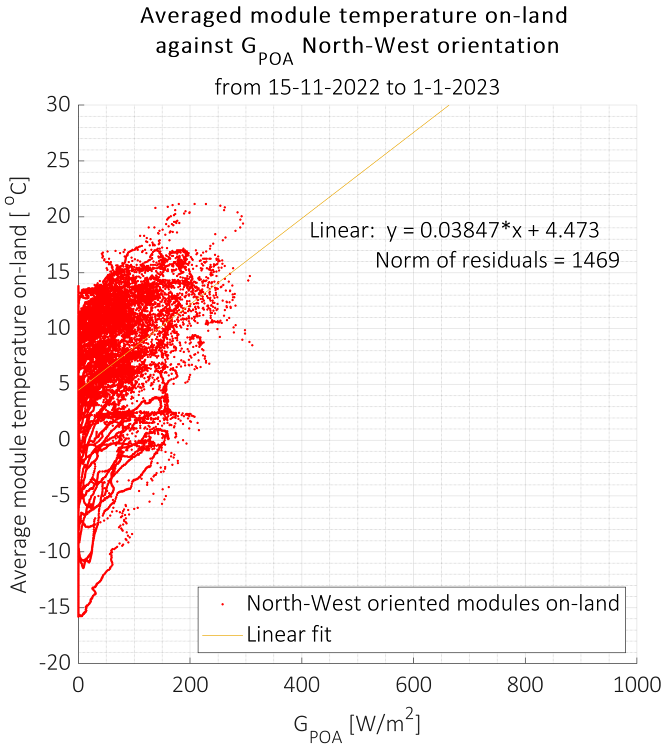

Figure 5.25: Averaged module temperature against G_{POA} for the on-land system North-West oriented modules.

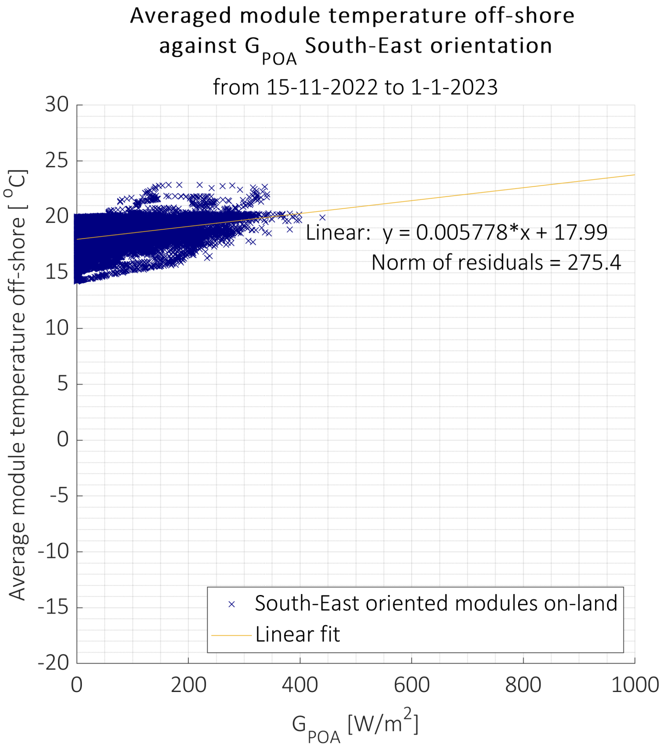

Figure 5.26: Averaged module temperature against G_{POA} for the on-land system South-East oriented modules.

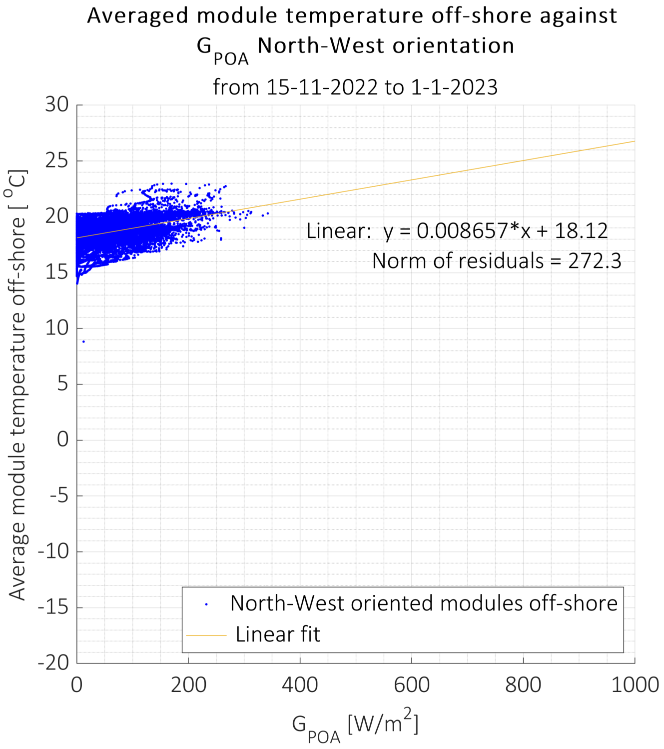

Figure 5.27: Averaged module temperature against G_{POA} for the off-shore system North-West oriented modules.

5.3.4. Module temperatures influence by ambient temperatures

The influence of ambient temperatures on the module temperatures recorded was studied and presented in Figure 5.28 and Figure 5.29.

It was observed that for the period of research, the ambient temperature on-land had a greater influence to increase module temperature than off-shore. Moreover, a 3D plot relating ambient temperature, GHI and module temperature was provided in Appendix E in Figure E.11 and Figure E.12, for the on-land and off-shore systems respectively.

Additionally Figure 5.30 is presented to show the correlation between ambient, water and module temperatures off-shore. During this time period a positive trend is observed between ambient and water temperatures. Furthermore, the lowest module temperatures were recorded at low water and ambient temperatures, while the highest module temperatures were recorded at high ambient and water temperatures. This remains an observation that should further be studied during a longer experimental period, ideally of a year.

The influence of water temperature and wind speed off-shore is thus suspected to have a dominant influence on module temperature off-shore. This study was performed within Section 5.4 to provide an observation of the parameters influencing module temperature, which in turn will affect the final power performance. The effects of wind, wave and sea water are presented under the environmental effects, in Section 5.4.

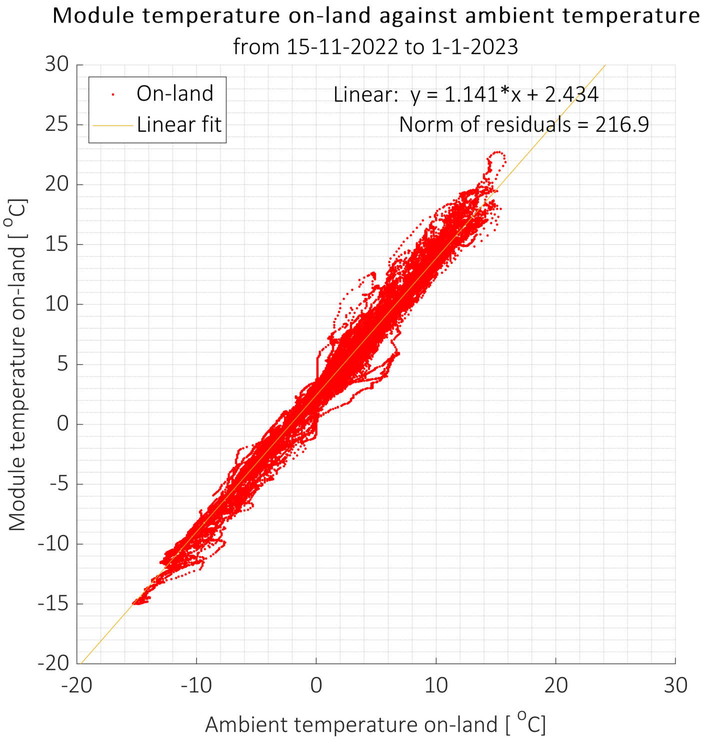

Figure 5.28: Averaged module temperature against ambient temperature on the on-land system, from 15-11-2022 to 1-1-2022

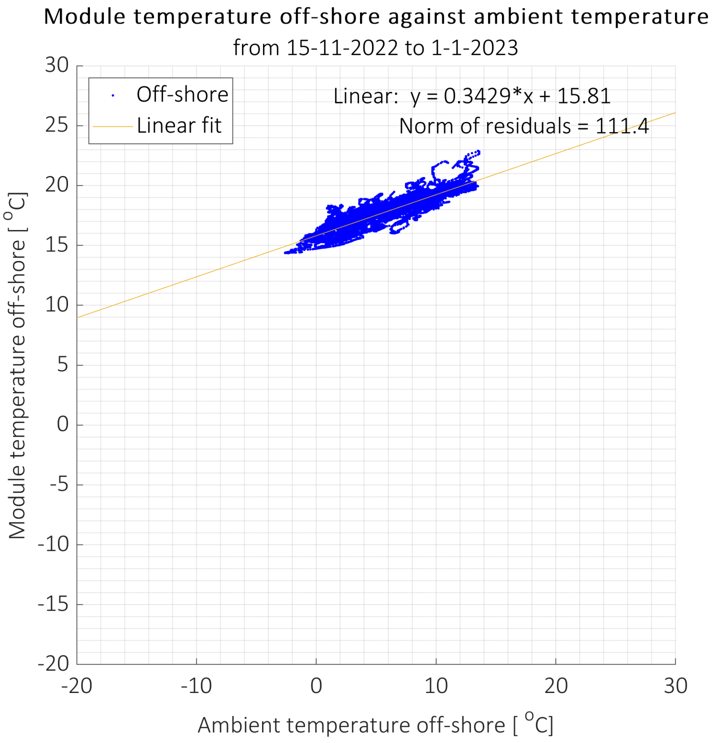

Figure 5.29: Averaged module temperature against ambient temperature on the off-shore system, from 15-11-2022 to 1-1-2022

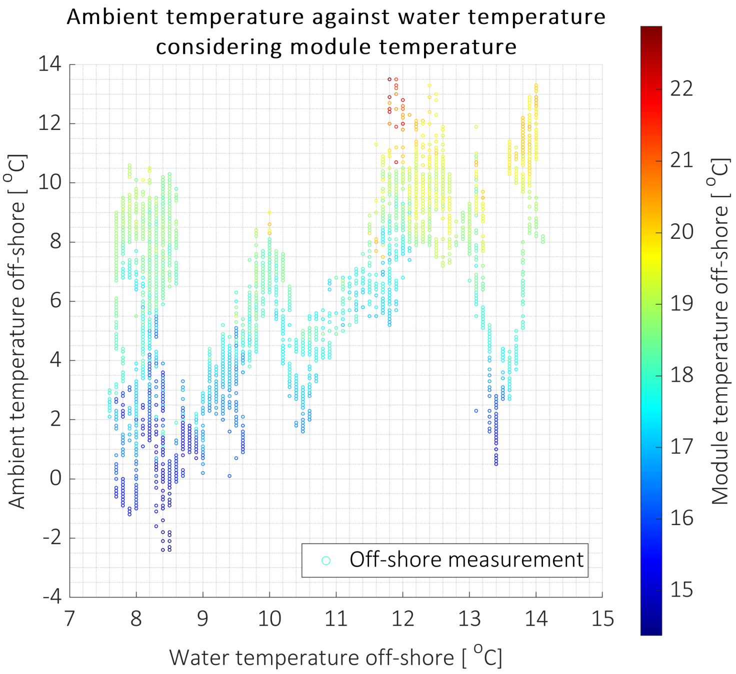

Figure 5.30: Averaged module temperature off-shore with respect to ambient and water temperatures recorded, from 15-11-2022 to 1-1-2023.

5.3.5. Module gradient temperatures

To understand the thermal behaviour within one module off-shore, and to also investigate the appearance of hot-spots, one module off-shore and also one module on-land were equipped with 5 thermal sensors; in the corners and in the middle. The location and selection of this positions was explained in Chapter 3. These results aim to provide thermal observations as a gradient on a module and if long-term (one month) environmental effects off-shore such as salt or algae deposition could be seen through the appearance of hot-spots on this locations at the end of the experiment period.

The mean temperature on the first month of the experimental period (November), on a sunny day between 08:00 and 18:00, was recorded as this served as a basis to see if in the long term, environmental effects could change these temperature measurements, likely causing them to rise in the corners, which at the time was a hypothesis expecting algae and salt deposition in this locations due to sea water splashing.

Two plots are provided, one on 24th November 2022 and one a month later, on 26th December 2022. These days were selected for further study having similar irradiance (GHI) patterns and wave height levels (meters), with one month difference in between. It is important to highlight that on the off-shore system, the bottom left cell and the middle cell equipped with a PT100 sensor did not work correctly: For the middle sensor measurement it was assumed the measurement in the middle of the module on module number 9 (location described in Section 3, in the same orientation and POA as module number 7, could be used for comparison. The results presented in Figure 5.31 show slightly higher temperatures off-shore and with similar values throughout the module. On-land the middle temperature was slightly higher. Figure 5.32 shows a similar behaviour after a month, with the thermal sensor on the top left of the module showing more disperse results. It is suspected these sensors may have become de-attached from the module. This remains an observation that could not be verified on-site. The on-land system after one month showed a similar behaviour for all sensors, with the middle thermal sensor showing slightly higher values than the rest of the sensors on the module.

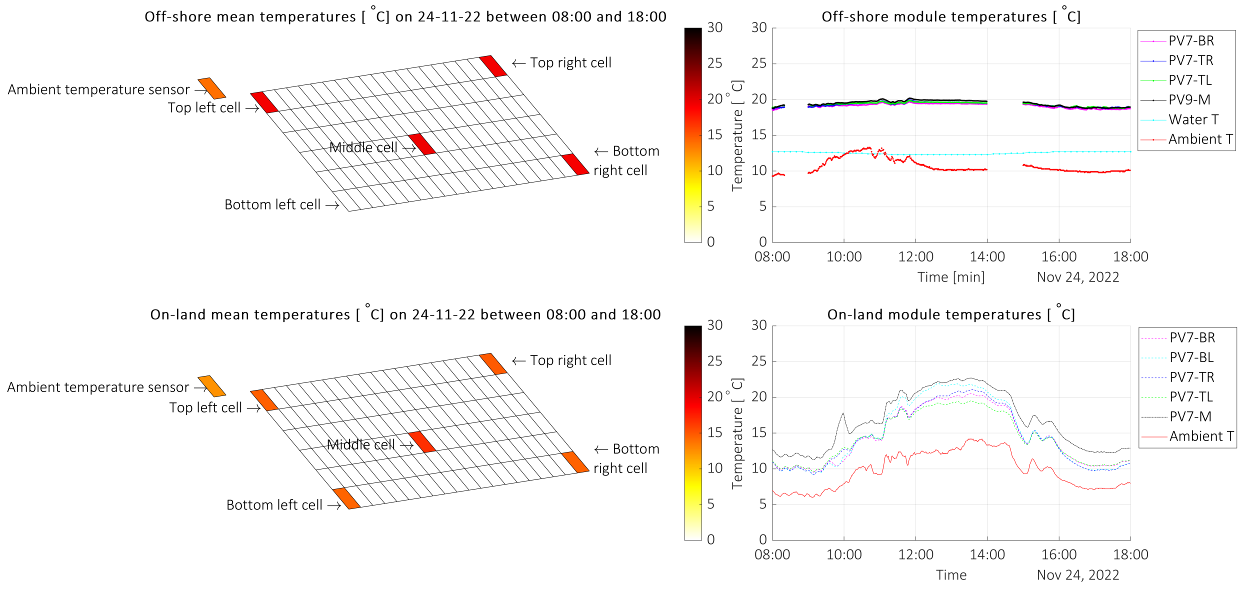

Figure 5.31: Module gradient temperatures on-land vs offshore on 24-11-2022, from 08:00 to 18:00

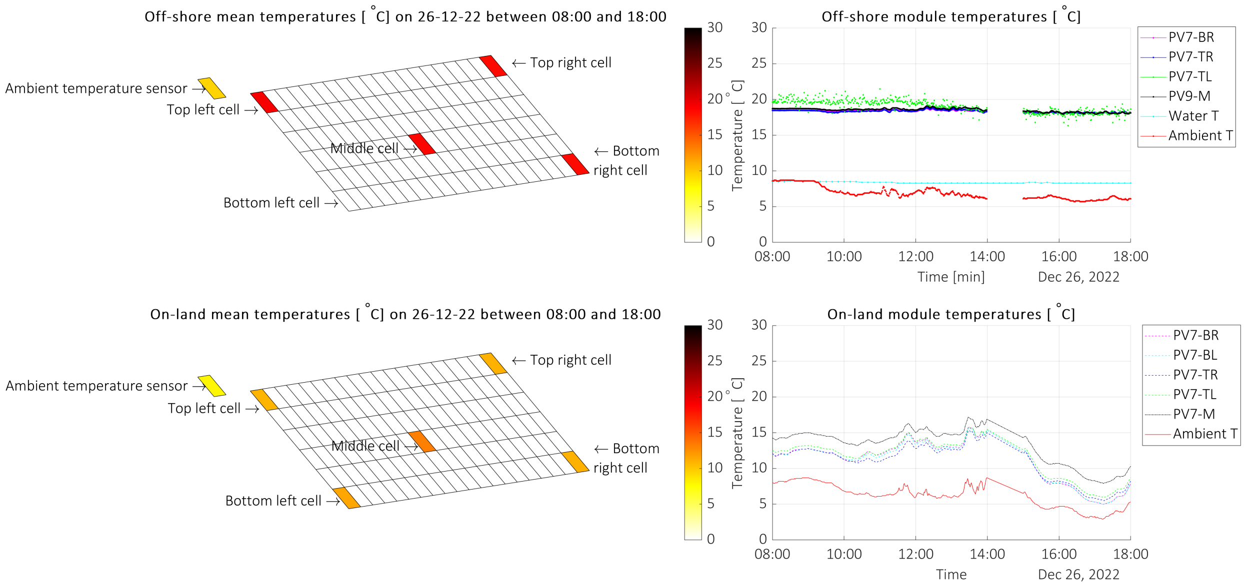

Figure 5.32: Module gradient temperatures on-land vs offshore on 26-12-2022, from 08:00 to 18:00

5.3.6. Floater gradient temperatures

Floater temperatures were studied to identify if there was a difference in temperature within the PV arrays during times of power production with respect to on-land and if these measurements results derived in different results in the long term during the experiment (one month). A comparison was made to see if any differences appeared within one month. Two days with similar levels of irradiance (GHI) where selected for comparison: 24-11-2022 and 26-12-2022.

For clarity of the plots discussed in this section, Figure 5.33 presents the schematic used to show the module temperatures throughout the floaters on-land and off-shore. Numbers 1 to 12 correspond to the PV module number, discussed previously in Section 3. Letters and number in red are provided to indicate that a thermal measurement and/or sensor was available (number for PV module, letters A for ambient temperature and W for water temperature). If in the final plots no color (white) shows at these locations, it indicates that data was not available at this location or there was a malfunction of the thermal sensor. Additionally Appendix E.1 provides the functioning status of the sensors during the experiment.

Figure 5.34 presents the schematic of temperatures measured throughout a floater on 24-11-2022 between 08:00 and 18:00, both off-shore (top) and on-land (bottom). Additionally, the average water and ambient temperature between 08:00 and 18:00 is provided. Figure 5.35 presents the same schematic of temperatures measured throughout a floater on 26-12-2022 between 08:00 and 18:00

Module temperatures seen throughout the off-shore system during radiation from 08:00 to 18:00 showed little difference throughout the floater. The on-land PV modules did show a larger difference is temperatures. This is suspected to be due to sea water and the 'heat sink' effect acting on the complete floater. These results suggests that the complete floater suffers a very similar thermal behaviour throughout the PV modules and thus, for future research, a lower amount of PT100 sensors may be used in one floater as it can be assumed the same module temperature will be expected throughout the modules in one floater. On-land, the sensors with lower measurements may indicate the PT100 sensor attachment to the module could be loose. Dismantling of modules was not possible during the period of research to verify this observation.

Furthermore, when comparing differences within one month, results did not show large differences between module temperatures of the same and thus it is suspected no permanent bio-fouling occurred at a specific location, such as the corners, where more water splashing was expected.

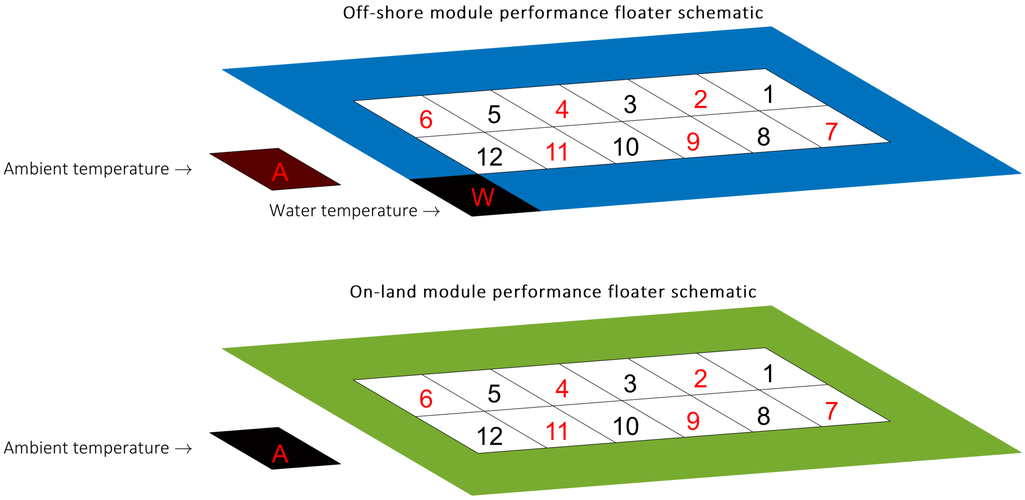

Figure 5.33: Floater schematic explanation with numbers corresponding to PV module location and red color indicating PT100 thermal sensor is present at the location.

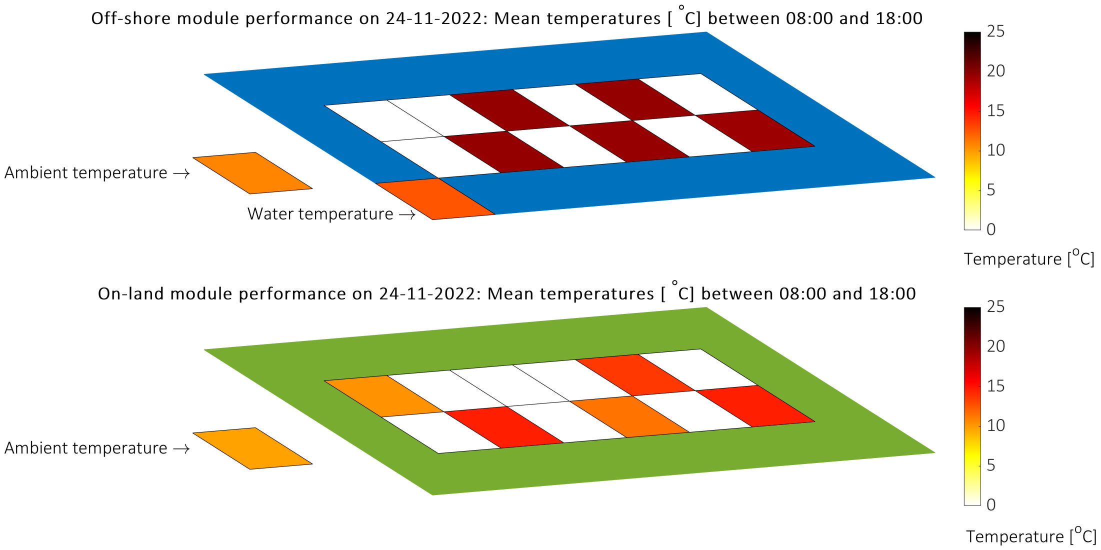

Figure 5.34: Floater gradient averaged module temperatures off-shore (top) and on-land (bottom) on 24-11-2022, using data from 08:00 to 18:00.

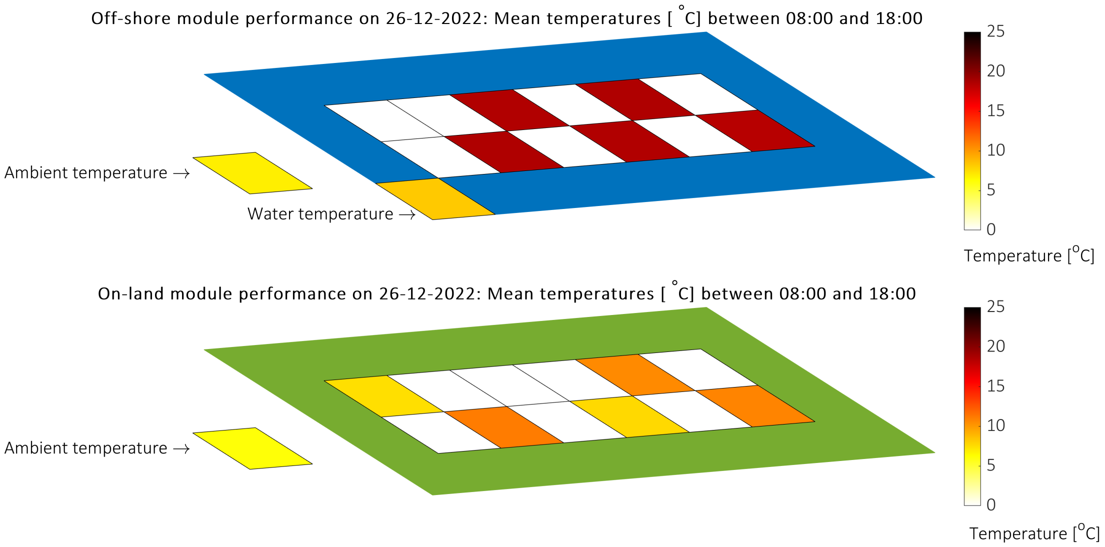

Figure 5.35: Floater gradient averaged module temperatures off-shore (top) and on-land (bottom) on 26-12-2022, using data from 08:00 to 18:00.

5.3.7. OFPV thermal models derived for off-shore conditions

To answer how FPV thermal models predicting PV module temperatures from literature compare to models derived from real measurements off-shore, four linear regression models are presented, which may determine the PV module temperature off-shore from environmental measurements. Note these models are developed from the time period 15-11-2022 to 1-1-2023 and thus, additional annual measurements would be required to provide an annual linear regression model.

The models were derived using 'Matlab2021b' linear regression modelling tool $fitlm$. An X matrix containing the measurements concerning ambient temperature, irradiance on the plane of array, wind speed, water temperature and wave height, was correlated with a Y matrix containing the actual module temperatures measured with the same time-steps. The command "film(X,Y,'RobustOpts','on')" was used to obtain the linear regression models for OFPV module temperatures. The root mean squared error (RMSE) and mean absolute error (MAE) when comparing the module temperature predicted against the actual module temperatures is also provided. The model with the lowest RMSE and MAE recommended for future use and study is OFPV model 1, as it gave the lowest RMSE and MAE values of the four models presented. This model is recommended to be revised with annual measurements to yield an annual model.

T_a stands for ambient temperature [^oC], G_M for irradiance on the modules plane of array [W/m^2], W_v for wind speed in [m/s], T_W for water temperature [^oC], w_h for wave height in [m]:

OFPV model 1 derived (considering T_a, G_M, W_v, T_W and w_h):

$$T_{m,OFPV,1} = 15.298 + 0.29923 * T_a + 0.0025804 * G_M + 0.01825 * W_v + 0.033178 * T_W + 0.19554 * w_h \tag{5.2}$$

$RMSE = 0.360 \quad MAE = 0.2968$

OFPV model 2 derived (considering T_a, G_M and W_v):

$$T_{m,OFPV,2} = 15.62 + 0.31353 * T_a + 0.0027643 * G_M + 0.035544 * W_v \tag{5.3}$$

$RMSE = 0.382 \quad MAE = 0.3081$

OFPV model 3 derived (considering T_a, G_M, W_v and T_W):

$$T_{m,OFPV,3} = 15.376 + 0.30305 * T_a + 0.002723 * G_M + 0.038365 * W_v + 0.028356 * T_W \tag{5.4}$$

$RMSE = 0.375 \quad MAE = 0.3027$

OFPV model 4 derived (considering T_a, G_M, W_v and w_h):

$$T_{m,OFPV,4} = 15.583 + 0.31225 * T_a + 0.002621 * G_M + 0.017038 * W_v + 0.17706 * w_h \tag{5.5}$$

$RMSE = 0.369 \quad MAE = 0.3036$

Also note irradiance at the POA of the South-East orientation was used for this derivation and average module temperature of the complete floater was used (both PV strings), having found that the module temperatures throughout both strings remained the same.

To visualize the OFPV linear regression model 1 temperature predictions against real PV module temperature measurements recorded off-shore, Figure 5.36 is presented. Additionally, Figure 5.37 presents the 4 OFPV linear regression models against the Duffie-Beckman model (Smets et al., 2016), Kamuyu's models (2 models) (Kamuyu et al., 2018) and Hayibo's model adapted from Kamuyu et al., 2018 (Hayibo, 2021).

Appendix E.12 also provides all 4 OFPV linear regression models for the complete period of research as well as a close up for one week from 21-11-2022 to 28-11-2022. Additionally a close up of the linear regression fit for OFPV model 1, is provided in the Appendix E.12.

OFPV thermal models comparison with FPV models from literature

The 4 OFPV models were compared with FPV models from literature. Also regression fits were studied with Matlab2021b and the multiple linear regression command:

$$[b, bint, r, rint, stats] = regress(Calculated_{Temperature}, Measured_{Temperature}) \tag{5.6}$$

Furthermore, these 4 OFPV models were compared with results obtained from the Duffie-Beckman model (Smets et al., 2016), Kamuyu's models (2) (Hayibo, 2021) and Hayibo's model adapted from Kamuyu et al., 2018 (Hayibo, 2021), providing the same inputs concerning ambient temperature, irradiance, wind speed and water temperatures. The outputs are presented in Figure 5.38, which provide the linear regression fits, a linear fit and the R^2 value for each model. Additionally the mean absolute error found when comparing the predictions with module temperatures recorded off-shore are presented under each model equation used.

Duffie Beckman's 2006 model (Smets et al., 2016) was used as reference to compare an empirical PV cell temperature model used on on-land systems. The model used was used as:

$$T_c = T_a + \frac{T_{NOCT} - 20^o}{800} G_M (\frac{9.5}{5.7 + 3.8 * w_s})(1 - \frac{\eta_m}{T * \alpha}) \tag{5.7}$$

With respect to temperature measurements of the OFPV system: $MAE = 10.9521$

With T_c as PV cell temperature [^oC], T_a as ambient temperature [^oC], $G_M$as irradiance on module [W/m^2], w_s as wind speed [m/s], η_m as module efficiency at STC [%], T_{NOCT} as NOCT temperature [^oC], assumed at 45^oC and adding $+18^oC$ for a direct mount of the PV modules on the floater (Smets et al., 2016). Also with G_{NOCT} as $800W/m^2$. The transmittance and absorptivity term $T * \alpha$ was assumed as 0.9 (Smets et al., 2016).

The FPV models used for comparison concerned 3 models, with T_a as ambient temperature [^oC], G_T as irradiance on module [W/m^2], V_w as wind speed [m/s] and T_w as water temperature [^oC].

Kamuyu's 2018 models (Kamuyu et al., 2018) used for comparison were:

$$T_{Kamuyu,FPV1,m} = 2.0458 + 0.9458T_a + 0.0215G_T - 1.2376V_w \tag{5.8}$$

With respect to temperature measurements of the OFPV system: $MAE = 20.4460$

$$T_{Kamuyu,FPV2,m} = 1.8081 + 0.9282T_a + 0.021G_T - 1.2210V_w + 0.0246T_w \tag{5.9}$$

With respect to temperature measurements of the OFPV system: $MAE = 20.4092$

Hayibo's 2021 model (Hayibo, 2021) was used as:

$$T_{Hayibo,FPV,m} = -13.2554 + 1.2645T_a + 0.0128G_T - 0.0875T_w \tag{5.10}$$

With respect to temperature measurements of the OFPV system: $MAE = 34.506$

From results presented in Figure 5.38, the 4 OFPV models derived have a linear relation with R^2 ranging from 0.8769 as the maximum (OFPV model 1) to 0.8719 as the minimum (OFPV model 2). Depending on the environmental variables available, one may used on of the 4 models provided for the period of this research.

Furthermore, when comparing to models from literature, Duffie-Beckman's model follows a linear regression with R^2 equal to 0.8539. Additionally, the other 3 FPV models do not follow a linear regression when compared to the module temperatures measured off-shore, with R^2 between 0.0186 and 0.0712 depending on the model. It is observed that for this period of research, these FPV models are not considered accurate to estimate the module temperatures, having a MAE of 10.95, 20.45, 20.41 and 34.51 for the Duffie-Beckman model, Kamuyu models 1 and 2, Hayibo's model respectively.

From these results it is observed that empirical FPV models to determine PV module temperatures are set to be site and design specific. Within this experiment, the 4 OFPV models derived provide a better estimation of the measured module temperatures off-shore for the period of research than the FPV empirical models selected from literature.

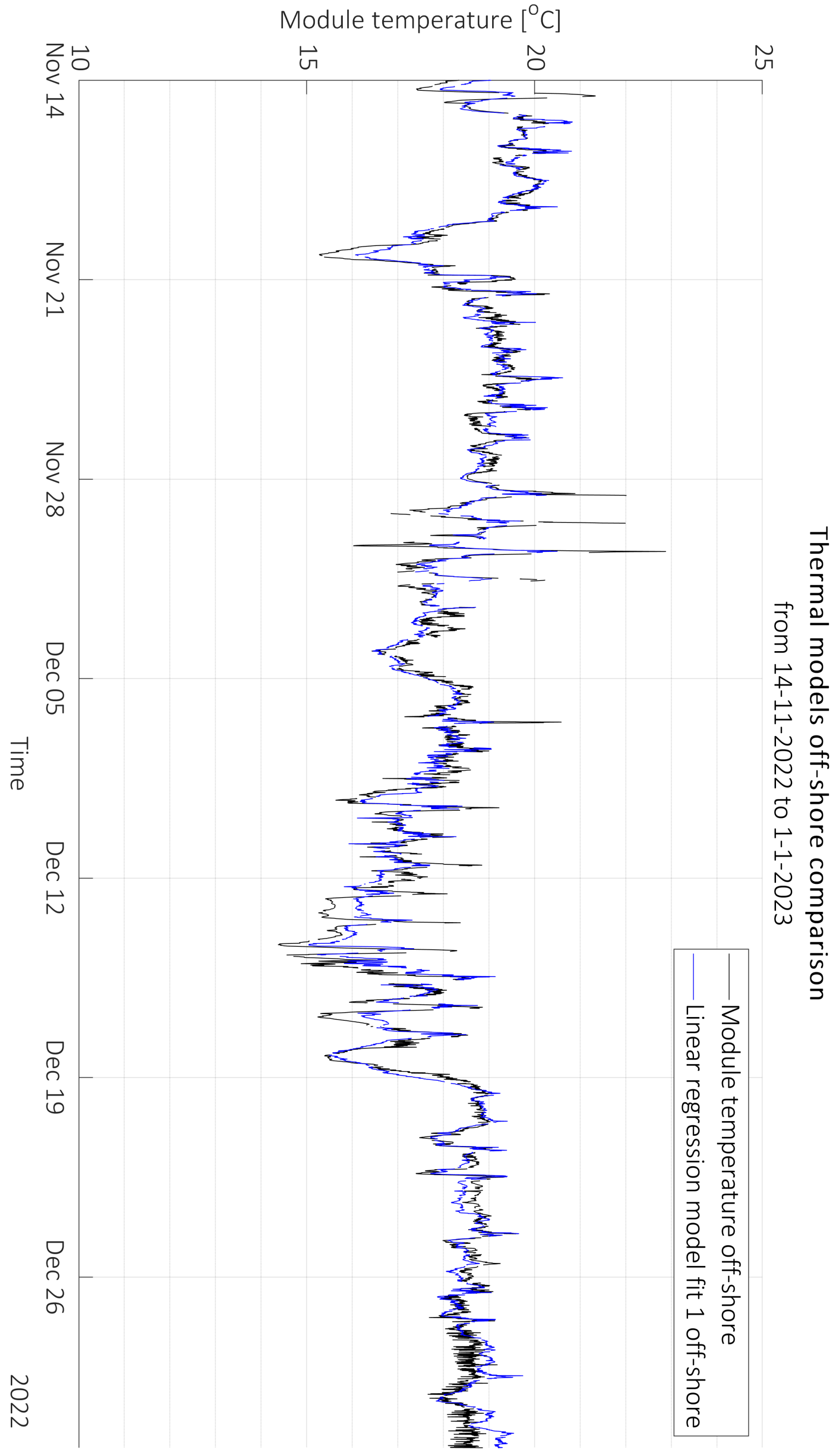

Figure 5.36: OFPV linear regression model 1 plotted together with module temperatures measured.

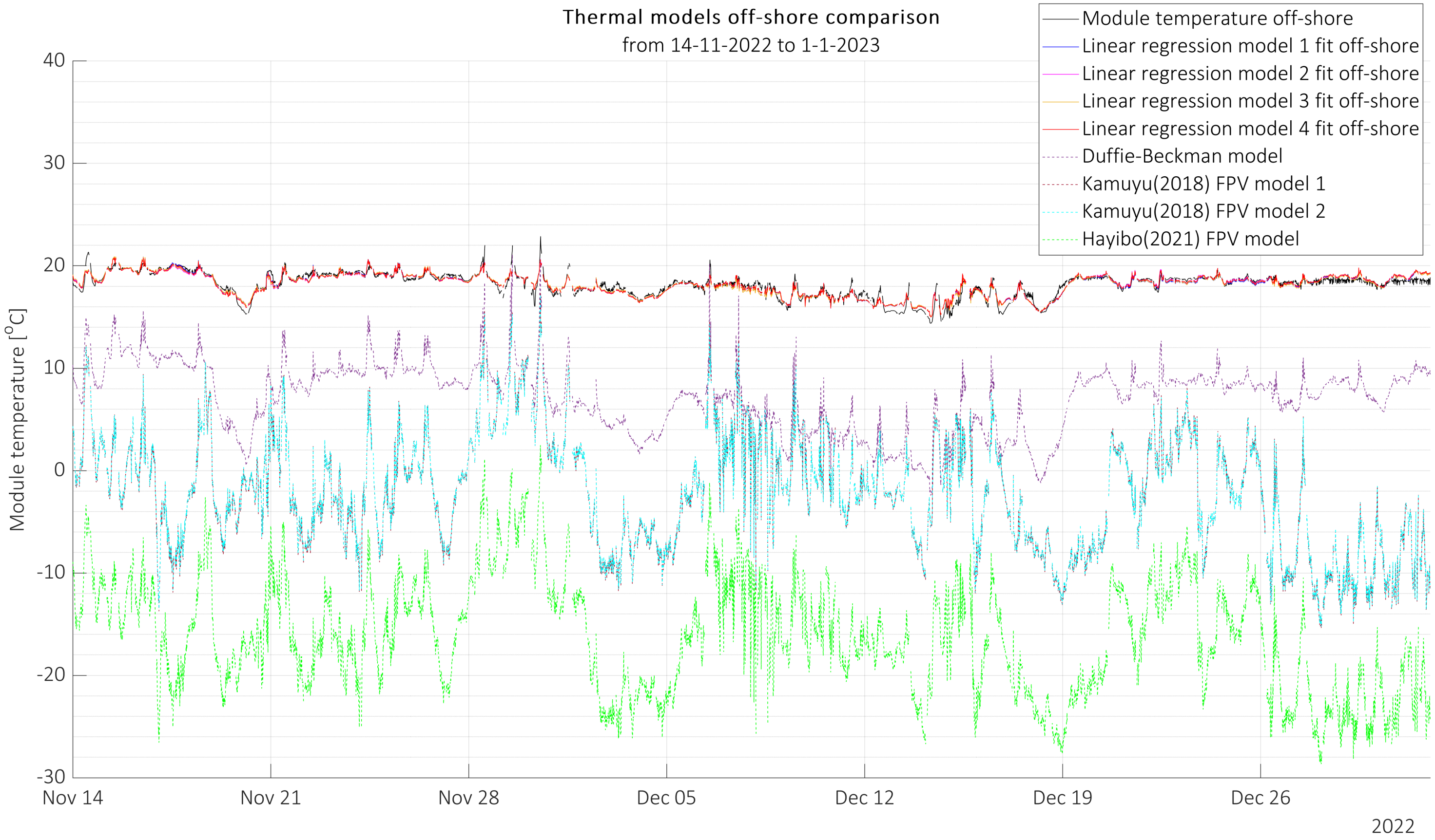

Figure 5.37: OFPV linear regression model plotted together with module temperatures measured off-shore.

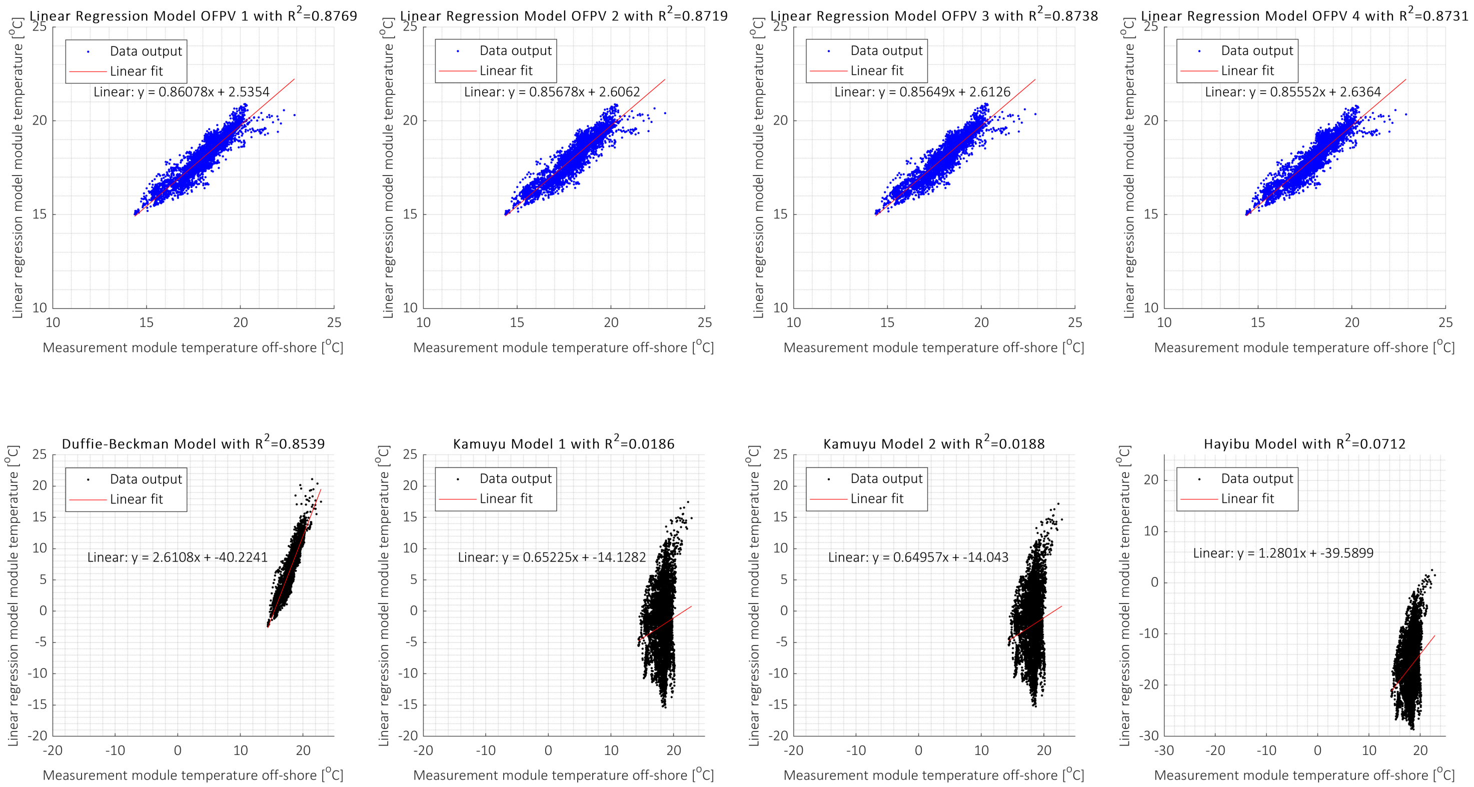

Figure 5.38: Regression fit of module temperatures measured off-shore against empirical module temperature models during the period of research.

5.3.8. Temperature measurements summary

From the results presented in the temperature measurements section, the following observations were found for the period from 15-11-2022 to 1-1-2023:

Firstly, ambient temperatures from climate data presents a similar behaviour than ambient temperatures measured off-shore. Additionally, ambient temperatures from climate data on-land differ from ambient temperature measurements for extreme values. Both the climate data and ambient temperature measurements indicate that for this period of the year off-shore temperatures are higher than on-land. The measured ambient temperature difference was of 0.9 ^{o}C between the locations off-shore and on-land.

Secondly, PV module temperatures off-shore were higher and more stable (less temperature variance) than on-land, as presented through the use of box-plots. It is observed that the sea water temperature was higher than ambient temperature off-shore and thus the water actually was suspected to be affecting the module temperature to remain higher than on-land but more stable, in what is called a 'heat sink' effect. An additional observation is that the 'heat sink' effect can cause the module temperatures to remain stable and thus potentially reduce thermomechanical stresses and thus increase the lifetime of the PV module. However this does not take into consideration other environmental and module characteristic factors.

Thirdly, module temperatures on-land were found to be directly correlated with incoming irradiance at the plane of array (G_{POA}), higher irradiance values lead to a higher PV module temperatures. However, when analyzing the off-shore module temperature measurements against G_{POA}, module temperatures had a lower influence by the G_{POA} than on-land.

Fourthly, module temperatures gradient on one PV module suggest that off-shore temperatures throughout a module remain constant. On-land it was found that the temperature in the middle of the PV module had a tendency to remain slightly higher. The presence of hot-spots was not detected from these measurements after one month. Module temperatures, when looking at the complete array and floater, showed that temperatures off-shore remained the same throughout the PV array. This variation on-land was higher.It was suspected some PT100 sensors may have become de-attached from the module, however, these was not able to be verified.

Finally, 4 OFPV empirical thermal models were developed, for module temperature prediction using measurements from the period of research. These models were statistically analysed through linear regression fits and it was observed that for the OFPV system researched, the OFPV models provided more accurate results than FPV empirical models selected from literature, as these are subject to site and design specific conditions. This observations should be further verified with annual measurements to yield annual conclusions.

5.4. Environmental effects

In this section environmental effects are presented. The correlations from module temperatures are investigated, as it is of interest to identify which environmental factors affect these temperatures and the power performance. The off-shore environmental effects are presented to show the influence of ambient temperatures, water temperatures, wind speed, wind direction, wave height and soiling on the PV system and module temperatures.

Wind and wave measurements were not available directly from the system set-up off-shore. Therefore KNMI weather station Hollandse Kust Zuid Alpha (HKZA) data, located in the decimal coordinates 52.319, 4.043, was used. It is located $2\ km$ off-shore from the location of the on-land system. The data and measurements used from 15-11-2022 to 1-1-2023 are presented in Appendix E, Table E.3.

Figure 5.39 is provided to display the wind, wave and temperature measurements recorded at the off-shore location as a function of time. From Figure 5.39, the middle graph presents wind speed as a function of the wind direction angle (North direction corresponding to 0 ^{o}, South to 180 ^{o}, East to 90 ^{o} and West to 270 ^{o}).

From these measurements, highest and lowest wind speed recorded off-shore were 20.9 m/s and 0.4 m/s respectively, with the average being 9.1 m/s, which was larger than the wind speeds predicted by Meteonorm at the off-shore location. Additionally, the highest and lowest waves recorded during the period of research were 3.4 m and 0.3 m respectively, with the average being 1.3 m.

For reference, Table 5.8 presents location specific climate data obtained from the meteorological tool Meteonorm for both the on-land and off-shore locations. Additional outputs are presented in Appendix D.

Location	Month	GHI [kWh/m^2]	DHI [kWh/m^2]	DNI [kWh/m^2]	Wind [m/s]
On-land	November	24	16	27	3,9
Off-shore	November	23	15	29	6,4
On-land	December	16	11	24	4,4
Off-shore	December	16	11	25	6,9

Table 5.8: Meteonorm 8.1.1 climate data for the months of November and December, presenting average wind speeds for each location.

From the outputs displayed in Figure 5.39, individual analyses were made: first with respect to influences of sea water temperatures and secondly with respect to wind and wave effects. This is followed by the results and analysis of the tilt, soiling and shading effects.

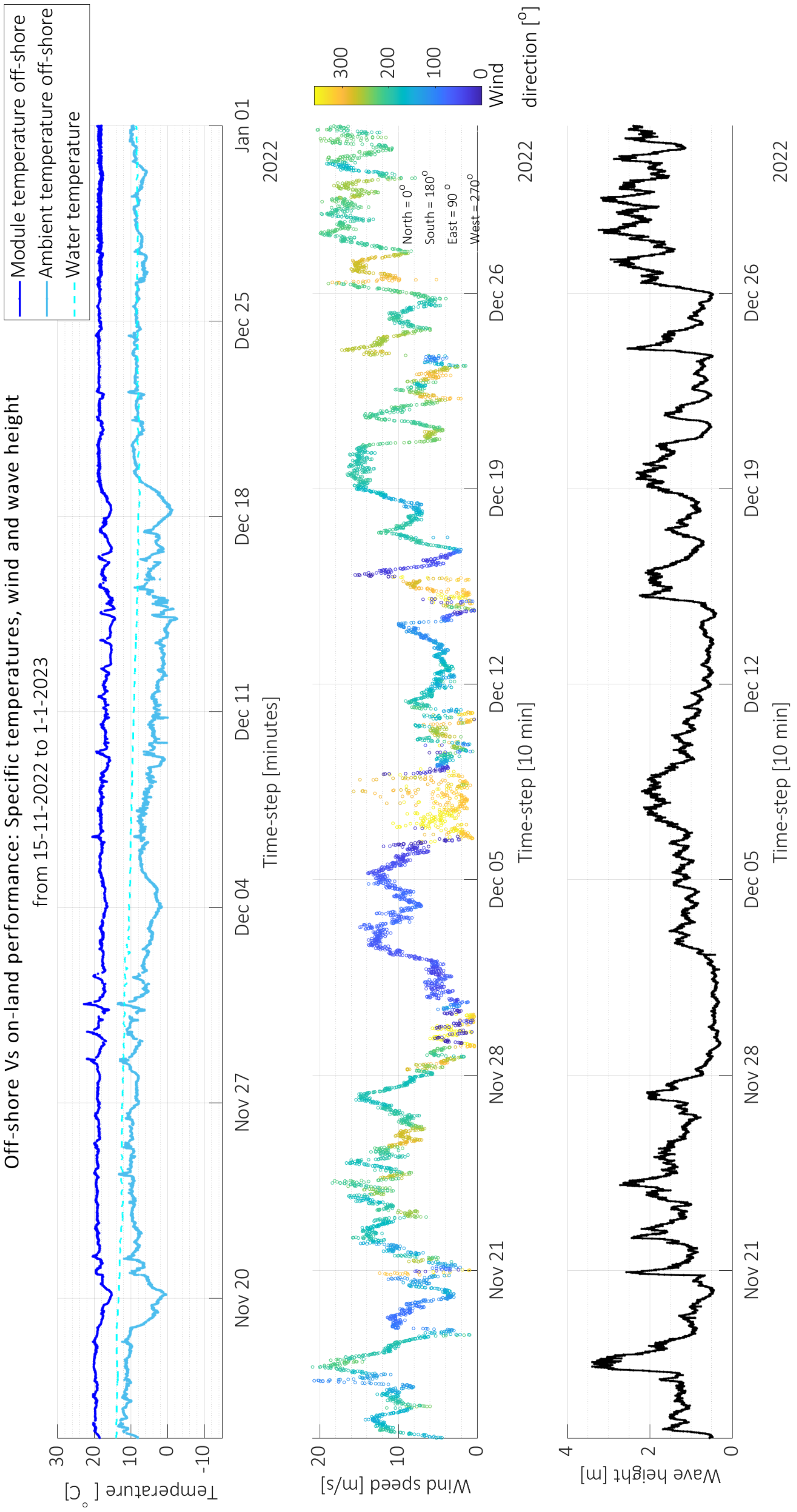

Figure 5.39: Timeline during period of research with module, ambient and water temperatures (top), wind speed and direction (middle) and wave height (bottom), from 15-11-2022 to 1-1-2023.

5.4.1. Off-shore water, wind and wave effects on module temperature

Off-shore water effects were first investigated. After the module temperature comparison between the off-shore and on-land systems, it was identified that the off-shore system had a lower module temperature variability. This temperature cycling increase on the on-land system could potentially lead to higher thermomechanical stresses and to failures of the solder bonds and diodes (Kawai et al., 2017). Water cooled bodies systems are more likely to experience small thermal variations than air cooled bodies on both daily and on a longer-term basis (Micheli, 2022). Therefore the water cooling effect on the OFPV system was further studied. Figure 5.40 was produced and it was observed that PV module temperature with respect to water temperature showed a positive trend, shown with a linear regression fit. It is observed that module temperatures increase as higher water temperatures increase, within the experimental period.

The trend presented for module temperatures is also influenced by more parameters: the correlation between module, ambient and water temperatures previously presented in Figure 5.30, showed a positive trend correlation between ambient temperature and water temperature. It was observed that the lowest module temperatures were obtained at low ambient and water temperatures and high module temperatures were obtained at higher ambient and water temperatures. However, these observations should be performed for a larger time period, ideally a year, to confirm these trends.

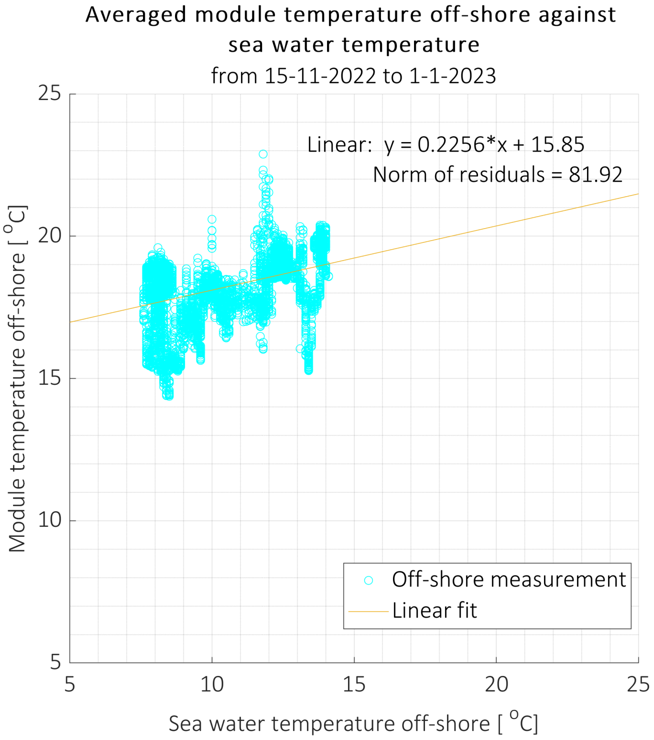

Figure 5.40: Averaged module temperature off-shore against sea water temperature with linear fitting, from 15-11-2022 to 1-1-2023.

To further understand the OFPV system, and to see if the behaviour was best represented by a water or an air cooled system, results were compared with a study from Lindholm et al., 2021. In this study water and wind influences on FPV systems and cell temperatures were analyzed. Figure 5.41 shows the two types of systems, an air cooled dominant system and a water cooled dominant system. Moreover, Figure 5.42 is presented to show the cell temperature behaviour estimated by Lindholm et al., 2021 when the system is predominantly water or air cooled. If the system was air cooled dominant, with constant air temperature, the cell temperature of the module would be more independent of water temperature as wind speed increased. If the system was water dependent, then the system would depend predominantly on the water temperature rather than on the wind speed, which would still influence the module temperature, but would not be the dominant effect.

When comparing Figure 5.40 together with these findings and with the lower module temperature variability identified when compared to the on-land system, the system was observed to be subject to the water temperature influence effect, also previously mentioned as the 'water heat sink' effect.

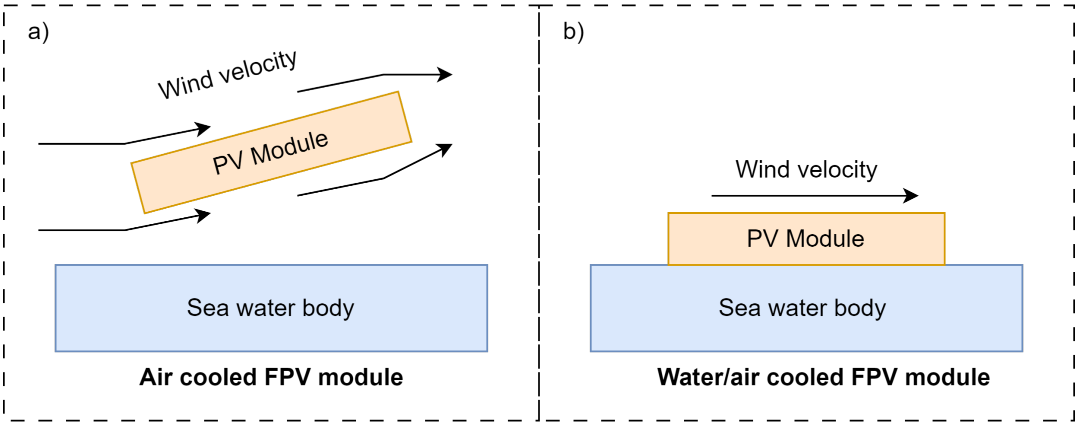

Figure 5.41: Air cooled FPV module (a) and water cooled FPV module. Adapted from Lindholm et al., 2021.

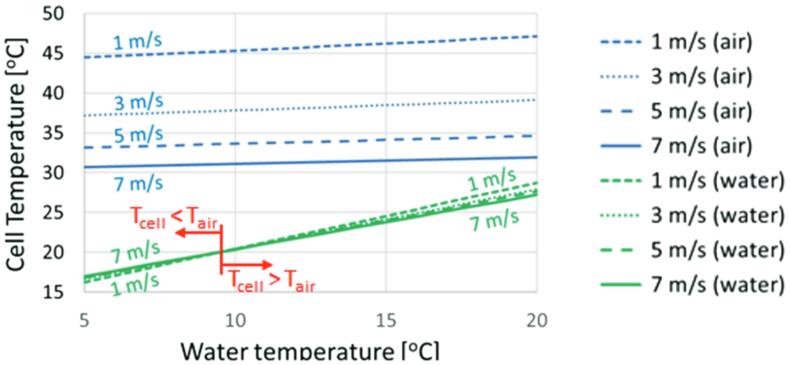

Figure 5.42: Air cooled FPV module (blue) and water cooled FPV module (green) cell temperatures with respect to water temperatures and wind speeds at a constant ambient temperature of 20 ^{o}C (Lindholm et al., 2021).

After studying the off-shore water effect on the PV modules temperature, wind effects were analyzed from measurements to understand their influence on the PV module temperatures recorded off-shore.

The results of the wind speeds recorded against the module temperature at the same time-step are presented in Figure 5.43. A linear fit of the results is also displayed, from which it was observed that during the time of the experiment, module temperatures with respect to wind speeds showed a positive trend. However, when looking at the same wind speed value, different module temperatures were recorded, indicating that a change in wind speed alone did not directly change the module temperature significantly (Figure 5.42). Also from Figure 5.42 it was observed that, predominantly, module temperatures increased with higher ambient temperatures while same module temperatures were recorded for different wind speeds. This observation showed a lower influence of wind speed changes causing a considerable change in module temperatures.

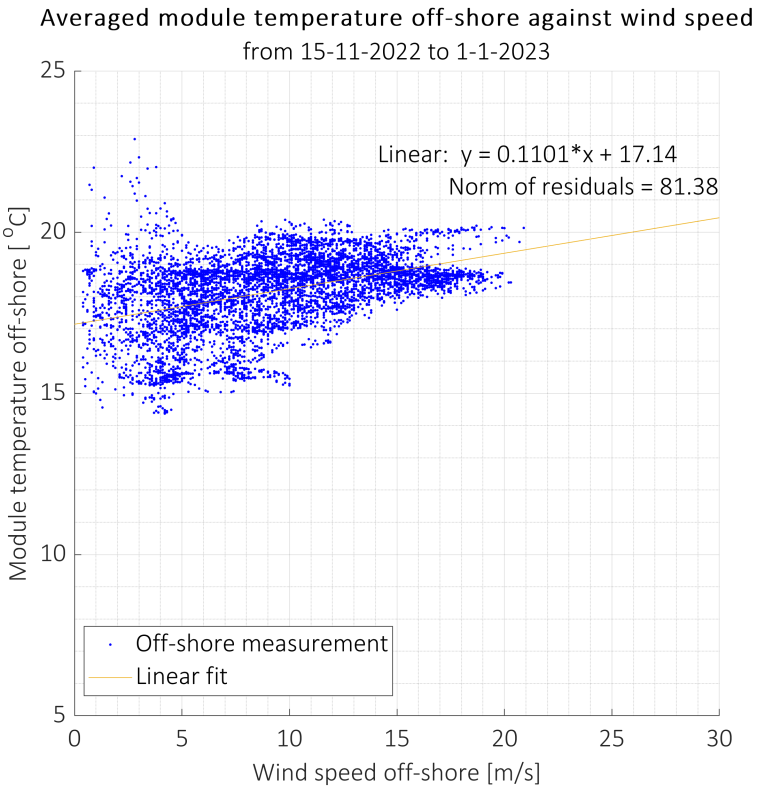

Figure 5.43: Averaged module temperature off-shore against wind speed with linear fitting, from 15-11-2022 to 1-1-2023.

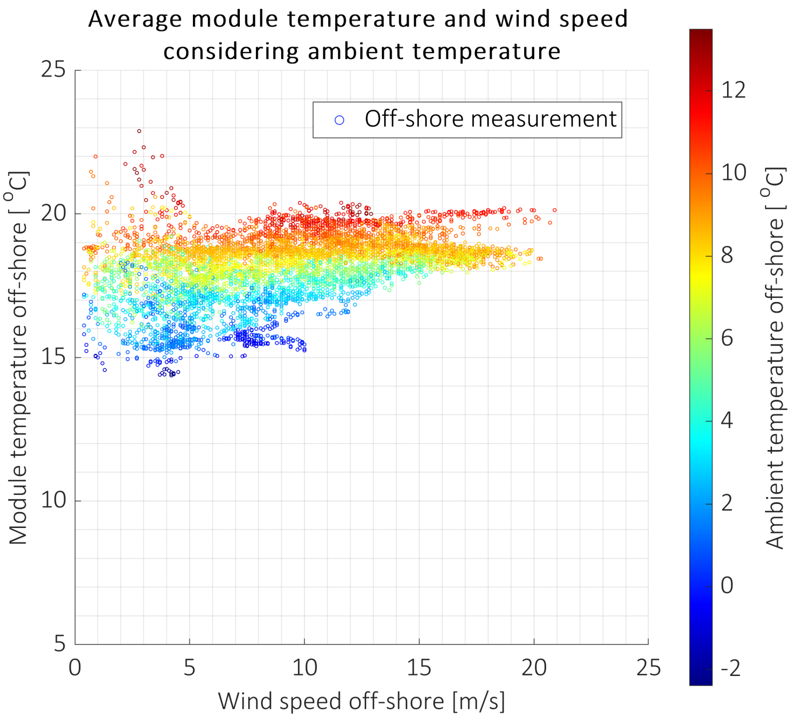

Figure 5.44: Averaged module temperature off-shore against wind speed considering ambient temperature, from 15-11-2022 to 1-1-2023.

The dominant wind direction off-shore was also studied to see if the location of the utility floater, where the BoS components were installed (previously presented in Chapter 3), had a considerable influence on protecting the PV system from the wind and in turn, on the module temperatures.

The wind rose off-shore is presented in Figure 5.45, from which the highest and most frequent winds came from the South-West direction. Since the utility floater was located in the North-West side with respect to the PV floater, it was observed that the utility floater did not act as a protector against the wind for this direction. A top view visualization showing the South-West wind direction with respect to the utility and PV floater locations and orientations is provided in Figure 5.46. If the wind was blowing from a North-West orientation, which was not the dominant case according to the wind rose, the PV floater would be subject a larger influence by the utility floater BoS components protection against the wind. Therefore, the utility floater influence with respect to wind was discarded, as it was not considered a large and constant influence affecting module temperatures during the experimental period.

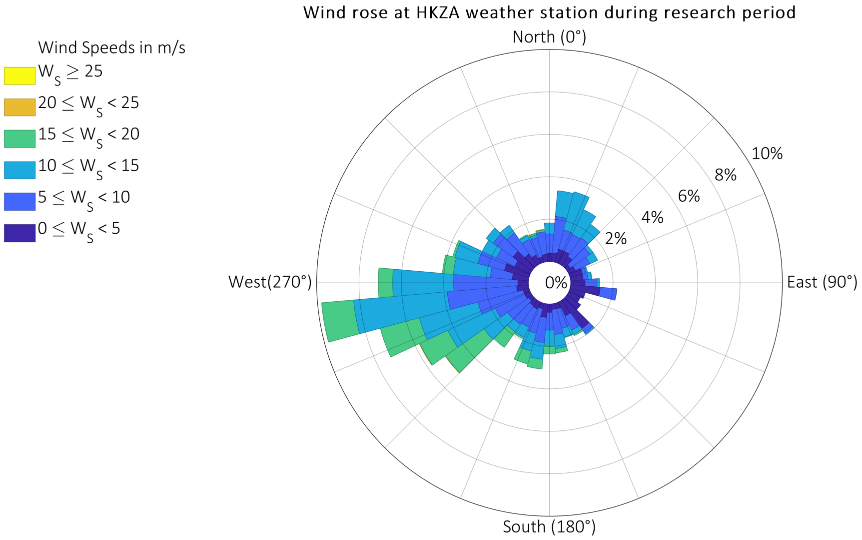

Figure 5.45: Wind rose at HKZA weather station from 14-11-2022 to 1-1-2023.

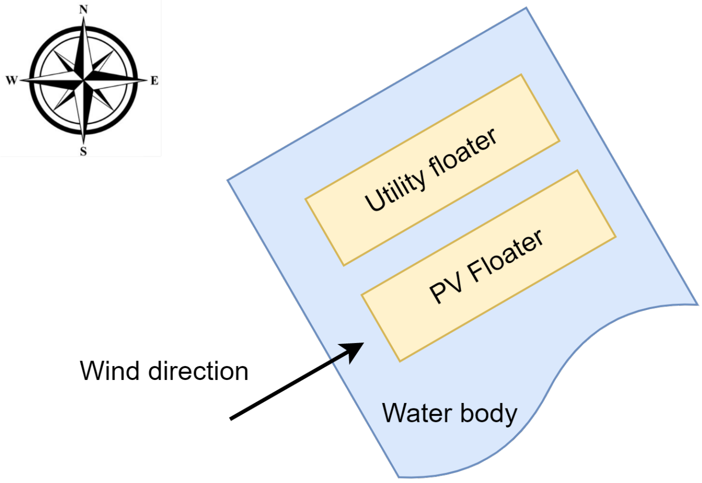

Figure 5.46: South-West wind direction with respect to off-shore system considering utility and a PV floater locations and orientations (top view).

The correlation between wind speed and wave height at the off-shore location was studied and is presented in Figure 5.47, showing a positive trend with respect to module temperature off-shore. This is displayed with linear and quadratic regression fits. Additionally, to study the hypothesis that water splashing would change the module temperature, the wave height was plotted together with the water temperature. No clear correlation was found, indicating module temperature changes as a function of wave height and water temperature alone (Figure 5.49).

Timeline plots of ambient temperatures, wind and wave influences were produced with respect to module temperatures and are presented in Appendix E.

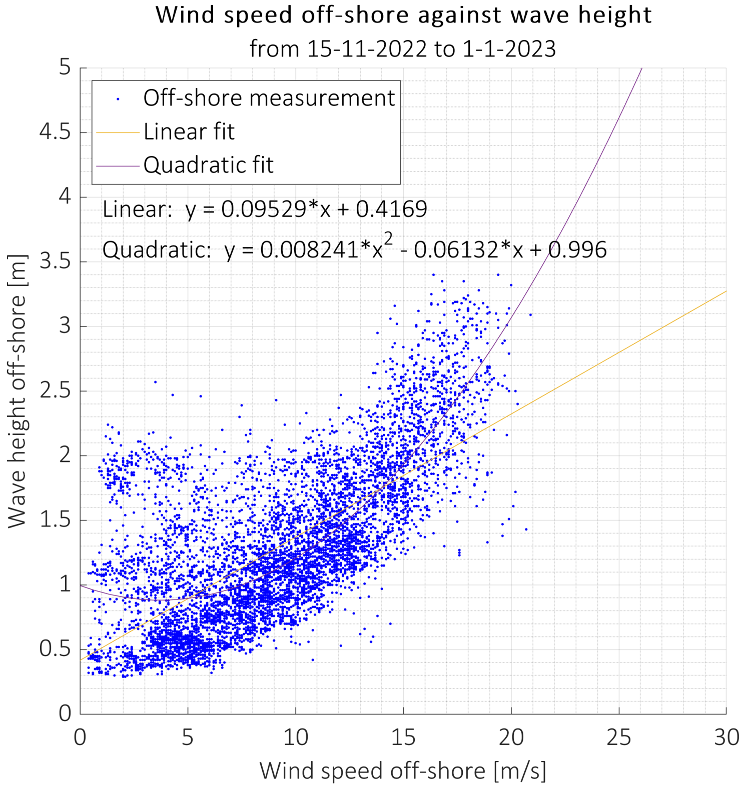

Figure 5.47: Wave height as a function of wind speed with linear and quadratic fittings, from 15-11-2022 to 1-1-2023.
)

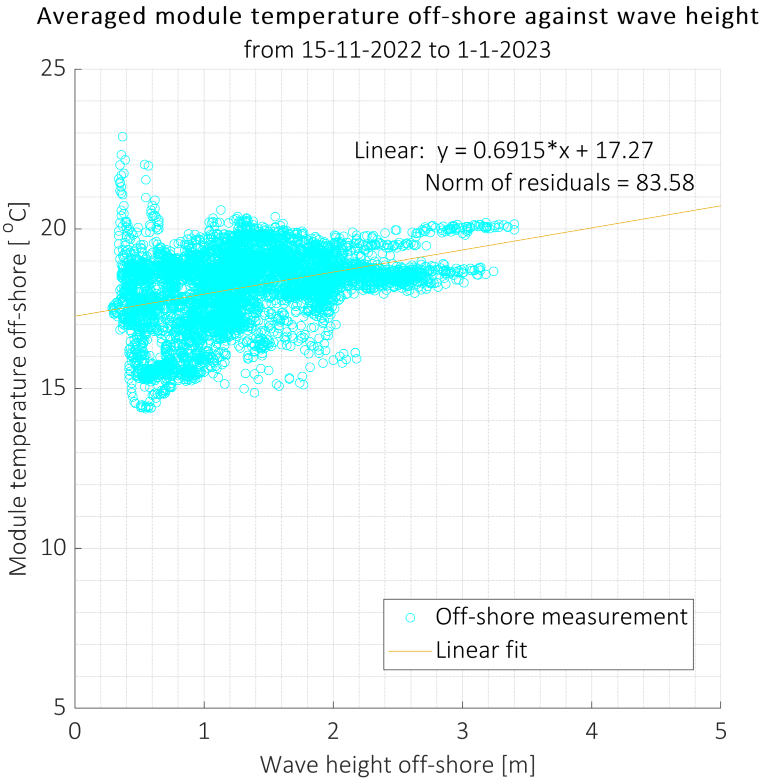

Figure 5.48: Averaged module temperature off-shore against wave height with linear fitting, from 15-11-2022 to 1-1-2023.

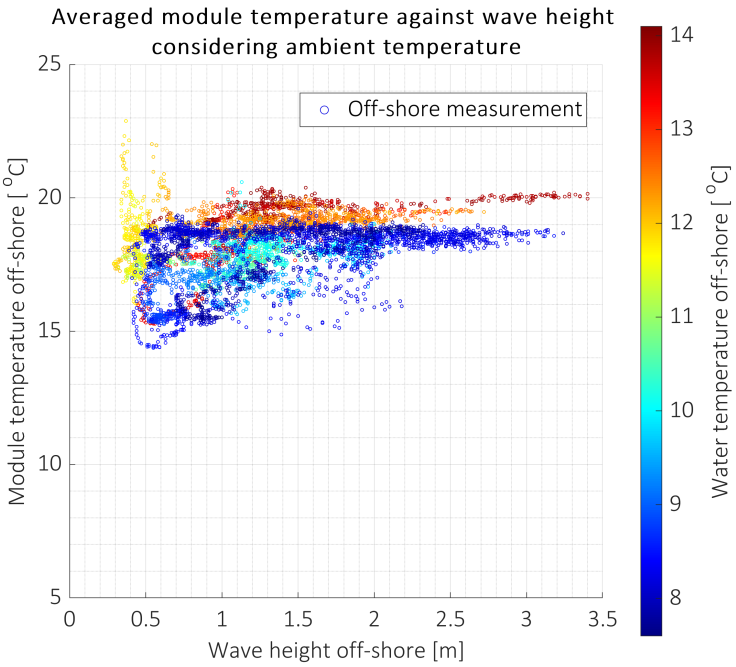

Figure 5.49: Averaged module temperature off-shore against wave height considering sea water temperature, from 15-11-2022 to 1-1-2023.

5.4.2. Tilt effects

This section aims to present the measurements of the tilt effects seen off-shore and the maximum values recorded to further understand its effect on PV performance. To measure these values, the inclinometer was installed in the utility floater. To calculate the inclinometer measurement off-set, once the off-shore system was floating on-port, before being deployed in the North-Sea 2 demonstrator location of Oceans of Energy, the inclinometer was calibrated with measurements taken during the day at port. The formula used for calibration is shown in Equation 5.11, including the offsets considered as presented in Equation 5.12. The formulas used, provided in the product data sheet in Appendix H, registered at 0^o positions from the angles measured in the X and Y axis are displayed in Equations 5.13 and 5.14 respectively. Where the X axis offset $V_{out,X}$ was found to be 1.458725 and where the Y axis offset $V_{out,Y}$ was found to be 1.67813 when the system was at 0 ^{o} floating on the port, protected from wave movements prior to deployment off-shore.

$$Angle = sin^{-1}(\frac{V_{out} - Offset}{4}) * 0.9 \tag{5.11}$$

$$Offset = V_{out}\ (in\ 0^o\ position) \tag{5.12}$$

$$Angle_X = sin^{-1}(\frac{V_{out} - 1.458725}{4}) * 0.9 \tag{5.13}$$

$$Angle_Y = sin^{-1}(\frac{V_{out} - 1.67813}{4}) * 0.9 \tag{5.14}$$

It is important to state that the inclinometer was located adjacent to the PV floater, on the utility floater. Measurements are presented to show the inclination that the floater was subjected to with respect to the X and Y axis. Terminology for rotation around X axis is referred as 'pitch', rotation around Y axis as 'roll' and change in azimuth as 'yaw'. Figure 5.50 presents the inclinometer tilt axis, yaw, pitch and roll for reference within results, with floater at an azimuth of 150 ^{o}, with respect to the North (0 ^{o}).

Figure 5.51 presents the pitch (X axis) and roll (Y axis) angles against the GHI [W/m^2] recorded by the pyranometer off-shore: maximum pitch and roll angles did not record high GHI values, suggesting the largest inclinations suffered by the system were during times of low or no-solar irradiance, such as night-time. Furthermore, the predominant roll and pitch angles were studied though the use of histograms.

Figure 5.52 presents the angles which the floaters where subjected to during the period of research (first two graphs from top). These angles are presented in a normalized histogram (third and fourth graphs from top), showing the probability of occurrence of each angle. Additionally the GHI is plotted together with the inclination angles (bottom two graphs). From here it is observed the system had a higher probability to be tilted on the Y axis towards South-East, in reference to the pre-set azimuth of 150 ^{o} with respect to North and to be tilted on the X axis towards South-West. In other words a negative roll, and a negative pitch, indicated the South-East orientation string off-shore had a more favourable orientation than the North-West string off-shore for power production due to the influence of inclination caused by the waves, current and wind influences. It is important to note that the anchoring and mooring system also had an influence on these angles, restricting the free movement with respect to waves. The restriction from these influences limited the tilt angles of the system, with a maximum tilt in X and Y direction of 13.33 ^{o} and 17.36 ^{o} respectively when experiencing waves of up to 3.4 meters during the experimental period.

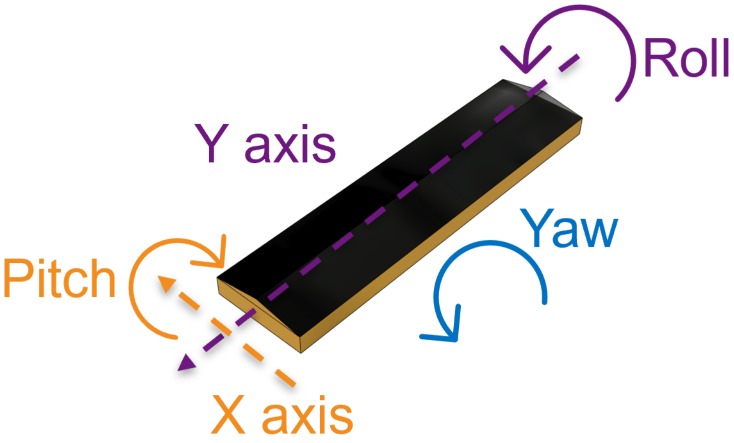

Figure 5.50: Tilt axis x (orange) and y (purple) with respect to floater at 150 ^{o} azimuth.

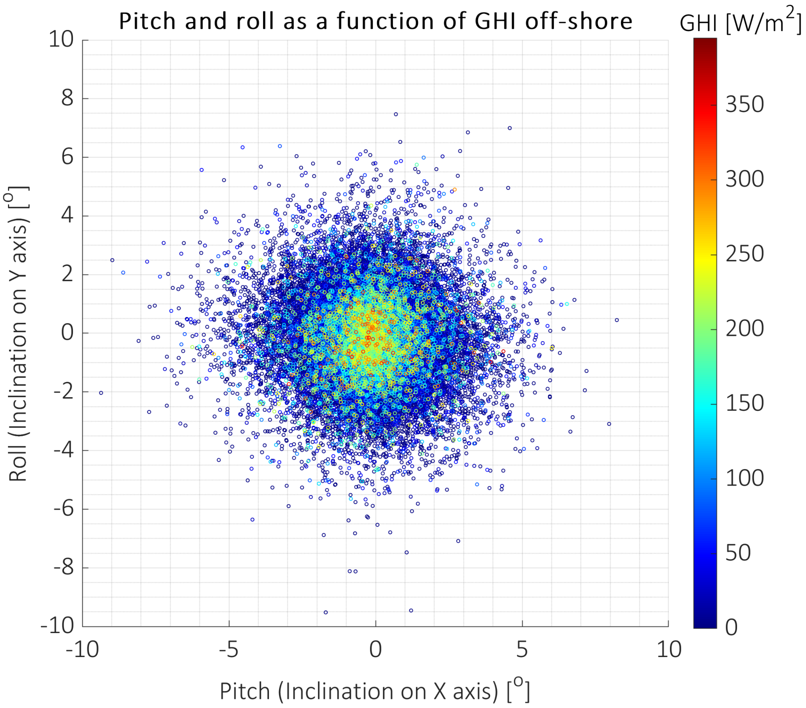

Figure 5.51: GHI [W/m^2] recorded against raw and pitch angles during the research period.

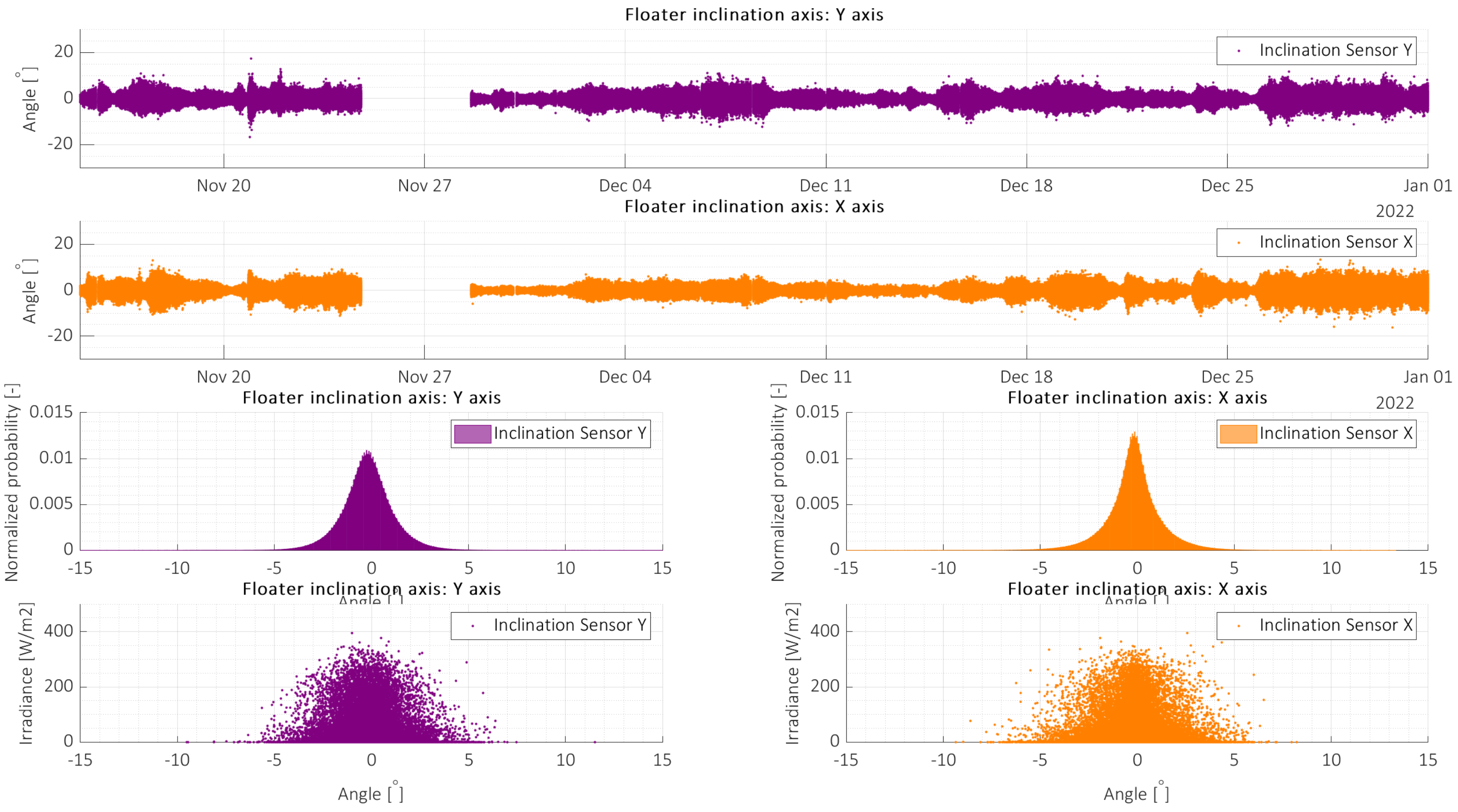

Figure 5.52: Tilt angles (top) in x (orange) and y (purple) directions together with a histogram of normalized probability of each tilt and the measured GHI at the respective tilt, for the period from 14-11-2022 to 1-1-2023.

5.4.3. Soiling and shading effects

Soiling and shading effects were studied visually, to further understand their implications related to hot-spots, incoming irradiance and module temperature influences, focusing on the off-shore system.

It is important to note that the off-shore system was equipped with a camera pointing at PV module 7 to identify and investigate any possible changes in temperature within this module due to environmental factors such as water splashing and bio-fouling. The PV module being monitored had its location previously described in Chapter 3. The interest to see the behaviour at this location was subject to the hypothesis that in the corner of the floater, a module facing a South-east orientation would be subject to higher bio-fouling and water splashing, which in turn could reduce the PV power performance of the system. When looking at the temperature in the corner of the OFPV floater, with respect to the rest of the PV module temperatures recorded in the OFPV floater, as discussed in Section 5.3.6, temperatures throughout the module were identified to be relatively similar, suggesting bio-fouling, and in turn hot-spots, appearances in the corner were not found to be higher than in the rest of the floater. Nevertheless, the sample time is recommended to be increased to be over a year to yield annual conclusions on the differences in long term bio-fouling and soiling throughout a OFPV floater.

During the period of research, from visual images being recorded for the off-shore system during the period of research as well as from the PV module temperatures recorded on the corners and middle locations of PV module number 7, previously discussed in Section 5.3.5, no permanent soiling was detected, as PV panels remained relatively clean and no large increase in temperatures within the module was detected. However, minor causes of dynamic soiling were detected and thus presented. The most frequent environmental factor detected was wave splashing followed by soiling, which was only detected for brief period of time as wave splashing would tend to remove the soiling detected. The three environmental factors detected in brief periods of time in this experimental period were wave splashing, soiling and snow, which where all observed during the period of research and are provided in Figure 5.53, with images corresponding to the off-shore PV module being monitored.

Shading off-shore was avoided by placing the utility floater on the North-West side. The visual camera installed on a adjacent floater may have caused shading in the very early hours of the sun-rise, but was assumed negligible.

The system on-land was placed in the best location available, however, this location did not avoid shading in the very first hour of sun-rise, before 9:30 am. The influence of the shading on-land was additionally studied through horizon measurements. Figure 5.54 presents the sun path seen for the on-land system taken with a horizon measurement device, in this case with a device called 'Horicatcher'. The picture from the 'Horicatcher' was processed through the meteorological tool 'Meteonorm'. During experiments, no shading from trees was seen on-site during day-light time, which suggests the Horicatcher set up when taking the image was slightly inclined and thus a branch of a tree is seen to cover the sun path at the 11:00 during the lowest sun path provided. The custom horizon used and the slight inclination when performing the measurement as well as the orientation with respect to North, taken into account from the Horicatcher measurement is presented in Appendix E. The monthly irradiance outputs from Meteonorm 8.1.1 at the on-land location with and without shading are presented in Appendix E. Table 5.9 provides the Global Horizontal Irradiance (GHI) including the raised horizon at the location, Diffuse Horizontal Irradiance (DHI) and Direct Normal Irradiance (DNI) monthly outputs for the simulations performed for November and December. From the monthly outputs, shading was found to cause a reduction of 1 kWh/m^2 with respect to the GHI for the month of December.

Location	Month	GHI [kWh/m^2]	DHI [kWh/m^2]	DNI [kWh/m^2]
On-land	November	24	16	27
On-land including custom horizon	November	24	16	27
On-land	December	17	11	24
On-land including custom horizon	December	16	11	24

Table 5.9: Meteonorm 8.1.1 outputs for the months of November and December„ with an azimuth of 150 ^{o} with respect to North at an inclination of 4 ^{o}.

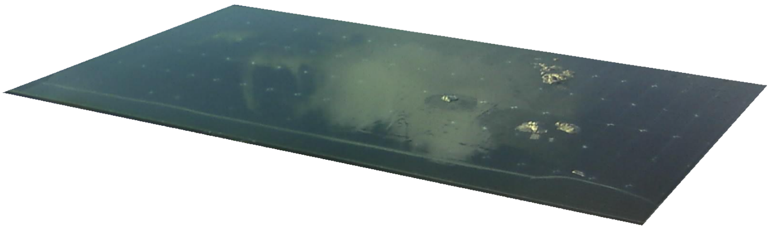

(a) OFPV module off-shore conditioned to soiling spread on 15-12-2022 15:00.

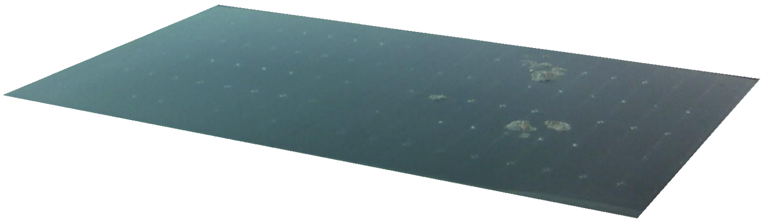

(b) OFPV module off-shore conditioned to soiling on 15-12-2022 16:00.

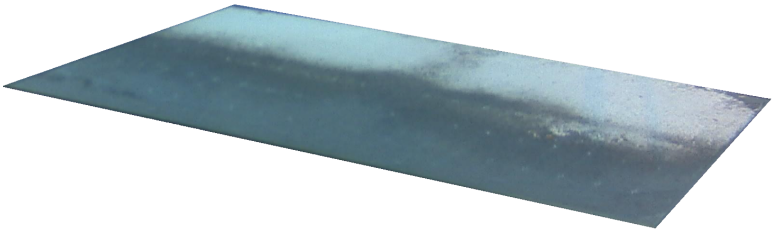

(c) OFPV module off-shore conditioned to snow on 18-12-2022 09:00.

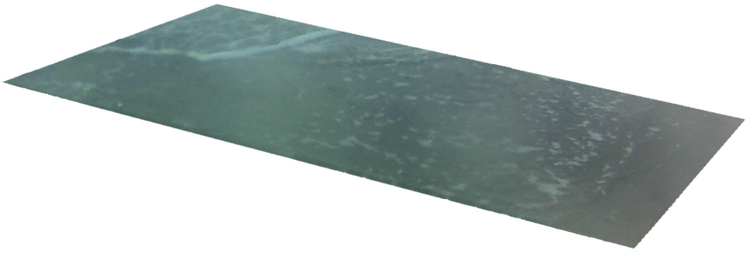

(d) OFPV module off-shore conditioned to wave splashing on 27-12-2022 16:00.

Figure 5.53: OFPV module with specific soiling effects observed during the period of research.

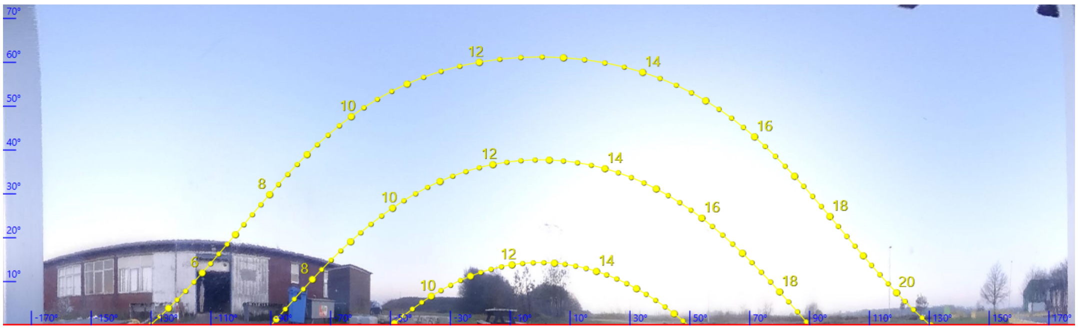

Figure 5.54: Sun paths and horizon for the on-land location found using Meteonorm.

5.4.4. Environmental effects summary

Firstly, the off-shore water effects were investigated; the lower module temperature variability detected on the off-shore system when compared to the on-land system indicated that the system was influenced by the water. From here, the correlation between module temperature and water temperature off-shore was provided, showing a positive trend. These findings were further analyzed and discussed to inspect the system and determine the possibility of a water dominant cooling effect. Afterwards, the wind influence was studied, correlating its influence with module and ambient temperatures. Additionally, the wind rose at the location off-shore was presented. From there, the predominant wind affecting the system was found to come from the South-West direction during the period of research, thus the utility floater did not act as a protection against the wind and was considered negligible. Additionally, the correlation between wind speed and wave height at the location was presented, showing a positive trend. The water splashing effect was investigated, however a clear correlation between wave height and module temperature was not found.

Secondly, tilt effects corroborate a more favourable inclination for the South-East string off-shore. Tilt angles, limited by the system design, mooring and anchoring, reached 13.33 ^{o} of inclination with respect to the X axis and 17.37 ^{o} of inclination with respect to the Y axis. Additionally, highest tilts were found to be predominantly recorded during times of low or no irradiance during the period of research.

Finally, horizon measurements on-land were taken to analyze whether the location was subject to large shading patterns. Furthermore, soiling and bio-fouling effects were analyzed and discussed. Long-term soiling off-shore from salt or algae was not detected during the period of research. However dynamic soiling (short-term) was identified, as well as snow and wave splashing, the latter being the most predominant.

6

Conclusions and recommendations

From the research objectives and questions made to be answered within this research project, the following conclusions and observations are presented.

1. What is the PV performance of the off-shore system compared to the on-land system?
    (a) What PV performance indicators can be used to compare OFPV systems?

    Performance indicators were presented to identify which parameters should be used to measure OFPV performance. The performance ratio was identified as a key parameter used in the industry to be able to compare PV systems. Additionally, other indicators were found to be of interest when comparing off-shore and on-land PV systems: module and string efficiencies, module temperature differences and their influence on efficiency, capacity factors and cumulative energy yield. These PV performance indicators were used to provide a comparison between the off-shore and on-land PV systems to further understand and identify differences experienced by both set-ups.

    (b) Which monitoring technologies are needed to track OFPV performance?

    Monitoring technologies were identified in order to obtain the required measurements by the performance indicators to compare a system on-land and off-shore. Mainly reference cells and pyranometers, together with power-meters are needed to track PV performance. Additionally, when considering possible influences on PV performance off-shore, the effect of the environment on module temperatures meant ambient temperature sensors as well as water temperature sensors were recommended to be included. To further understand the effect of the off-shore environment and the change in the POA the following sensors were also recommended: inclination sensors, anemometers, wave buoys and soiling sensors.

    (c) What off-shore environmental influences cause changes in the OFPV system set up when compared to on-land?

    Water, wave and wind influences were found as different environmental causes affecting PV performance between the systems off-shore and on-land. These affect changes in the plane of array, azimuth and module temperature.

    Soiling and bio-fouling effects were also identified in literature to affect off-shore systems, predominantly by algae and salt deposition from water splashing, which in turn could enhance the appearance of hot-spots.

    (d) How does the floater POA change in off-shore conditions?

    The POA was found to change dynamically from the double-axis inclinometer, influenced by wave conditions. Tilt effects, analyzed though histograms, showed a more favourable inclination for the South-East string off-shore. Tilt angles, limited by the system design, mooring and anchoring reached 13.33 ^{o} of inclination with respect to the X axis and 17.37 ^{o} of inclination with respect to the Y axis of the floater. Additionally, highest tilts were found to be predominantly recorded during times of low or no irradiance during the period of research.

(e) Does soiling appear on an OFPV system? And if there is, what type of soiling is it?

Two approaches were performed to detect soiling off-shore: through the use of thermal sensors aiming to detect hot-spots and through visual images during the period of research. From these studies no long-term soiling, after one month of measurements, was detected. However, wave splashing, soiling spreads and small soiling drops, as well as snow, were all identified during the period of research, with water splashing being the predominant and most frequent effect.

(f) What is the efficiency of the off-shore system compared to on-land?

The efficiencies found per PV string off-shore where of 25.43 % and 22.26 % for the South-East and North-West strings respectively. However, the efficiency of the South-East string off-shore was found to have an error due to a malfunction of the Hall effect sensor used to measure the current. On-land the PV string efficiencies were 17.376 % and 20.246 % respectively.

The PV module efficiencies, derived from module characteristics, module temperature measurements and irradiance, resulted in 20.17 % and 20.15 % for the South-East and North-West strings off-shore respectively.The PV module efficiencies found on-land were 20.78 % and 20.92 % for the South-East and North-West strings respectively.

(g) What is the energy production of the off-shore system compared to on-land?

The energy production was recorded for the period from 15-11-2022 to 1-1-2023: the on-land system recorded 96.3 kWh while the off-shore system recorded 93.4 kWh, on the DC side of the systems. Note the off-shore system measurements were taken from the MPPT charge controller instead of from the power meters, since there was a data outage error for the power meters of the South-East string off-shore.

(h) What is the performance ratio (PR) of the off-shore system compared to on-land?

The off-shore PR is found to be 92 % for the North-West string, while on-land the PR is found to be 87 % for the South-East string and 100 % for the North-West string, meaning the average PR ratio found on-land was of 93.5 %. It is suspected that the Hall effect sensors had a measurement misreading with the South-East string off-shore, which also had a data gap, meaning the PR for this string could not be determined.

2. What is the thermal behaviour of OFPV modules when compared to PV modules on-land?

(a) How is module temperature of PV and FPV systems being predicted in literature?

Numerous models to predict PV module temperature for on-land systems are present in literature, however, the models found in literature were designed for on-land systems and do not take into account the water influence, concerning water temperature. Fluid dynamic models, as well as empirical models may be used for FPV as they are subject to site and design specifics.

Three empirical FPV models were found in literature to predict module temperatures, which constructed regression models based on empirical measurements concerning ambient temperature, irradiance on the modules, wind speed and water temperature: these three empirical FPV models were selected for further analysis under off-shore conditions and can be found in the works of Kamuyu et al., 2018 and Hayibo, 2021.

(b) How can the module temperature of an OFPV module be predicted?

Current OFPV systems found were subject to different PV design types. Thus individual prediction models may be developed depending on the OFPV system: a prediction model for OFPV module temperatures can be derived using linear regression modelling tools, correlating measured module temperatures off-shore, together with ambient temperature, irradiance at the POA, wind speed, wave height and sea water temperatures. Within this research four linear regression models were derived from empirical measurements off-shore with the intention to provide an approach and to serve as a future reference depending on parameters available. The model using all parameters mentioned previously, named 'OFPV model 1', gave the lowest root mean squared error (RMSE) and mean absolute error (MAE) values for module temperatures predicted, 0.360 and 0.297 respectively. It is recommended to develop an annual model with a larger data-set in order to yield annual conclusions.

(c) How do FPV thermal models from literature compare to models derived from real measurements off-shore?

To make a comparison between FPV models found in literature and the OFPV models derived, a statistical analysis was made between these model predictions and actual PV module temperatures recorded off-shore.

When comparing the three FPV models indentified in literature with the module temperatures recorded off-shore it is found that there is a large difference between predicted and measured module temperatures, which is suspected to be due to models being design and site specific: The mean absolute error of module temperatures found for the FPV models ranged from 20.309 to 34.506. From the four OFPV emprical models derived and their comparison with the emprirical FPV models, it was found that the OFPV models derived were found to predict best the module temperatures within this experiment for the months of November and December, being site and design specific, with mean absolute errors ranging from 0.297 to 0.308. The OPFV models derived should be extended with data from a complete year to yield annual conclusions.

(d) How does the module temperature change between off-shore and on-land? How does the temperature change throughout one OFPV module? And how does the module temperatures change throughout a floater array?

A lower PV module temperature cycle variability was identified for the off-shore system when compared to on-land, giving an indication of the influence of the water on the system. This lower temperature variations off-shore could potentially lead to lower thermomechanical stress variations on the PV modules off-shore and yield a longer lifetime. However this observation only considers the influence of temperature changes on the module and not the influence of humidity or other conditions in the off-shore environment. The averaged module temperatures found off-shore and on-land during the period of research were 18.2 ^{o}C and 6.9 ^{o}C respectively.

Irradiance and ambient temperature influences were found to be different between the off-shore and the on-land system: the module temperatures off-shore were found to be less influenced by ambient temperatures when compared to the on-land system, as well as the irradiance on the plane of array having a lower influence on the module temperature off-shore when compared with the on-land system. These differences were further investigated with respect to water and wind effects and the system was observed to have a water dominant effect on module temperatures. No clear correlation between wave height and module temperature was found.

Module temperatures off-shore were constant within a module. Also, PV modules within the same floater were found to have similar temperatures. On the on-land system the thermal sensor in the middle of the module recorded higher temperatures than in the corners of the module. The module temperatures of the floater on-land differed per module and were lower than off-shore. After one month of measurements, no hot-spot in the corner of the modules was detected, suggesting no large bio-fouling was fixed onto the PV modules.

3. What guidelines are required to implement an off-shore off-grid system?

(a) What are the design steps required for an OFPV off-grid system?

From the design guidelines presented for an off-shore off-grid PV system, it is recommended to follow an approach starting with project procedures, where policy, regulations and verification procedures should be performed, as well as a planning and site assessment. Afterwards, from the site environmental conditions, the correct Ingress Protection rating should be selected for the protection of the complete system. A selection of the PV modules of the system should consider the high humidity within the marine environment. Orientation, tilt and mismatch effects under off-shore conditions, as well as lightning protection should be analysed and implemented into the design decisions. Additionally mooring and anchoring types should be selected according to the project requirements. Once these steps are taken, the off-grid PV system sizing should be performed taking into account the load requirements. Finally, after the design implementation, monitoring, safety and maintenance actions should be taken regularly during the operational period of the PV system.

(b) Which system adaptations are required for an off-shore off-grid photovoltaic system when compared to an on-land system?

System adaptations required for an off-grid off-shore system should include water protection of the electrical system. IP67 and IP68 ratings are recommended to protect the system from off-shore conditions. If the equipment does not have these ratings, it is recommended that IP67 protection boxes together with the use of appropriate IP67 glands are used to protect this systems. Additionally, wave movements causing a change in tilt means all components must be mounted into the IP67 protection boxes in such way that they do not become de-attached. It was found that for monitoring equipment, such as power meters, techniques such as 3D printing may be used to provide additional mounting protection. In case an off-grid monitoring system is required to have a dissipation unit, it should be protected with an IP67 protection box and additionally cooling through the use of IP68 fans should be considered to avoid overheating of the system.

Recommendations

After the completion of the research, it is recommended to perform the off-shore and on-land PV systems comparison for a longer period of time, ideally a year, as it can yield conclusions rather than observations over a period of time: additionally, the summer period should be used to corroborate the 'heat sink' effect of the sea water cooling the PV modules.

Monitoring devices presented and used in this project are recommended when performing such a comparison. Power optimizers could also be implemented to maximize the energy output at each PV module. Additionally, Hall effect sensors are recommended to have a fixed position and to take into account the separation from other PV cables to reduce noise on the current measurements. It is also recommended, if the monitoring cables are in a protected environment, to have reference cells and pyranometers placed in the same floater which the PV modules are on. The addition of an anemometer, optical sensor, an upgraded water temperature sensor and a wave buoy may yield more precise results, since this research correlated on-site data together with a weather station off-shore $2km$ away, with 10 minute time-step measurements. Placing the inclination sensor on the PV floater instead of on the utility floater could be done to have more precise measurements. Additionally, GPS tracking systems to know the azimuth of the floater off-shore would allow further explanations and validations within power performance.

Furthermore, if research is carried out for a year, annual empirical data recorded could be used to further investigate and validate the OFPV system behaviour with respect to an on-land system. Additionally, monthly linear regression models used to predict module temperatures could be developed, providing further understandings of the OFPV system under different off-shore conditions.

A

Background additional information

A.1. IEA additional graphs

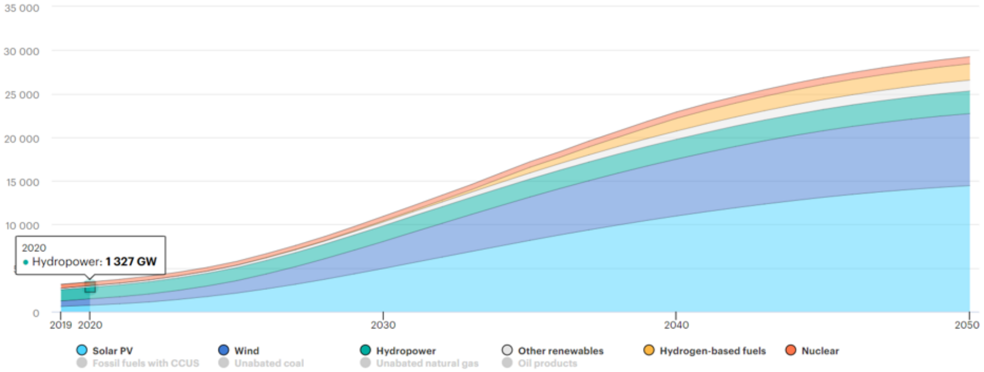

Figure A.1: Electrical capacity by technology from 2019 to 2050 in the NZE scenario (IEA, 2021b).

A.2. FPV investment costs and LCOE

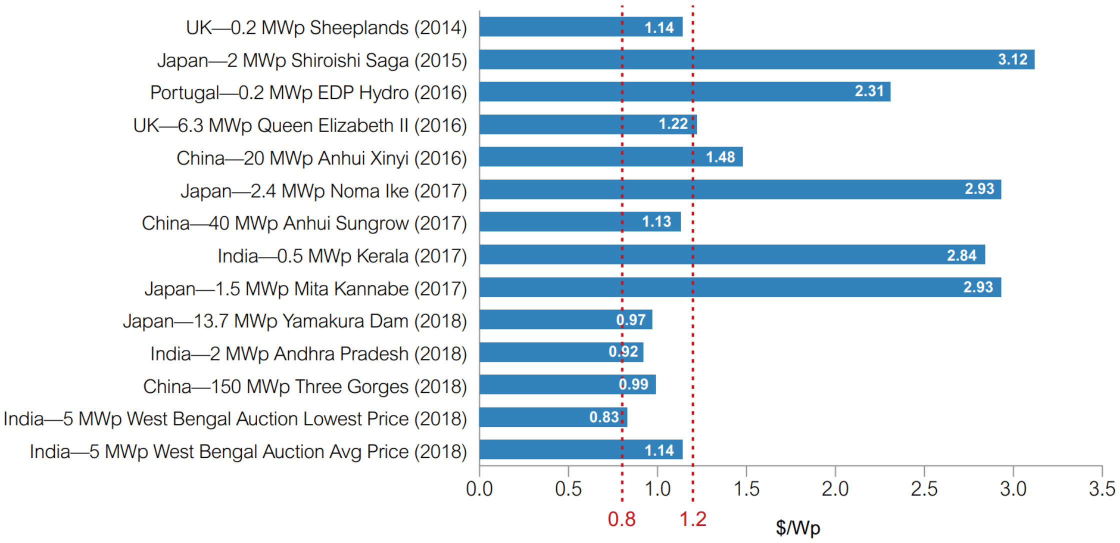

Source: Authors' compilation based on media releases and industry information.

Note: Using the 2017 $ annual exchange rates, as released by OECD. PV = photovoltaic; $/Wp = U.S. dollars per watt-peak.

Figure A.2: Investment costs of FPV in 2014-2018 (realized and auction results (WorldBankGroup, 2019b).

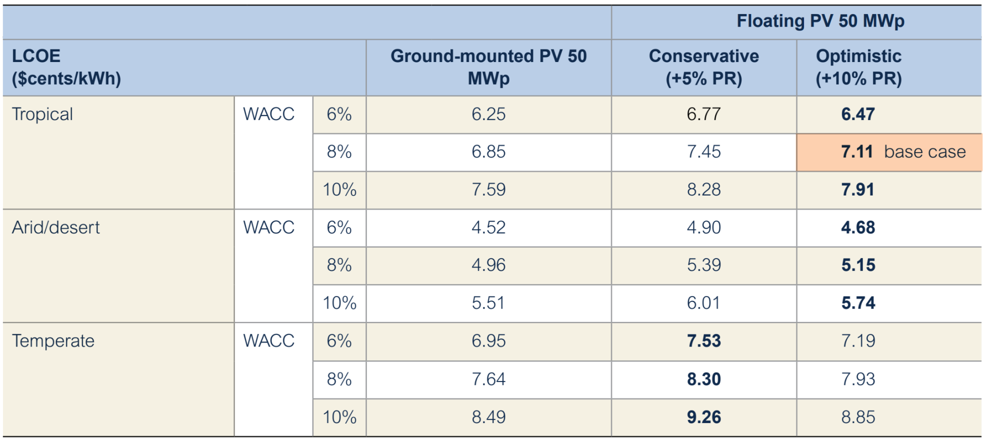

				Floating PV 50 MWp	
LCOE ($cents/kWh)			**Ground-mounted PV 50 MWp**	**Conservative (+5% PR)**	**Optimistic (+10% PR)**
Tropical	WACC	6%	6.25	6.77	**6.47**
		8%	6.85	7.45	**7.11** base case
		10%	7.59	8.28	**7.91**
Arid/desert	WACC	6%	4.52	4.90	**4.68**
		8%	4.96	5.39	**5.15**
		10%	5.51	6.01	**5.74**
Temperate	WACC	6%	6.95	**7.53**	7.19
		8%	7.64	**8.30**	7.93
		10%	8.49	**9.26**	8.85

Source: SERIS calculations.

Notes: kWh = kilowatt-hour; LCOE = levelized cost of electricity; MWp = megawatt-peak; PV = photovoltaic; WACC = weighted average cost of capital. The bold LCOE values are the "more likely" cases per type of climate.

Figure A.3: Pre-tax calculations by WorldBankGroup, 2019b for the Levelized Cost of Energy (LCOE) of Floating Photovoltaics (FPV) against ground-mounted PV, divided per climate.

A.3. Empirical PV models identified in literature for prediction of cell and module temperatures

Model author Additional source	**Empirical thermal model**
Ross Jr, 1976 Kamuyu et al., 2018	$T_c = T_a + kG_T$ where $k = \Delta(T_c - T_a)/\Delta G_T$
Rauschenbach, 1980 Kamuyu et al., 2018	$T_c = T_a + (G_T/G_{T,NOCT}) - (T_c - T_{c,NOCT})(1 - \eta_m/\gamma)$
Risser and Eventes, 1984 Kamuyu et al., 2018	$T_c = 3.81 + 0.0282 * G_T * 1.31. * T_a - 165. * V_w$
Schott, 1985 Kamuyu et al., 2018	$T_c = T_a + 0.028 * G_T - 1$
Ross Jr and Smokler, 1986 Kamuyu et al., 2018	$T_c = T_a + 0.035 * G_T$
Lasnier and Ang, 2017 Kamuyu et al., 2018	$T_c = 30.006 + 0.0175(G_T - 300) + 1.14(T_a - 25)$
Duffie and Beckman, 2013 Kamuyu et al., 2018	$T_c = T_a + (G_T/G_{NOCT})(9.5/(5.7 * 3.8 * V_w)) * (T_{NOCT} - T_{a,NOCT})(1 - \eta_m)$
Koehl et al., 2011 Kamuyu et al., 2018	$T_c = T_a + G_T/(U_0 + U_1 * V_w)$
Kurtz et al., 2009 Kamuyu et al., 2018	$T_c = T_a + G_T * e^{-3.473 - 0.0594 * V_w}$
Skoplaki and Palyvos, 2009 Kamuyu et al., 2018	$T_c = T_a + (G_T/G_{NOCT}) * (T_{NOCT} - T_{a,NOCT}) * h_{w,NOCT}/h_w$ $([1 - \eta_{STC}/\tau * \alpha(-\beta_{STC}T_{STC}))$
Faiman, 2008 Micheli, 2022	$T_m = T_a + G_{POA}/(U_0 + U_1) * w_s$
King et al., 2004 Micheli, 2022	$T_c = T_a + G_{POA} * e^{a + b * w_s} + (G_{POA}/1000) * \Delta T$ with $-2.8 < a < -3.6 - 0.04 < b < -1.1$
Veldhuis et al., 2015 Micheli, 2022	$T_m = T_r + (T_r - T_a) * v_w^{\alpha} * h$ with $T_r = T_a + (k + \gamma * (1 - RH)) * G_{POA} - r$
Kamuyu et al., 2018 Micheli, 2022	$T_{FPV1,m} = 2.0458 + 0.9458T_a + 0.0215G_T - 1.2376V_w$ $T_{FPV2,m} = 1.8081 + 0.9282T_a + 0.021G_T - 1.2210V_w + 0.0246T_w$
Hayibo, 2021 Micheli, 2022	$T_{FPV,m} = -13.2554 + 1.2645T_a + 0.0128G_T - 0.0875T_w$

Table A.1: Empirical photovoltaic thermal models. Based on Kamuyu et al., 2018 and Micheli, 2022 (only included are models with complete sources).

Empirical models to estimate PV cell and module temperatures found in literature are presented to identify what parameters are used as inputs and to identify what additional parameters are included in FPV models, which were found to additionally include water temperature measurements.

Models presented are based on the studies of Kamuyu et al., 2018 and Micheli, 2022. Table A.1 presents the PV models, authors and the study it was retrieved from.

Models provided within the study by Kamuyu et al., 2018, calculate cell temperature T_c [^oC], with G_T referring to irradiance on the module [W/m^2], with T_a referring to ambient temperature [^oC], V_w as the wind speed [m/s] and η_m as the module efficiency.

Models provided within the study by Micheli, 2022 present cell and module temperature equations as well as FPV empirical models which also take into account water temperature.

From Faiman, 2008 T_m and T_a are the PV module and ambient temperatures [^oC], w_s is the wind speed [m/s], and U_0 and U_1 are heat loss coefficients.

From King et al., 2004 T_c refers to cell temperature [^oC], T_a refers to ambient temperature [^oC], G_{POA} to solar irradiance on module [W/m^2], w_s to wind speed [m/s], ΔT to temperature difference between the cell and the module back surface at an irradiance level of 1000 W/m^2. And with coefficients a as the empirically-determined coefficient establishing the upper limit for module temperature at low wind speeds and high solar irradiance and b as the empirically-determined coefficient establishing the rate at which module temperature drops as wind speed increases.

From Veldhuis et al., 2015 T_m refers to back surface module temperature [^oC], T_r refers to module temperature due to the radiative heat transfer [^oC], v_w is the wind speed [m/s], α is an empirical exponential factor influencing the impact which the wind speed has on the convective heat transfer, RH is the relative humidity and h is the convective heat transfer coefficient. The Ross coefficient k is an empirical value, relating the irradiance to the PV module temperature T_m. γ is a constant which influences the extent which the RH has on the impact of the irradiance G_POA on the PV module temperature and r s the average temperature difference between the ambient and PV module temperature due to radiative cooling during night time.

From Kamuyu et al., 2018 and Hayibo, 2021 $T_{FPV,m}$ refers to the module temperature of a FPV system [^oC], T_a refers to ambient temperature [^oC], G_T to solar irradiance on module [W/m^2], V_w is the wind speed [m/s] and T_W is the water temperature [^oC]. These last three FPV models, additionally considering water temperature, were selected for further study and comparison with OFPV module temperature performance.

A.4. PV module temperature models expansion

A.4.1. Steady state and Duffie-Beckman thermal models

Firstly the Duffie-Beckman thermal model is investigated as it is considers the influence of wind. In offshore conditions this model could be relevant since high wind speeds can greatly influence the cooling of the panel. This model is an expansion of the steady state model, including the efficiency of the cell as well as the influence of the wind (Smets et al., 2016) It is presented in Equation A.1. In here $T * \alpha$ is taken as 0.9, which considers the absorptivity of the module α.

A simulation is performed with the PV panel characteristics of STC (Standard Testing Conditions) and NOCT to determine the temperatures. This was performed on 25th October, a day with a maximum irradiance reaching 500 W/m^2 and a low presence of cloud coverage.

$$T_M = T_a + \frac{T_{NOCT} - 20^o}{800} G_M \tag{A.1}$$

$$T_M = T_a + \frac{T_{NOCT} - 20^o}{800} G_M \left(\frac{9.5}{5.7 + 3.8 * w_s}\right)\left(1 - \frac{\eta_{cell}}{T * \alpha}\right) \tag{A.2}$$

The simulated temperature differed in a range of 5 degrees Celsius. This could be due to stronger winds simulated rather than actual winds on the test site. The winds where taken from Katwijk and Zee weather station.

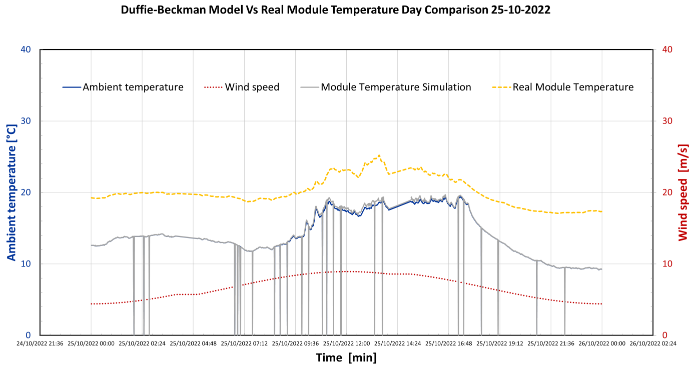

Figure A.4: Duffie-Beckman thermal model comparison with real module temperatures.

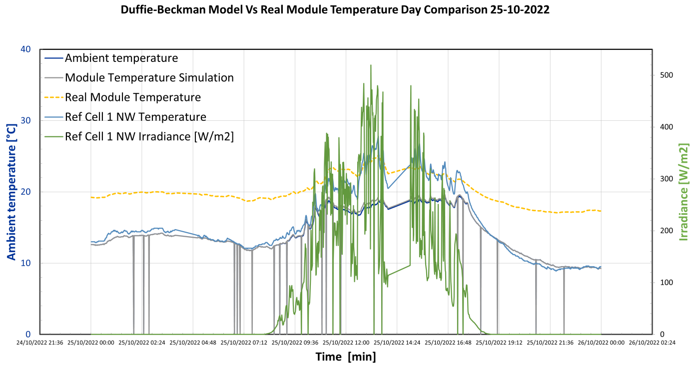

Figure A.5: Duffie-Beckman thermal model comparison with real module temperatures including irradiance.

A.4.2. Fluid dynamic model adaptations for FPV

An accurate fluid dynamic model allows to estimate the module temperature and thus better predict the performance of the PV system. To better understand the parameters affecting module temperatures, and in turn PV performance, the following fluid dynamic model is provided. The fluid dynamic model was developed by Smets et al., 2016. Adaptations are made substituting ground temperature parameters with water temperature parameters. It is assumed the floater temperature corresponds to the water temperature. Depending on the FPV technology, the radiative heat transfer of the back of the module should be adapted with the floater design and material influence between the floater and the water surface.

In this model heat transfer principles are applied. Conduction, convection and radiation principles are used. An overview of the influences that can be considered in this model are presented in Figure A.6. This concept and formulas are derived from the theory of the Solar Book by TUDelft (Smets et al., 2016).

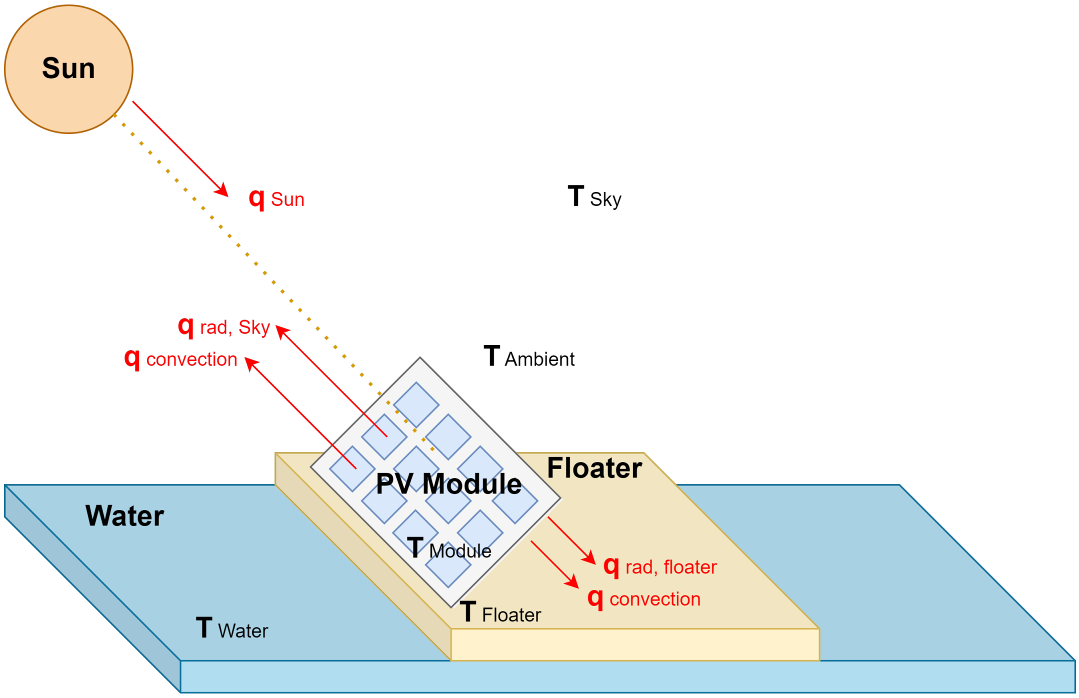

Figure A.6: FPV schematic for fluid dynamic model. Adapted from Smets et al., 2016.

Looking at Figure A.6, direct sun irradiance means the module receives heat from the sun. This is shown in Equation A.3, where α is absorptivity of the module which is related to the reflectivity and efficiency of the module, shown in Equation A.4.

$$H_{SunIrradiance} = \alpha * G_{Module} \tag{A.3}$$

$$\alpha = (1 - R)(1 - \eta) \tag{A.4}$$

Convective heat exchange between the surroundings and the front and rear sides of the modules, assuming each module is separated, is shown in Equation A.5.

$$Convective_{HE} = h_c(T_M - T_a) \tag{A.5}$$

Radiative heat exchange between the upper module and the sky (assuming no water splashing in this explanation) is defined in Equation A.7. It is important to note γ is the Stefan-Boltzmann constant, ϵ_{Top} = 0.84 is the emmissitivity of the modules front glass and ϵ_{Top} = 0.89 as the emmissivity of the back.

$$Ratiative_{HETop} = \epsilon_{Top} * \gamma((T_M)^4 - (T_{Sky})^4 \tag{A.6}$$

$$Ratiative_{HEBack} = \epsilon_{Back} * \gamma((T_M)^4 - (T_{Water})^4 \tag{A.7}$$

Conductive heat transfer between the mounting and the module can be assumed negligible if there is a small size of contact for heat transfer.

Thus, the combination of this heat transfer factors results in the following heat transfer balance in Equation A.8

$$mc\frac{dT_M}{dt} = H_{SunIrradiance} - Convective_{HE} - Ratiative_{HETop} - Ratiative_{HEBack} \tag{A.8}$$

This differential equation assumes the entire module as a single unit mass. However in reality this will differ, since materials throughout the module can vary. This temperature will be higher than the surface temperature. This is since there is heat produced within the cell due to light absorption. Uniform heat distribution approximation is accepted since the heat capacity and the thickness are both low, thus stating an assumption of low thermal resistance of the cell.

The steady state assumption means that module temperature is assumed to be constant for each time step measurement. By assuming steady state then the formula can be rearranged as a function of T_M.

Lineratizaion is done applying the mathematical relation shown in Equation A.9

$$(a^4 - b^4) = (a^2 - b^2)(a + b)(a - b) \tag{A.9}$$

applied to

$$((T_M)^2 + (T_{Sky})^2(T_M + T_{Sky}) \tag{A.10}$$

gives

$$h_{r,Sky} = \epsilon_{Top}\gamma((T_M)^2 + (T_{Sky})^2(T_M + T_{Sky}) \tag{A.11}$$

$$h_{r,Water} = \epsilon_{Back}\gamma((T_M)^2 + (T_{Water})^2(T_M + T_{Water}) \tag{A.12}$$

this makes Equation A.8 to become:

$$0 = \alpha G_M - h_c(T_M - T_a) - h_{r,sky}(T_M - T_{Sky}) - h_{r,Water}(T_M - T_{Water}) \tag{A.13}$$

rearranging gives the final module temperature formulation as:

$$T_M = \frac{\alpha * G + h_c T_a + h_{r,Sky}T_{Sky} + h_{r,Water} * T_{Water}}{h_c + h_{r,Sky} + h_{r,Water}} \tag{A.14}$$

From here, the convective heat transfer coefficients must be calculated. The mixed convective heat transfer coefficient can be defined as:

$$h_{c,top} = h^3_{mixed} = h^3_{forced} + h^3_{free} \tag{A.15}$$

We will now look at the heat transfer at the top and back sides of the module separately: Convective heat transfer for the top surface is given by:

$$h_{forced,laminar} = \frac{0.86Re^{(} - 0.5) * \rho * c_{air} * w}{Pr^{0.67}} \tag{A.16}$$

$$h_{forced,turbulent} = \frac{0.028Re^{(} - 0.2) * \rho * c_{air} * w}{Pr^{0.4}} \tag{A.17}$$

Prandtl number is assumed to be 0.71 for air. The Reynolds (Re) number is defined as:

$$Re = \frac{wD_h}{v} \tag{A.18}$$

with the hydraulic dyameter (D_h) defined as:

$$D_h = \frac{2LW}{L+W} \tag{A.19}$$

When these parameters were investigated, laminar flow was found to occur up to 3 $m/s.$ h_{forced} and w are found to be proportional and can be simplified to:

$$h_{forced,laminar} = w^{0.5} \tag{A.20}$$

$$h_{forced,turbulent} = w^{0.8} \tag{A.21}$$

Now that we have the forced transfer terms, for the free transfer coefficients we can use Nusselt (Nu) and Grashof (Gr) numbers, which express the ratios between convective and conductive heat transfer and buoyancy and viscous forces respectively:

$$Nu = \frac{h_{free}D_h}{k} = 0.21(Gr * Pr)^{0.32} \tag{A.22}$$

with Gr defined as:

$$Gr = \frac{g\beta(T-T_a)D_h^3}{v^2} \tag{A.23}$$

where g is gravitational acceleration and β is the volumetric thermal expansion of air, approximated as:

$$\beta = \frac{1}{T} \tag{A.24}$$

The back convection is calculated by a scaling factor given at INOCT conditions

$$h_{c,back} = R * h_{c,Top} \tag{A.25}$$

with R defined as the following ratio:

$$R = \frac{\alpha G_M - h_{c,Top}(T_{INOCT} - T_a) - \epsilon_{top}\gamma(T_{INOCT}^4 - T_{Sky}^4)}{h_{c,Top}(T_{INOCT} - T_a) + \epsilon_{top}\gamma(T_{INOCT}^4 - T_{Sky}^4)} \tag{A.26}$$

Finally the overall heat transfer coefficient will be:

$$h_c = h_{c,top} + h_{c,back} \tag{A.27}$$

Furthermore the sky temperature on a cloudy day can be assumed to be the same as ambient temperature T_a, however on a sunny day the sky temperature can drop to:

$$T_{Sky} = 0.0552 * T_a^{1.5} \tag{A.28}$$

The wind measurement must be adapted to sea level by:

$$w = w_r(\frac{H_{module}}{H_{Weather_{station}}})^{s_{landscape}} \tag{A.29}$$

With $s_{landscape}$ as the landscape parameter, in this case open sea approximated as 0.16.

The absortivity can be calculate with the module efficiency and the reflectivity (R) being assumed to be 0.1 in:

$$\alpha = (1-R)(1-\eta) \tag{A.30}$$

Finally module absorptivity of top and bottom is ϵ_{Top} is equal to 0.84 and ϵ_{Back} is equal to 0.89.

B

Additional monitoring devices considered

Sensor	Grade	Supplier	Notes
SR30-M2-D1	Class A with heating and tilt	Hukseflux	Additional protection
SR15-D1	Class B with heating	Hukseflux	Additional protection
SR05-D1A3	Class C	Hukseflux	No protection
SR05-D1A3-PV	Class C	Hukseflux	No protection
SMP3	Class C	Kipp and Zonnen	Additional protection
SMP10	Class A with tilt and internal humidity	Kipp and Zonnen	Additional protection
SMP22	Class A most accurate	Kipp and Zonnen	Additional protection

Table B.1: Pyranometers of interest found for this research.

Sensor	Specifications	Supplier
Atonometrics PV Cell	Reference Cell with cell temperature	Atonometrics
Fraunhofer PV Cell	WPVS (N-Type A+) high precission	Fraunhofer
IngenIeurbüro PV Cell	Si-rS485TC-2T w/ cell temperature	IngenIeurbüro
IngenIeurbüro PV Cell	Si-rS485TC-2T w/ cell and ambient temperatures	IngenIeurbüro
IngenIeurbüro PV Cell	Si-rS485TC-2T-v w/ cell, ambient temperatures and wind speed	IngenIeurbüro

Table B.2: Reference cells of interest for this research.

Type	Specifications
PT100	RS PRO PT100 RTD Sensor, 6mm Dia, 35mm Long, 2 Wire, Probe, Class B +250°C Max
PT100	Electrotherm PT100 RTD Sensor, 6mm Dia, 20mm Long, 4 Wire, M6, +200°C Max
PT100	Jumo PT100 RTD Sensor, 25mm Dia, 50mm Long, 3 Wire, Strip Sensor, Class B +180°C Max
PT100	Jumo PT100 RTD Sensor, 25mm Dia, 50mm Long, 3 Wire, Strip Sensor, Class B +180°C Max
PT100	Electrotherm PT100 RTD Sensor, M8 Dia, 40mm Long, M8, F0.3 +200°C Max
PT100	Jumo PT100 RTD Sensor, 5.4mm Dia, 29mm Long, 2 Wire, Wall, Class B +80°C Max
PT100	Electrotherm PT100 RTD Sensor, 4.5mm Dia, 40mm Long, G1/4, F0.3 +200°C Max
PT100	Electrotherm PT100 Sensor 0°C min +200°C max 110mm length x 20mm diameter
PT100	RS PRO PT100 RTD Sensor, 12.7mm Dia, 75mm Long, 4 Wire, Wall, Class B +150°C Max

Table B.3: Thermal sensors for water and ambient temperatures of interest for this research

Sensor	Specifications
PT100	Self-Adhesive Patch PT100 Sensor with PFA insulated outer jacket
PT100	RS PRO PT100 RTD Sensor, 13mm Dia, 40mm Long, 4 Wire, Patch Sensor, Class B +150°C
PT100	RS PRO PT100 RTD Sensor, 6mm Dia, 35mm Long, 2 Wire, Probe, Class B +250°C
PT100	RS PRO PT100 RTD Sensor, 30mm Long, Patch Sensor, +150°C
PT100	Electrotherm PT100 RTD Sensor, 12mm Dia, 4mm Long, Patch Sensor, F0.3 +90°C
PT100	RS PRO PT1000 RTD Sensor, 15mm Dia, 30mm Long, 2 Wire, Patch Sensor, Class B +150°C
PT100	Jumo PT100 RTD Sensor, 5.4mm Dia, 29mm Long, 2 Wire, Wall, Class B +80°C
PT100	Electrotherm PT100 RTD Sensor, 4.5mm Dia, 40mm Long, G1/4, F0.3 +200°C
PT100	Electrotherm PT100 Sensor 0°C min +200°C max 110mm length x 20mm diameter
PT100	RS PRO PT100 RTD Sensor, 13mm Dia, 40mm Long, 4 Wire, Patch Sensor, Class B +150°C
PT100	Electrotherm PT100 RTD Sensor, 3mm Dia, 50mm Long, Probe, F0.3 +400°C
PT100	RS PRO PT100 RTD Sensor, 12.7mm Dia, 75mm Long, 4 Wire, Wall, Class B +150°C

Table B.4: Thermal sensors for module and ambient temperatures of interest for this research.

Sensor	Specifications	Supplier
DustIQ	Optical soiling sensor self-solar powered	Kipp and Zonen
Mars	Optical soiling sensor	Atonometrics

Table B.5: Optical soiling sensors of interest found for this research.

C

Methodology additional information

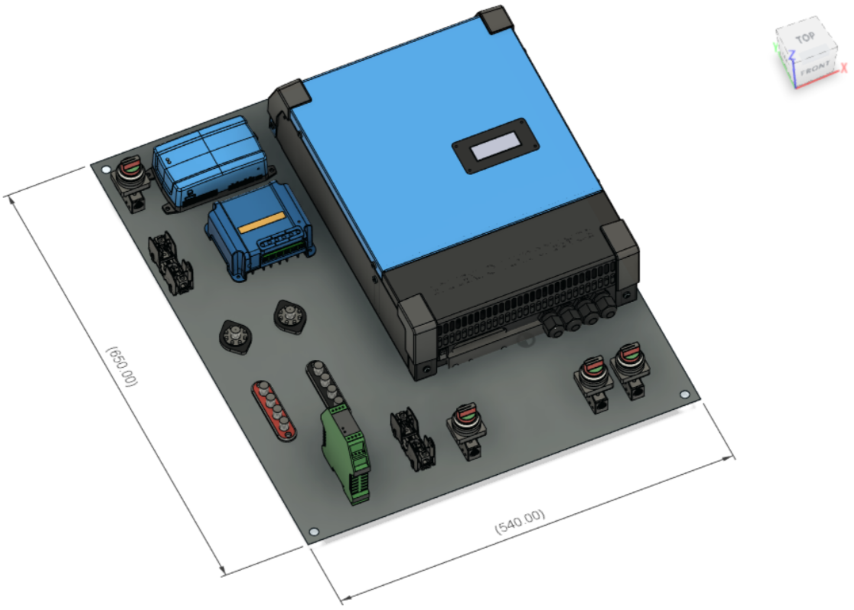

Figure C.1: Layout of power box off-shore components in Fusion360 (CAD). Dimensions in mm.

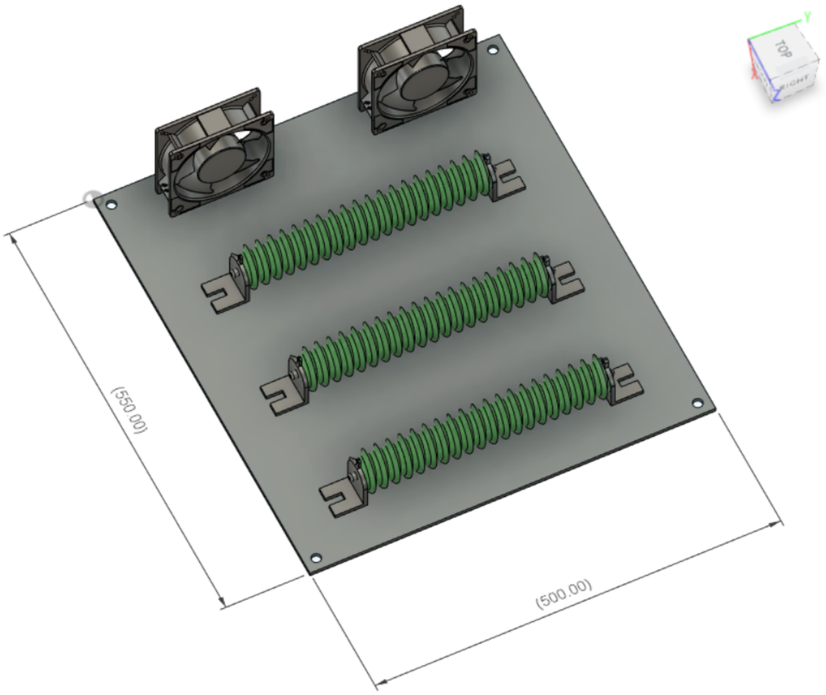

Figure C.2: Layout of resistors box off-shore components in Fusion360 (CAD). Dimensions in mm.

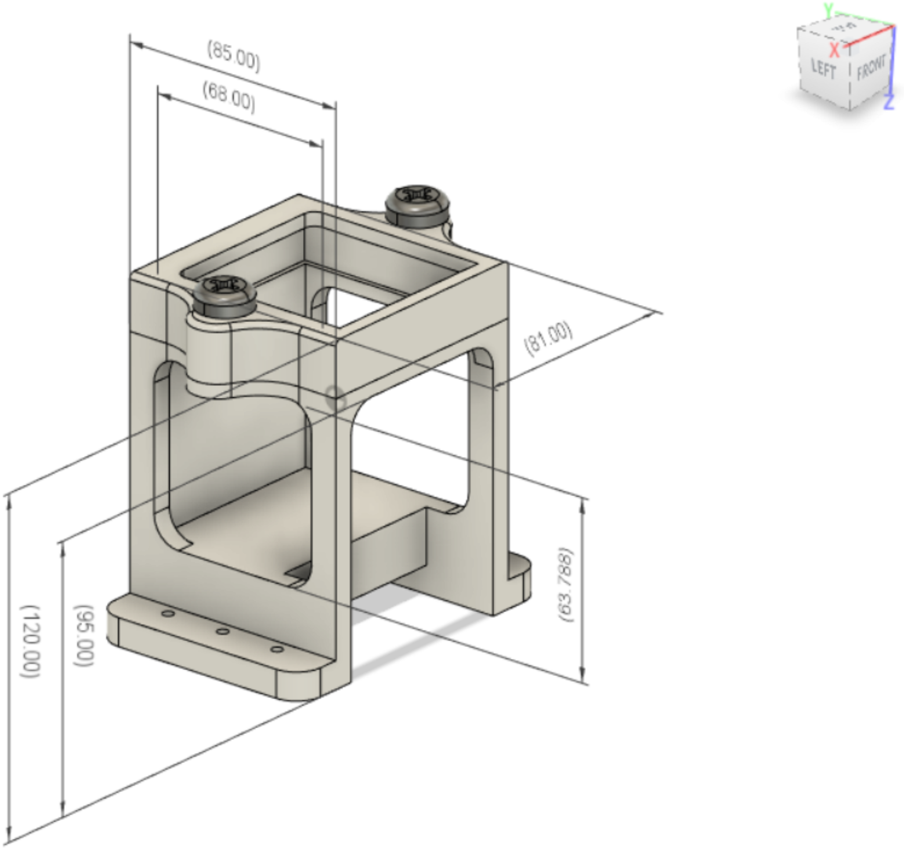

Figure C.3: Power meter mount designed in Fusion360 (CAD). Dimensions in mm.

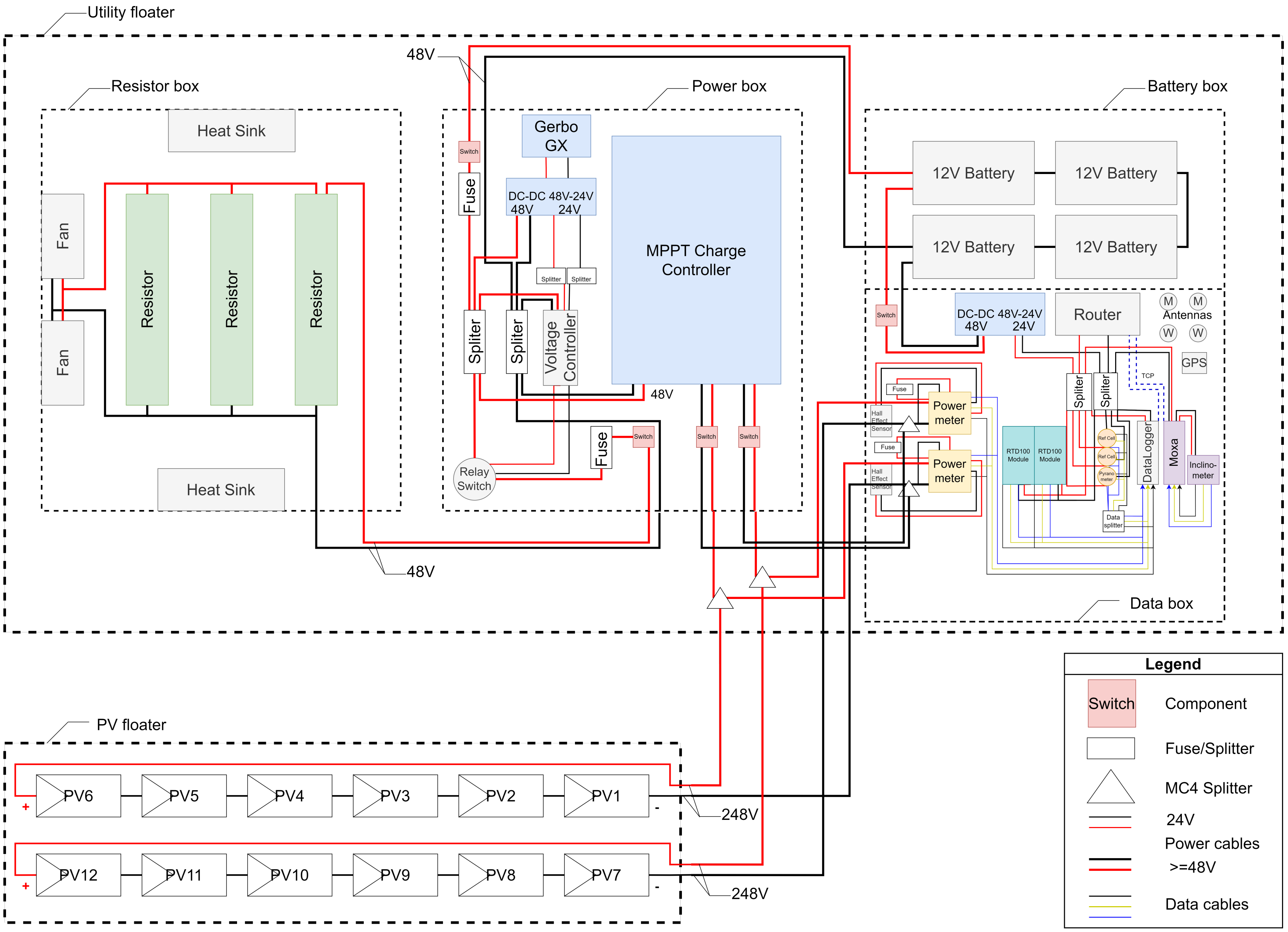

Figure C.4: Single line diagram for PV system off-shore enlarged. Components not to size.

C.1. Loss of Load probability additional calculation

The loss of load probability (LLP) is an additional calculation that can be used to determine the chances of the storage system being depleted due to a system failure and not being able to power the monitoring devices. As described by Smets et al., 2016, this concerns the chance of the PV system not being able to deliver enough energy to avoid full discharge of the batteries. This energy that the PV system was not able to deliver to the electric load, is referred as E_{fail}. The energy that was not used by the battery, when they were full, and thus in this experiment was sent to the dissipation unit, was called E_{dump}. For a latitude between 50^o and 60^o, 15 days of autonomy are recommended Smets et al., 2016. This first term is then divided by the load power required over a year. As a reference, the recommended LLP for telecommunication systems is 10^{-4} and for appliances is in the range 10^{-1} Smets et al., 2016. The lower this number, the more stable and reliable the system is. The LLP is presented in equation C.2. 15 days of autonomy correspond to 360 hours, which was the value used in this case for the PV system being unable to power the load due to a system failure. It was assumed for the case in which a cable or device failed, and an off-shore reparation could take place within this time (15 days). Knowing the total energy consumption of the monitoring devices, the specific LLP can be found. If the LLP result was in the range between 10^{-1} and 10^{-2}, the LLP could be considered acceptable.

$$LLP = \frac{E_{fail}}{\int_0^{365} P_L(t)dt} \tag{C.1}$$

$$LLP = \frac{E_{fail}}{\int_0^{8760h} P_L(t)dt} = \frac{6.8kWh}{164.7kWh} = 0.041 \tag{C.2}$$

D

Meteonorm outputs

Table D.1 presents the most relevant values for the months of November and December both off-shore and on-land.

Location	Month	GHI [kWh/m^2]	DHI [kWh/m^2]	DNI [kWh/m^2]	T_a [C^o]	Wind [m/s]
On-land	November	24	16	27	7,5	3,9
Off-shore	November	23	15	29	8,7	6,4
On-land	December	16	11	24	3,8	4,4
Off-shore	December	16	11	25	5,7	6,9

Table D.1: Meteonorm results for the months of November and December

This outcomes yield very similar results as the location differs only on 20 km. Radiance simulations are performed facing the South-East orientation (azimuth at 150 ^{o} with respect to North) and at a set angle of 4^o. This is since this orientation (South) faces the highest values for irradiance, which are critical when comparing and sizing the PV system. The estimated monthly radiation for both locations is displayed in Table D.1. Very similar results are obtained in this case. Furthermore, the daily global irradiation outputs are presented.

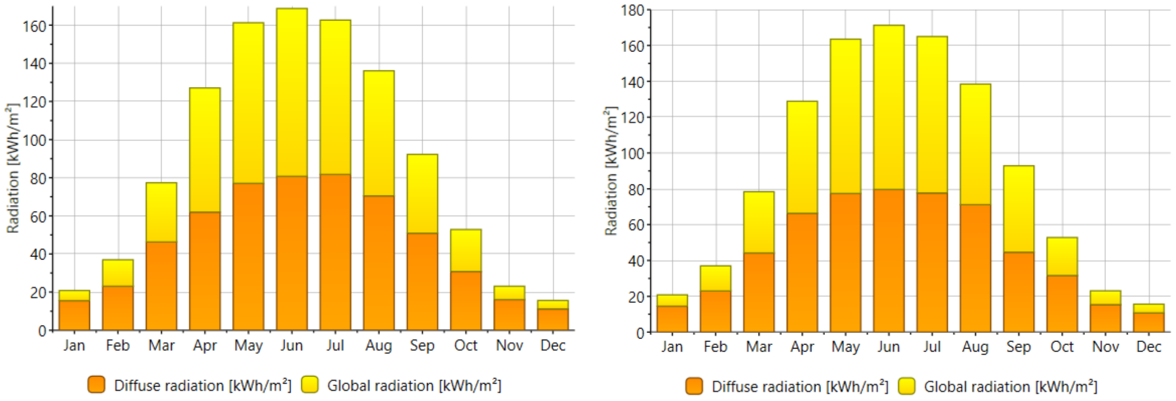

(a) Meteonorm estimated annual incoming radiation for the on-land location.

(b) Meteonorm estimated annual incoming radiation for the off-shore location.

Figure D.1: Irradiance predicted by Meteonorm for on-land (left) and off-shore (right) with azimuth 150 ^{o} with respect to North and an inclination of 4 ^{o}.

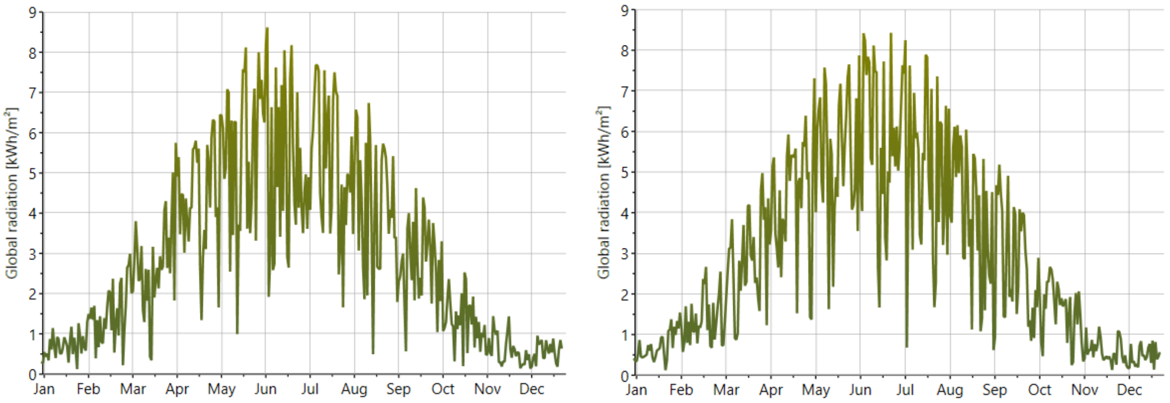

(a) Meteonorm estimated daily global radiation for the on-land location.

(b) Meteonorm estimated daily global radiance for the off-shore location.

Figure D.2: Daily global radiance predicted by Meteonorm for on-land (left) and off-shore (right) with azimuth 150 ^{o} with respect to North and an inclination of 4 ^{o}.

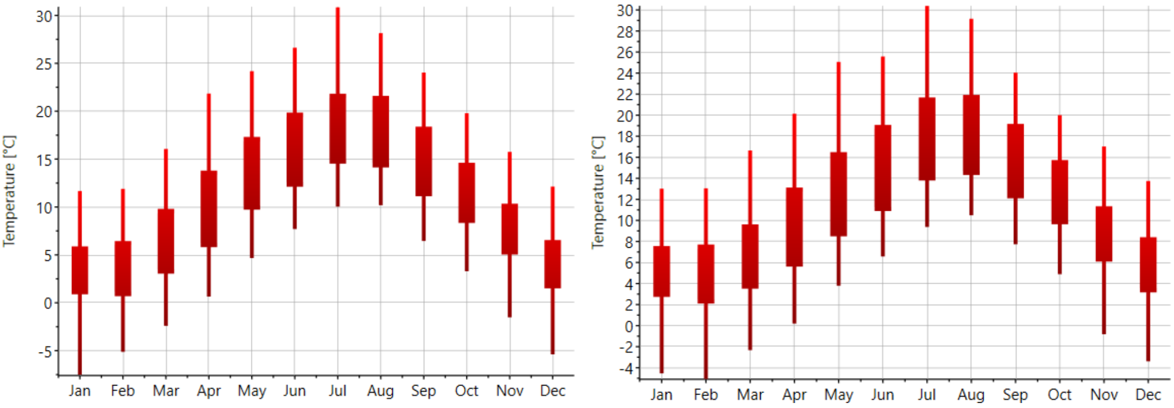

(a) Meteonorm boxplot of monthly predicted temperatures for the on-land location.

(b) Meteonorm boxplot of monthly predicted temperatures for the off-shore location.

Figure D.3: Box-plot of ambient temperatures predicted by Meteonorm for on-land (left) and off-shore (right).

E

Additional results

E.1. Sensors operational status during experiment period

During the experiment period from 15-11-2022 to 1-1-2023, 56 measurements were taken directly from each PV system, all in 1 minute time-steps with the exception of the inclination measurements, which where taken in a frequency of 1 Hz. Additionally 5 measuremnts concerning wind, water and wave data was also retrieved externally from KNMI, having a 10 minute time-step.

A total of 32 thermal measurements were taken directly from the system set ups. 17 measurements off-shore and 15 thermal measurements on-land. Their working or non working status, or data issues for each measurement is shown in Table E.1.

Furthermore, an additional 24 data measurements where taken offshore and 11 data measurements on land. This concern power, voltage, current, inclination, irradiance, standard deviation of measurements from device and MPPT controller states. These data measurements and their working status during the period of research are stated in Table E.2.

ID	Temperature	Unit	Location	Off-shore	On-land
1	Module	C	Module 2	Working	Working
2	Module	C	Module 4	Working	Working
3	Module	C	Module 6	Data errors	Working
4	Module	C	Module 7 - top right	Working	Data errors
5	Module	C	Module 7 - top left	Working	Working
6	Module	C	Module 7 - bottom right	Working	Working
7	Module	C	Module 7 - bottom left	No data	Working
8	Module	C	Module 7 - middle	Data errors	Working
9	Module	C	Module 9	Working	Working
10	Module	C	Module 11	Working	Data errors
11	Ambient	C	Reference cell North-West	Working	Working
12	Ambient 2	C	Reference cell South-East	Influenced by irradiance	-
13	Water	C	Floater side	Influenced by connection	-
14	Carrier relay	C	Power box	Working	-
15	Data box	C	Data box	-	Working
16	Reference cell body	C	Ref Cell NW	Working	Working
17	Reference cell body	C	Ref Cell SE	Working	Working
18	Pyranometer body	C	Ref Cell SE	Working	Working

Table E.1: Thermal sensor operational status during period of research from 15-11-2022 to 23-11-2023.

ID	Data measurement	Unit	Device	Off-shore	On-land
1	Power North-West string	W	Power-meter	Working	Working
2	Power South-East string	W	Power-meter	Working	Working
3	Voltage North-West string	V	Power-meter box	Working	Working
4	Voltage South-East string	V	Power-meter	Working	Working
5	Current North-West string	A	Power-meter	Working	Working
6	Current South-East string	A	Power-meter	Working	Working
7	Floater inclination in X axis	V to ^{o}	Inclinometer	Working	-
8	Floater inclination in Y axis	V to ^{o}	Inclinometer	Working	-
9	Irradiance North-West	W/m^2	Reference cell	Working	Working
10	Irradiance South-East	W/m^2	Reference cell	Working	Working
11	Global Horizontal Irradiance	W/m^2	Pyranometer	Working	Working
12	Pyranometer standard deviation	$-$	Pyranometer	Working	Working
13	Voltage DC-DC converter	V	Pyranometer	Working	Working
14	MPPT Controller Output Power	W	MPPT Controller	Working	-
15	MPPT Controller Output Voltage	V	MPPT Controller	Working	-
16	MPPT Controller Output Current	A	MPPT Controller	Working	-
17	MPPT Controller Input Power	W	MPPT Controller	Working	-
18	MPPT Controller Tracker 1 Power	W	MPPT Controller	Working	-
19	MPPT Controller Tracker 1 Voltage	V	MPPT Controller	Working	-
20	MPPT Controller Tracker 1 Current	A	MPPT Controller	Working	-
21	MPPT Controller Tracker 2 Power	W	MPPT Controller	Working	-
22	MPPT Controller Tracker 2 Voltage	V	MPPT Controller	Working	-
23	MPPT Controller Tracker 2 Current	A	MPPT Controller	Working	-
24	MPPT Controller Charge State	$-$	MPPT Controller	Working	-

Table E.2: Sensors operational status during period of research from 15-11-2022 to 23-11-2023.

E.2. Additional data from KNMI weather station HKZA

ID	Data	Unit	Time-step	Off-shore	On-land
1	Wave height	cm	10 min	Available	Not available
2	Swell height	cm	10 min	Available	Not available
3	Wind speed	m/s	10 min	Available	Not available
4	Wind speed reference 10 meters	m/s	10 min	Available	Not available
5	Wind direction	^{o}	10 min	Available	Not available
6	Wind gust	m/s	10 min	Available	Not available
7	Water temperature	^oC	10 min	Available	Not available

Table E.3: Data retrieved from KNMI weather station HKZA from 15-11-2022 to 1-1-2023.

E.3. Additional power graphs

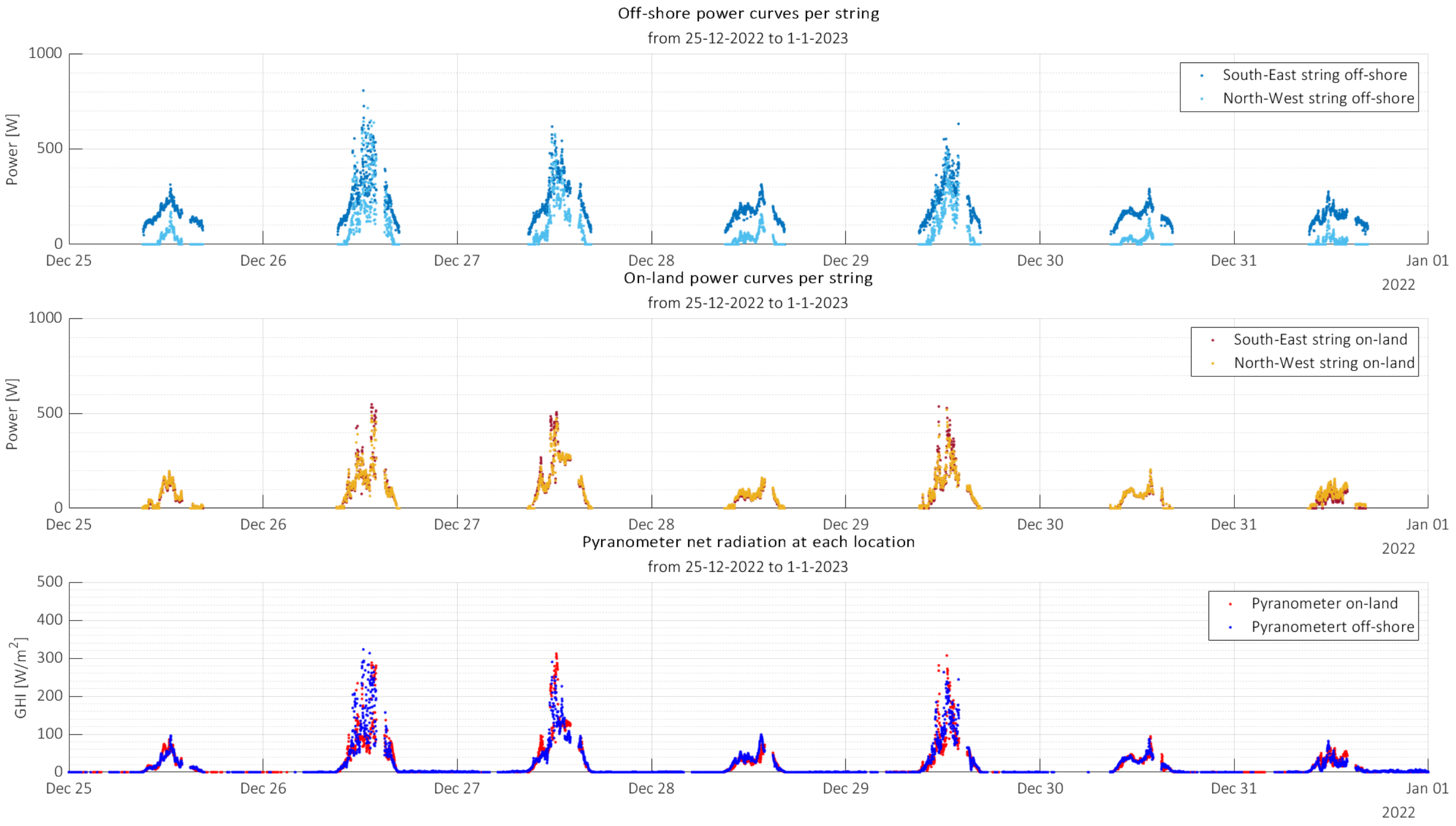

Figure E.1: Power performance of each string for the on-land and offshore systems, provided with GHI from pyranometer measurements at each location for a week, from 25-12-2022 until 1-1-2023.

E.4. Additional voltage and current graphs

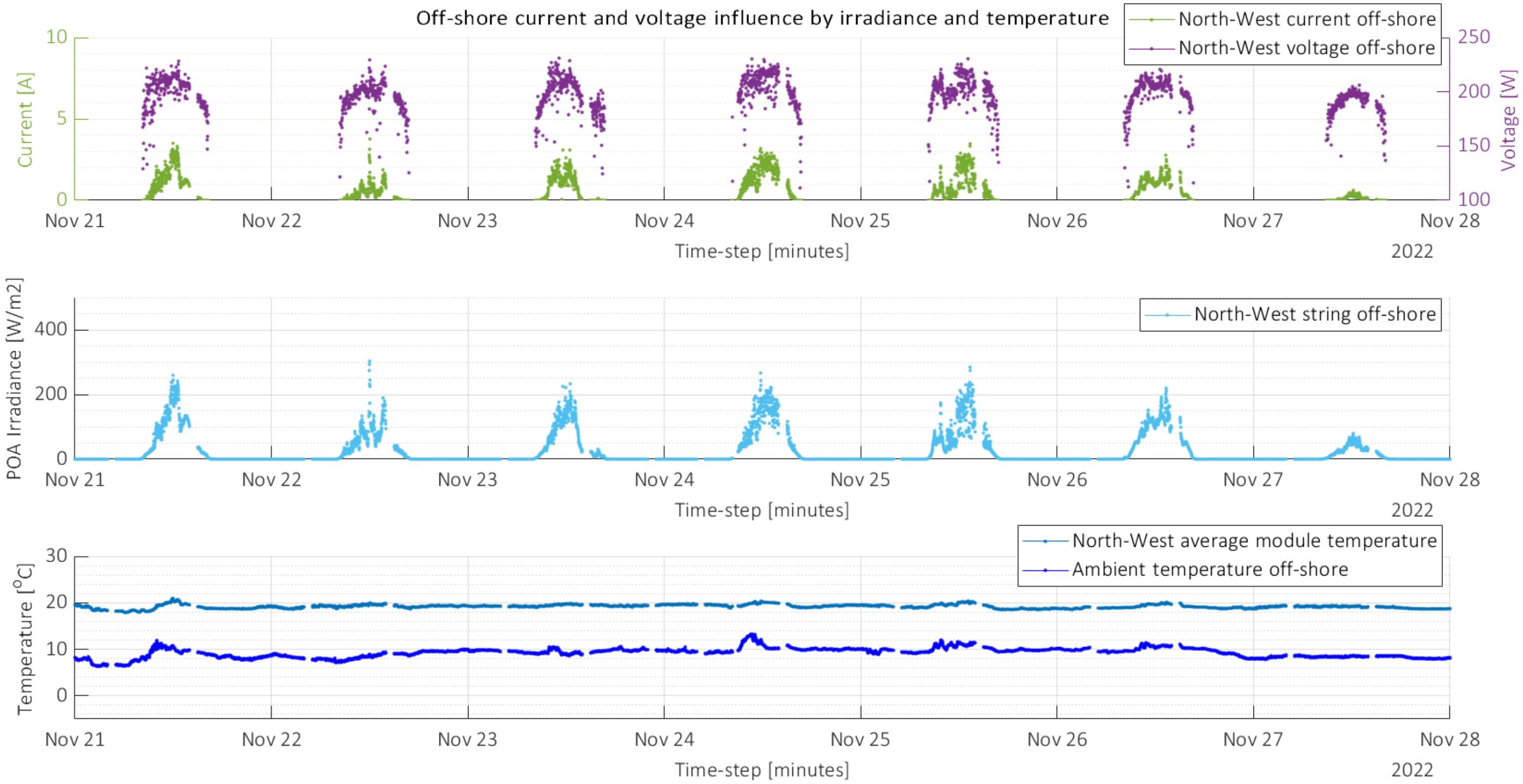

Figure E.2: Off-shore voltage and current measurements coupled with POA irradiance and surrounding temperatures for North-West string during a week, from 21-11-2022 until 28-11-2022.

E.5. Irradiance at the Plane of Array comparison for each PV system

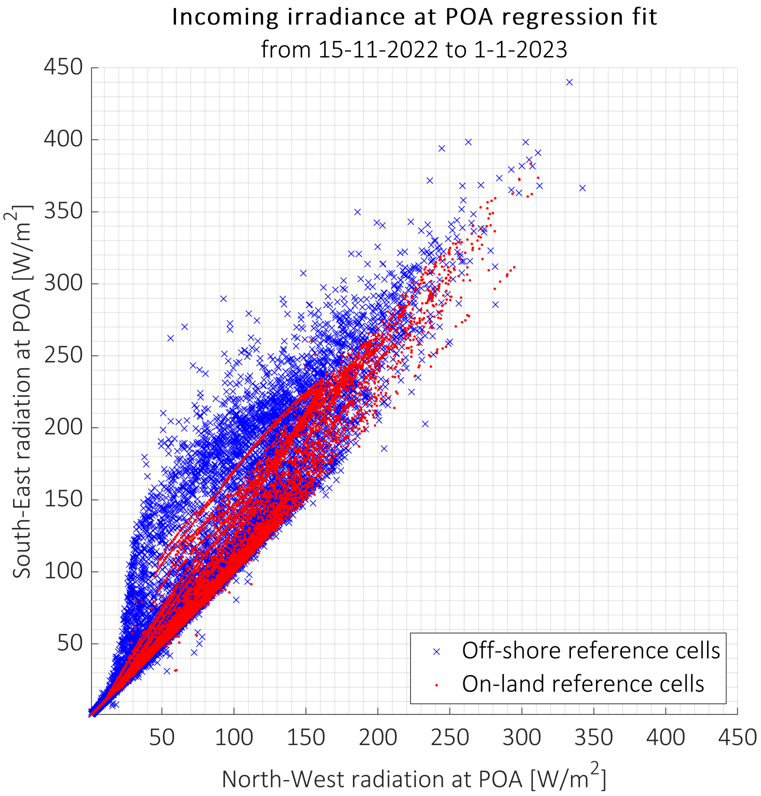

Figure E.3: Measured irradiance at POA regression fit for the PV strings of each system. Off-shore system shown in blue and on-land system in red.

E.6. Calculation of module efficiencies

Module efficiency were theoretically derived through a model provided in (Smets et al., 2016). Since in the experimental set ups, power was not measured per module, but only per string, this was used to provide an estimation of what the module efficiencies are at each orientation were expected to be, from theory. The input parameters were the module characteristics ($V_{OC}(STC)$, $I_{SC}(STC)$, FF, A_M), the ambient temperatures recorded (T) and the irradiance level (G_M) perceived by the module. By combining the effects of module temperature and light intensity for c-Si, the module efficiency was derived with Equation E.6. It is important to mention this method does not use power measurements as an input. The equations from (Smets et al., 2016) were inplemented in Matlab, and experimental measurements were used to calculate the module efficiency.

Firstly, module efficiency only taking into account irradiance, module characteristics and ambient temperature was given by:

$$\eta(25^oC, G_M) = \frac{P_{MPP}25^oC, G_M}{G_M A_M} \tag{E.1}$$

which was derived from:

$$V_{OC}(25^oC, G_M) = V_{0C}(STC) + \frac{nk_bT}{q} * ln(\frac{G_M}{G_{STC}}) \tag{E.2}$$

$$I_{SC}(25^oC, G_M) = I_{SC}(STC) * \frac{G_M}{G_{STC}} \tag{E.3}$$

$$P_{MPP}(25^oC, G_M) = FF * V_{OC}(25^oC, G_M) * I_{SC}(25^oC, G_M) \tag{E.4}$$

Combination of the calculated module efficiency at STC with the module temperatures was done though Equation E.6.

$$\eta(T_M, G_M) = \eta(25^o, G_m)[1 + k(T_M - 25^oC)] \tag{E.5}$$

It is important to note that for c-Si, k was be taken as -0.0035/^oC (Smets et al., 2016) and the ideality factor (n) was assumed to be 1.5 for c-Si.

Moreover, the input measurements for this calculations from data collected were: Ambient temperature off-shore and on-land recorded at each site, irradiance from each reference cell at each POA of the modules for each location and string, and module temperatures for determining the efficiency at each orientation and location, which were averaged per string. Therefore a module average module temperature was obtained for the North-West and South-East strings for both on-land and off-shore systems. It is important to note only measurements between sun-rise and sun-set for module, ambient and irradiance measurements were used. This was for the period from 15-11-202 to 1-1-2023. Results are provided in Table 5.5.

Additionally, Equation E.1 could be substituted with Equation E.6. However the values of a and b, which depend on a proportionality factor λ, current and fill factor, should be determined experimentally and this was outside the scope for this research.The complete derivation is in (Smets et al., 2016) Equation E.1, The equation was provided in case further investigations were developed for efficiency purposes.

$$\eta(25^oC, G_M) = a * ln(G_M) + b \tag{E.6}$$

To clearly present how module temperature affects efficiency, Figure E.4 and Figure E.5 are presented to show how the efficiency from equation E.1, where module efficiency only takes into account irradiance at POA (G_M), compares with Equation , which takes into account module temperature (T_M). This effieicencies are presented for the South-East string orientations. The complete overview for derived module efficiencies can be found in the results section. In conclusion, lower module temperatures increase efficiency, and thus, on-land module temperatures registered for the period of research were lower than module temperatures off-shore. Thus higher efficiencies are achieved per module. Neverthelesss, lower variance in module temperature off-shore showcase a stable module efficiency off-shore.

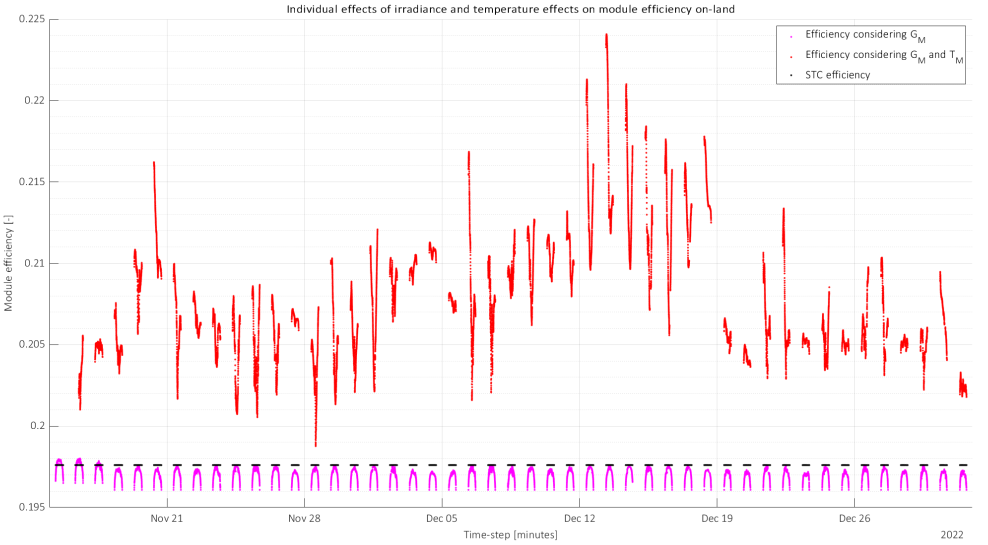

Figure E.4: Module efficienies comparing influence of irradiance and module temperature off-shore for South-East string, from 15-11-2022 to 1-1-2022

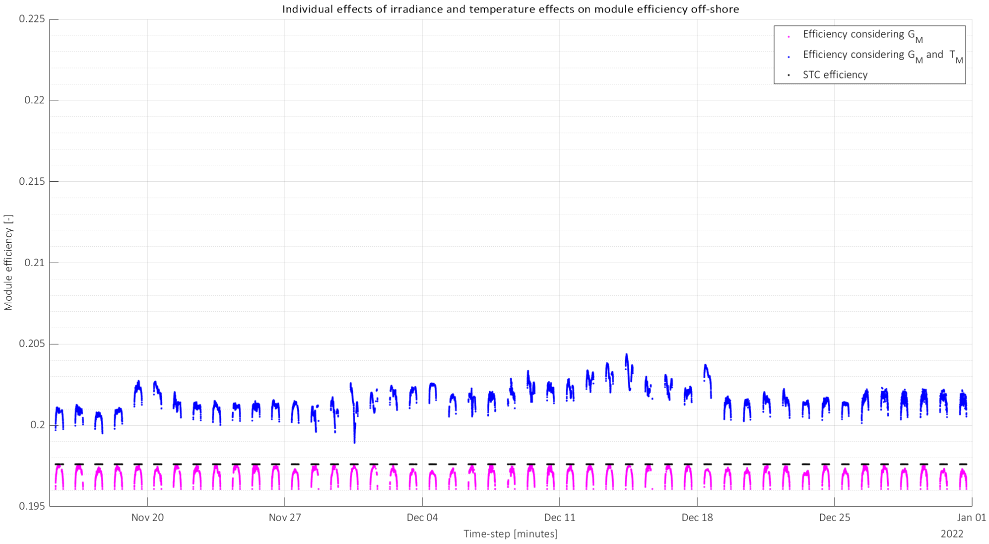

Figure E.5: Module efficiencies comparing influence of irradiance and module temperature off-shore for South-East string, from 15-11-2022 to 1-1-2022

E.7. Additional power and irradiance comparison between PV strings

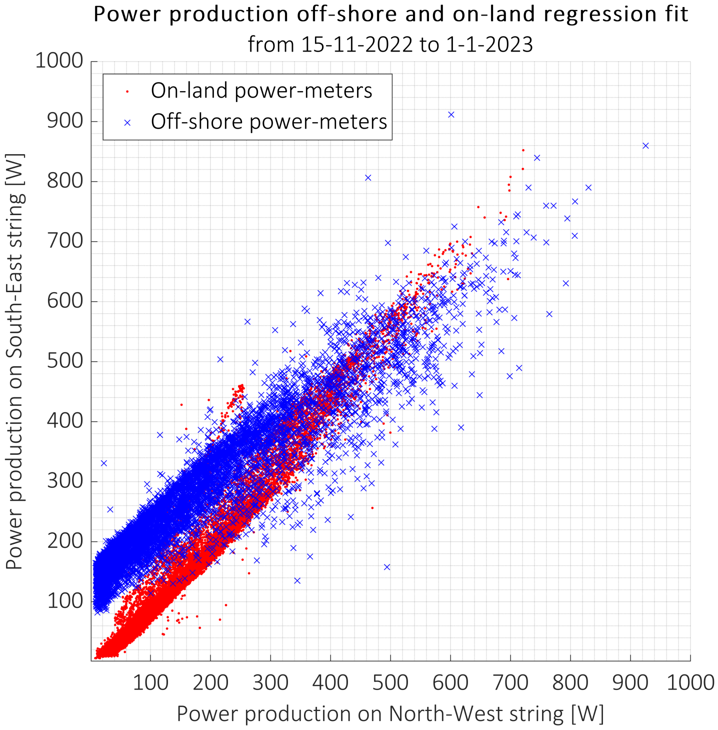

Figure E.6: Power regression fit for both systems off-shore (blue) and on-land (red) from 15-11-2022 to 1-1-2023.

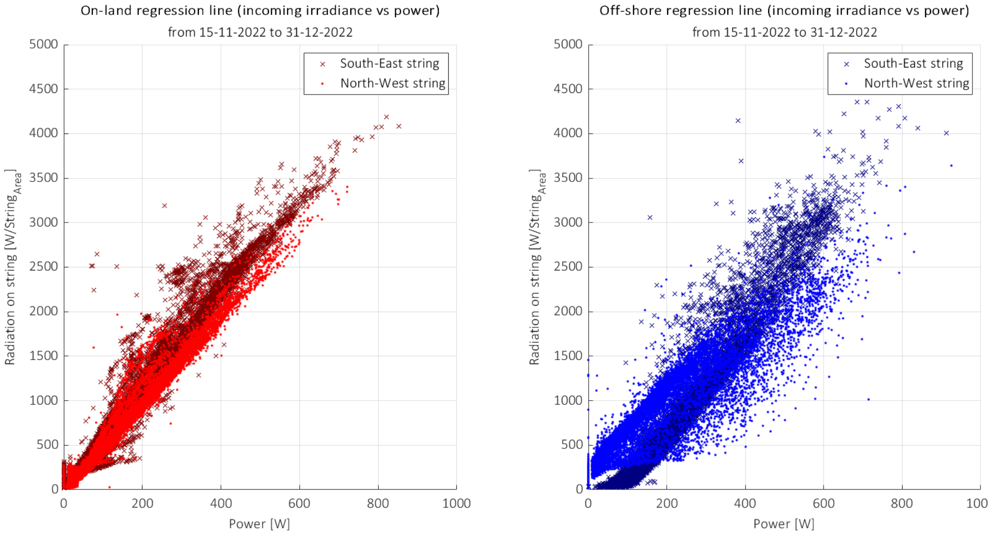

Figure E.7: PV string comparison of power production against incoming irradiation on POA surface of total string (6 panels) for both on-land and off-shore.

E.8. Additional PV energy graphs

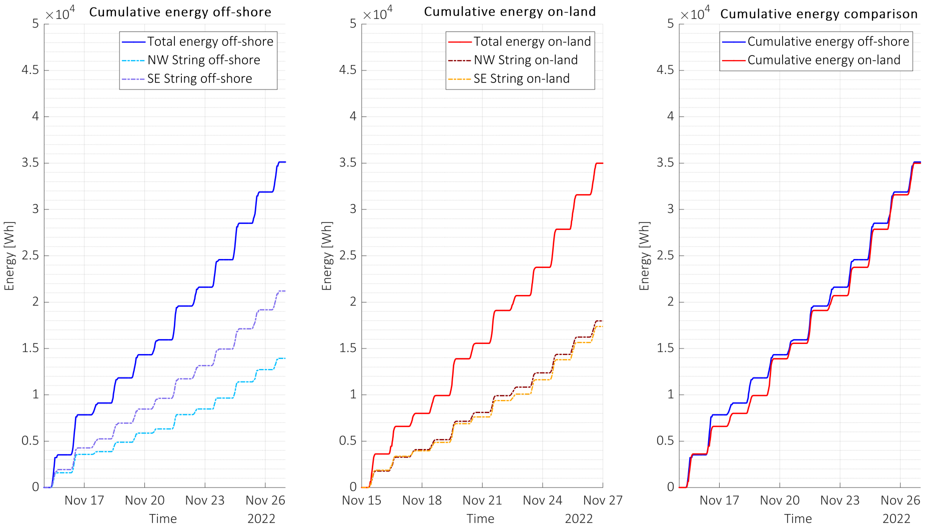

Figure E.8: Cumulative energy outputs from power meters off-shore (left) and on-land (right) for the initial two weeks, from 15-11-20222 to 28-11-2022.

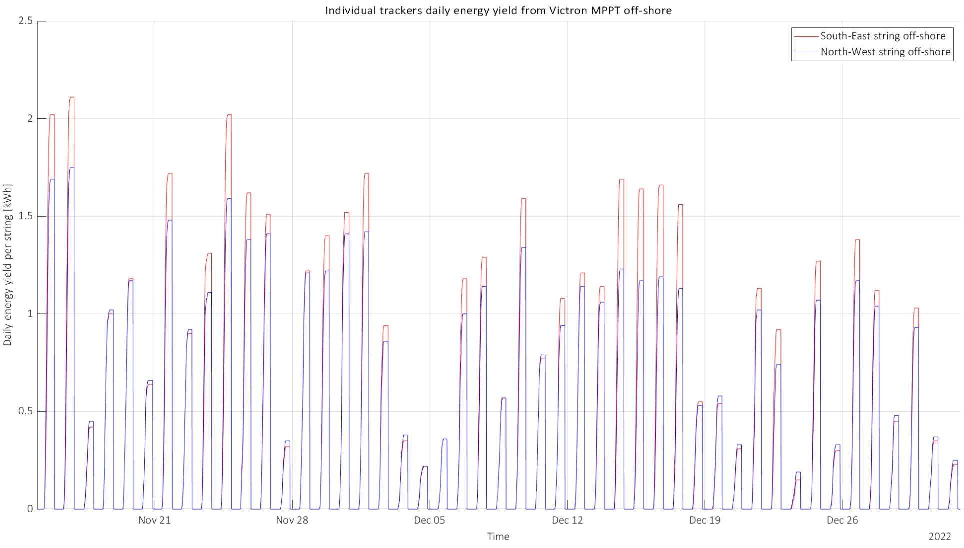

Figure E.9: MPPT controller outputs for individual strings off-shore daily energy yield, from 15-11-2022 to 1-1-2023.

E.9. PT100 test experiment: PT100 measurements of off-shore system before deployment

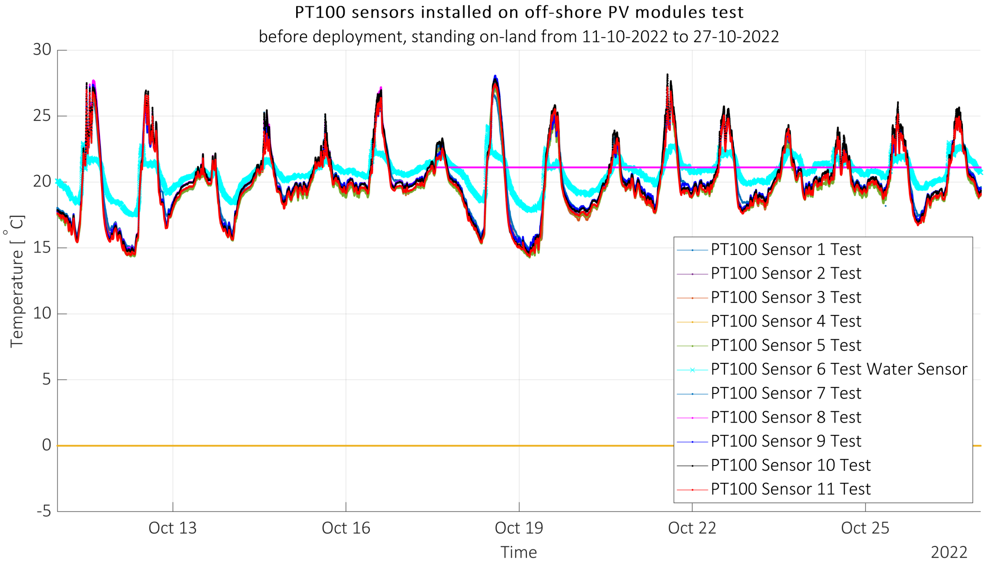

Figure E.10: PT100 sensors installed test for off-shore system, before deployment, standing on-land, with data from 11-10-2022 to 27-10-2022.

E.10. Ambient temperature and irradiance influence on module temperatures

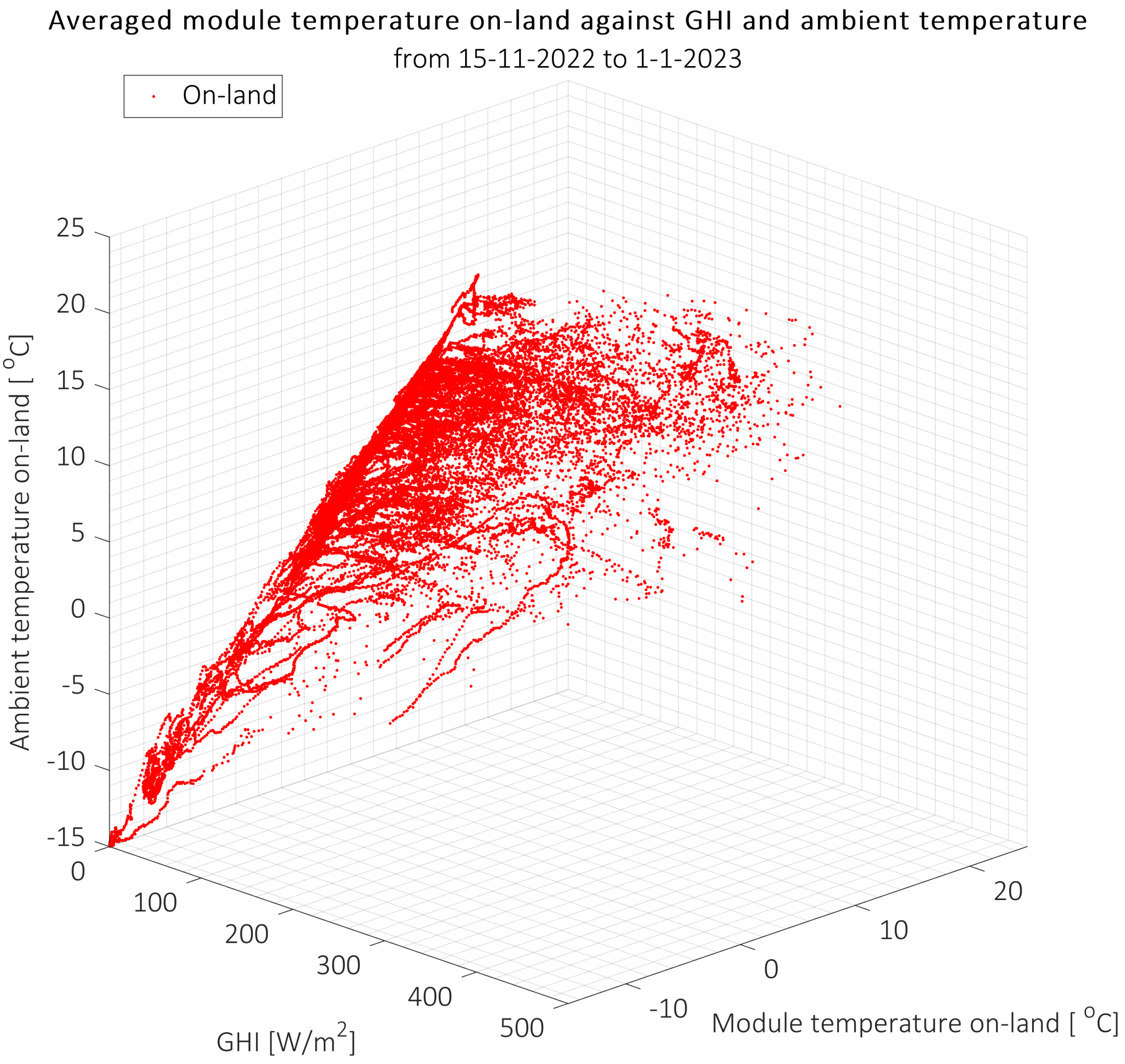

Figure E.11: Averaged module temperature against GHI and ambient temperature on the on-land system, with data from 15-11-2022 to 1-1-2023.

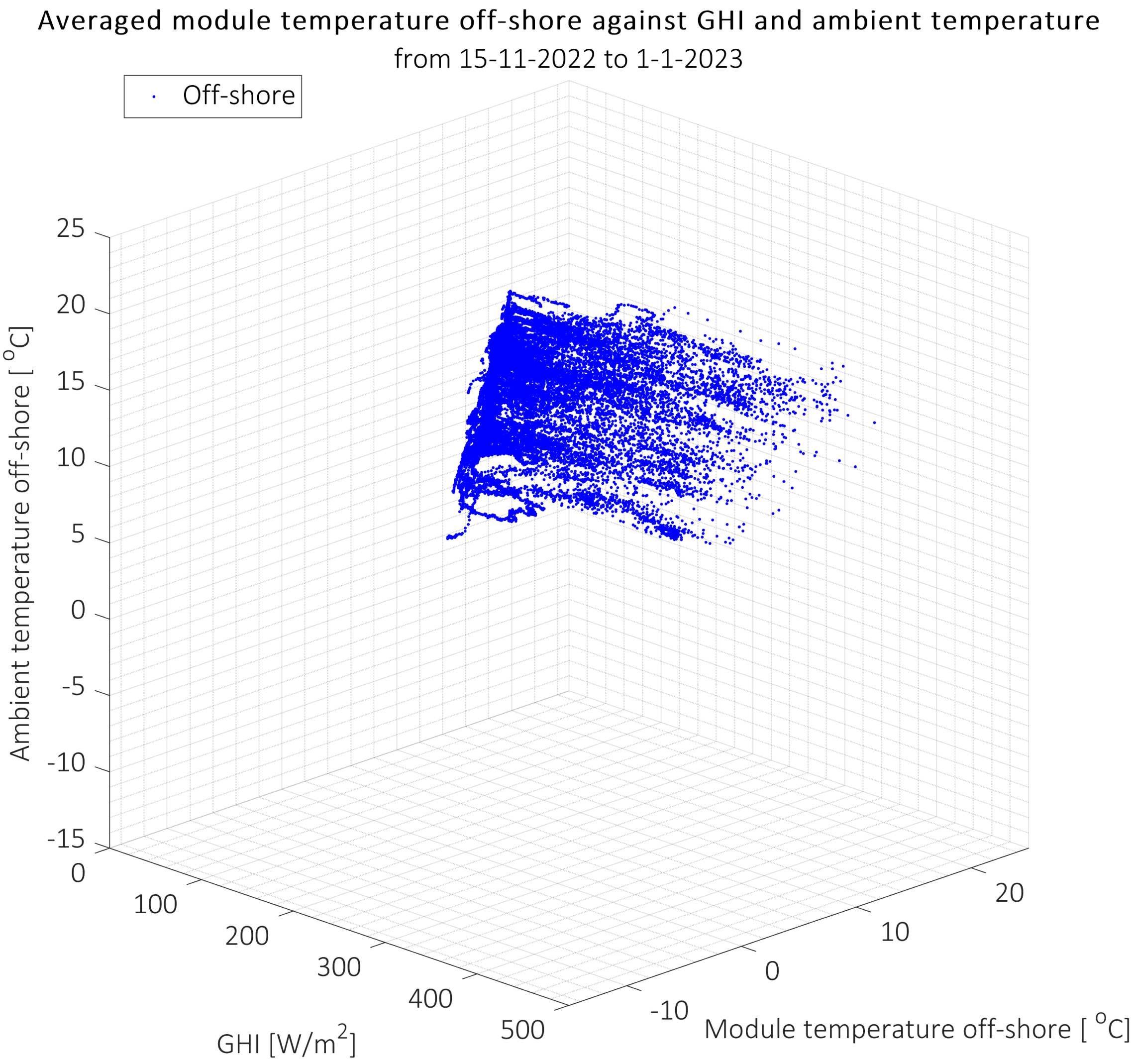

Figure E.12: Averaged module temperature against GHI and ambient temperature on the off-shore system, with data from 15-11-2022 to 1-1-2023.

E.11. OFPV linear regression PV thermal models additional information

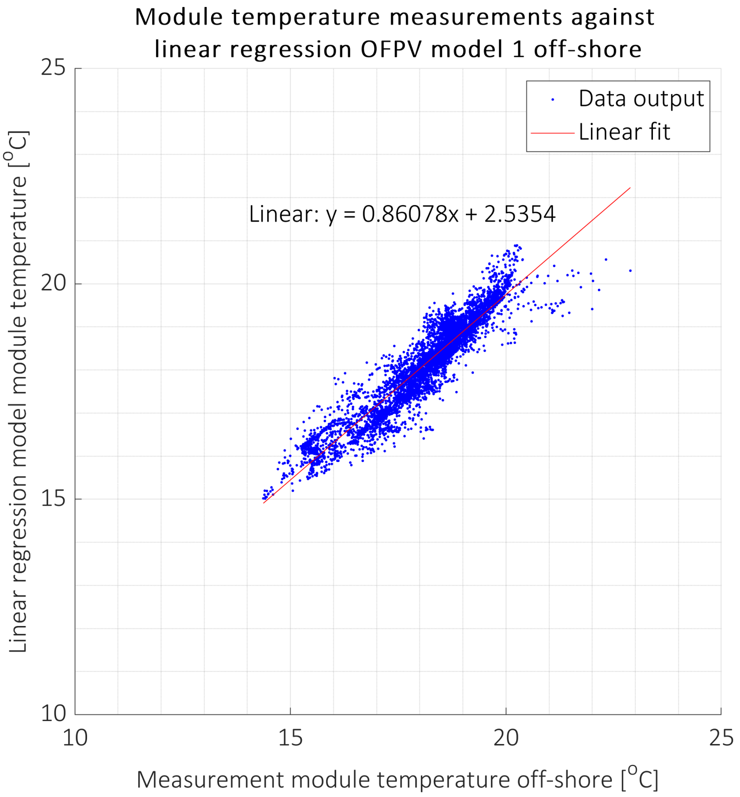

Figure E.13: Regression fit of module temperatures measured off-shore against empirical OFPV module temperature model 1 from 14-11-2022 to 1-1-2023.

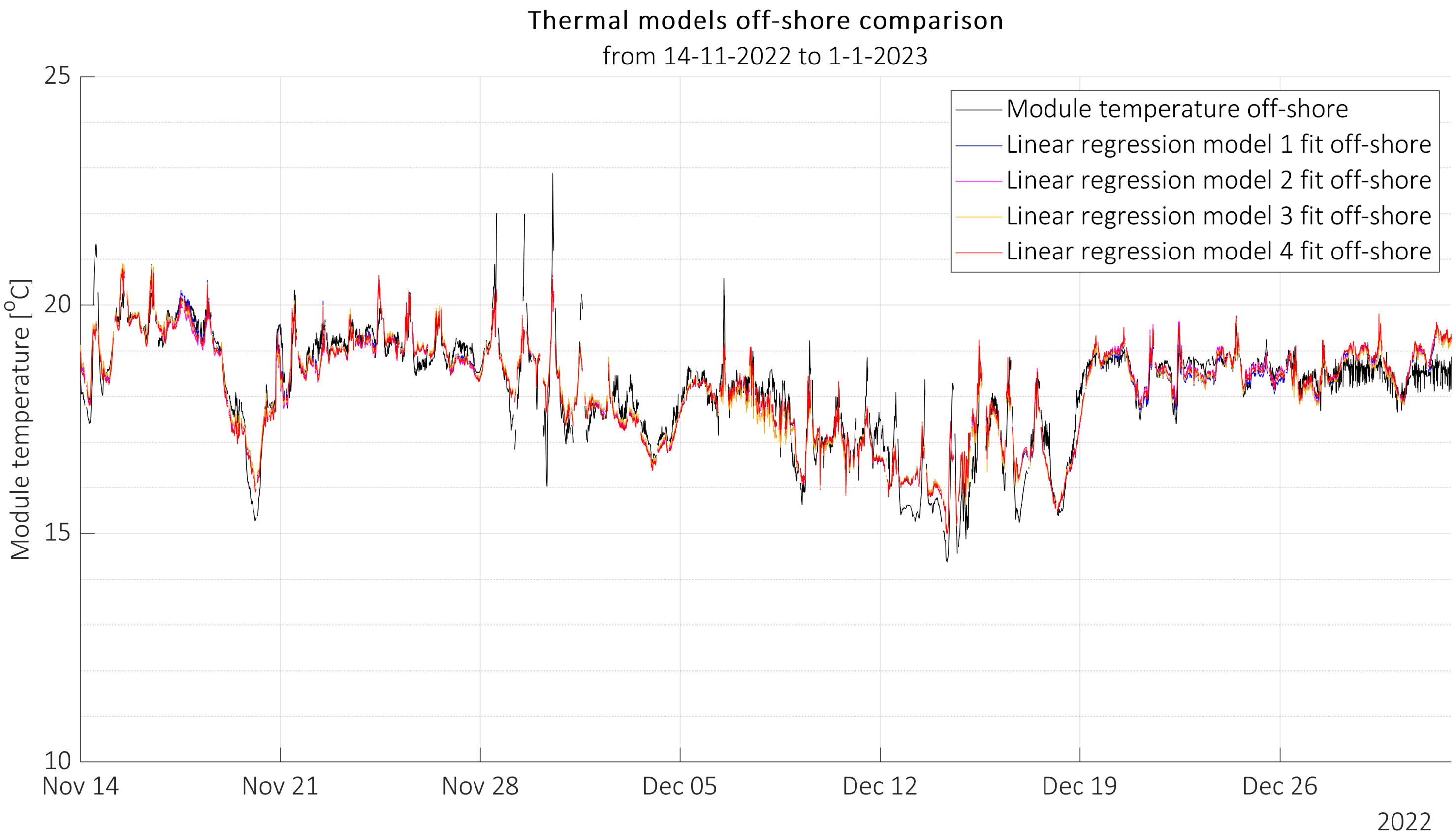

Figure E.14: Module temperatures measured off-shore against empirical module temperature OFPV models from 14-11-2022 to 1-1-2023.

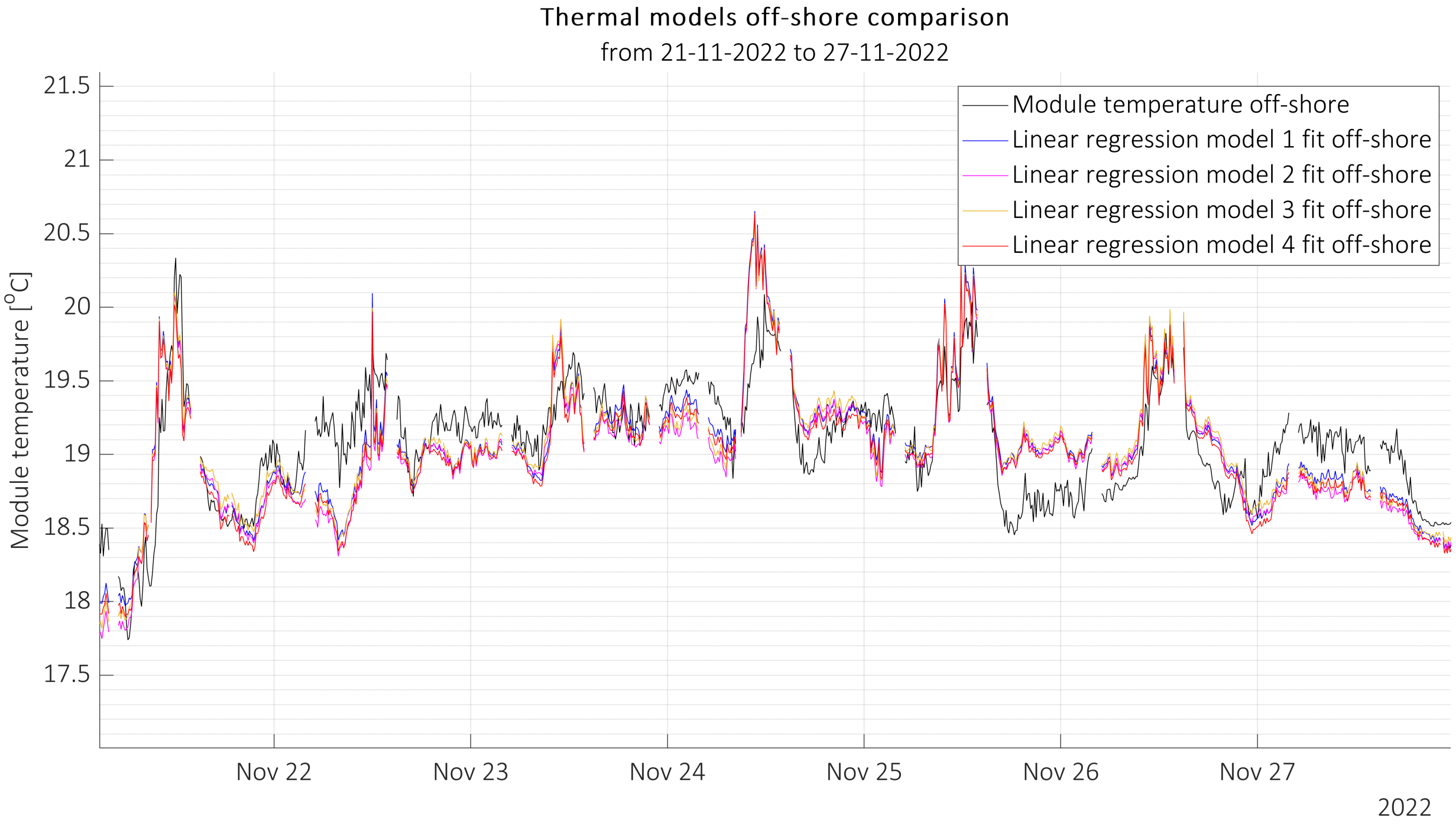

Figure E.15: Close up on module temperatures measured off-shore against empirical module temperature OFPV models from 21-11-2022 to 27-11-2022 included.

E.12. Module temperatures off-shore against environmental influences on timeline plots

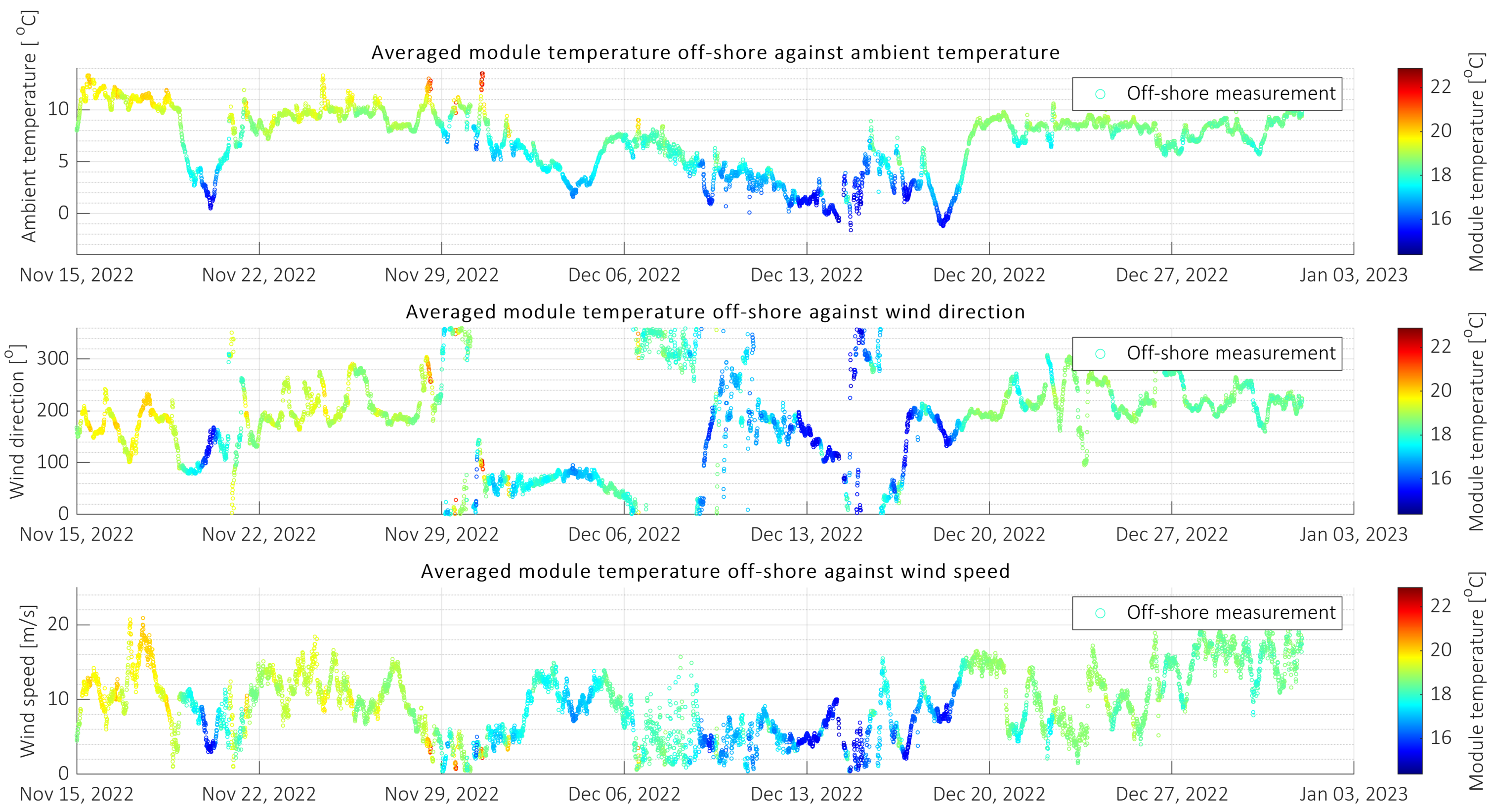

Figure E.16: Module temperature off-shore with respect ambient temperatures (top) to wind direction (middle) and direction (bottom). Timeline from 15-11-2022 to 1-1-2023.

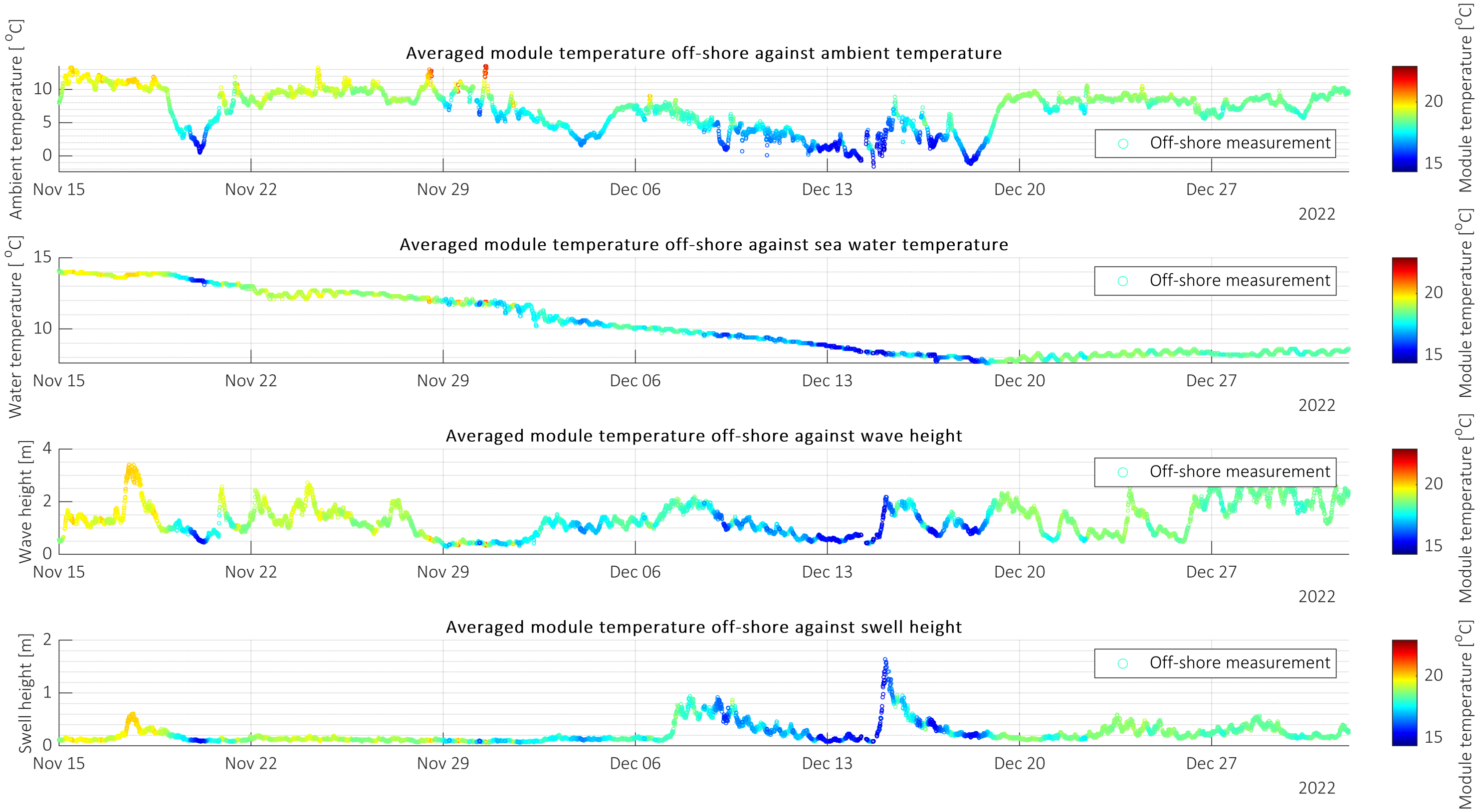

Figure E.17: Module temperature off-shore with respect ambient temperatures (top), to water temperature (second from top), to wave height (second from bottom) and swell height (bottom). Timeline from 15-11-2022 to 1-1-2023.

E.13. Horicatcher set-up and Meteonorm outputs on-land including custom horizon.

Figure E.18: Horicatcher orientation and inclinations taken into account during horizon measurement on-land.

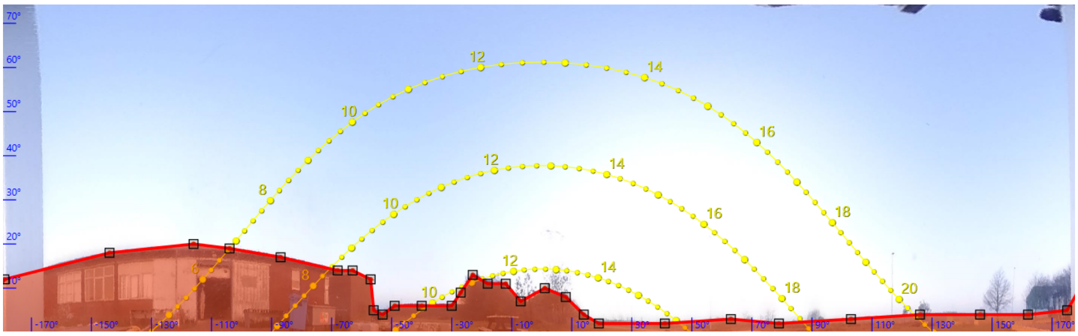

Figure E.19: Sun paths and raised horizon (red) for the on-land location found using Meteonorm.

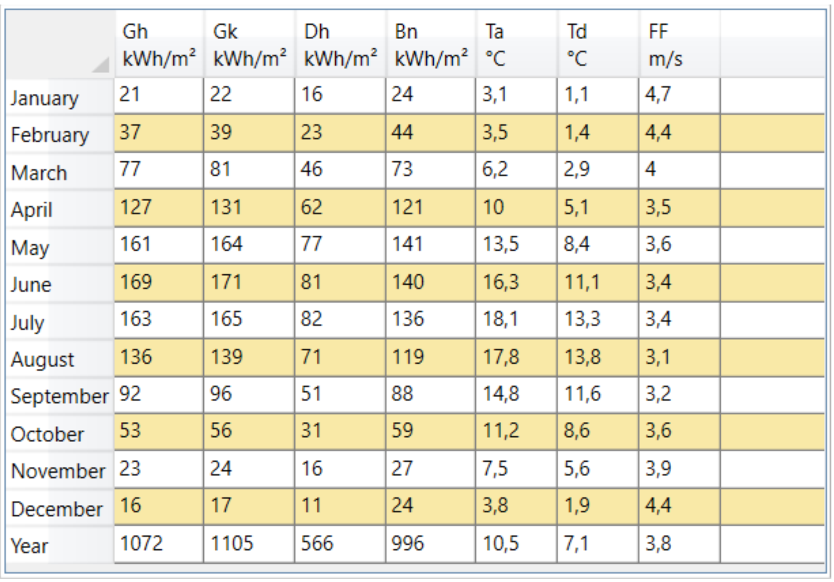

	Gh kWh/m^2	Gk kWh/m^2	Dh kWh/m^2	Bn kWh/m^2	Ta °C	Td °C	FF m/s
January	21	22	16	24	3,1	1,1	4,7
February	37	39	23	44	3,5	1,4	4,4
March	77	81	46	73	6,2	2,9	4
April	127	131	62	121	10	5,1	3,5
May	161	164	77	141	13,5	8,4	3,6
June	169	171	81	140	16,3	11,1	3,4
July	163	165	82	136	18,1	13,3	3,4
August	136	139	71	119	17,8	13,8	3,1
September	92	96	51	88	14,8	11,6	3,2
October	53	56	31	59	11,2	8,6	3,6
November	23	24	16	27	7,5	5,6	3,9
December	16	17	11	24	3,8	1,9	4,4
Year	1072	1105	566	996	10,5	7,1	3,8

Figure E.20: Meteonorm 8.1.1 outputs without the custom horizon on-land.

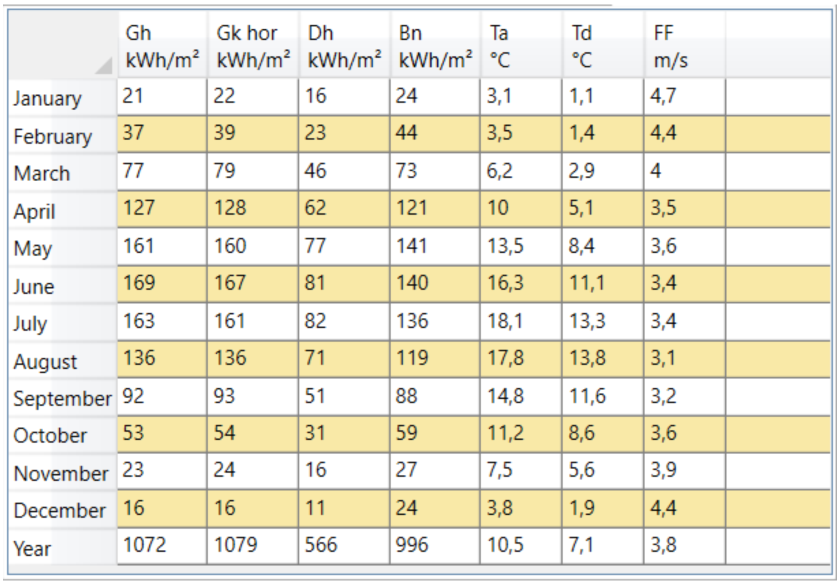

	Gh kWh/m^2	Gk hor kWh/m^2	Dh kWh/m^2	Bn kWh/m^2	Ta °C	Td °C	FF m/s
January	21	22	16	24	3,1	1,1	4,7
February	37	39	23	44	3,5	1,4	4,4
March	77	79	46	73	6,2	2,9	4
April	127	128	62	121	10	5,1	3,5
May	161	160	77	141	13,5	8,4	3,6
June	169	167	81	140	16,3	11,1	3,4
July	163	161	82	136	18,1	13,3	3,4
August	136	136	71	119	17,8	13,8	3,1
September	92	93	51	88	14,8	11,6	3,2
October	53	54	31	59	11,2	8,6	3,6
November	23	24	16	27	7,5	5,6	3,9
December	16	16	11	24	3,8	1,9	4,4
Year	1072	1079	566	996	10,5	7,1	3,8

Figure E.21: Meteonorm 8.1.1 outputs with the custom horizon included on-land.

F

Victron MPPT 450-100 Outputs

F.1. PV production and battery storage

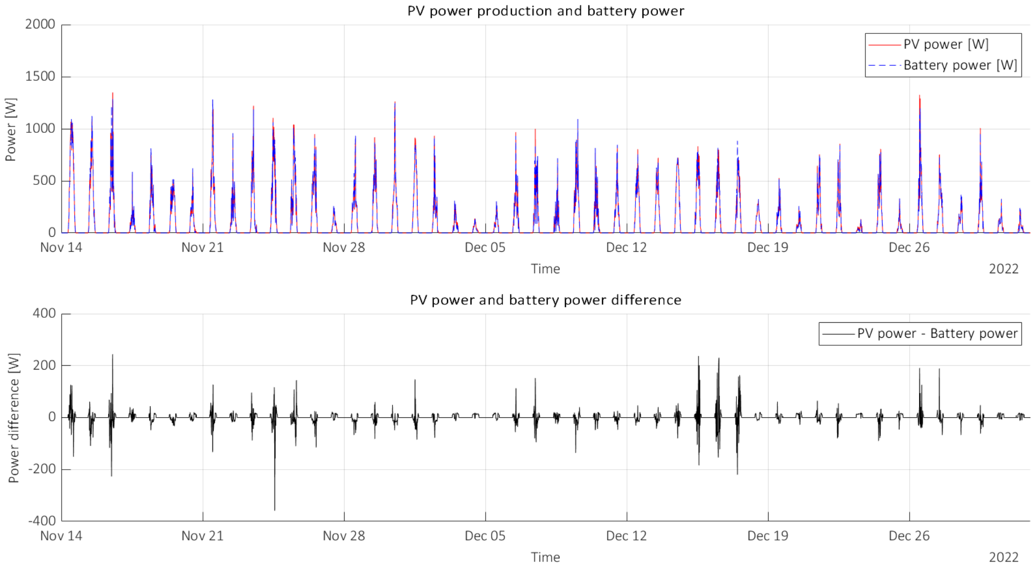

Figure F.1: Victron MPPT 450-100 Output: PV power and battery power from 14-11-2022 to 1-1-2023

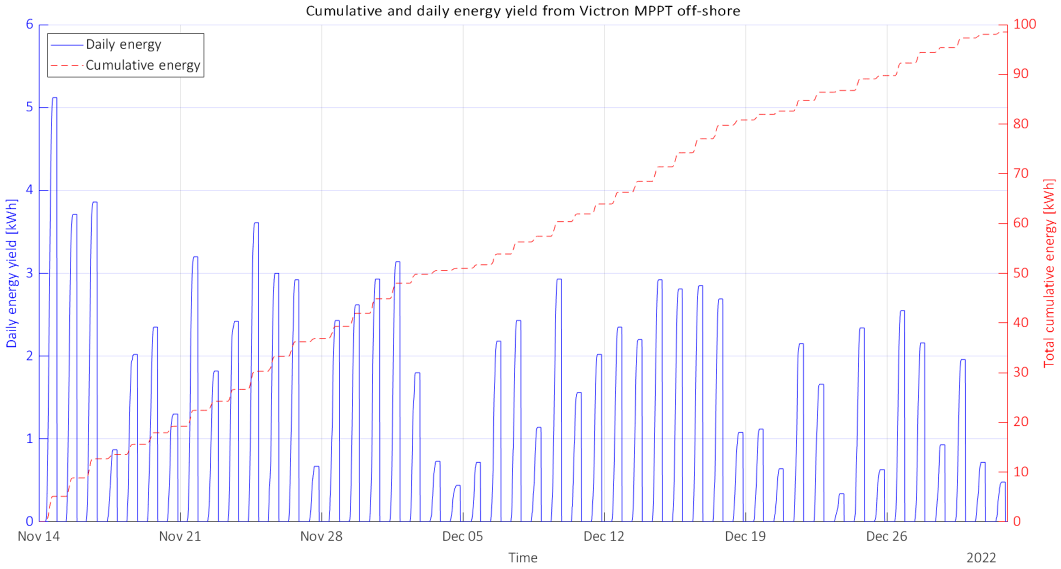

Figure F.2: Victron MPPT 450-100 Output: Total daily energy and cumulative energy yield from 14-11-2022 to 1-1-2023

F.1.1. 3 day selection

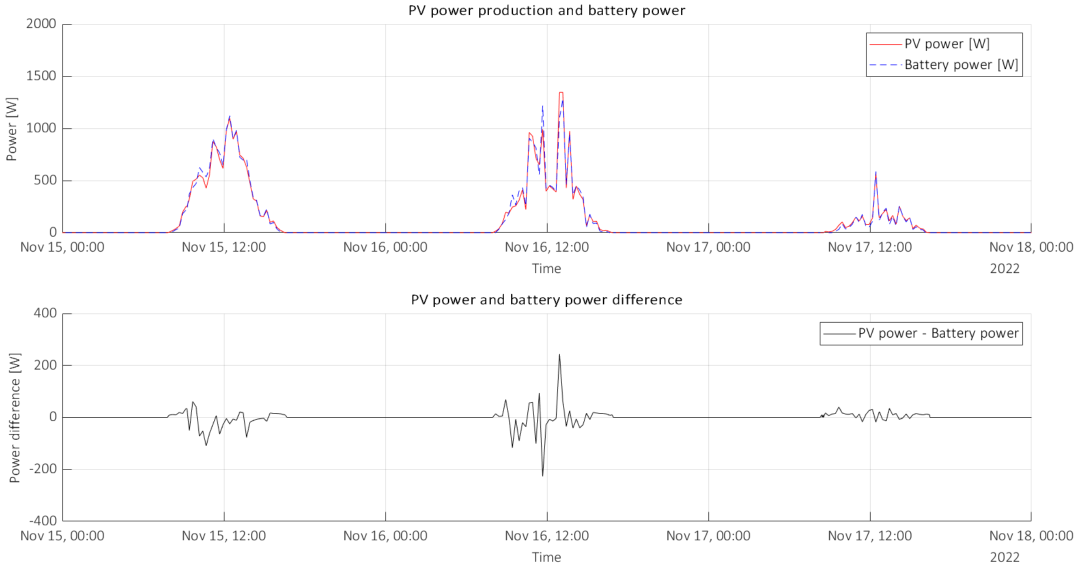

Figure F.3: Victron MPPT 450-100 Output: PV power and battery from 15-11-2022 to 17-11-2022.

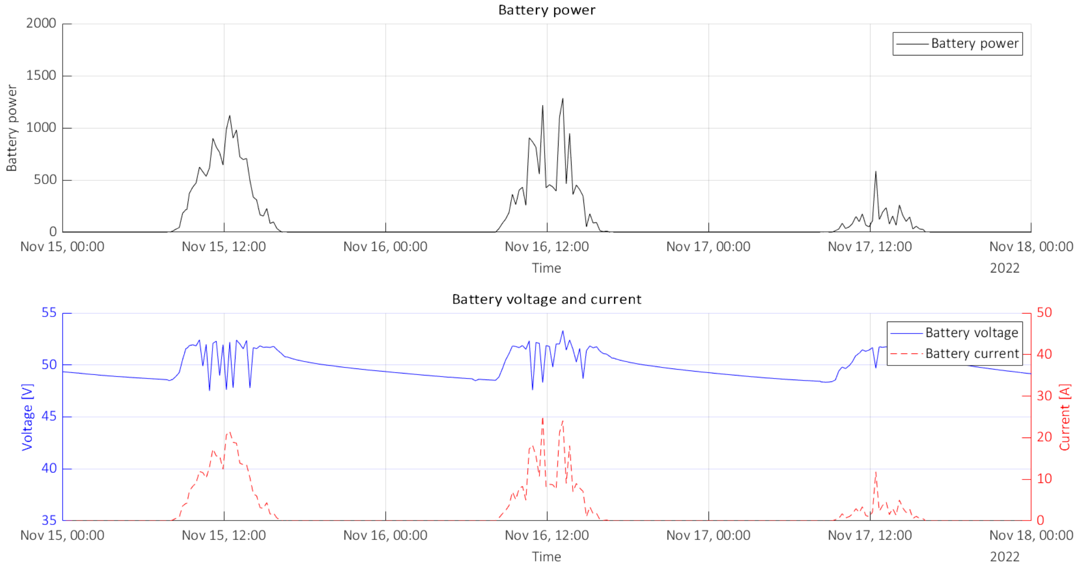

Figure F.4: Victron MPPT 450-100 Output: Battery power, voltage and current from 15-11-2022 to 17-11-2022.

F.2. Additional outputs

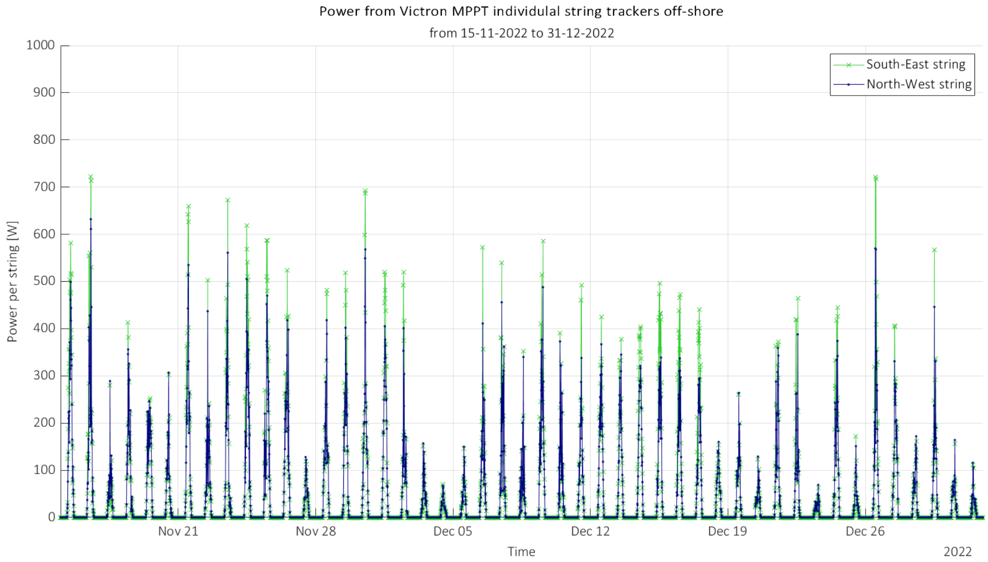

Figure F.5: Power recorded from the MPPT controller trackers for off-shore system from 15-11-2022 until 1-1-2023.

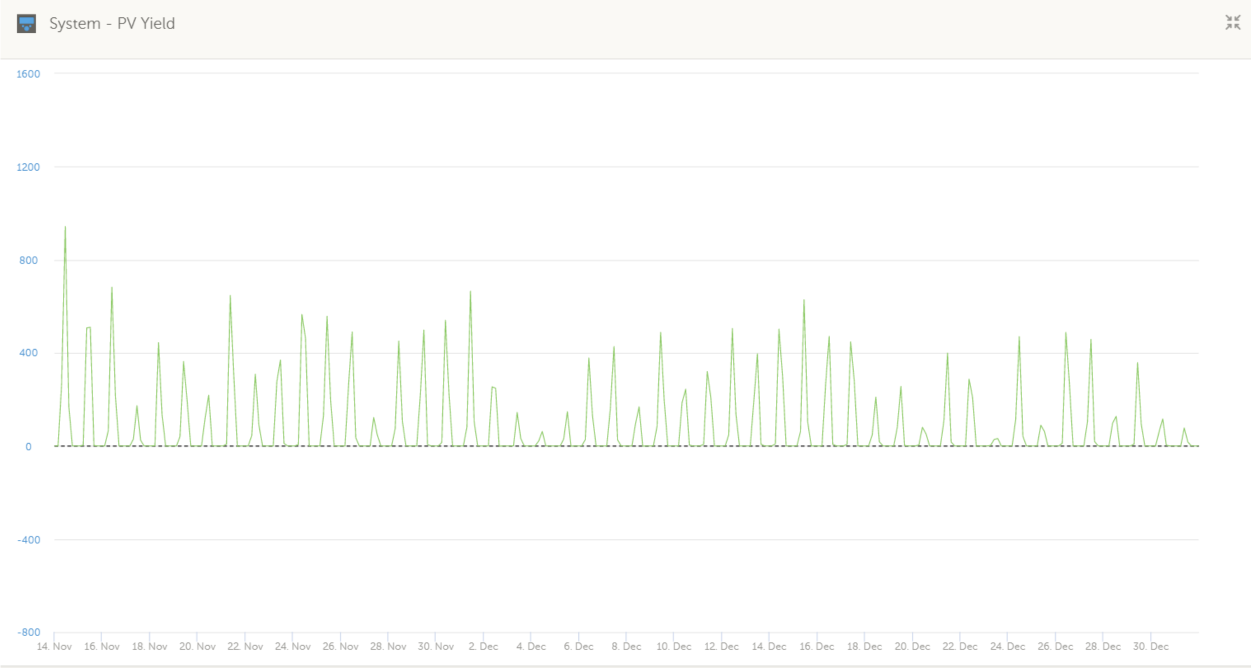

Figure F.6: VRM Victron MPPT 450-100 Output: PV power from 14-11-2022 to 1-1-2023.

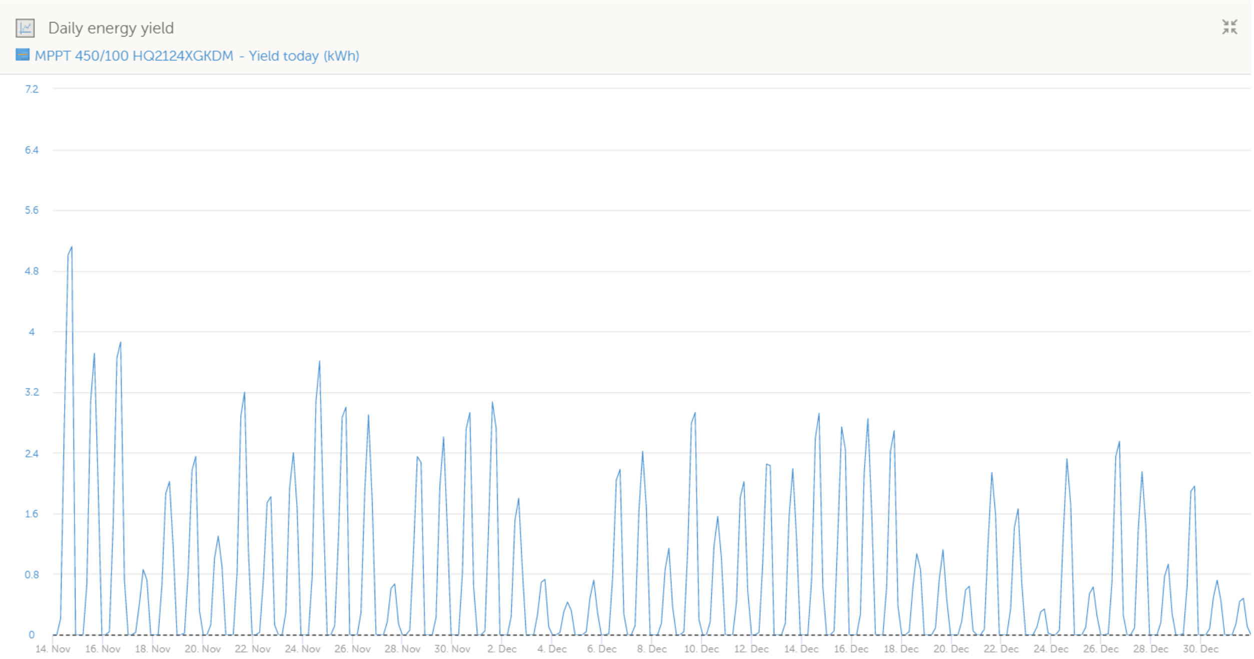

Figure F.7: VRM Victron MPPT 450-100 Output: Daily energy yield from 14-11-2022 to 1-1-2023.

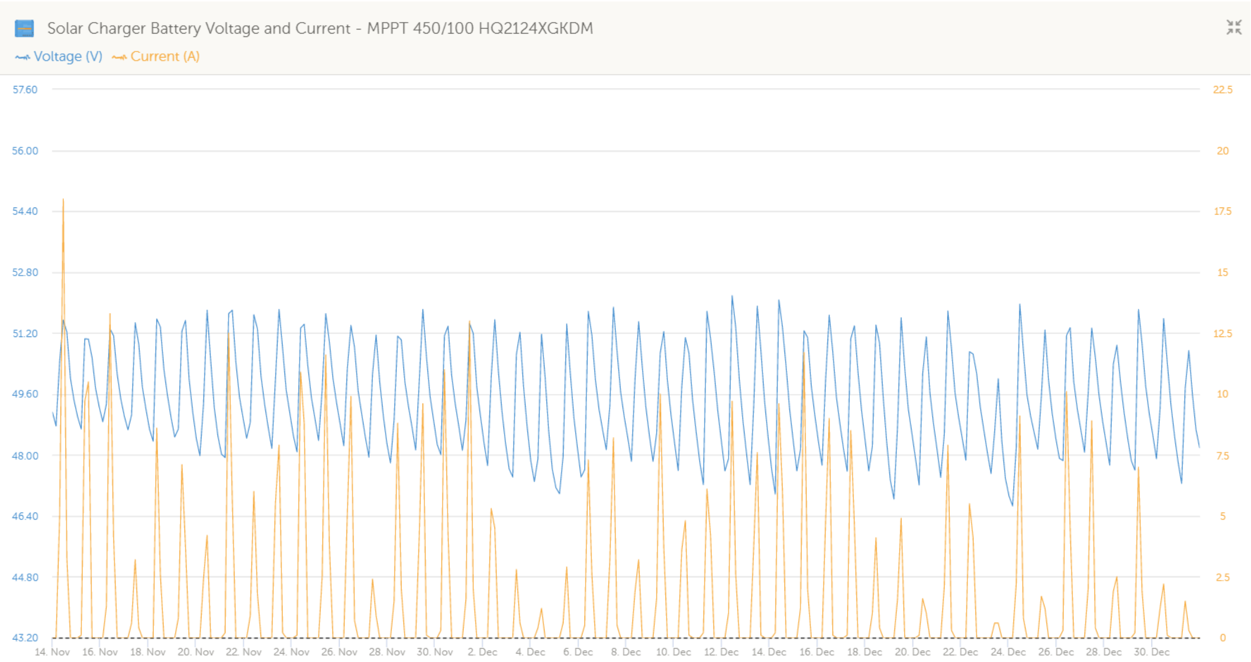

Figure F.8: VRM Victron MPPT 450-100 Output: Battery voltage and current from 14-11-2022 to 1-1-2023.

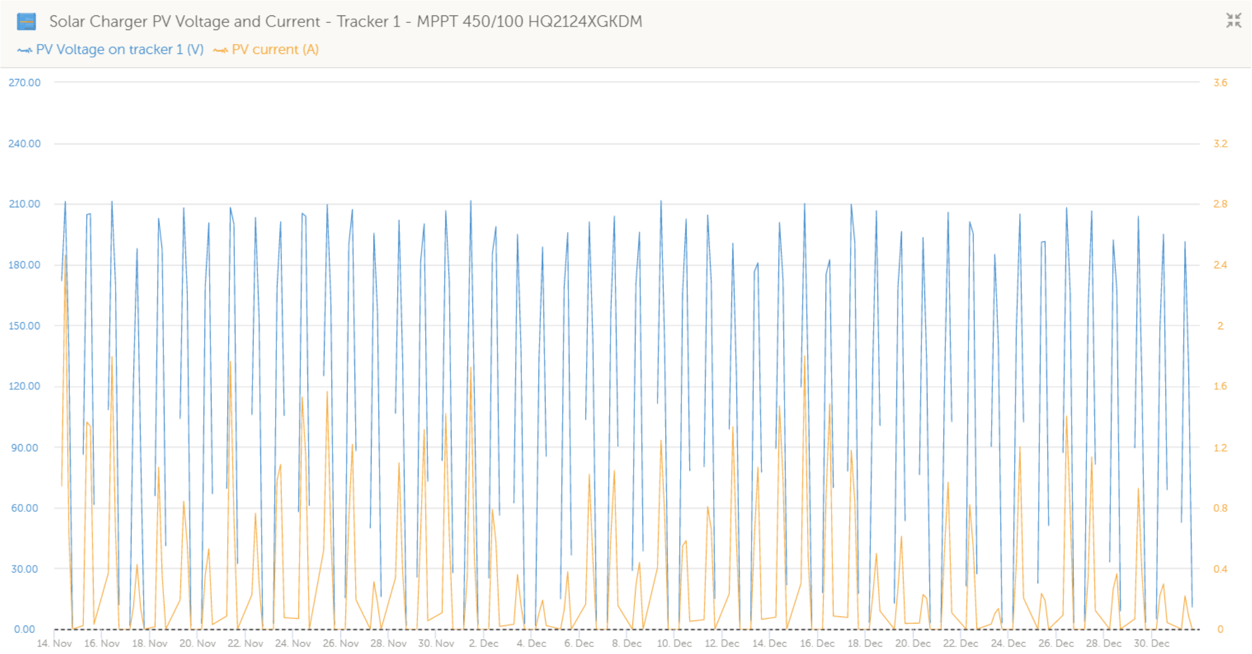

Figure F.9: VRM Victron MPPT 450-100 Output: Tracker 1 (South-East) voltage and current from 14-11-2022 to 1-1-2023.

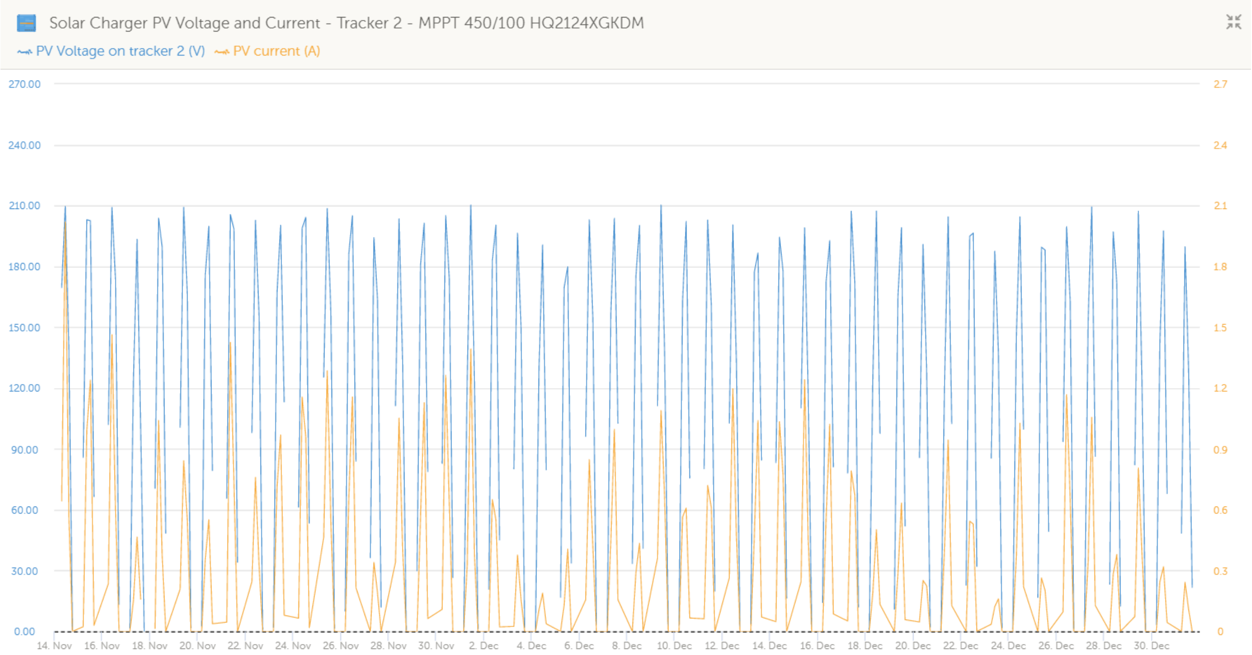

Figure F.10: VRM Victron MPPT 450-100 Output: Tracker 2 (North-West) voltage and current from 14-11-2022 to 1-1-2023.

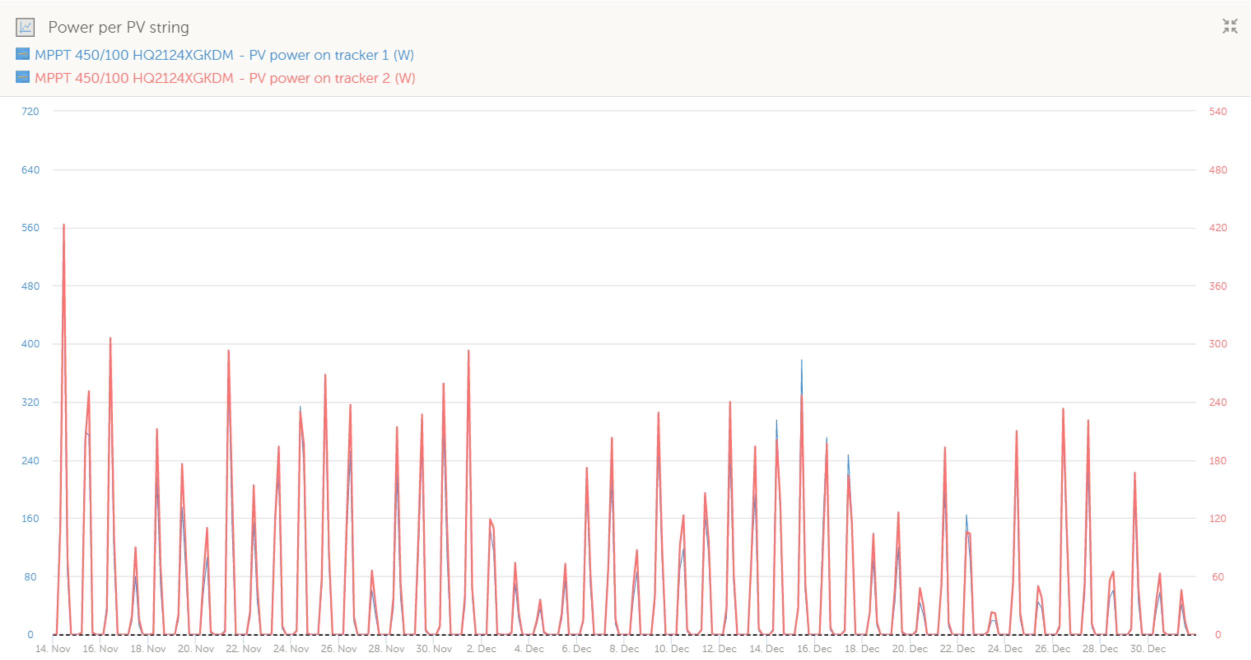

Figure F.11: VRM Victron MPPT 450-100 Output: PV power per tracker from 14-11-2022 to 1-1-2023.

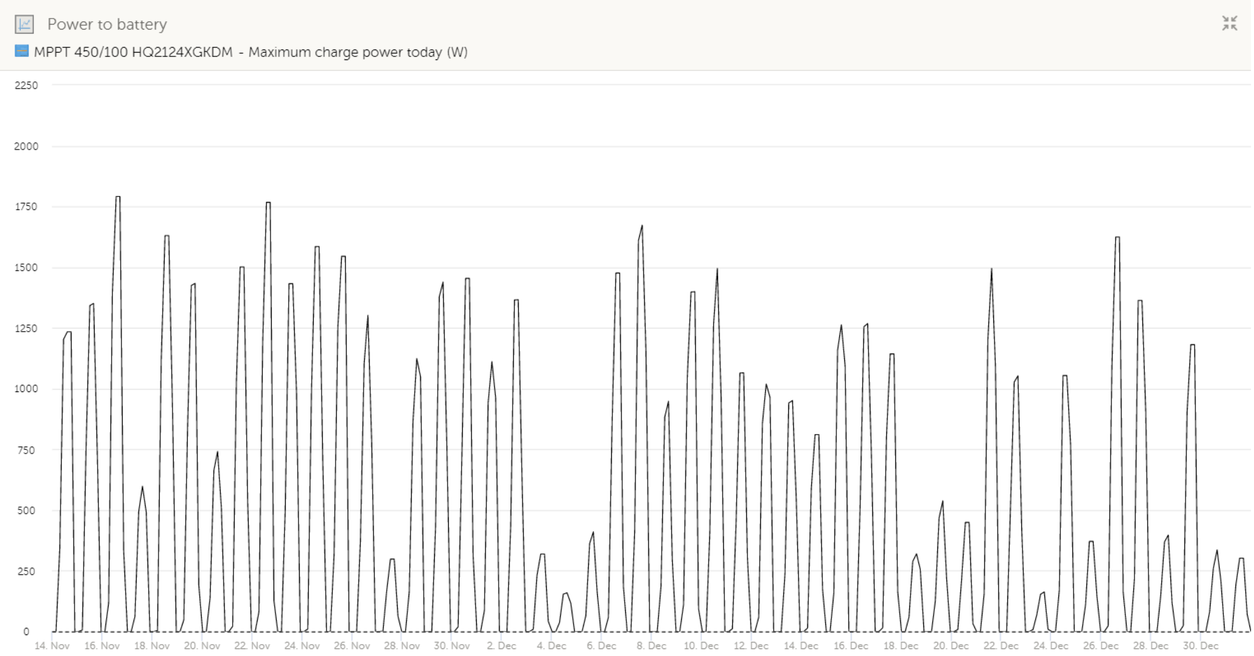

Figure F.12: VRM Victron MPPT 450-100 Output: Daily maximum charge power from 14-11-2022 to 1-1-2023.

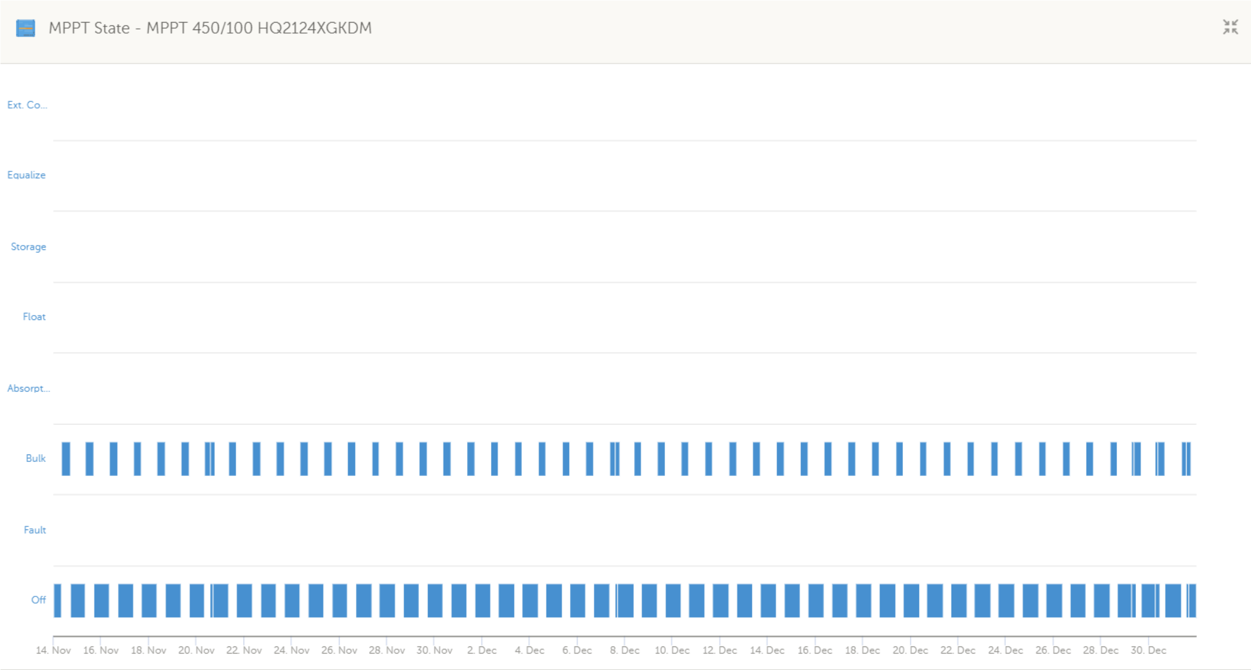

Figure F.13: VRM Victron MPPT 450-100 Output: MPPT state from 14-11-2022 to 1-1-2023.

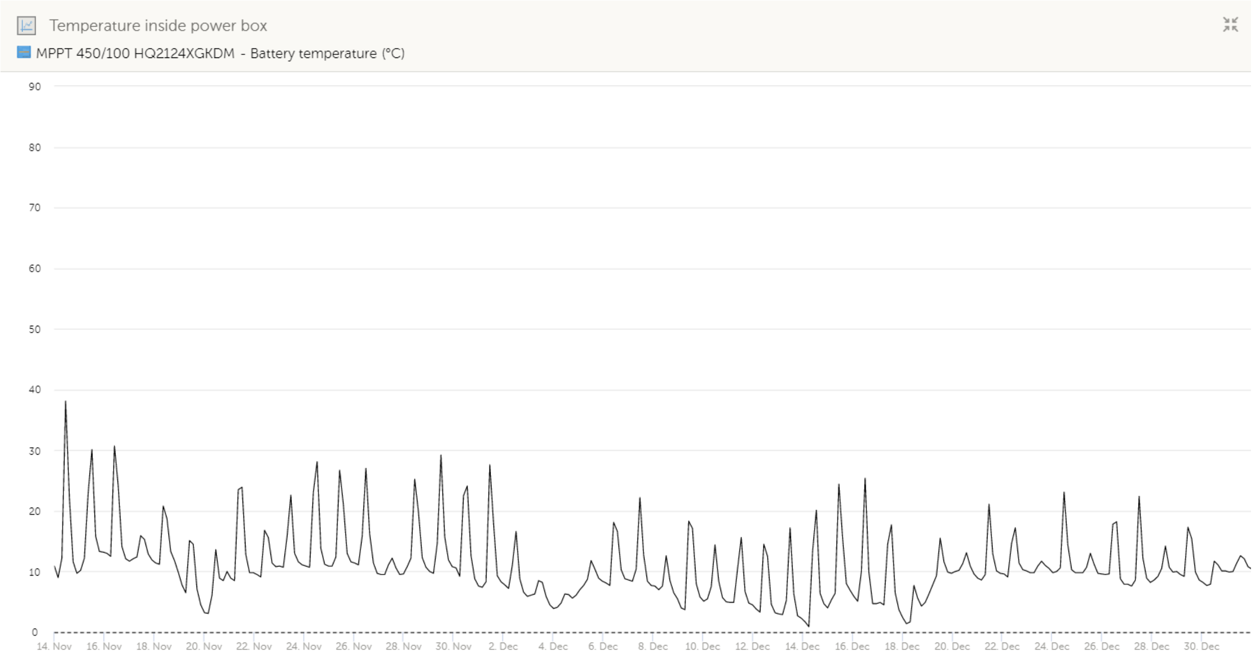

Figure F.14: VRM Victron MPPT 450-100 Output: Temperature on power box from 14-11-2022 to 1-1-2023.

G

KNMI Weather station HKZA additional information

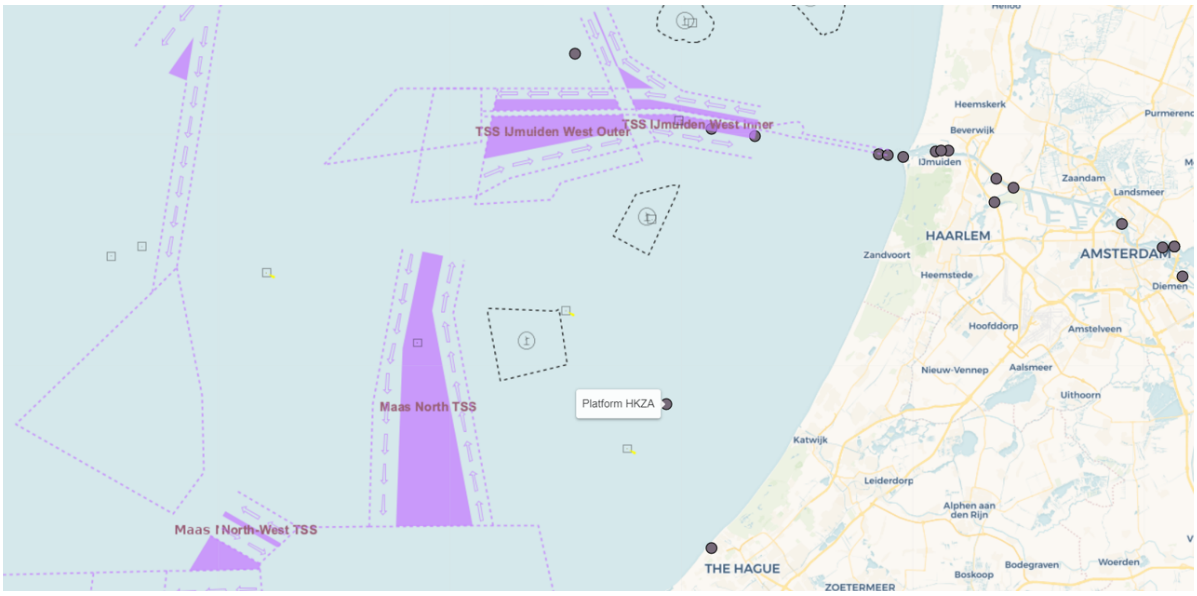

Figure G.1: Sea map from KNMI weather station with Hollandse Kust Zuid Alpha (HKZA), located in the decimal coordinates 52.319, 4.043.

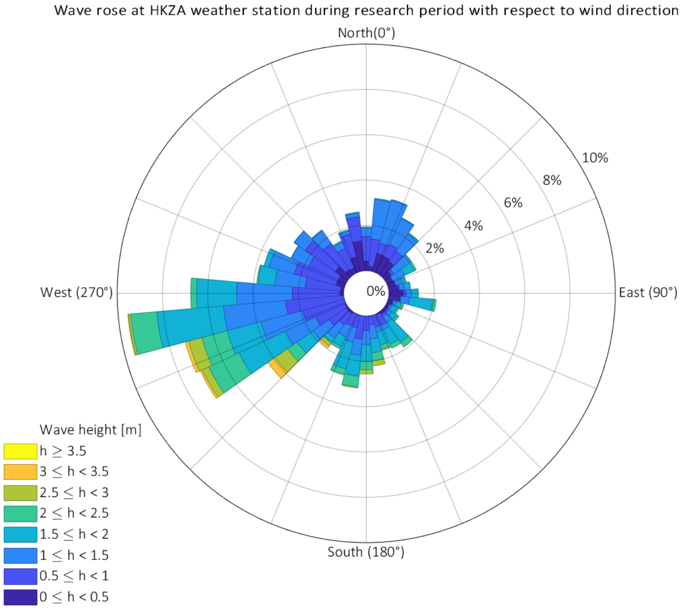

Figure G.2: Wave rose with respect to wind direction at HKZA weather station (2km away from off-shore system) for the period 14-11-2022 to 1-1-2023.

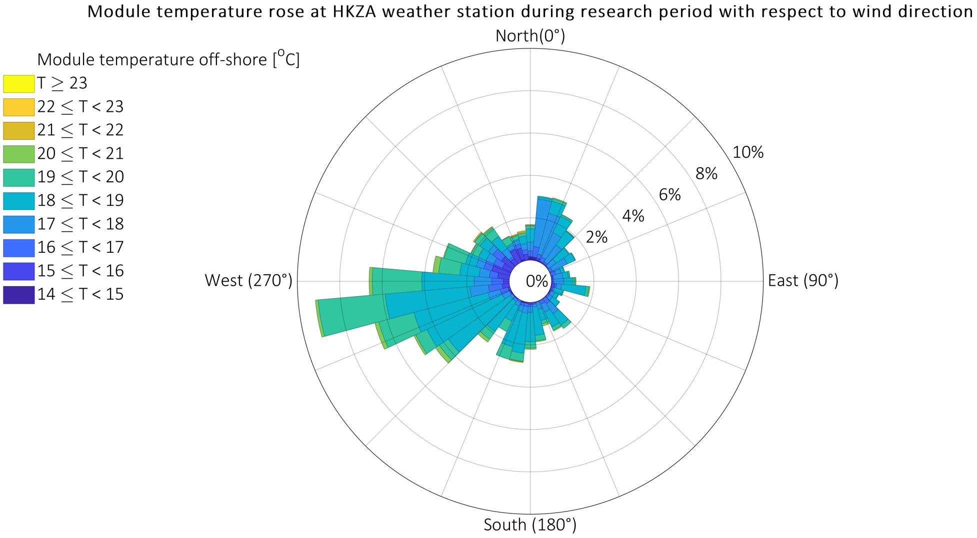

Figure G.3: Module temperature rose with respect to wind direction off-shore, from 14-11-2022 to 1-1-2023.

H

Datasheets

SmartSolar MPPT RS 450|100 & 450|200 - Isolated

5.76 kW & 11.52 kW Solar Charge Controller with 450 V PV input

www.victronenergy.com

SmartSolar MPPT RS 450|100

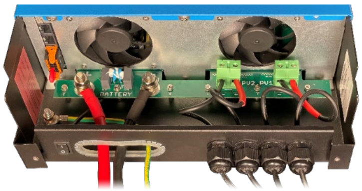

Inside the SmartSolar MPPT RS 450|100

Ultra-fast Maximum Power Point Tracking (MPPT) Solar Charge Controller

The MPPT RS SmartSolar is a 48 V Solar charge controller with up to 450 VDC PV input and either 100 A, or 200 A output. It is used in on-grid and off-grid solar applications where maximum battery charging power is required.

Multiple independent MPPT tracking inputs

With multiple MPPT trackers, you can optimize your solar panel design for maximum performance for your specific location.

Isolated PV connections for additional safety

Full galvanic isolation between PV and battery connections provide additional overall system safety.

Wide MPPT voltage range

80 – 450 VDC PV operating range, with a 120 VDC PV startup voltage.

Light weight, efficient and quiet

Thanks to high frequency technology and a new design this powerful charger weighs only 7.9 kg for the 100 A model. In addition to this it has an excellent efficiency, low standby power, and a very quiet operation.

Display and Bluetooth

The display reads battery, and controller parameters. The parameters can be accessed with a smartphone or other Bluetooth enabled device. In addition, Bluetooth can be used to set up the system and to change settings with VictronConnect.

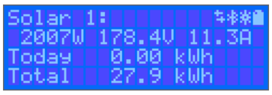

```
Solar 1:
 2007W 178.4V 11.3A
Today    0.00 kWh
Total    27.9 kWh
```

PV Isolation resistance monitoring for peace of mind at higher voltages

The MPPT RS continuously monitors the PV array and can detect if there are faults that reduce the isolation of the panels to unsafe levels.

VE.Can and VE.Direct port

For connection to a GX device for system monitoring, data logging, and remote firmware updates. VE.Can allows for up to 25 units to be connected together in parallel and synchronize their charging.

I/O Connections

Programmable Relay, temperature sensor, auxiliary, digital input and voltage sensor connections. The remote input can accept the Victron smallBMS, and other BMS with allow-to-charge signal.

Configure and monitor with VictronConnect →

The built-in Bluetooth Smart connection allows for quick monitoring and settings adjustment.

The built-in 30-day history shows individual performance of the separate MPPT trackers.

Try the VictronConnect demo to see the full range of configuration and display options with sample data.

MPPT 450/100 HQ1939R1H8L

3636 W

Solar

	Today	Yesterday	2 days ago	3 days ago	4 days ago	5 days ago
☀ Total						
Yield	9.14kWh	17.99kWh	14.52kWh	13.84kWh	8.21kWh	13.18kWh
P max	3660W	4703W	4473W	4668W	3684W	4632W
V max	418.72V	422.13V	426.18V	416.58V	429.17V	424.51V
☀ Solar 1						
Yield	2.93kWh	4.28kWh	3.29kWh	3.60kWh	1.91kWh	2.84kWh
P max	1385W	1481W	1564W	1486W	1144W	1451W
V max	282V	286V	287V	288V	286V	286V
☀ Solar 2						
Yield	6.21kWh	13.71kWh	11.23kWh	10.24kWh	6.30kWh	10.34kWh
P max	2389W	3315W	3509W	3182W	3167W	3457W
V max	419V	422V	426V	417V	429V	425V

Solar 1
Voltage 211.71V
Power 1249.85W
Current 5.9A

Solar 2
Voltage 305.14V
Power 2387.64W
Current 7.8A

Battery
Voltage 55.03V
Current 61.40A
Temperature 28°C

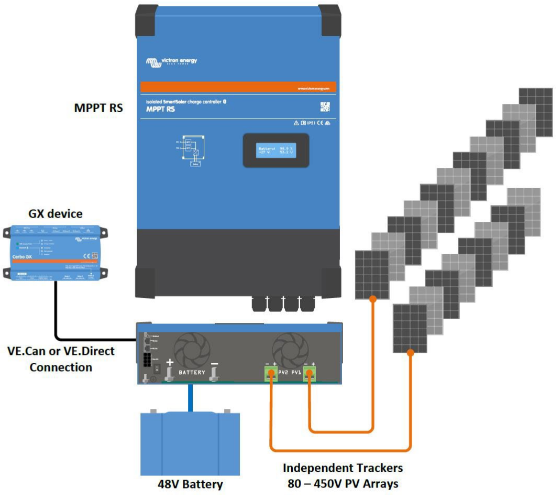

System example diagram
The 100 A MPPT RS combined with a GX device, charging a 48 V battery with 2 separate solar PV strings.

VRM Portal
When the MPPT RS is connected to a GX device with internet connection, or the GlobalLink 520 with built in 4G connectivity, you can access our free remote monitoring website (VRM). This will display all your system data in a comprehensive graphical format. Alarms can be received by e-mail.

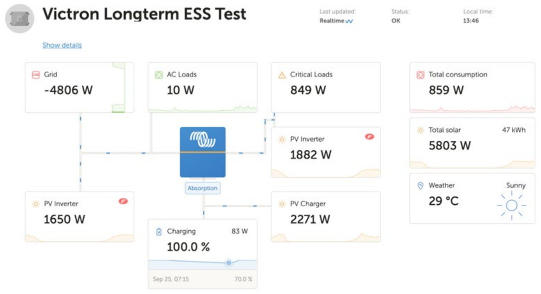

Victron Longterm ESS Test

Last updated: Realtime
Status: OK
Local time: 13:46

Show details

Grid -4806 W
AC Loads 10 W
Critical Loads 849 W
Total consumption 859 W
PV Inverter 1882 W
Total solar 47 kWh 5803 W
Weather Sunny 29 °C
PV Inverter 1650 W
Absorption
PV Charger 2271 W
Charging 83 W 100.0 %
Sep 25, 07:15 70.0 %

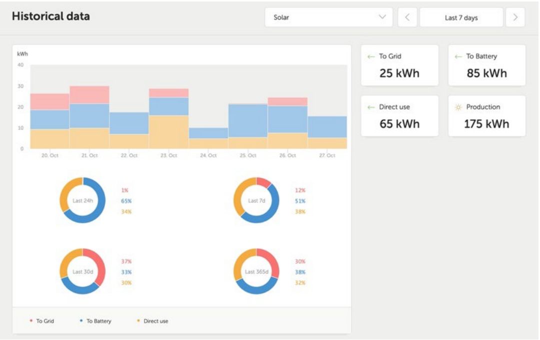

Historical data

Solar
Last 7 days

To Grid 25 kWh
To Battery 85 kWh
Direct use 65 kWh
Production 175 kWh

Last 24h: 1% 65% 34%
Last 7d: 12% 51% 38%
Last 30d: 37% 33% 30%
Last 365d: 30% 38% 32%

Isolated SmartSolar MPPT RS	450|100	450|200
CHARGER		
Battery voltage	48 V	
Rated charge current	100 A	200 A
Maximum charge power	5,8 kW at 57,6 V	11,5 kW at 57,6 V
Charge voltage 'absorption'	Default setting: 57,6 V (adjustable)	
Charge voltage 'float'	Default setting: 55,2 V (adjustable)	
Programmable voltage range	Minimum: 36 V Maximum: 60 V (7)	
Charge algorithm	Multi-stage adaptive (adjustable)	
Battery temperature sensor	Included	
Maximum efficiency	96 %	
Self-consumption	15 mA	
SOLAR		
Maximum DC PV voltage	450 V	
Start-up voltage	120 V	
MPPT operating voltage range	80 – 450 V (1)	
Number of trackers	2	4
Max. PV operational input current	18 A per tracker	
Max. PV short circuit current (2)	20 A per tracker	
Max. DC output charging power	4000 W per tracker 5760 W total	4000 W per tracker 11520 W total
Maximum PV array size per tracker (3)	7200 Wp (450 V x 20 A) (3)	
PV Isolation fail level (4)	100 kΩ	
GENERAL		
Synchronised Parallel Operation	Yes, up to 25 units with VE.Can	
Programmable relay (5)	Yes	
Protection	PV reverse polarity Output short circuit Over temperature	
Data communication	VE.Direct port, VE.Can port & Bluetooth (6)	
Bluetooth frequency	2402 – 2480 MHz	
Bluetooth power	4dBm	
General purpose analogue/digital in port	Yes, 2x	
Remote on-off	Yes	
Operating temperature range	-40 to +60 °C (fan assisted cooling)	
Humidity (non-condensing)	max 95 %	
ENCLOSURE		
Material & Colour	steel, blue RAL 5012	
Protection category	IP21	
Battery-connection	M8 bolts	
Power terminals PV input	2 16 mm^2	
Weight	7.9 kg	13.7 kg
Dimensions (h x w x d) in mm	440 x 313 x 126	487 x 434 x 146
STANDARDS		
Safety	EN-IEC 62109-1, EN-IEC 62109-2	
Country of Origin	Designed in The Netherlands, made in India	

1) MPPT operating voltage range is constrained by battery voltage - PV VOC should not exceed 8 x battery float voltage. For example, a 52,8 V float voltage results in a maximum PV VOC of 422,4 V. See product manual for further information.

2) A higher short circuit current may damage the controller if PV array is connected in reverse polarity.

3) Max. 450 VOC result in appr. 360 Vmpp, therefor the maximum PV array is appr. 360 V x 20 A = 7200 Wp.

4) The MPPT RS will test for sufficient resistive isolation between PV+ and GND, and PV- and GND. In the event of a resistance below the threshold, the unit will stop charging, display the error, and send the error signal to the GX device (if connected) for audible and email notification.

5) Programmable relay which can be set for general alarm, DC under voltage or genset start/stop function. DC rating: 4 A up to 35 VDC and 1 A up to 70 VDC

6) The MPPT RS is currently not compatible with VE.Smart Networks.

7) The Charger set-point (float and absorption) can be set to max 60 V. The output voltage at the charger terminals can be higher, due to temperature compensation as well as compensation for voltage drop over the battery cables. The maximum output current is reduced on a linear basis from full current at 60 V to 5A at 62 V. The equalization voltage can be set to max 62V, the equalization current percentage can be set to max 6%.

Orion-Tr DC-DC converters isolated

100 / 250 / 400 Watt

www.victronenergy.com


Orion-Tr 24/12-20 (240 W)


Orion-Tr 24/12-20 (240 W)

Remote on-off

The remote on-off eliminates the need for a high current switch in the input wiring. The remote on-off can be operated with a low power switch or by for example the engine run/stop switch (see manual).

All models are short circuit proof and can be paralleled to increase output current

An unlimited number of units can be connected in parallel.

High temperature protected

The output current will reduce at high ambient temperature.

IP43 protection

When installed with the screw terminals oriented downwards.

Screw terminals

No special tools needed for installation.

Input fuse (not replaceable)

On 12 V and 24 V input models only.

Adjustable output voltage

Not intended for battery charging.
Please consider using an Orion-Tr Smart for battery charging.

Isolated converters 110 – 120 W	Orion-Tr 12/12-9 (110 W)	Orion-Tr 12/24-5 (120 W)	Orion-Tr 24/12-9 (110 W)	Orion-Tr 24/24-5 (120 W)	Orion-Tr 24/48-2,5 (120 W)	Orion-Tr 48/12-9 (110 W)	Orion-Tr 48/24-5 (120 W)	Orion-Tr 48/48-2,5 (120 W)
Input voltage range (1)	8-17 V	8-17 V	16-35 V	16-35 V	16-35 V	32-70 V	32-70 V	32-70 V
Under voltage shut down	7 V	7 V	14 V	14 V	14 V	28 V	28 V	28 V
Under voltage restart	7,5 V	7,5 V	15 V	15 V	15 V	30 V	30 V	30 V
Nominal output voltage	12.2 V	24.2 V	12.2 V	24.2 V	48.2 V	12.2 V	24.2 V	48.2 V
Output voltage adjust range	10-15 V	20-30 V	10-15 V	20-30 V	40-60 V	10-15 V	20-30 V	40-60 V
Output voltage tolerance	+/- 0.2 V							
Output noise	2mV rms							
Cont. output current at nominal output voltage and 25 °C	9 A	5 A	9 A	5 A	2.5 A	9 A	5 A	2.5 A
Maximum output current (10 s) at nominal output voltage	12.5 A	6.3 A	12.5 A	6.3 A	3.0 A	12.5 A	6.3 A	3.0 A
Short circuit output current	32 A	23 A	39 A	30 A	19 A	27 A	25 A	17 A
Cont. output power at 25 °C	110 W	120 W	110 W	120 W	120 W	110 W	120 W	120 W
Cont. output power at 40 °C	85 W	110 W	85 W	115 W	115 W	85 W	100 W	85 W
Efficiency	87 %	88 %	85 %	87 %	88 %	87 %	86 %	89 %
No load input current	< 50 mA	< 80 mA	< 40 mA	< 60 mA	< 120 mA	< 50 mA	< 60 mA	< 80 mA
Galvanic isolation	200 V dc between input, output and case							
Operating temperature range	-20 to +55 °C (derate 3 % per °C above 40 °C)							
Humidity	Max. 95 % non-condensing							
DC connection	Screw terminals							
Maximum cable cross-section	6 mm^2 AWG10							
Weight	0,42 kg (1 lb)							
Dimensions hxwxd	100 x 113 x 47 mm (4.0 x 4.5 x 1.9 inch)							
Standards: Safety Emission Immunity Automotive Directive	EN 60950 EN 61000-6-3, EN 55014-1 EN 61000-6-2, EN 61000-6-1, EN 55014-2 ECE R10-5							

1) If set to nominal or lower than nominal, the output voltage will remain stable within the specified input voltage range (buck-boost function).
If the output voltage is set higher than nominal by a certain percentage, the minimum input voltage at which the output voltage remains stable (does not decrease) increases by the same percentage.

See page two for 250 W and 400 W models

Isolated converters 220 - 280 Watt	Orion-Tr 12/12-18 (220 W)	Orion-Tr 12/24-10 (240 W)	Orion-Tr 24/12-20 (240 W)	Orion-Tr 24/24-12 (280 W)	Orion-Tr 24/48-6 (280 W)	Orion-Tr 48/12-20 (240 W)	Orion-Tr 48/24-12 (280 W)	Orion-Tr 48/48-6 (280 W)
Input voltage range (1)	8-17 V	8-17 V	16-35 V	16-35 V	16-35 V	32-70 V	32-70 V	32-70 V
Under voltage shut down	7 V	7 V	14 V	14 V	14 V	28 V	28 V	28 V
Under voltage restart	7,5 V	7,5 V	15 V	15 V	15 V	30 V	30 V	30 V
Nominal output voltage	12.2 V	24.2 V	12.2 V	24.2 V	48.2 V	12.2 V	24.2 V	48.2 V
Output voltage adjust range	10-15 V	20-30 V	10-15 V	20-30 V	40-60 V	10-15 V	20-30 V	40-60 V
Output voltage tolerance	+/- 0,2 V							
Output noise	2 mV rms							
Cont. output current at nominal output voltage and 40 °C	18 A	10 A	20 A	12 A	6 A	20 A	12 A	6 A
Maximum output current (10 s) at nominal output voltage	25 A	15 A	25 A	15 A	8 A	25 A	15 A	8 A
Short circuit output current	40 A	25 A	50 A	30 A	25 A	50 A	30 A	25 A
Cont. output power at 25 °C	280 W	280 W	300 W	320 W	320 W	280 W	320 W	320 W
Cont. output power at 40 °C	220 W	240 W	240 W	280 W	280 W	240 W	280 W	280 W
Efficiency	87 %	88 %	88 %	89 %	89 %	87 %	89 %	89 %
Off load current	< 80 mA	< 100 mA	< 100 mA	< 80 mA	< 120 mA	< 80 mA	< 80 mA	< 80 mA
Galvanic isolation	200 VDC between input, output and case							
Operating temperature range	-20 to +55 °C (derate 3 % per °C above 40 °C)							
Humidity	Max. 95 % non-condensing							
DC connection	Screw terminals							
Maximum cable cross-section	16 mm² AWG6							
Weight	1,3 kg (3 lb)							
Dimensions hxwxd	130 x 186 x 70 mm (5.1 x 7.3 x 2.8 inch)							
Standards: Safety Emission Immunity Automotive Directive	EN 60950 EN 61000-6-3, EN 55014-1 EN 61000-6-2, EN 61000-6-1, EN 55014-2 ECE R10-5							

Isolated converters 360 - 400 Watt	Orion-Tr 12/12-30 (360 W)	Orion-Tr 12/24-15 (360 W)	Orion-Tr 24/12-30 (360 W)	Orion-Tr 24/24-17 (400 W)	Orion-Tr 24/48-8,5 (400 W)	Orion-Tr 48/12-30 (360 W)	Orion-Tr 48/24-16 (380 W)	Orion-Tr 48/48-8 (380 W)
Input voltage range (1)	10-17 V	10-17 V	20-35 V	20-35 V	20-35 V	40-70 V	40-70 V	40-70 V
Under voltage shut down	7 V	7 V	14 V	14 V	14 V	28 V	28 V	28 V
Under voltage restart	7,5 V	7,5 V	15 V	15 V	15 V	30 V	30 V	30 V
Nominal output voltage	12.2 V	24.2 V	12.2 V	24.2 V	48.2 V	12.2 V	24.2 V	48.2 V
Output voltage adjust range	10-15 V	20-30 V	10-15 V	20-30 V	40-60 V	10-15 V	20-30 V	40-60 V
Output voltage tolerance	+/- 0,2 V							
Output noise	2 mV rms							
Cont. output current at nominal output voltage and 40°C	30 A	15 A	30 A	17 A	8,5 A	30 A	16 A	8 A
Maximum output current (10 s) at nominal output voltage minus 20%	40 A	25 A	45 A	25 A	15 A	40 A	25 A	15 A
Short circuit output current	60 A	40 A	60 A	40 A	25 A	60 A	40 A	25 A
Cont. output power at 25°C	430 W	430 W	430 W	480 W	480 W	430 W	430 W	430 W
Cont. output power at 40°C	360 W	360 W	360 W	400 W	400 W	360 W	380 W	380 W
Efficiency	87 %	88 %	88 %	89 %	89 %	87 %	89 %	89 %
Off load current	< 80 mA	< 100 mA	< 100 mA	< 80 mA	< 120 mA	< 80 mA	< 80 mA	< 80 mA
Galvanic isolation	200 VDC between input, output and case							
Operating temperature range	-20 to +55 °C (derate 3 % per °C above 40 °C)							
Humidity	Max. 95 % non-condensing							
DC connection	Screw terminals							
Maximum cable cross-section	16 mm² (AWG6)							
Weight	12 V input and/or 12 V output models: 1.8 kg (3 lb). Other models: 1,6 kg (3.5 lb)							
Dimensions hxwxd	12 V input and/or 12 V output models: 130 x 186 x 80 mm (5.1 x 7.3 x 3.2 inch) Other models: 130 x 186 x 70 mm (5.1 x 7.3 x 2.8 inch)							
Standards: Safety Emission Immunity Automotive Directive	EN 60950 EN 61000-6-3, EN 55014-1 EN 61000-6-2, EN 61000-6-1, EN 55014-2 ECE R10-5							

1) If set to nominal or lower than nominal, the output voltage will remain stable within the specified input voltage range (buck-boost function).
If the output voltage is set higher than nominal by a certain percentage, the minimum input voltage at which the output voltage remains stable (does not decrease) increases by the same percentage.

Cerbo GX, Cerbo-S GX and GX Touch

www.victronenergy.com

Cerbo GX

Cerbo GX: communication-centre

This communication-centre allows you to always have perfect control over your system from wherever you are and to maximise its performance. Simply access your system via our Victron Remote Management (VRM) portal, or access it directly, using the optional GX Touch screen, a Multi-Functional Display (MFD) or our VictronConnect app thanks to its Bluetooth capability.

GX Touch: display accessory

The GX Touch 50 and GX Touch 70 are display accessories for the Cerbo GX. The five inch and seven inch touch screen displays give an instant overview of your system and allows you to adjust settings. Simply connect the display to the Cerbo GX with just one cable. Both GX Touch displays have a waterproof design, a top-mountable setup and are simple to install.

Remote Console on VRM

Monitor, control and configure the Cerbo GX remotely, over the internet. Just like if you were standing in front of the device, using Remote Console. The same functionality is also available on the local network LAN, or using the WiFi Access Point of the Cerbo GX.

Accessories included
with the Cerbo GX

Perfect monitoring & control

Instantly monitor the battery state of charge, power consumption, power harvest from PV, generator, and mains, or check tank levels and temperature measurements. Easily control the shore power input current limit, (auto)start/stop generator(s) or change any setting to optimise the system. Follow up on alerts, perform diagnostic checks and resolve complications remotely.

Simple mounting and configuration

The Cerbo GX is easily mountable and can also be mounted on a DIN-Rail using the DIN35 adapter small, (not included). Its separate touchscreen can be bolted on a dashboard, eliminating the need to create perfect cut-outs (like with the Color Control GX). Connection is easy via just one cable, taking away the hassle of having to bring many wires to the dashboard. The Bluetooth feature enables a quick connection and configuration via our VictronConnect app.

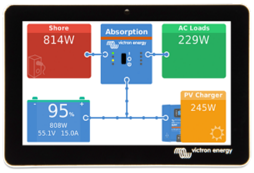

GX Touch (optional display for
Cerbo GX)

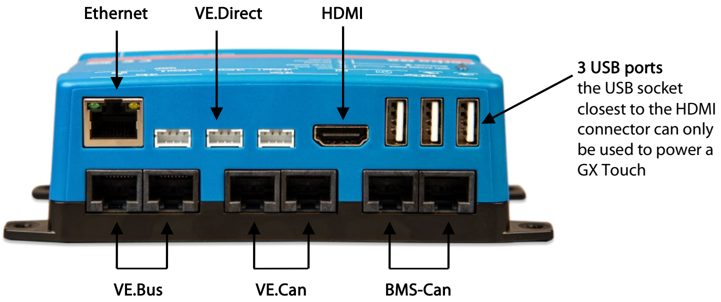

3 USB ports
the USB socket
closest to the HDMI
connector can only
be used to power a
GX Touch

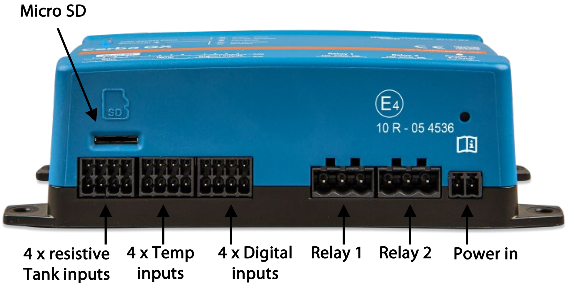

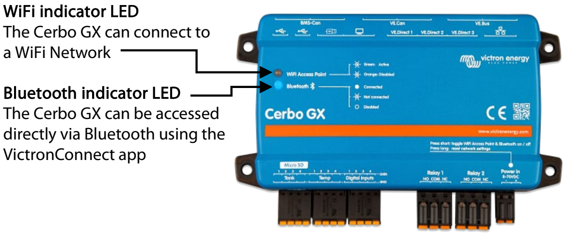

WiFi indicator LED
The Cerbo GX can connect to
a WiFi Network

Bluetooth indicator LED
The Cerbo GX can be accessed
directly via Bluetooth using the
VictronConnect app

Accessories included
with the GX Touch

	Cerbo GX	Cerbo-S GX
Supply voltage	8 – 70V DC	
Mounting	Wall or DIN rail (35mm)(2)	
Communication ports		
VE.Direct ports (always isolated)	3 (3)	
VE.Bus (always isolated)	2 paralleled RJ45 sockets	
VE.Can	yes - non isolated	
BMS-Can port	yes	No
IO		
Resistive tank level inputs	4	0
Temperature sense inputs	4	0
Digital Inputs	4	4
Other		
Outer dimensions (h x w x d)	78 x 154 x 48 mm	
Operating temperature range	-20 to +50°C	
Standards		
Safety	IEC 62368-1	
EMC	EN 301489-1, EN 301489-17	
Automotive	ECE R10-6	
GX Touch 50 / GX Touch 70		
Mounting	With included mounting accessories	
Display Resolution	GX Touch 50: 800 x 480 GX Touch 70: 1024 x 600	
Other		
Outer dimensions (h x w x d)	GX Touch 50: 87 x 128 x 12.4 mm GX Touch 70: 113 x 176 x 13.5 mm	
Cable length	2 meter	

Notes

1. For more detailed information about the Cerbo GX and the GX Touch, please visit the Victron GX product range page at Victron live: www.victronenergy.com/live/venus-os:start
2. DIN rail mounting requires additional accessory - DIN35 Adapter.
3. The listed maximum on the `Performance` section in above table is the total connected VE.Direct devices such as MPPT Solar Charge controllers. Total means all directly connected devices plus the devices connected over USB. The limit is mostly bound by CPU processing power. Note that there is also a limit to the other type of devices of which often multiple are connected: PV Inverters. Up to three or four three phase inverters can typically be monitored on a CCGX. Higher power CPU devices can monitor more.

Optional accessories

GX Touch adapter for CCGX cut-out
This adapter is designed to easily replace the CCGX display with the newer GX Touch 50 or the GX Touch 70. Contents of the packaging are the metal bracket, the plastic bezel, and four mounting screws.

Temperature sensor for Quattro, MultiPlus and GX Device (such as the Cerbo GX)

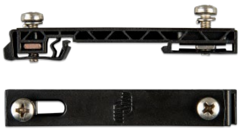

DIN35 adapter small
DIN-Rail adapter to easily mount a device on a DIN-Rail. Suitable for the Cerbo GX.

AcuDC 240

DC Power & Energy Meter Datasheet

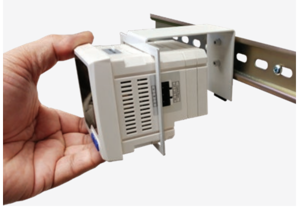

DESCRIPTION

The AcuDC 240 is a DC energy meter designed to monitor and control DC power systems with a wide range of measurement parameters such as voltage, current, power and energy. Ideal for renewable energy applications, it supports bi-directional current measurement used in net metering, solar PV, and wind turbine power generation as well as other applications such as transportation systems, telecommunications, and power distribution systems.

FEATURES

- 0.2% accuracy on voltage and current; 0.5% on power and energy
- Optional data logging with adjustable log size
- Optional RS485 Modbus-RTU communications
- Compatible with DC current sensors, DC voltage sensors, Hall effect sensors, & shunts
- Equip with a variety of I/O options including Analogue Output, Analogue Input, Relay Output or Digital Output
- Standard 72mm x 72mm DIN size for drawer-type panel installation

KEY FEATURES

High Accuracy Measurements

+ With 0.5% accuracy on power & energy* and 0.2% accuracy on voltage & current, the AcuDC 240 meter captures precision metrics across DC systems up to 1000Vdc. Meter critical, real-time voltage, current, power, energy, and amp-hour parameters while viewing real-time data instantly on the multi-function display.

Modbus-RTU Communications

+ Communicate all DC metered data to SCADA, PLC, or other external systems using industry-standard Modbus-RTU protocol via an on-board RS485 communication port. Daisy-chain multiple meters together for efficient data collection.

I/O Modules

+ A variety of optional analogue, digital, relay, and alarm output combinations are available via field-swappable, plug-in I/O modules. Each module features a unique combination of DI, AO, AI, RO, or DO options to extend the capabilities of the AcuDC 240 meter. Certain modules also feature a Hall effect sensor power supply for additional flexibility.

Built-In Data Logging

+ The AcuDC offers three, configurable log files where meter parameters such as power, energy, voltage, current, amp hour, and DI count data are recorded. Log at a 1 minute interval for up to four months for later analysis.

**0.2% accuracy on power & energy available upon request.*

APPLICATIONS

+ DC Energy Management Systems
+ Power Distribution Systems
+ Renewable Energy
+ Industrial DC Control Systems
+ Metallurgy & Electroplating Industries
+ Light Rail Transit Systems
+ Electric Vehicle Charging
+ Data Centers
+ Cellular Tower Monitoring

SPECIFICATIONS

Metering

PARAMETERS	ACCURACY	RESOLUTION	RANGE
Voltage	0.2%	0.001V	0~9999V
Current	0.2%	0.001A	0~±50000A
Power*	0.5%	0.001kW	0~±60000kW
Energy*	0.5%	0.01kWh	0~9999999.99kWh
Drift with Temperature	<100ppm/°C		
Stability	0.5‰/year		

* 0.2% accuracy on Power and Energy available upon request

Input

CURRENT INPUTS *(Each Channel)*

Nominal Current Options	0~±10A(Direct Input, pick up current 0.01A) 0~±50000A (via Shunt or Hall Effect Sensor, programmable range)
Shunt	50~100mV (programmable)
Hall Effect Sensor	0~±5V/0-±4V, 4~20mA/12mA±8mA
Power Consumption	2W (Max)
Accuracy	0.20%

VOLTAGE INPUTS *(Each Channel)*

Nominal Full Scale	Direct Input: 0~1000V Via Hall Effect Sensor: 0~9999V
Input Impedance	2MΩ
Load	<0.6W
Accuracy	0.20%

ENERGY ACCURACY

Active	0.50%

Communications

RS-485

2-Wire Shielded Twisted Pair Cable Connection
Half duplex, Optically Isolated
1200 to 38400bps
Isolation Voltage: 2500Vac

PROTOCOLS

Modbus-RTU

Control Power

AC/DC CONTROL POWER

Operating Range	(P1) 100-240Vac, 50/60Hz, 100-300Vdc (P2) 20-60Vdc
Power Consumption	3W (typical)

Operating Environment

Operating Temperature	-25°C to 70°C -13°F to 158°F
Storage Temperature	-40°C to 85°C -40°F to 176°F
Relative Humidity	5% to 95% Non-Condensing

I/O Options

DIGITAL INPUT

Optical Isolated Voltage	2500Vac
Input Type	Dry
Input Resistance	100kΩ
Input Voltage Range	20~160 Vac/dc
Input Current (Max)	2mA
Start Voltage	15V
Stop Voltage	5V
Pulse Frequency (Max)	100Hz, 50% Duty Ratio (5ms ON and 5ms OFF)
SOE Resolution	2ms

DIGITAL OUTPUT *(Photo-Mos)*

Voltage Range	0~250Vac/dc
Load Current	100mA (Max)
Output Frequency	25Hz, 50% Duty Ratio (20ms ON, 20ms OFF)
Isolation Voltage	2500Vac

RELAY OUTPUT *(RO)*

Type	Mechanical contact, Form A
Switching Voltage (Max)	250Vac, 30Vdc
Load Current	5A(R), 2A(L)
Set Time	10ms (Max)
Contact Resistance	30mΩ (Max)
Isolation Voltage	2500Vac
Mechanical Life	$1.5x10^7$

ANALOGUE OUTPUT *(AO)*

Output Range	0~5V/1~5V, 0~20mA/4~20mA (Optional)
Accuracy	0.50%
Temperature Drift	50ppm/°C Typical
Isolation Voltage	500Vdc
Open Circuit Voltage	15V
Load Capacity	Current type, max load resistance: 750 Ohm Voltage type, max load current: 20 mA

Standard Compliance & Certifications

Safety Standard	IEC 61010-1
EMC Standard	IEC 55011, IEC 61000-6-2, IEC 61000-3-2, IEC 61000-3-3

FUNCTION LIST

● Function; ⊙ Option; Blank NA

	Function	Parameters	AcuDC 243
Metering	Voltage	V	●
	Current	I	●
	Power	P	●
	Energy	E	●
	Ampere-hour	Ah	●
I/O	X1: 2DI+2AO (4~20mA/0~20mA)	Support DI count	⊙
	X2: 2DI+2AO (0-5V/1-5V)		⊙
	X3: 2DI+2RO		⊙
	X4: 2DI+2DO		⊙
	X5: 2DI+±15Vdc		⊙
	X6: 2AI±15Vdc (4~20mA/0~20mA)		⊙
	X7: 2AI±15Vdc (0~5V/1~5V)		⊙
Datalogging	All metering parameters can be recorded (Voltage, Current, Power, Energy, Ampere-hour, DI Count); Interval 1 minute; Can record 4 months		⊙
Communication	RS485 , Modbus RTU		⊙
Display	LCD		●
Dimension	72.0 × 72.0 × 64.5mm (Cutout: 68.0×68.0 mm) / 2.84 × 2.84 × 2.54 inch (Cutout: 2.68 × 2.68 inch)		

DIMENSIONS

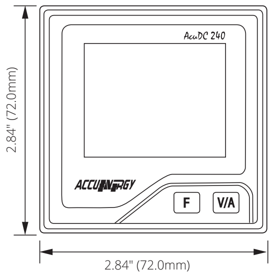

Front View

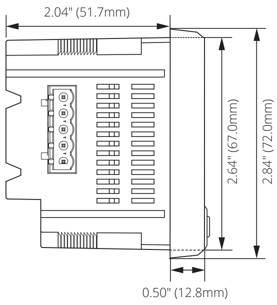

Side View

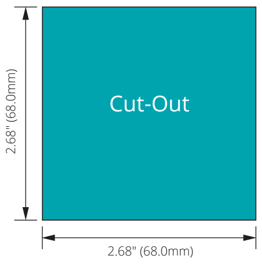

Cut Out

I/O Module Dimensions

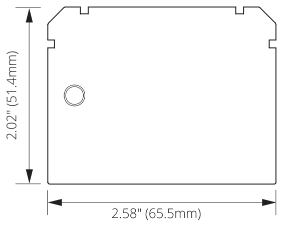

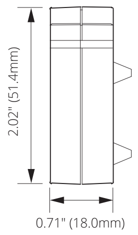

DIN Rail Dimensions

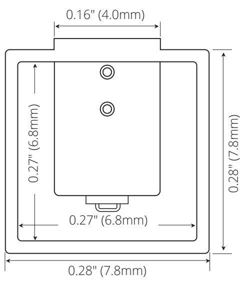

Front View

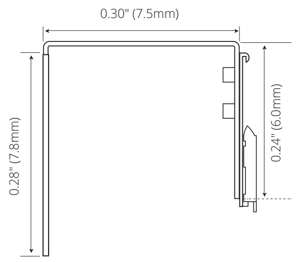

Side View

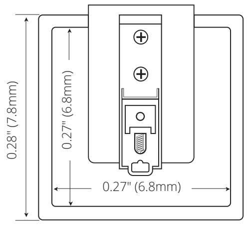

Back View

WIRING DIAGRAMS

Current Direct Wiring

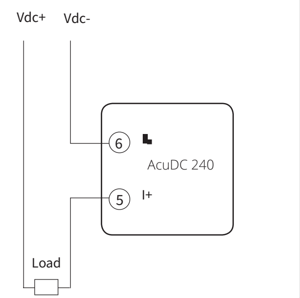

Current Wiring Using Shunt

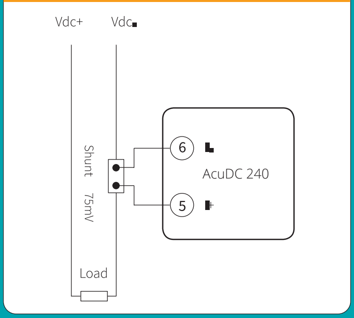

Voltage Direct Wiring

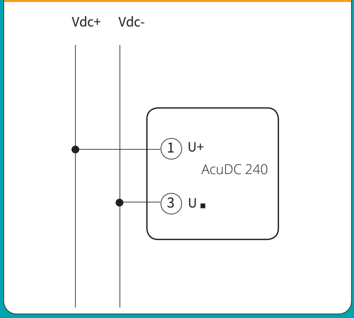

Voltage Wiring using Voltage Hall Effect Sensor*

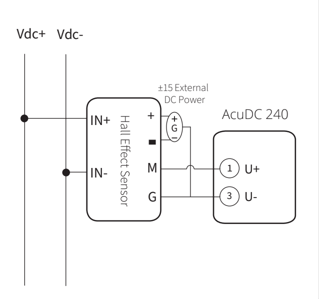

Voltage & Current Direct Wiring

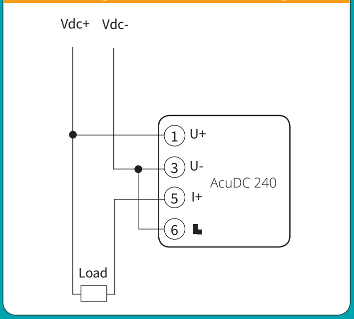

Voltage & Current Wiring using Shunt*

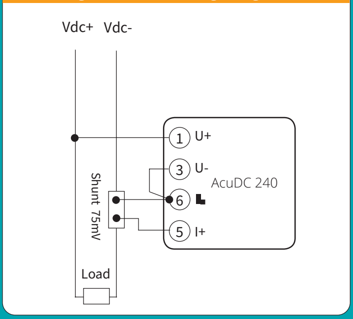

Voltage & Current Wiring using Current Hall Effect Sensor**

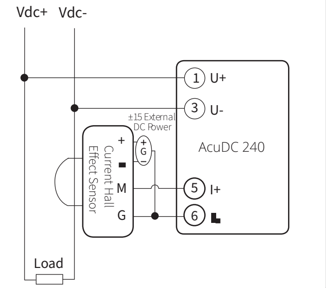

Voltage & Current Wiring using Hall Effect Sensors**

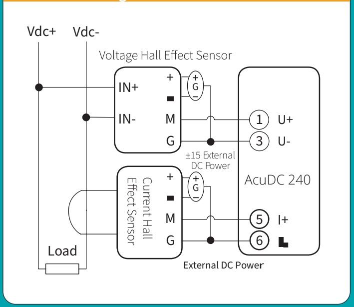

Digital Input

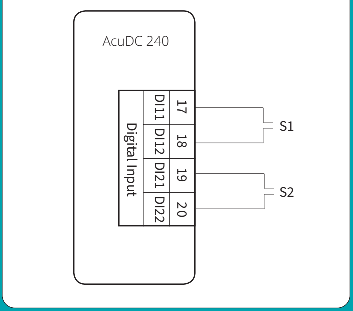

Analogue Output 4~20mA, R<500Ω

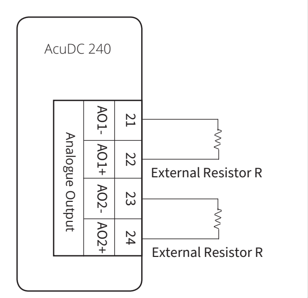

External Power Supply < 250Vac or 30Vdc I < 3A

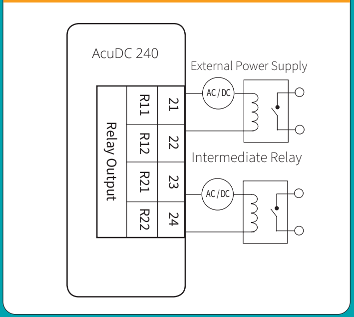

Power Supply Wiring

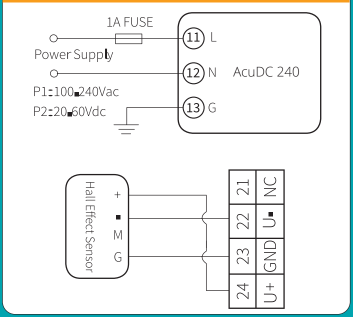

*A physical jumper from terminal 3 to 6 must be connected.

**Hall effect sensors can also be powered using the ±15V power supply from the X5, X6, or X7 modules.

ACCESSORIES

DIN Rail Mounting Adapter

The AcuDC DIN Rail Mounting Adapter is the easy way to mount the AcuDC energy meter on horizontal DIN rail. The adapter quickly secures to the DC meter plus any additional I/O options for a quick, secure installation.

USB RS485 Converter

This professional-grade, plug-and-play USB to Serial RS485 Converter is compliant with both USB 1.1 and 2.0 standards and is designed to provide a convenient, reliable USB connection to the AcuDC energy meter and other serial devices.

ORDERING INFORMATION

Meter Model	Voltage Option	Current Option	Power Supply Option	I/O Option	Communication	Datalogging
AcuDC 243: Multifunction	**1000V:** Nominal Input Voltage 1000Vdc	**A0:** 0~±10A	**P1:** 100-240Vac 50/60Hz, 100-300Vdc	**X0:** No I/O	**NC:** No Communication	**ND:** No Datalogging
	600V: Nominal Input Voltage 600Vdc	**A1:** Shunt (50~100mV)	**P2:** 20-60Vdc	**X1:** 2DI+2AO (4~20mA/0~20mA)	**C:** RS485, Modbus RTU	**D:** Datalogging
	300V: Nominal Input Voltage 300Vdc	**A2:** Current Hall Effect Sensor (4~20mA/12mA±8mA)		**X2:** 2DI+2AO (0~5V/1~5V)		
	60V: Nominal Input Voltage 60Vdc	**A3:** Voltage Hall Effect Sensor (0~±5/0~±4V)		**X3:** 2DI+2RO		
	5V: Via Hall Effect Sensor (0-5V/0-4V), ratio settable			**X4:** 2DI+2DO		
				X5: 2DI+ ±15Vdc		
				X6: 2AI ±15Vdc (4~20mA/0~20mA)		
				X7: 2AI ±15Vdc (0~5V/1~5V)		
Ordering Example:	**AcuDC 243 - 300V - A2 - P1 - X1 - C - D**					

Accessories *(Optional)*	
USB-RS485:	USB-to-RS485 Converter
DC-DIN:	DIN Rail Mounting Accessory
Ordering Example:	**USB-RS485**

Note: When the input voltage is above 1000V, or the system design requires an isolation sensor, the voltage input can be selected as Via Hall Effect Sensor (0~5V). The Voltage Hall Effect Sensor output range requires 0~5V.

Accuenergy (Canada) Inc.
Los Angeles - Toronto - Beijing - Pretoria
North America Toll Free: 1-877-721-8908
Web: www.accuenergy.com
Email: marketing@accuenergy.com

Revision Date: Feb 2022 Version: 1.0.1
Specs Subject To Change Without Notice.

ISO9001 Certified

ACCUENERGY

HAK Series

Hall Effect DC Current Sensor

DATASHEET

HAK Series

HAK21

Hall Effect DC Current Sensor Datasheet

The HAK Series Hall effect DC current sensors provide precision measurements of DC current up to 200A with a standard 4-20mA or 0-5V output signal for broad compatibility. Featuring a hinged split-core design for fast, easy installation into existing systems, the HAK provides accurate 0.5% measurements for any DC project and is available as either a uni-directional or bi-directional device.

Features

- Accuracy class: 0.5%
- Multiple current input options for wide compatibility
- Two available output options: 4-20mA or 0-5V
- Features a hinged split-core design for fast installation
- Measure up to 200A DC current (depending on model)
- Choose uni-directional or bi-directional measurements

CE RoHS COMPLIANT

Accuenergy (Canada) Inc.
Los Angeles - Toronto - Beijing - Pretoria
North America Toll Free: 1-877-721-8908
Web: www.accuenergy.com
Email: marketing@accuenergy.com

Revision Date: Oct 2021 Version: 1.0.1
Specs Subject To Change Without Notice

Specifications

RATED CURRENT	50A, 100A, 200A
Current Range	10-120% of rated current
Output	4-20mA or 0-5V
Accuracy	0.5%
MECHANICAL/ENVIRONMENTAL	
Form Factor	Hinged Split-Core CT
Window Size	Ø 21.0mm (0.83”)
Exterior Dimensions	60.0mm x 61.0mm x 16.0mm 2.36” x 2.40” x 0.63”
Case Material	Epoxy encapsulated housing, UL 94V-0
Lead Wires	Terminal Output
Operating Temperature	-10°C to 85°C / 14°F to 185°F
Storage Temperature	-40°C to 90°C / -40°F to 194°F
Operating Humidity	Non-condensing, 0 to 95% RH
Installation Conditions	Indoor Use
ELECTRICAL	
Wire Polarity	Follow markings on terminal block connector
Phase Orientation	Choose: Uni- or Bi-Directional
Frequency Range	DC
Power Supply	±15V
SAFETY/COMPLIANCE	
Dielectric Strength	5,000V RMS @ 50HZ for 1 minute
Certifications	CE, RoHS

Dimensions

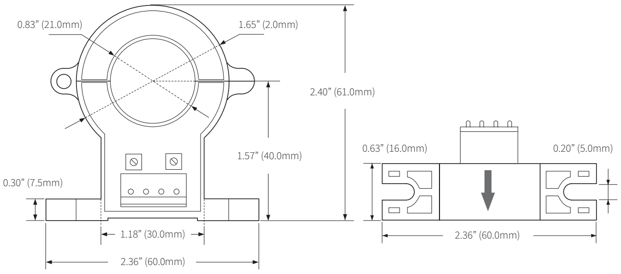

Ordering Information

	Model		*Rated Input*		*Rated Output*		*Directional*
Ordering Number		-		:		-	
Ordering Example	**HAK21**	**-**	**100**	**:**	**A2**	**-**	**B**
			50: 50A		A2: 4-20mA		Blank - *Uni-directional*
			100: 100A		A3: 0-5V		B - *Bi-directional*
			200: 200A				

HAK Series

HAK40

Hall Effect DC Current Sensor Datasheet

The HAK Series Hall effect DC current sensors provide precision measurements of DC current up to 1000A with a standard 4-20mA or 0-5V output signal for broad compatibility. Featuring a hinged split-core design for fast, easy installation into existing systems, the HAK provides accurate 0.5% measurements for any DC project and is available as either a uni-directional or bi-directional device.

Features

- Accuracy class: 0.5%
- Multiple current input options for wide compatibility
- Two available output options: 4-20mA or 0-5V
- Features a split-core design for fast installation
- Measure up to 1000A DC current (depending on model)
- Choose uni-directional or bi-directional measurements

Accuenergy (Canada) Inc.
Los Angeles - Toronto - Beijing - Pretoria
North America Toll Free: 1-877-721-8908
Web: www.accuenergy.com
Email: marketing@accuenergy.com

Revision Date: Oct 2021 Version: 1.0.1
Specs Subject To Change Without Notice

Specifications

RATED CURRENT	400A, 600A, 1000A
Current Range	10-120% of rated current
Output	4-20mA or 0-5V
Accuracy	0.5%
MECHANICAL/ENVIRONMENTAL	
Form Factor	Hinged Split-Core CT
Window Size	Ø 40.0mm (1.58”)
Exterior Dimensions	100.0mm x 100.0mm x 24.0mm 3.94” x 3.94” x 0.94”
Case Material	Epoxy encapsulated housing, UL 94V-0
Operating Temperature	-10°C to 85°C / 14°F to 185°F
Storage Temperature	-40°C to 90°C / -40°F to 194°F
Operating Humidity	Non-condensing, 0 to 95% RH
Installation Conditions	Indoor Use
ELECTRICAL	
Wire Polarity	Follow markings on terminal block connector
Phase Orientation	Choose: Uni- or Bi-Directional
Frequency Range	DC
Power Supply	±15V
SAFETY/COMPLIANCE	
Dielectric Strength	5,000V RMS @ 50HZ for 1 minute
Certifications	CE, RoHS

Dimensions

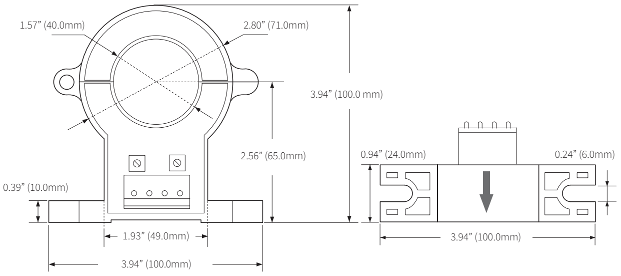

Ordering Information

	Model		*Rated Input*		*Rated Output*		*Directional*
Ordering Number		-		:		-	
Ordering Example	**HAK40**	**-**	**600**	**:**	**A2**	**-**	**B**
			400: 400A		A2: 4-20mA		Blank - *Uni-directional*
			600: 600A		A3: 0-5V		B - *Bi-directional*
			1000: 1000A				

CMP3 | SMP3

Applications

Solar Monitoring for PV
Weather Services
Agriculture
Horticulture
Industry

Pyranometer

For reliable entry-level measurement of solar irradiance

IEC61724 Class C
ISO 9060 Spectrally Flat Class C
Internal desiccant
Analog and digital outputs
5 year warranty

ISO 9060 & IEC 61724 Class C

If you are looking for reliable solar radiation measurement to comply with ISO 9060 Spectrally Flat Class C and IEC 61724-1 Class C the CMP3 or SMP3 are the right pyranometers to choose. They are compact, light and provide reliable and good quality data in a wide range of operational environments. SMP3 is ideal for efficiency monitoring in small commercial PV installations.

Internal desiccant

Both models are fitted with a maintenance-free internal drying cartridge to provide stable measurements and have an IP67 ingress protection rating. The pyranometers feature a snap-on white sun shield, integrated leveling and a high quality connector which is supplied pre-wired with 10 m of signal cable for simple installation.

Analog or digital outputs

CMP3 does not require any power. Incoming solar radiation generates a continuous millivolt output, which is converted in a data logger to irradiance in W/m^2 using the calibrated sensitivity. For easy integration into SCADA systems SMP3 has Modbus® RTU RS-485 serial communication, plus an amplified analog output. The sensitivity is stored inside for standardized outputs and it features improved response time and digital temperature compensation.

5 Year Warranty

All pyranometers from Kipp & Zonen come with a 5 year warranty and we have service and calibration centers around the world.

an OTT HydroMet brand

Technical Specifications

	CMP3	**SMP3**
Classification to ISO 9060:2018	Spectrally Flat Class C	Spectrally Flat Class C
Sensitivity	10 to 32 μV/W/m^2	-
Impedance	20 to 200 Ω	-
Expected output range (0 to 1500 W/m^2)	0 to 55 mV	-
Maximum operational irradiance	2000 W/m^2	2000 W/m^2
Analogue output • V-version	-	0 to 1 V
Analogue output range*	-	-200 to 2000 W/m^2
Analogue output • A-version	-	4 to 20 mA
Analogue output range*	-	0 to 1600 W/m^2
Serial output	-	RS-485 Modbus® RTU
Serial output range	-	-400 to 2000 W/m^2
Response time (63 %)	< 6 s	< 1,5 s
Response time (95 %)	< 20 s	< 12 s
Spectral range (20 % points)	285 to 3000 nm	285 to 3000 nm
Spectral range (50 % points)	300 to 2800 nm	300 to 2800 nm
Zero offsets (unventilated)		
(a) thermal radiation (at 200 W/m^2)	< 15 W/m^2	< 15 W/m^2
(b) temperature change (5 K/h)	< 5 W/m^2	< 5 W/m^2
(c) total zero offset	< 20 W/m^2	< 20 W/m^2
Additional signal processing errors	n.a.	< 3 %
Non-stability (change/year)	< 1 %	< 1 %
Non-linearity (100 to 1000 W/m^2)	< 2 %	< 2 %
Directional response (up to 80 ° with 1000 W/m^2 beam)	< 20 W/m^2	< 20 W/m^2
Clear sky GHI spectral error	< 0.2 %	< 0.2 %
Spectral selectivity (350 to 1500 nm)	< 3 %	< 3 %
Tilt response (0 ° to 90 ° at 1000 W/m^2)	< 1.5 %	< 1.5 %
Temperature response	< 4 % (-10 °C to +40 °C)	< 3 % (-20 °C to +50 °C) < 4 % (-40 °C to +70 °C)
Field of view	180 °	180 °
Accuracy of bubble level	< 0.2 °	< 0.2 °
Power consumption (at 12 VDC)	-	V-version: 55 mW A-version: 100 mW
Supply voltage	-	5 to 30 VDC
Software, Windows™	-	SmartExplorer Software, for configuration, test and data logging
Detector type	Thermopile	Thermopile
Operating and storage temperature range	-40 °C to +80 °C	-40 °C to +80 °C
Humidity range	0 to 100 %	0 to 100 %
MTBF (Mean Time Between Failures)	> 10 years	> 10 years**
Ingress Protection (IP) rating	67	67
Recommended applications	Economical solution for routine measurements in weather stations, field testing, agriculture, horticulture and hydrology	Economical solution for efficiency and maintenance monitoring of PV power installations, routine measurements in weather stations

** adjustable with SmartExplorer Software ** extrapolated after introduction in January 2012*
Note: The performance specifications quoted are worst-case and/or maximum values

Dimensions

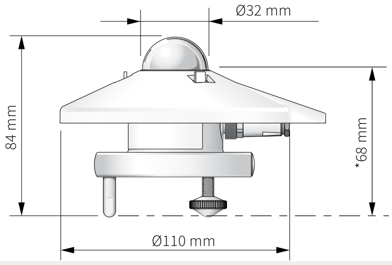

SILICON IRRADIANCE SENSOR

Measurement of Solar Irradiance

Silicon irradiance sensors (Si sensor) show a cost-effective, but rugged and reliable solution for the measurement of solar irradiance, especially for the monitoring of Photovoltaic (PV) systems. Based on the construction of the sensor element corresponding to a PV module they are ideal as reference for the monitoring of PV systems. Especially the spectral response comparable to PV modules as well as the similar inclination error (incident angle modifier) allow an exact analysis of PV energy yields using Si sensor data.

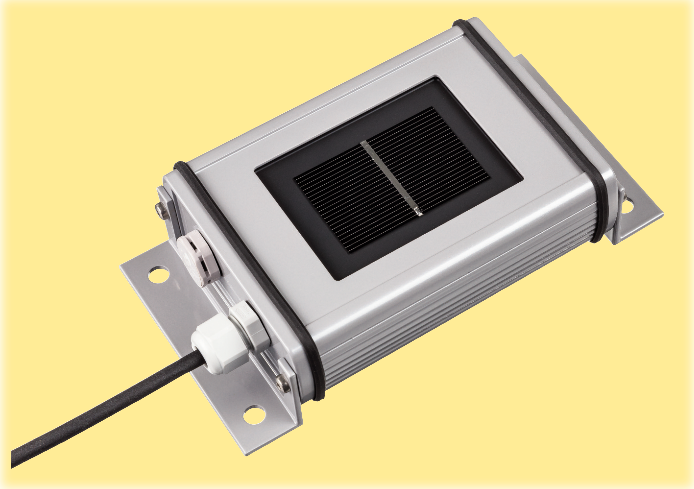

General Information

Mode of Operation

A silicon solar cell can be used as an irradiance sensor, because the short-circuit current is proportional to the irradiance. Our sensors are build out of a monocrystalline Si solar cell connected to a shunt. Due to the low resistance of the shunt the cell operates next to short-circuit.

To minimize influences of temperature to the measuring signal all of our sensors with the extension „TC“ have an active temperature compensation via a temperature sensor laminated to the back surface of the solar cell.

All sensors are calibrated in artificial sunlight against a reference cell calibrated at the Physikalisch-Technische Bundesanstalt (PTB, National Metrology Institute of Germany).

Mechanical Construction

The solar cell is embedded in Ethylen-Vinyl-Acetat (EVA) between glass and Tedlar. The laminated cell is integrated into a case of powder-coated aluminium. Therefore the sensor construction is comparable to that of a standard PV module. The electrical connection is realized by a 3 m cable or a waterproof (IP67) connector.

Optional Temperature Measurement

Additionally to the irradiance measurement our silicon sensors with the extension "-T" are able to measure the temperature of the solar cell using a temperature sensor laminated to the back of the cell. This solar cell temperature can approximately be used as module temperature.

INGENIEURBÜRO
Mencke & Tegtmeyer GmbH

Meßgeräte für die Solartechnik
Made in Germany

INGENIEURBÜRO
Mencke & Tegtmeyer GmbH

Schwarzer Weg 43A
31789 Hameln
Germany
Tel: +49 51 51 / 40 36 99 - 0
Fax: +49 51 51 / 40 36 99 - 19
email: info@ib-mut.de
http://www.ib-mut.de

SILICON IRRADIANCE SENSOR

Technical Data

SI-SENSOR

General Information

- Solar cell: Monocrystalline silicon (50 mm x 33 mm)
- Operating temperature: -35°C to 80°C
- Electrical connection: 3 m shielded cable
- Load impedance for Si-V-1.5TC-batt: minimal 1 MΩ
- Load impedance for Si-V-1.5TC(-T), Si-V-10TC(-T): min. 10 kΩ
- Load impedance for Si-I-420TC(-T): minimal 20 Ω and maximal 400 Ω
- Case, protection mode: Powder-coated aluminium, IP 65
- Dimension, weight: 155 mm x 85 mm x 39 mm, approx. 350 to 470 g
- Customs number for all sensors: 90 15 80 20

Digital

- Protocol: M&T (type -MT), MODBUS RTU (type -MB)
- Interface: RS485 up to 38.4 kBaud
- Galvanic isolation: 1.000 V between power supply and bus

DIMENSIONS

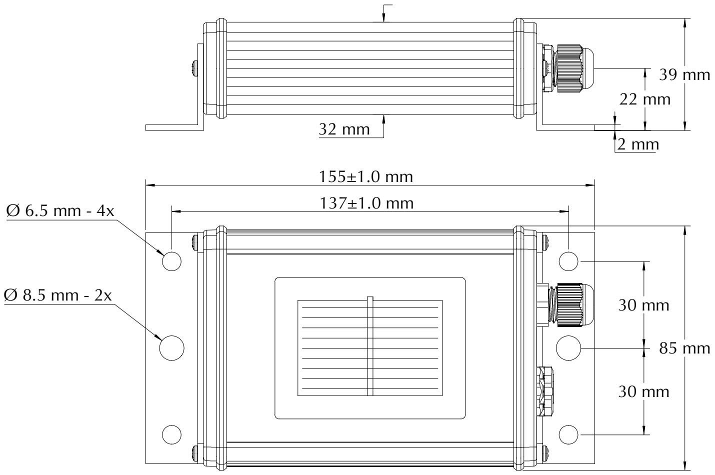

INCIDENT ANGLE MODIFIER

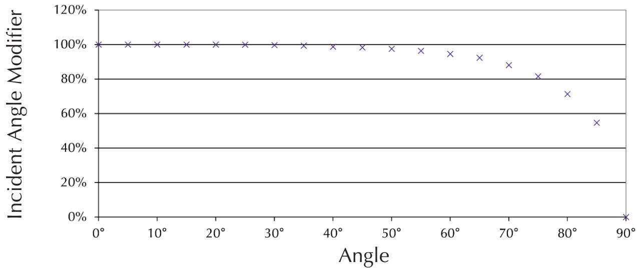

SPECTRAL RESPONSE

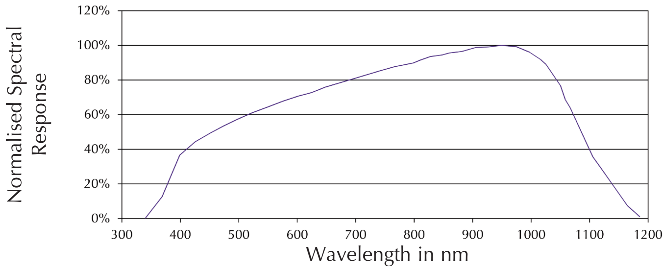

SILICON IRRADIANCE SENSOR

Technical Data

Sensor Types:

Type	Irradiance			Cell Temperature
Measured Variable	Power Supply Current Consumption	Temperature compensation	Output Signal	Output Signal
Si-V-1.5TC-batt Irradiance	2*Mignon a 1.5 V typic 15 µA	Yes	0 to 1.5 V for 0 to 1,500 W/m^2	./.
Si-V-1.5TC Irradiance	24 V_{DC} (4 to 28 V_{DC}) typic < 1 mA	Yes	0 to 1.5 V for 0 to 1,500 W/m^2	./.
Si-V-1.5TC-T Irradiance, Cell Temperature	24 V_{DC} (5.5 to 28 V_{DC}) typic < 1 mA	Yes	0 to 1.5 V for 0 to 1,500 W/m^2	0 to 2 V for -40 to +90°C
Si-mV-85-Pt100(0)(-4L) **Si-mV-85** Irradiance	./. ./.	No	approx. 85 mV for 1,500 W/m^2	Pt100 / Pt1000 ./.
Si-V-10TC Irradiance	24 V_{DC} (12 to 28 V_{DC}) typic < 1 mA	Yes	0 to 10 V for 0 to 1,500 W/m^2	./.
Si-V-10TC-T Irradiance, Cell Temperature	24 V_{DC} (12 to 28 V_{DC}) typic <1 mA	Yes	0 to 10 V for 0 to 1,500 W/m^2	0 to 10 V for -40 to +90°C
Si-I-420TC Irradiance	24 V_{DC} (12 to 28 V_{DC}) typic 5 to 23 mA	Yes	4 to 20 mA for 0 to 1,500 W/m^2	./.
Si-I-420TC-T Irradiance, Cell Temperature	24 V_{DC} (12 to 28 V_{DC}) typic 10 to 46 mA	Yes	4 to 20 mA for 0 to 1,500 W/m^2	4 to 20 mA for -40 to +90°C
Si-RS485TC-T Irradiance, Cell Temperature	24 V_{DC} (12 to 28 V_{DC}) typic 25 mA	Yes	M&T, MODBUS 0 to 1,500 W/m^2	M&T, MODBUS -40 to +90°C
Si-RS485TC-2T Irradiance, Cell Temperature, Ambient Temperature (sensor firmly connected with 3 m cable)	24 V_{DC} (12 to 28 V_{DC}) typic 25 mA	Yes	M&T, MODBUS 0 to 1,500 W/m^2	M&T, MODBUS -40 to +90°C
Si-RS485TC-T-Tm Irradiance, Cell Temperature, Module Temperature (sensor firmly connected with 3 m cable)	24 V_{DC} (12 to 28 V_{DC}) typic 25 mA	Yes	M&T, MODBUS 0 to 1,500 W/m^2	M&T, MODBUS -40 to +90°C
Si-RS485TC-2T-v Irradiance, Cell Temperature Accessories: External Temperature, Wind Speed	24 V_{DC} (12 bis 28 V_{DC}) typic 25 mA	Yes	M&T, MODBUS 0 to 1,500 W/m^2	M&T, MODBUS -40 to +90°C
Si-RS485TC-3T Irradiance, Cell Temperature, Accessories: Two External Temperatures	24 V_{DC} (12 to 28 V_{DC}) typic 25 mA	Yes	M&T, MODBUS 0 to 1,500 W/m^2	M&T, MODBUS -40 to +90°C

SILICON IRRADIANCE SENSOR

Measurement Uncertainty of Irradiance
(does not apply for sensors with filter glass or polycrystalline cells)

Parameter	Sensor Type	Typical Measurement Uncertainty
Response time (99 %) **for G > 50 W/m^2**	Si-mV-85(-Pt100(0))	0.001 s
	Si-V-1.5TC(-T), Si-V-10TC(-T), Si-I-420TC(-T)	0.15 s
	Si-RS485TC-XX	1 s
Offset	Si-mV-85(-Pt100(0))	0 W/m^2
	Si-V-1.5TC(-T), Si-V-10TC(-T)	2 W/m^2
	Si-I-420TC(-T)	2.2 W/m^2
	Si-RS485TC-XX	1 W/m^2
Stability per anno [1]	all	0.50 %
Non-Linearity [1]	all	0.10 %
Temperature Dependancy [1] **for -35 to +80°C**	Si-mV-85-Pt100(0) (with external temperature comp.) [2]	0.20 %
	Si-mV-85(-Pt100(0)) (without external temperature comp.)	3.00 %
	Si-V-1.5TC(-T), Si-V-10TC(-T), Si-I-420TC(-T)	0.40 %
	Si-RS485TC-XX	0.40 %
Factory-Calibration	all (repeatability against reference)	0.75 %
	all (measurement uncertainty of reference at STC and vertical light beam)	0.50 %

Sensortyp	Measurement Uncertainty in ± W/m^2 ± % of Reading[3]		
	100…1500 W/m^2	0…<100 W/m^2	Meas. Uncertainty acc. IEC61724-1
Si-mV-85-Pt100(0) [2]	± 0.2 ± 2.0 %	± 0.3 ± 2.0 %	Class A
Si-mV-85	± 0.2 ± 5.0 %	± 0.3 ± 5.0 %	Class B
Si-V-10/1.5TC(-T)	± 2.5 ± 2.0 %	± 4.0 ± 2.0 %	Class B
Si-I-420TC(-T)	± 3.0 ± 2.0 %	± 4.5 ± 2.0 %	Class B
Si-RS485TC-XX	± 1.0 ± 2.0 %	± 2.0 ± 2.0 %	Class A

Sensor Type	Measurement Uncertainty of the internal Temperature Measurement	
	Condition	Measurement Uncertainty
Si-mV-85-Pt100(0)(-4L)	-35 to +80°C	IEC 60751, class A
Si-V-1.5TC-T	-35 to +70°C / -35 to +80°C	1.0 K / 1.1 K
Si-V-10TC-T	-35 to +70°C / -35 to +80°C	1.0 K / 1.1 K
Si-I-420TC-T	-35 to +60°C / -35 to +80°C	1.0 K / 1.3 K
Si-RS485TC-XX	-35 to +80°C	1.0 K

[1] Percentage rate referred to the measurement value

[2] External temperature compensation must be calculated on data acquisition side (temperature coefficient at AM 1.5: 0.0005 1/K)

[3] Based on GUM (Guide to the Expression of Uncertainty in Measurement) with k=2, valid for spectrum AM 1.5, vertical light beam and complete operating temperature range

SILICON IRRADIANCE SENSOR

ACCESSORIES FOR Si-RS485TC-2T-v

- **Tamb-Si**, Ambient temperature sensor in stainless steel sleeve with 3 m cable and connector (IP67), measuring range: -40 to +90°C
- **Tmodul-Si**, Module temperature sensor in aluminium block with 3 m cable and connector (IP67), measuring range: -40 to +90°C
- **Vwind-Si**, Wind speed sensor with 5 m cable and connector (IP67), measuring range: 0.9 to 40 m/s

EXTEND OF SUPPLY

- Silicon sensor with shielded cable, 0.14 mm^2, UV- and temperature resistant, 3m length and ferrules (except Si-V-1.5TC-batt)
- Mignon cells not included
- Calibration protocol and quick reference guide

Options

- DaKKS calibration certificate
- Customized cable lengths
- Version with waterproof connector (Si-V-1.5TC-batt always with connector)
- Adaptation of spectral response to different PV materials
- Customised scaling or measuring range

SILICON IRRADIANCE SENSOR

Option Connector

ELECTRICAL CONNECTION

Optional Version with Connectors

The electrical connection of the Si sensor is realized with the inbuilt connector and the suitable plug.

Technical Data of the Plug

- Cable dimensions (best / max.): 0.14 mm² / 0.25 mm² (AWG26 / AWG24)
- Diameter of cable: 3.5 … 5 mm
- Protection mode: IP67 in conjunction with the suitable connector

The connection of the different Silicon irradiance sensors are listed in the following table. The pin numbers are printed at the inside of the plug. Please take care of the mounting of the plugs as shown at the end of this page. Only if these mounting steps are realised the plug meets IP67 when connected.

Type	Pin Numbers of the Plug			
	Pin 1	Pin 2	Pin 3	Pin 4
Si-V-1.5TC-batt	Plus Signal Irradiance	Minus Signal Irradiance	not available	not available
Si-V-1.5TC	Plus Signal Irradiance	Minus Signal* Irradiance	Plus Signal Power Supply	not available
Si-V-1.5TC-T	Plus Signal Temperature	Plus Signal Irradiance	Plus Signal Power Supply	Minus Signal* Irradiance
Si-mV-85	Plus Signal Irradiance	Minus Signal Irradiance	not available	not available
Si-mV-85-Pt100 Si-mV-85-Pt1000	Plus Signal Irradiance	Minus Signal Irradiance	Pt100 Pt1000	Pt100 Pt1000
Si-I-420TC	Plus Signal Irradiance	Minus Signal* Irradiance	Plus Signal Power Supply	not available
Si-I-420TC-T	Plus Signal Temperature	Plus Signal Irradiance	Plus Signal Power Supply	Minus Signal* Irradiance
Si-V-10TC	Plus Signal Irradiance	Minus Signal* Irradiance	Plus Signal Power Supply	
Si-V-10TC-T	Plus Signal Temperature	Plus Signal Irradiance	Plus Signal Power Supply	Minus Signal* Irradiance

* Minus signals of all sensors are identical to supply ground.

MOUNTING OF PLUG

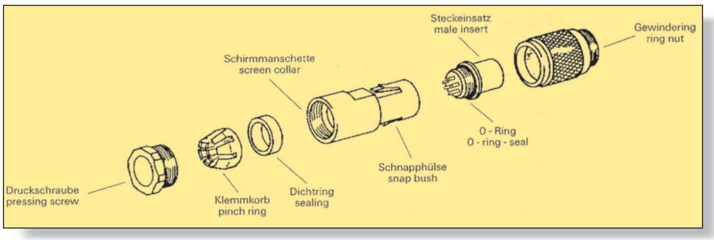

electrotherm
Gesellschaft für Sensorik und
thermische Meßtechnik mbH

Cable-sensor

Type K4RS

Issue 11/19

Sensor

1 x Pt100 F0,3 (old cl. B) DIN EN 60751
2-, 3- or 4-wire-circuit

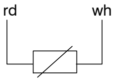

1xPt100 2-wire

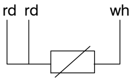

1xPt100 3-wire

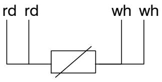

1xPt100 4-wire

Protective tube material

1.4571

thread x insert length

M6 x 20 mm (200°C) 4-wire -> 1
M6 x 30 mm (200°C) 4-wire -> 2
M8 x 40 mm (200°C) 2- or 3-wire -> 3
M10 x 40 mm (400°C) 2- or 3-wire -> 4

Cable

TeSi 2x0,34 or 3x0,34 or 4x0,14 (200°C)
GlGlV 2x0,34 or 3x0,22 (400°C)

Cable length

2500 mm

Order example
K4-E-4LS-200 - 1

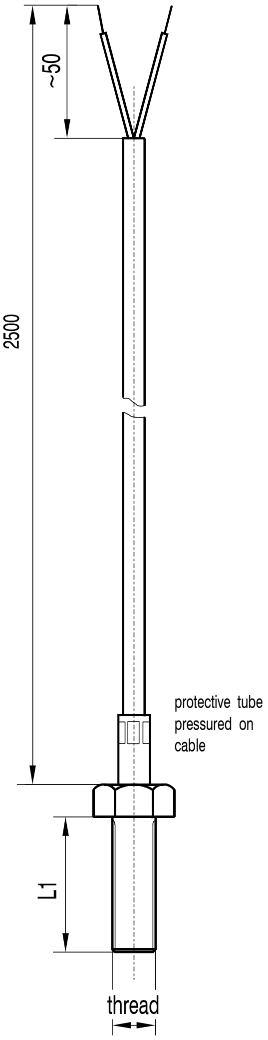

Self Adhesive Patch PT100 Sensor with PFA insulated outer jacket - Type PRT

Click here to view product

Product Code	XE-3685
Sensor Type	Silicone rubber patch with self adhesive foil backing
Element	Pt100
Patch dimensions	L40 x W15mm x D5mm
Cable Length	1, 3 or 5m
Cable Type	PFA insulated outer jacket
Core / Strands	7/0.1mm
Cable Termination	Bare Tails
Max. Temperature	+150°C
Min. Temperature	-50°C

Accuracy	Class B
Number of Wires	4

KELAG Künzli Elektronik AG
Ringstrasse 5
CH-8603 Schwerzenbach
Schweiz / Switzerland

Telefon +41 44 806 22 00
Fax +41 44 806 22 08
E-Mail kelag@kelag.ch
www.inclinometer.ch/en

Two Axis Inclination Sensor
KAS90x and KAS93x

The sensors are based one an advanced “bulk micro machined” technology. The three dimensional structure of these sensors comprise a pendulum made of mono crystalline silicon. The pendulum is hermetically enclosed between two silicon discs. From this construction results a long term stable, high resolution und shock resistant sensor. A gas damping prevents overshooting and interfering resonance oscillation. An ASIC measures the capacitive change caused by the movement of the pendulum.

- **senses in positive and negative direction**
- **static and dynamic acceleration measured**
- **high repeatability up to 0.01% over range**
- **high resolution: up to 0.001% over range**
- **shock resistance of the pendulum min. 20’000g**
- **Temperature range -30 ... +85°C**
- **active and passive temperature compensation**
- **small, solid brass housing with fixing holes**
- **M8 sensor plug connector or rugged PVC cable**
- **Large output span: 0.5 ... 4.5V output over measuring range**
- **Power supply requirement: 7... 30 VDC, stabilized**

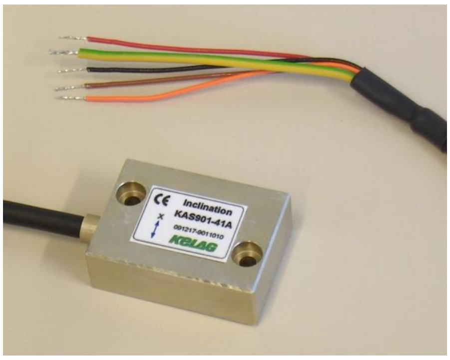

Wire Variant KAS90x-xx

Plug Variant KAS93x-xx

Specifications

Parameter	**Conditions**	**KAS902-50** **KAS932-50**	**KAS901-51** **KAS931-51**	**KAS901-52** **KAS931-52**	**Units**
Measuring range [4]		+/- 0.34 +/- 20	+/- 0.5 +/- 30	+/- 1 +/- 90	g °
Repeatability at 0° (horizontal position) [1]	at 20°C, typ.	0.25 0.014	0.25 0.014	0.25 0.014	mg °
Resolution at 0° / 1g	DC…10Hz DC…1Hz	0.05 0.003 0.015 0.001	0.05 0.003 0.015 0.001	0.05 0.003 0.015 0.001	mg °
typ. Offset temperature dependency [8]	20...60°C	-0/+0.066 -0/+0.006	-0/+.,066 -0/+0.006	-0/+0.066 -0/+0.006	mg / °C ° / °C
long term stability [6]	10 years [6]	0.62 0.036	0.62 0.036	0.62 0.036	mg °
Measuring direction	horizontal	x	x	x	Axis
Cross axis sensitivity [2]	Max.	4	4	4	%
Mechanical Damping	-3 dB	18	18	18	Hz [5]
Operating temperature range		-30 [7] ... +85	-30 [7] ... +85	-30 [7] ... +85	°C
Shock resistance Chip		20’000	20’000	20’000	g
Output signal V_{out} Offset = V_{out} in 0° / position Sensitivity		0.5 ... 4.5 2.5 5.88	0.5 ... 4.5 2.5 4	0.5 ... 4.5 2.5 2	V V V/g
Power supply [3]		7... 30	7... 30	7... 30	VDC
PVC-cable shielded	nominal	1.0	1.0	1.0	m
Analog resitive output load	Vout to Vdd or GND	Min. 10	Min. 10	Min. 10	kOhm
Analog capacitive output load		Max. 20	Max. 20	Max. 20	nF

1) Repeatability: maximum offset occurring with position change after return to initial position (corresponds to achievable precision, including temperature hysteresis after temperature compensation and linearization).
2) Cross axis sensitivity: maximum error occurring with (additional) inclination or acceleration from another direction than the measuring plane
3) Supply stabilized
4) Measuring range: Trigonometric function:

$$\text{angle} = \arcsin\left(\frac{\text{Vout} - 2{,}5\,(\text{Offset})}{\text{Sensitivity}}\right)$$

(paste values without units)
5) Typical values;
6) Long term stability: calculated values from HTB tests. Test results available at request.
7) Cable is specified for -15°C for dynamic and -30°C for static applications
8) Related to sensing element

Connection

Wire Variant KAS90x-xx

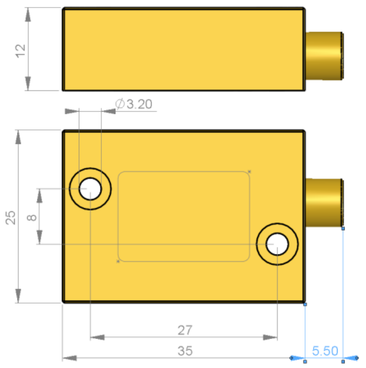

Red: +7 …30 VDC
Black: 0 VDC
Braun: Out X
Orange: Out Y
Shield: Casing

The outputs are not protected!

Plug Variant KAS93x-xx

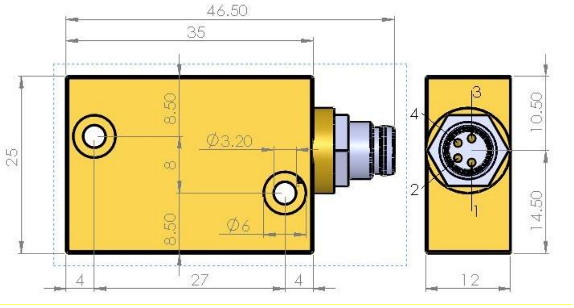

1	+7 …30 VDC
2	0 VDC
3	Out X
4	Out Y

The outputs are not protected!

Mechanical installation

X-Axis

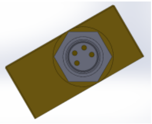
0.5…2.5V

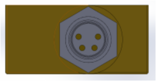
0° = 2.5V

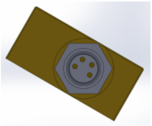
2.5…4.5V

Y-Axis

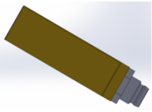
0.5…2.5V


0° = 2.5V

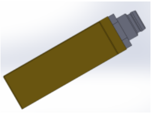
2.5…4.5V

ADAM-4115
ADAM-4015

Robust 6-Ch RTD Input Module

6-ch RTD Module with Modbus

ADAM-4115

ADAM-4015

Specifications

General

Certification	CE, FCC, UL
Connectors	2 x plug-in terminal blocks (#14 ~ 28 AWG)
Power Consumption	1.2 W @ 24 V_{DC}
Watchdog Timer	System (1.6 s) & Communication
Supported Protocols	ASCII command and Modbus/RTU
Interface	RS-485, Micro USB
Burnout Detection	Yes

RTD Input

Channels	6 differential
Input Connections	2, 3-wire
Sampling Rate	10/100 Hz total channels (selected by utility)
Input Impedance	10 MΩ
Input Type	Pt, Balco and Ni RTD
RTD Types and Temperature Ranges	
Pt100	-50~150°C 0~100°C 0~200°C 0~400°C -200~200°C

Supports both IEC 60751 ITS90 (0.0385 W/W/°C) and JIS C 1604 (0.0392 W/W/°C)

Pt1000	-40~160°C
Balco (500)	-30~120°C
Ni (518)	-80~100°C 0~100°C
Accuracy	±0.1% (Typical)
CMR @ 50/60 Hz	120 dB
Span Drift	± 25 ppm/°C
Zero Drift	±6 μV/° C

Specifications

General

Certification	CE, FCC
Connectors	2 x plug-in terminal blocks (#14 ~ 28 AWG)
Power Consumption	Typical: 0.5 W @ 24 V_{DC} Max.: 0.9 W @ 24 V_{DC}
Watchdog Timer	System (1.6 s) & Communication
Supported Protocols	ASCII command and Modbus/RTU
Burnout Detection	Yes

Analog Input

Channels	6 differential
Input Connections	2, 3-wire
Sampling Rate	10 Hz total channels
Input Impedance	10 MΩ
Input Type	Pt, Balco, Ni and BA1 RTD
RTD Types and Temperature Ranges	
Pt100	-50~150°C 0~100°C 0~200°C 0~400°C -200~200°C

Supports both IEC 60751 ITS90 (0.0385 W/W/°C) and JIS C 1604 (0.0392 W/W/°C)

Pt1000	-40~160°C
Balco (500)	-30~120°C
Ni (518)	-80~100°C 0~100°C
Ni (508)	0~100°C -50~200°C
BA1	-200~600°C
Accuracy	±0.1% (Typical)
CMR @ 50/60 Hz	120 dB
Span Drift	± 25 ppm/°C
Zero Drift	± 6 μV/°C

Common Specifications

General

Power Input	10 ~ 30 V_{DC} ADAM-4115: 10 ~ 48 V_{DC}

Environment

Operating Humidity	5 ~ 95% RH
Operating Temperature	-10 ~ 70°C (14 ~ 158°F) ADAM-4115: -40 ~ 85°C (-40 ~ 185°F)
Storage Temperature	- 25 ~ 85°C (-13 ~ 185°F) ADAM-4115: -40 ~ 85°C (-40 ~ 185°F)

Ordering Information

ADAM-4115	Robust 6-Ch RTD Input Module
ADAM-4015	6-ch RTD Module with Modbus

ioLogik E1200 Series

Ethernet remote I/O with 2-port Ethernet switch

Features and Benefits

- User-definable Modbus TCP Slave addressing
- Supports RESTful API for IIoT applications
- Supports EtherNet/IP Adapter
- 2-port Ethernet switch for daisy-chain topologies
- Saves time and wiring costs with peer-to-peer communications
- Active communication with MX-AOPC UA Server
- Supports SNMP v1/v2c
- Easy mass deployment and configuration with ioSearch utility
- Friendly configuration via web browser
- Simplifies I/O management with MXIO library for Windows or Linux
- Class I Division 2, ATEX Zone 2 certification[1]
- Wide operating temperature models available for -40 to 75°C (-40 to 167°F) environments

Certifications

Introduction

The ioLogik E1200 Series supports the most often-used protocols for retrieving I/O data, making it capable of handling a wide variety of applications. Most IT engineers use SNMP or RESTful API protocols, but OT engineers are more familiar with OT-based protocols, such as Modbus and EtherNet/IP. Moxa's Smart I/O makes it possible for both IT and OT engineers to conveniently retrieve data from the same I/O device. The ioLogik E1200 Series speaks six different protocols, including Modbus TCP, EtherNet/IP, and Moxa AOPC for OT engineers, as well as SNMP, RESTful API, and Moxa MXIO library for IT engineers. The ioLogik E1200 retrieves I/O data and converts the data to any of these protocols at the same time, allowing you to get your applications connected easily and effortlessly.

Daisy-Chained Ethernet I/O Connection

This industrial Ethernet remote I/O comes with two switched Ethernet ports to allow for the free flow of information downstream to another local Ethernet device, or upstream to a control server via expandable daisy-chained Ethernet I/O arrays. Applications such as factory automation, security and surveillance systems, and tunneled connections can make use of daisy-chained Ethernet for building multidrop I/O networks over standard Ethernet cables. Many industrial automation users are familiar with multidrop as the configuration most typically used in fieldbus solutions. The daisy-chain capabilities supported by ioLogik Ethernet remote I/O units not only increase the expandability and installation possibilities for your remote I/O applications, but also lower overall costs by reducing the need for separate Ethernet switches. Daisy-chaining devices in this way will also reduce overall labor and cabling expenses.

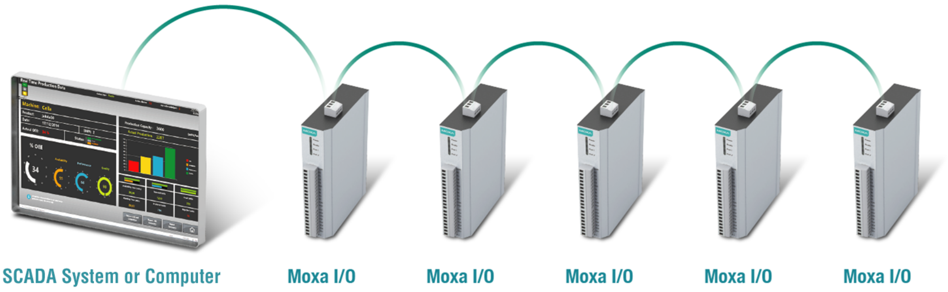

---

[1] Class I Division 2 and ATEX currently do not apply to the E1213/E1213-T models.

Save Time and Wiring Costs with Peer-to-Peer Communications

In remote automation applications, the control room and sensors are often far removed, making wiring over long distances a constant challenge. With peer-to-peer networking, users may now map a pair of ioLogik Series modules so that input values will be directly transferred to output channels, greatly simplifying the wiring process and reducing wiring costs.

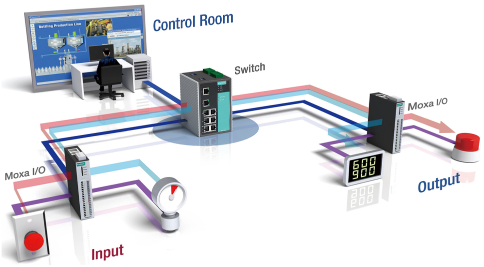

User-Definable Modbus TCP Addressing for Painless Upgrading of Existing Systems

For Modbus devices that are controlled and detected by fixed addresses, users need to spend a vast amount of time researching and verifying initial configurations. Users need to locate each device's networking details, such as I/O channels or vendor-defined addresses, to enable the initial or start address of a SCADA system or PLC. Devices that support user-definable Modbus TCP addressing offer greater flexibility and easier setup. Instead of worrying about individual devices, users simply configure the function and address map to fit their needs.

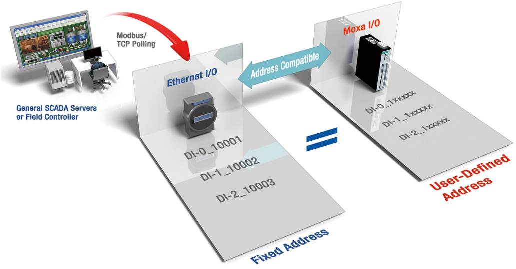

Push Technology for Events

When used with MX-AOPC UA Server, devices can use active push communications when communicating changes in state and/or events to a SCADA system. Unlike a polling system, when using a push architecture for communications with a SCADA system, messages will only be delivered when changes in state or configured events occur, resulting in higher accuracy and lower amounts of data that need to be transferred.

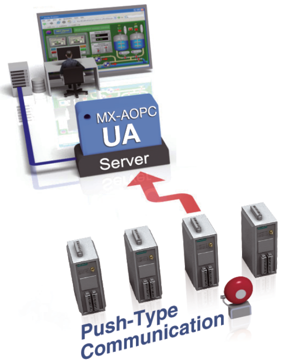

Specifications

Input/Output Interface

Digital Input Channels	ioLogik E1210 Series: 16 ioLogik E1212/E1213 Series: 8 ioLogik E1214 Series: 6 ioLogik E1242 Series: 4
Digital Output Channels	ioLogik E1211 Series: 16 ioLogik E1213 Series: 4
Configurable DIO Channels (by jumper)	ioLogik E1212 Series: 8 ioLogik E1213/E1242 Series: 4
Relay Channels	ioLogik E1214 Series: 6
Analog Input Channels	ioLogik E1240 Series: 8 ioLogik E1242 Series: 4
Analog Output Channels	ioLogik E1241 Series: 4
RTD Channels	ioLogik E1260 Series: 6

Thermocouple Channels	ioLogik E1262 Series: 8
Isolation	3k VDC or 2k Vrms
Buttons	Reset button

Digital Inputs

Connector	Screw-fastened Euroblock terminal
Sensor Type	Dry contact Wet contact (NPN or PNP)
I/O Mode	DI or event counter
Dry Contact	On: short to GND Off: open
Wet Contact (DI to COM)	On: 10 to 30 VDC Off: 0 to 3 VDC
Counter Frequency	250 Hz
Digital Filtering Time Interval	Software configurable
Points per COM	ioLogik E1210/E1212 Series: 8 channels ioLogik E1213 Series: 12 channels ioLogik E1214 Series: 6 channels ioLogik E1242 Series: 4 channels

Digital Outputs

Connector	Screw-fastened Euroblock terminal
I/O Type	ioLogik E1211/E1212/E1242 Series: Sink ioLogik E1213 Series: Source
I/O Mode	DO or pulse output
Current Rating	ioLogik E1211/E1212/E1242 Series: 200 mA per channel ioLogik E1213 Series: 500 mA per channel
Pulse Output Frequency	500 Hz (max.)
Over-Current Protection	ioLogik E1211/E1212/E1242 Series: 2.6 A per channel @ 25°C ioLogik E1213 Series: 1.5 A per channel @ 25°C
Over-Temperature Shutdown	175°C (typical), 150°C (min.)
Over-Voltage Protection	35 VDC

Relays

Connector	Screw-fastened Euroblock terminal
Type	Form A (N.O.) power relay
I/O Mode	Relay or pulse output
Pulse Output Frequency	0.3 Hz at rated load (max.)
Contact Current Rating	Resistive load: 5 A @ 30 VDC, 250 VAC, 110 VAC
Contact Resistance	100 milli-ohms (max.)
Mechanical Endurance	5,000,000 operations
Electrical Endurance	100,000 operations @ 5 A resistive load

Breakdown Voltage	500 VAC
Initial Insulation Resistance	1,000 mega-ohms (min.) @ 500 VDC
Note	Ambient humidity must be non-condensing and remain between 5 and 95%. The relays may malfunction when operating in high condensation environments below 0°C.

Analog Inputs

Connector	Screw-fastened Euroblock terminal
I/O Mode	Voltage/Current
I/O Type	Differential
Resolution	16 bits
Input Range	0 to 10 VDC 0 to 20 mA 4 to 20 mA 4 to 20 mA (with burn-out detection)
Accuracy	ioLogik E1240/E1242: ±0.1% FSR @ 25°C ±0.3% FSR @ -10 to 60°C ioLogik E1240-T/E1242-T: ±0.1% FSR @ 25°C ±0.3% FSR @ -10 to 60°C ±0.5% FSR @ -40 to 75°C
Sampling Rate	ioLogik E1240: 12 samples/sec per module (shared between up to 8 channels)[2] ioLogik E1242: 12 samples/sec per module (shared between up to 4 channels)[2]
Built-in Resistor for Current Input	120 ohms
Input Impedance	10 mega-ohms (min.)

Analog Outputs

Connector	Screw-fastened Euroblock terminal
I/O Mode	Voltage/Current
Output Range	0 to 10 VDC 0 to 20 mA 4 to 20 mA
Resolution	12-bit
Accuracy	ioLogik E1241: ±0.1% FSR @ 25°C ±0.3% FSR @ -10 to 60°C ioLogik E1241-T: ±0.1% FSR @ 25°C ±0.3% FSR @ -40 to 75°C
Load (Current Mode)	Internal power: 400 ohms (max.) 24 V external power: 1000 ohms (max.)
Voltage Output Short-Circuit Protection	10 mA

RTDs

Connector	Screw-fastened Euroblock terminal
Sensor Type	PT1000 (-200 to 350°C)

---

[2] If N channels are enabled, the sampling rate for each enabled channel = 12/N samples/sec.

	PT50, PT100, PT200, PT500 (-200 to 850°C)
Resistance Type	310, 620, 1250, and 2200 ohms
Input Connection	2- or 3-wire
Sampling Rate	ioLogik E1260: 12 samples/sec per module (shared between up to 6 channels)[3]
Resolution	0.1°C or 0.1 ohms
Accuracy	ioLogik E1260: ±0.1% FSR @ 25°C ±0.3% FSR @ -10 to 60°C ioLogik E1260-T: ±0.1% FSR @ 25°C ±0.3% FSR @ -40 to 75°C
Input Impedance	625 kilo-ohms (min.)

Thermocouples

Connector	Screw-fastened Euroblock terminal
Sensor Type	J, K, T, E, R, S, B, N
Millivolt Type	±19.532 mV ±39.062 mV ±78.126 mV Fault and over-voltage protection: -35 to +35 VDC (power off); -25 to +30 VDC (power on)
Resolution	16 bits
Millivolt Accuracy	ioLogik E1262: ±0.1% FSR @ 25°C ±0.3% FSR @ -10 to 60°C ioLogik E1262-T: ±0.1% FSR @ 25°C ±0.3% FSR @ -40 to 75°C
TC Accuracy	Types J, T, E, S, B: ±5°C Types K, R, N: ±8°C
CJC Accuracy	±0.5°C @ 25°C ±1.5°C @ -40 to 75°C
Sampling Rate	ioLogik E1262: 12 samples/sec per module (shared between up to 8 channels)[3]
Input Impedance	10 mega-ohms (min.)

Ethernet Interface

10/100BaseT(X) Ports (RJ45 connector)	2, 1 MAC address (Ethernet bypass)
Magnetic Isolation Protection	1.5 kV (built-in)

Ethernet Software Features

Configuration Options	Web Console (HTTP), Windows Utility (ioSearch), MCC Tool
Industrial Protocols	Modbus TCP Server (Slave), Moxa AOPC (Active Tag), MXIO Library, EtherNet/IP Adapter
Management	RESTful API, SNMPv1/v2c, SNMPv1 Trap, HTTP, DHCP Client, BOOTP, IPv4, TCP/IP, UDP

---

[3] If N channels are enabled, the sampling rate for each enabled channel = 12/N samples/sec.

MIB	Device Settings MIB
Security	Access control list

Security Functions

Authentication	Local database

LED Interface

LED Indicators	Power, Ready, Port 1, Port 2

Modbus TCP

Functions Supported	1, 2, 3, 4, 5, 6, 15, 16, 23
Mode	Server (Slave)
Max. No. of Client Connections	10

EtherNet/IP

Mode	Adapter
Max. No. of Scanner Connections	9 (for read-only), 1 (for read/write)

Power Parameters

Power Connector	Screw-fastened Euroblock terminal
No. of Power Inputs	1
Input Voltage	12 to 36 VDC
Power Consumption	ioLogik E1210 Series: 110 mA @ 24 VDC ioLogik E1211 Series: 200 mA @ 24 VDC ioLogik E1212 Series: 155 mA @ 24 VDC ioLogik E1213 Series: 130 mA @ 24 VDC ioLogik E1214 Series: 188 mA @ 24 VDC ioLogik E1240 Series: 121 mA @ 24 VDC ioLogik E1241 Series: 194 mA @ 24 VDC ioLogik E1242 Series: 139 mA @ 24 VDC ioLogik E1260 Series: 110 mA @ 24 VDC ioLogik E1262 Series: 118 mA @ 24 VDC

Physical Characteristics

Housing	Plastic
Dimensions	27.8 x 124 x 84 mm (1.09 x 4.88 x 3.31 in)
Weight	200 g (0.44 lb)
Installation	DIN-rail mounting, Wall mounting
Wiring	I/O cable, 16 to 26 AWG Power cable, 12 to 24 AWG

Environmental Limits

Operating Temperature	Standard Models: -10 to 60°C (14 to 140°F) Wide Temp. Models: -40 to 75°C (-40 to 167°F)
Storage Temperature (package included)	-40 to 85°C (-40 to 185°F)
Ambient Relative Humidity	5 to 95% (non-condensing)
Altitude	4000 m[4]

---

[4] Please contact Moxa if you require products guaranteed to function properly at higher altitudes.

Standards and Certifications

EMC	EN 55032/24, EN 61000-6-2/-6-4
EMI	CISPR 32, FCC Part 15B Class A
EMS	IEC 61000-4-2 ESD: Contact: 4 kV; Air: 8 kV IEC 61000-4-3 RS: 80 MHz to 1 GHz: 10 V/m IEC 61000-4-4 EFT: Power: 2 kV; Signal: 1 kV IEC 61000-4-5 Surge: Power: 2 kV; Signal: 1 kV IEC 61000-4-6 CS: 10 V IEC 61000-4-8 PFMF
Hazardous Locations	ATEX, Class I Division 2[5]
Safety	UL 508
Shock	IEC 60068-2-27
Freefall	IEC 60068-2-32
Vibration	IEC 60068-2-6

Declaration

Green Product	RoHS, CRoHS, WEEE

MTBF

Time	ioLogik E1210 Series: 671,345 hrs ioLogik E1211 Series: 923,027 hrs ioLogik E1212 Series: 561,930 hrs ioLogik E1213 Series: 715,256 hrs ioLogik E1214 Series: 808,744 hrs ioLogik E1240 Series: 474,053 hrs ioLogik E1241 Series: 888,656 hrs ioLogik E1242 Series: 502,210 hrs ioLogik E1260 Series: 660,260 hrs ioLogik E1262 Series: 631,418 hrs
Standards	Telcordia SR332

Warranty

Warranty Period	ioLogik E1214: 2 years[6] ioLogik E1210/E1211/E1212/E1213/E1240/E1241/E1242/E1260/E1262: 5 years
Details	See www.moxa.com/warranty

Package Contents

Device	1 x ioLogik E1200 Series remote I/O
Installation Kit	1 x terminal block, 8-pin, 3.81 mm 1 x terminal block, 12-pin, 3.81 mm 1 x terminal block, 3-pin, 5.00 mm
Documentation	1 x quick installation guide 1 x warranty card

---

[5] ATEX and Class I Division 2 currently do not apply to the ioLogik E1213/E1213-T models.

[6] Because of the limited lifetime of power relays, products that use this component are covered by a 2-year warranty.

Dimensions

Unit: mm (inch)

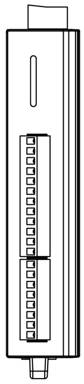

Front View

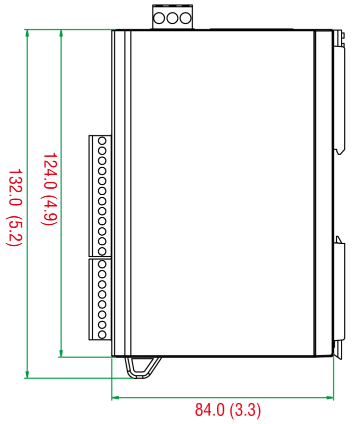

Side View

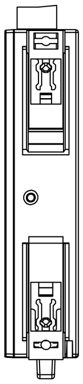

Rear View

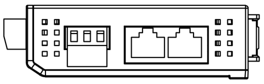

Top View

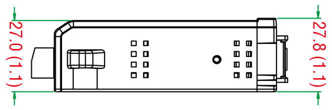

Bottom View

Ordering Information

Model Name	Input/Output Interface	Digital Output Type	Operating Temp.
ioLogik E1210	16 x DI	–	-10 to 60°C
ioLogik E1210-T	16 x DI	–	-40 to 75°C
ioLogik E1211	16 x DO	Sink	-10 to 60°C
ioLogik E1211-T	16 x DO	Sink	-40 to 75°C
ioLogik E1212	8 x DI, 8 x DIO	Sink	-10 to 60°C
ioLogik E1212-T	8 x DI, 8 x DIO	Sink	-40 to 75°C
ioLogik E1213	8 x DI, 4 x DO, 4 x DIO	Source	-10 to 60°C
ioLogik E1213-T	8 x DI, 4 x DO, 4 x DIO	Source	-40 to 75°C
ioLogik E1214	6 x DI, 6 x Relay	–	-10 to 60°C
ioLogik E1214-T	6 x DI, 6 x Relay	–	-40 to 75°C
ioLogik E1240	8 x AI	–	-10 to 60°C
ioLogik E1240-T	8 x AI	–	-40 to 75°C
ioLogik E1241	4 x AO	–	-10 to 60°C
ioLogik E1241-T	4 x AO	–	-40 to 75°C
ioLogik E1242	4 DI, 4 x DIO, 4 x AI	Sink	-10 to 60°C
ioLogik E1242-T	4 DI, 4 x DIO, 4 x AI	Sink	-40 to 75°C
ioLogik E1260	6 x RTD	–	-10 to 60°C
ioLogik E1260-T	6 x RTD	–	-40 to 75°C
ioLogik E1262	8 x TC	–	-10 to 60°C
ioLogik E1262-T	8 x TC	–	-40 to 75°C

Accessories (sold separately)

Software

MX-AOPC UA Server	OPC UA Server software for converting fieldbus to the OPC UA standard

Data sheet

VG M12-K67

Weidmüller Interfaces GmbH & Co. KG

Postfach 3030

32760 Detmold

Tel. +49 5231 14-0

Fax. +49 5231 14-2083

info@weidmueller.com

www.weidmueller.com

Similar to illustration

In addition to the extensive range of enclosures, Weidmüller offers a variety of cable glands for a wide range of applications.
The cable glands made of brass, plastic and stainless steel meet the most various IP protection classes to suit any industrial enclosure.
Depending on the series of cable glands and the application, the cable glands are approved and tested according to VDE, UL, UR, cULus, DNV GL or EN 45545.

General ordering data

Version	VG K (standard plastic cable gland), Cable glands, straight, M 12, 8 mm, OD min. 3 - OD max. 6.5 mm, Polyamide 6
Order No.	1909660000
Type	VG M12-K67
GTIN (EAN)	4032248536580
Qty.	100 pc(s).

VG M12-K67

Technical data

Dimensions and weights

Length	30.5 mm	Length (inches)	1.201 inch
Net weight	3.66 g		

Temperatures

Operating temperature	-20 °C...80 °C	Operating temperature, min.	-20 °C
Operating temperature, max.	80 °C		

General information

AF size 1	15 mm	Cable glands	metric
External thread	M 12	Halogen	No, Yes
Length of thread	8 mm	Material	Polyamide 6
Operating temperature range, max.	100 °C	Operating temperature range, min.	-20 °C
Outer cable diameter, max.	6.5 mm	Outer cable diameter, min.	3 mm
Pitch of thread	1.5 mm	Protection degree	IP67
Seal insert	NBR	Silicone	No
Standards	EN/IEC 62444	Tightening torque	2 Nm
Torque for cap nut, max.	2.5 Nm	Torque for cap nut, min.	1.5 Nm
Torque for connecting adapter, max.	3.5 Nm	Torque for connecting adapter, min.	2.5 Nm
Torque for lock nut, max.	3.5 N/m	Torque for lock nut, min.	2.5 N/m
UL 94 flammability rating	V-2		

Classifications

ETIM 6.0	EC000441	ETIM 7.0	EC000441
ETIM 8.0	EC000441	ECLASS 9.0	27-14-44-32
ECLASS 9.1	27-14-44-32	ECLASS 10.0	27-14-44-32
ECLASS 11.0	27-14-44-32	ECLASS 12.0	27-14-08-01

Approvals

Approvals	CE
ROHS	Conform

Downloads

Engineering Data	CAD data – STEP
Engineering Data	WSCAD
Catalogues	Catalogues in PDF-format
Brochures	

Accessories

Polyethylene flat gasket - GWDR PO

In addition to cable glands for a wide range of applications, the product portfolio is rounded off by plugs, pressure compensation elements, adaptors and the corresponding accessories such as locknuts, sealing rings, flat washers and earthing rings.

General ordering data

Type	GWDR M12-PO	Version
Order No.	1777920000	GWDR PO (flat gasket - polyethylene), Sealing ring, M 12, Polyethylene
GTIN (EAN)	4032248158188	
Qty.	50 pc(s).	

Plastic lock nuts, grey

In addition to cable glands for a wide range of applications, the product portfolio is rounded off by plugs, pressure compensation elements, adaptors and the corresponding accessories such as locknuts, sealing rings, flat washers and earthing rings.

General ordering data

Type	SKMU M12 - K GR	Version
Order No.	1772440000	SKMU PA (plastic locknut), Locknut, M 12, 5 mm, Polyamid 6 (PA6 - GF30)
GTIN (EAN)	4032248130184	
Qty.	100 pc(s).	

Data sheet

VG M12-K67

Accessories

Neoprene flat gasket - GWDR NP

In addition to cable glands for a wide range of applications, the product portfolio is rounded off by plugs, pressure compensation elements, adaptors and the corresponding accessories such as locknuts, sealing rings, flat washers and earthing rings.

General ordering data

Type	GWDR M12-NP	Version
Order No.	1913320000	GWDR NP (flat gasket - neoprene), Sealing ring, M 12, Neoprene
GTIN (EAN)	4032248543663	
Qty.	50 pc(s).	

Bibliography

Protocol, K. (1997). United nations framework convention on climate change. *Kyoto Protocol, Kyoto*, *19*(8), 1–21.

Schleussner, C.-F., Rogelj, J., Schaeffer, M., Lissner, T., Licker, R., Fischer, E. M., Knutti, R., Levermann, A., Frieler, K., & Hare, W. (2016). Science and policy characteristics of the paris agreement temperature goal. *Nature Climate Change*, *6*(9), 827–835. https://doi.org/10.1038/nclimate3096

Agreement, P. Paris agreement. In: In *Report of the conference of the parties to the united nations framework convention on climate change (21st session, 2015: Paris). retrived december*. *4*. HeinOnline. 2015, 2017.

de Graaf, T. V., & Lesage, D. (2009). The international energy agency after 35 years: Reform needs and institutional adaptability. *The Review of International Organizations*, *4*(3), 293–317. https://doi.org/10.1007/s11558-009-9063-8

IEA. (2022). World energy outlook 2022. *IEA*. https://www.iea.org/reports/world-energy-outlook-2022

IEA. (2021a). Net zero by 2050. *IEA*. https://www.iea.org/reports/net-zero-by-2050

IEA. (2021b). Net zero by 2050 data explorer. https://www.iea.org/data-and-statistics/data-tools/net-zero-by-2050-data-explorer

Gorjian, S., Sharon, H., Ebadi, H., Kant, K., Scavo, F. B., & Tina, G. M. (2021). Recent technical advancements, economics and environmental impacts of floating photovoltaic solar energy conversion systems. *Journal of Cleaner Production*, *278*, 124285. https://doi.org/10.1016/j.jclepro.2020.124285

Rosa-Clot, M., & Tina, G. M. Current status of FPV and trends. In: In *Floating PV plants*. Elsevier, 2020, pp. 9–18. https://doi.org/10.1016/b978-0-12-817061-8.00002-6.

Sahu, A., Yadav, N., & Sudhakar, K. (2016). Floating photovoltaic power plant: A review. *Renewable and Sustainable Energy Reviews*, *66*, 815–824. https://doi.org/10.1016/j.rser.2016.08.051

Ranjbaran, P., Yousefi, H., Gharehpetian, G., & Astaraei, F. R. (2019). A review on floating photovoltaic (FPV) power generation units. *Renewable and Sustainable Energy Reviews*, *110*, 332–347. https://doi.org/10.1016/j.rser.2019.05.015

Farfan, J., & Breyer, C. (2018). Combining floating solar photovoltaic power plants and hydropower reservoirs: A virtual battery of great global potential. *Energy Procedia*, *155*, 403–411. https://doi.org/10.1016/j.egypro.2018.11.038

Vo, T. T. E., Ko, H., Huh, J., & Park, N. (2021). Overview of possibilities of solar floating photovoltaic systems in the OffShore industry. *Energies*, *14*(21), 6988. https://doi.org/10.3390/en14216988

Claus, R., & López, M. (2022). Key issues in the design of floating photovoltaic structures for the marine environment. *Renewable and Sustainable Energy Reviews*, *164*, 112502. https://doi.org/10.1016/j.rser.2022.112502

Ziar, H. (2021). Floating solar stations. *10 breakthrough ideas in energy for the next 10 years*, (2), 30–43.

Kakoulaki, G., Sanchez, R. G., Amillo, A. G., Szabo, S., Felice, M. D., Farinosi, F., Felice, L. D., Bisselink, B., Seliger, R., Kougias, I., & Jaeger-Waldau, A. (2023). Benefits of pairing floating solar photovoltaics with hydropower reservoirs in europe. *Renewable and Sustainable Energy Reviews*, *171*, 112989. https://doi.org/10.1016/j.rser.2022.112989

WorldBankGroup. (2019b). *Where sun meets water: Floating solar market report* (W. B. Group, Ed.). World Bank. https://openknowledge.worldbank.org/handle/10986/31880

Liu, H., Krishna, V., Leung, J. L., Reindl, T., & Zhao, L. (2018). Field experience and performance analysis of floating PV technologies in the tropics. *Progress in Photovoltaics: Research and Applications*, *26*(12), 957–967. https://doi.org/10.1002/pip.3039

OOE. (2023a). A world's first: Offshore floating solar farm installed at the dutch north sea. *Oceans of Energy*. https://oceansofenergy.blue/a-worlds-first-offshore-floating-solar-farm-installed-at-the-dutch-north-sea/

Cazzaniga, R., & Rosa-Clot, M. (2021). The booming of floating PV. *Solar Energy*, *219*, 3–10. https://doi.org/10.1016/j.solener.2020.09.057

DNV. (2021). Dnv-rp-0584 design, development and operation of floating solar photovoltaic systems - recommended practice. *DNV*. https://www.dnv.com/energy/standards-guidelines/dnv-rp-0584-design-development-and-operation-of-floating-solar-photovoltaic-systems.html

Lee, N. (2020). Hybrid floating solar photovoltaics-hydropower systems: Benefits and global assessment of technical potential. *Renewable Energy*, *162*(6), 1415–1427. https://doi.org/10.1016/j.renene.2020.08.080

Lund, P. D., Lindgren, J., Mikkola, J., & Salpakari, J. (2015). Review of energy system flexibility measures to enable high levels of variable renewable electricity. *Renewable and Sustainable Energy Reviews*, *45*, 785–807. https://doi.org/10.1016/j.rser.2015.01.057

U.S.EnergyDepartment. (2023). Pumped storage hydropower. *Office of energy efficiency and renewable energy*. Website article retrieved on 23/02/2023. https://www.energy.gov/eere/water/pumped-storage-hydropower

Rehman, S., Al-Hadhrami, L. M., & Alam, M. M. (2015). Pumped hydro energy storage system: A technological review. *Renewable and Sustainable Energy Reviews*, *44*, 586–598. https://doi.org/10.1016/j.rser.2014.12.040

Garanovic, A. (2021a). Albania's first floating solar plant starts commercial operations (video). *Offshore Energy*. https://www.offshore-energy.biz/albanias-first-floating-solar-plant-starts-commercial-operations-video/

Petrushevska, D. (2022). Statkraft resumes operations at floating solar park in albania. *Renewables Now*. https://renewablesnow.com/news/statkraft-resumes-operations-at-floating-solar-park-in-albania-780250/

Santos, B. (2022). Spic, ocean sun switch on offshore floating solar-wind pilot. *PV Magazine*. https://www.pv-magazine.com/2022/11/02/spic-ocean-sun-build-worlds-first-offshore-floating-solar-wind-park/

López, M., Rodríguez, N., & Iglesias, G. (2020). Combined floating offshore wind and solar PV. *Journal of Marine Science and Engineering*, *8*(8), 576. https://doi.org/10.3390/jmse8080576

Golroodbari, S., Vaartjes, D., Meit, J., van Hoeken, A., Eberveld, M., Jonker, H., & van Sark, W. (2021). Pooling the cable: A techno-economic feasibility study of integrating offshore floating photovoltaic solar technology within an offshore wind park. *Solar Energy*, *219*, 65–74. https://doi.org/10.1016/j.solener.2020.12.062

Isigenere. (2021). Isifloating floating solar system. https://www.isifloating.com/en/isifloating-english/

SolarisFloat. (2018). Solarisfloat protevs video. https://www.youtube.com/watch?v=7Yk2wMKdpk0

TNO. (2021). Launch of study on new flexible solar energy systems for offshore application. *TNO Newsroom*. https://www.tno.nl/en/newsroom/2021/11/launch-study-new-flexible-solar-energy/

SolarDuck. (2023). Artifuculated floating structure. https://solarduck.tech/patents/

OceanSun. (2023). Ocean sun - our products. https://oceansun.no/our-products/

OOE. (2023b). Technology - unique technology floating solar farm system. *Oceans of Energy*. https://oceansofenergy.blue/technology/

Garanovic, A. (2022a). China commissions first offshore floating solar plant integrated with wind turbine. *Offshore Energy*. News article retrieved on 17-02-2023. https://www.offshore-energy.biz/china-commissions-first-offshore-floating-solar-plant-integrated-with-wind-turbine/

Garanovic, A. (2023). Oceans of energy gets bureau veritas' nod of approval for offshore floating solar system. *Offshore Energy*. News article retrieved on 17/02/2023. https://www.offshore-energy.biz/oceans-of-energy-gets-bureau-veritas-nod-of-approval-for-offshore-floating-solar-system/

Swimsol. (2022). 456,25 kwp bawah reserve project, indonesia. *Swimsol*. Retrieved from website on 17-02-2023. https://swimsol.com/solar-projects/bawah-reserve-indonesia-solarsea-swimsol/

SolarDuck. (2021). Solar duck unveils design of its offshore floating solar technology. *Solar Duck*. Retrieved from website on 17-02-2023. https://solarduck.tech/solarduck-unveils-design-of-its-offshore-floating-solar-technology/

TNO. (2022). Sustainable solar on land and water - floating solar panels. *TNO*. Website article retrieved on 18/02/2023. https://www.tno.nl/en/sustainable/renewable-electricity/sustainable-solar-land-water/floating-solar-panels/

Isifloating. (2020). Netherlands challenging location – research and development project - oostvoornse lake. *Isifloating by Isigenere*. Website article retrieved on 18/02/2023. https://www.isifloating.com/en/project/challenging-location-rd-project-oostvoornse-lake-netherlands/

Garanovic, A. (2021b). Dutch look into flexible floating solar systems for offshore application. *Offshore energy*. News article retrieved on 17/02/2023. https://www.offshore-energy.biz/dutch-look-into-flexible-floating-solar-systems-for-offshore-application/

Garanovic, A. (2022b). Floating solar start-up goes after seed money. *Offshore Energy*. News article retrieved on 18/02/2023. https://www.offshore-energy.biz/floating-solar-start-up-goes-after-seed-money/

SunlitSea. (2022). Tofte pilot - 4 solar panels with a total of 357 wp per unit. Website article retrieved on 18/02/2023. https://sunlitsea.no/news

MossMaritime. (2022). Clean energy solutions. *Moss Maritime*. Website article retrieved on 18/02/2023. https://www.mossww.com/clean-energy-solutions/

Garanovic, A. (2021c). Industry majors streamlining offshore floating solar system for belgian north sea. *Offshore Energy*. News article retrieved on 17/02/2022. https://www.offshore-energy.biz/industry-majors-streamlining-offshore-floating-solar-system-for-belgian-north-sea/

Smets, A. H., Isabella, O., Swaaij, R. V., & Zeman, M. (2016). *Solar energy, the physics and engineering of photovoltaic conversion, technologies and systems*. UIT Cambridge.

IEC. (2023b). Ip ratings. *International Electrotechnical Commission*. Website article retrieved on 20/02/2023. https://www.iec.ch/ip-ratings

Khalid, A. M., Mitra, I., Warmuth, W., & Schacht, V. (2016). Performance ratio – crucial parameter for grid connected PV plants. *Renewable and Sustainable Energy Reviews*, *65*, 1139–1158. https://doi.org/10.1016/j.rser.2016.07.066

Reich, N. H., Mueller, B., Armbruster, A., van Sark, W. G. J. H. M., Kiefer, K., & Reise, C. (2012). Performance ratio revisited: Is PR > 90% realistic? *Progress in Photovoltaics: Research and Applications*, *20*(6), 717–726. https://doi.org/10.1002/pip.1219

Kaspar, F., Borsche, M., Pfeifroth, U., Trentmann, J., Drücke, J., & Becker, P. (2019). A climatological assessment of balancing effects and shortfall risks of photovoltaics and wind energy in germany and europe. *Advances in Science and Research*, *16*, 119–128. https://doi.org/10.5194/asr-16-119-2019

Kamuyu, W. C. L., Lim, J., Won, C., & Ahn, H. (2018). Prediction model of photovoltaic module temperature for power performance of floating PVs. *Energies*, *11*(2), 447. https://doi.org/10.3390/en11020447

Micheli, L. (2022). The temperature of floating photovoltaics: Case studies, models and recent findings. *Solar Energy*, *242*, 234–245. https://doi.org/10.1016/j.solener.2022.06.039

Hayibo, K. S. (2021). *Quantifying the value of foam-based flexible floating solar photovoltaic systems* (Doctoral dissertation). Michigan Technological University.

Ziar, H., Prudon, B., Lin, F.-Y. V., Roeffen, B., Heijkoop, D., Stark, T., Teurlincx, S., Domis, L. S., Goma, E. G., Extebarria, J. G., Alavez, I. N., Tilborg, D., Laar, H., Santbergen, R., & Isabella, O. (2020). Innovative floating bifacial photovoltaic solutions for inland water areas. *Progress in Photovoltaics: Research and Applications*. https://doi.org/10.1002/pip.3367

ESS. (2021). Pyranometer specifications explained. *ESS Earth Sciences*. Website article retrieved on 18/02/2023. https://www.essearth.com/understand-pyranometer-specifications/

Meydbray, J., Emery, K., & Kurtz, S. (2012). Pyranometers and reference cells, what's the difference? *PV Magazine*. https://www.researchgate.net/publication/254994979_Pyranometers_and_Reference_Cells_What's_the_Difference

DustIQ. (2022). Dustiq soiling monitoring system. https://www.kippzonen.com/Product/419/DustIQ-Soiling-Monitoring-System#.Y8wmtXbMKUk

Atonometrics. (2022). Mars optical soiling sensor – revolutionary new product. https://www.atonometrics.com/mars-optical-soiling-sensor-revolutionary-new-product/

KNMI. (2022). Water management centrum nederland. *KNMI*. https://waterberichtgeving.rws.nl/water-en-weer/metingen

PVSyst. (2023). Array ohmic wiring loss. https://www.pvsyst.com/help/ohmic_loss.htm#:~:text=Theohmicresistanceofthe,terminalsofthesub-array.

Victron. (2023). Victron energy - smartsolar mppt rs450-100-tr and 450-200-tr manuals. https://www.victronenergy.com/solar-charge-controllers/smartsolar-mppt-rs-450-tr#manuals

Mohanty, P., Muneer, T., & Kolhe, M. (Eds.). (2016). *Solar photovoltaic system applications*. Springer International Publishing. https://doi.org/10.1007/978-3-319-14663-8

IEC. (n.d.). *Iec 60529 ed. 2.2 b : 2013, second edition : Degrees of protection provided by enclosures ip code: Degrees of protection provided by enclosures ip code*. Commission, International Electrotechnical. Multiple. Distributed through American National Standards Institute (ANSI).

WorldBankGroup. (2019a). *Where sun meets water: Floating solar handbook for practitioners.* ESMAP; SERIS.

Aghaei, M., Fairbrother, A., Gok, A., Ahmad, S., Kazim, S., Lobato, K., Oreski, G., Reinders, A., Schmitz, J., Theelen, M., Yilmaz, P., & Kettle, J. (2022). Review of degradation and failure phenomena in photovoltaic modules. *Renewable and Sustainable Energy Reviews*, *159*, 112160. https://doi.org/10.1016/j.rser.2022.112160

Mannino, G., Tina, G. M., Cacciato, M., Merlo, L., Cucuzza, A. V., Bizzarri, F., & Canino, A. (2023). Photovoltaic module degradation forecast models for onshore and offshore floating systems. *Energies*, *16*(5), 2117. https://doi.org/10.3390/en16052117

Zahedi, R., Ranjbaran, P., Gharehpetian, G. B., Mohammadi, F., & Ahmadiahangar, R. (2021). Cleaning of floating photovoltaic systems: A critical review on approaches from technical and economic perspectives. *Energies*, *14*(7), 2018. https://doi.org/10.3390/en14072018

Hooper, T., Armstrong, A., & Vlaswinkel, B. (2021). Environmental impacts and benefits of marine floating solar. *Solar Energy*, *219*, 11–14. https://doi.org/10.1016/j.solener.2020.10.010

Harris, L., Tozzi, S., Wiley, P., Young, C., Richardson, T.-M. J., Clark, K., & Trent, J. D. (2013). Potential impact of biofouling on the photobioreactors of the offshore membrane enclosures for growing algae (OMEGA) system. *Bioresource Technology*, *144*, 420–428. https://doi.org/10.1016/j.biortech.2013.06.125

IEC. (2023a). Iec 61701:2020 photovoltaic (pv) modules - salt mist corrosion testing. *International Electrotechnical Commission*. Website article retrieved on 23/02/2023. https://webstore.iec.ch/publication/59588

Cazzaniga, R., Cicu, M., Rosa-Clot, M., Rosa-Clot, P., Tina, G., & Ventura, C. (2018). Floating photovoltaic plants: Performance analysis and design solutions. *Renewable and Sustainable Energy Reviews*, *81*, 1730–1741. https://doi.org/10.1016/j.rser.2017.05.269

Golroodbari, S. Z., & Sark, W. (2020). Simulation of performance differences between offshore and land-based photovoltaic systems. *Progress in Photovoltaics: Research and Applications*, *28*(9), 873–886. https://doi.org/10.1002/pip.3276

Soppe, W., Kingma, A., Hoogeland, M., vd Brink, R., JanKroon, & Folkerts, W. (2022). Challenges and potential for offshore solar. *TKI wind op zee, Topsector Energie, TNO*. Website article retrieved on 23/02/2023. https://topsectorenergie.nl/sites/default/files/uploads/20220331_RAP_Challengesandpotentialforoffshoresolar_Final.pdf

Bugeja, R., Stagno, L. M., & Branche, N. (2021). The effect of wave response motion on the insolation on offshore photovoltaic installations. *Solar Energy Advances*, *1*, 100008. https://doi.org/10.1016/j.seja.2021.100008

Bi, C., & Law, A. W.-K. (2023). Co-locating offshore wind and floating solar farms – effect of high wind and wave conditions on solar power performance. *Energy*, *266*, 126437. https://doi.org/10.1016/j.energy.2022.126437

Ravichandran, N., Ravichandran, N., & Panneerselvam, B. (2022). Comparative assessment of offshore floating photovoltaic systems using thin film modules for maldives islands. *Sustainable Energy Technologies and Assessments*, *53*, 102490. https://doi.org/10.1016/j.seta.2022.102490

Sobolewski, P. K., & Sobieska, M. E. Analysis of lightning protection of floating photovoltaic power plant. In: In *2022 36th international conference on lightning protection (ICLP)*. IEEE, 2022. https://doi.org/10.1109/iclp56858.2022.9942655.

DEHN. (2014, December). *Dehn and sohne lightning protection guide* (3rd ed.). DEHN. https://www.dehn-international.com/sites/default/files/media/files/lpg-2015-e-complete.pdf

Whittaker, T., Folley, M., & Hancock, J. Environmental loads, motions, and mooring systems. In: In *Floating PV plants*. Elsevier, 2020, pp. 47–66. https://doi.org/10.1016/b978-0-12-817061-8.00005-1.

Oliveira-Pinto, S., & Stokkermans, J. (2020). Assessment of the potential of different floating solar technologies – overview and analysis of different case studies. *Energy Conversion and Management*, *211*, 112747. https://doi.org/10.1016/j.enconman.2020.112747

Turner, R. (2000). Offshore mariculture: Mooring system design. *Basurco B.(ed.) Mediterranean offshore mariculture. Zaragoza: CIHEAM-IAMZ*, 159–172.

Hlal, M. I., Ramachandaramurthy, V. K., Sarhan, A., Pouryekta, A., & Subramaniam, U. (2019). Optimum battery depth of discharge for off-grid solar PV/battery system. *Journal of Energy Storage*, *26*, 100999. https://doi.org/10.1016/j.est.2019.100999

SMA. (n.d.). Performance ratio, quality factor for the pv plan. *SMA*. https://files.sma.de/downloads/Perfratio-TI-en-11.pdf

Kawai, S., Tanahashi, T., Fukumoto, Y., Tamai, F., Masuda, A., & Kondo, M. (2017). Causes of degradation identified by the extended thermal cycling test on commercially available crystalline silicon photovoltaic modules. *IEEE Journal of Photovoltaics*, *7*(6), 1511–1518. https://doi.org/10.1109/jphotov.2017.2741102

Lindholm, D., Kjeldstad, T., Selj, J., Marstein, E. S., & Fjær, H. G. (2021). Heat loss coefficients computed for floating PV modules. *Progress in Photovoltaics: Research and Applications*, *29*(12), 1262–1273. https://doi.org/10.1002/pip.3451

Ross Jr, R. Interface design considerations for terrestrial solar cell modules. In: In *12th photovoltaic specialists conference*. 1976, 801–806.

Rauschenbach, H. (1980). Solar cell array design handbook-the principles and technology of photovoltaic energy conversion. *NASA STI/Recon Technical Report A*, *80*, 34847.

Risser, V. V., & Eventes, M. K. Linear regression analysis of flat-plate photovoltaic system performance data. In: 1984.

Schott, T. Operation temperatures of pv modules: A theoretical and experimental approach. In: In *Ec photovoltaic solar energy conference. 6*. 1985, 392–396.

Ross Jr, R., & Smokler, M. (1986). Electricity from photovoltaic solar cells: Flat-plate solar array project final report. volume vi: Engineering sciences and reliability.

Lasnier, F., & Ang, T. G. (2017). *Photovoltaic engineering handbook*. Routledge. https://doi.org/10.1201/9780203743393

Duffie, J. A., & Beckman, W. A. (2013). *Solar engineering of thermal processes*. John Wiley & Sons, Inc. https://doi.org/10.1002/9781118671603

Koehl, M., Heck, M., Wiesmeier, S., & Wirth, J. (2011). Modeling of the nominal operating cell temperature based on outdoor weathering. *Solar Energy Materials and Solar Cells*, *95*(7), 1638–1646.

Kurtz, S., Whitfield, K., Miller, D., Joyce, J., Wohlgemuth, J., Kempe, M., Dhere, N., Bosco, N., & Zgonena, T. Evaluation of high-temperature exposure of rack-mounted photovoltaic modules. In: In *2009 34th ieee photovoltaic specialists conference (pvsc)*. IEEE. 2009, 002399–002404.

Skoplaki, E., & Palyvos, J. (2009). On the temperature dependence of photovoltaic module electrical performance: A review of efficiency/power correlations. *Solar Energy*, *83*(5), 614–624. https://doi.org/10.1016/j.solener.2008.10.008

Faiman, D. (2008). Assessing the outdoor operating temperature of photovoltaic modules. *Progress in Photovoltaics: Research and Applications*, *16*(4), 307–315. https://doi.org/10.1002/pip.813

King, D. L., Kratochvil, J. A., & Boyson, W. E. (2004). *Photovoltaic array performance model* (Vol. 8). Citeseer.

Veldhuis, A. J., Nobre, A. M., Peters, I. M., Reindl, T., Rüther, R., & Reinders, A. H. M. E. (2015). An empirical model for rack-mounted pv module temperatures for southeast asian locations evaluated for minute time scales. *IEEE Journal of Photovoltaics*, *5*(3), 774–782. https://doi.org/10.1109/JPHOTOV.2015.2405762